Retrieval of Vertical Profiles of Cloud Droplet Effective Radius using solar reflectance from cloud sides

Florian Ewald

Munich 2016

Retrieval of Vertical Profiles of Cloud Droplet Effective Radius using solar reflectance from cloud sides

Florian Ewald

Dissertation
at the Faculty of Physics
Ludwig–Maximilians–University
Munich

submitted by
Florian Ewald
Institute of Meteorology

Munich, March 2016

Supervisor: Prof. Dr. Bernhard Mayer
Second supervisor: Dr. Martin Weissmann
Date of submission: 02.03.2016
Date of oral exam: 26.07.2016

Zusammenfassung

Konvektive Wolken spielen eine entscheidende Rolle sowohl für das Klima der Erde, als auch für regionales Wettergeschehen, da sie einen großen Einfluss auf den globalen Strahlungshaushalt und den globalen Wasserkreislauf haben. Die Wolkenalbedo und die Bildung von Niederschlag werden im Besonderen durch Aerosolpartikel in Wolken beeinflusst. Um das Verständnis der beteiligten Prozesse zu verbessern, von der Aerosolaktivierung ueber das Wolkentröpfchenwachstum bis hin zu Veränderungen der Wolkeneigenschaften, werden Fernerkundungsmethoden zur Beobachtung dieser mikrophysikalischer Prozesse innerhalb von Wolken immer wichtiger.

Während passive Methoden zur weltraumgestützten Beobachtung weit entwickelt sind und alltäglich zur Ableitung der optischen Dicke und Tröpfchengröße von Wolkenoberkanten eingesetzt werden, bleiben Wolkenseiten weitgehend Neuland für die passive Fernerkundung. Konfrontiert mit der dreidimensionalen Struktur von Wolkenseiten verlieren 'klassische' passive Fernerkundungsmethoden, wie Nakajima-King, ihre Anwendbarkeit. Ziel dieser Arbeit ist es, die theoretische und praktische Machbarkeit zu untersuchen, ob reflektierte Solarstrahlung von Wolkenseiten genutzt werden kann, um neue Einblicke in die Vertikalentwicklung des Effektivradius zu gewinnen. Ein zentraler Aspekt dieser Studie war die Untersuchung welchen Einfluss eine unbekannte Wolkengeometrie auf die Ableitungen des Effektivradius hat. Um die räumlich hochaufgelösten Messungen von Wolkenseiten beherrschen zu können, wurde in dieser Arbeit der Nakajima-King Ansatz hinsichtlich einer unbekannten Wolkengeometrie neu durchdacht. An Hand umfangreicher Monte-Carlo Rechnungen zur Untersuchung von 3D-Effekten an konvektiven Wolkenseiten wurde die Sensitivität von reflektierter Solarstrahlung für die Wolkentröpfchengröße untersucht. Des Weiteren wurde eine Methode entwickelt, um Mehrdeutigkeiten des reflektierten Signals aufzulösen und damit die Sensitivität zu erhöhen. Dazu waren störende Einflüsse, wie Schatten, Bodenreflexionen und Eisphase zu untersuchen und entsprechende Filter zu erstellen. Auf der Grundlage der gewonnenen Erkentnisse wurde eine statische Herangehensweise gewählt, um ein Ableitung des Effektivradius zu entwickeln.

Um die Methode praktisch zu erproben wurde im Rahmen dieser Arbeit der neue hyperspektrale Wolken-Scanner specMACS (Spectrometer of the Munich Aerosol Cloud Scanner) entwickelt und in vollem Umfang charakterisiert. Zusätzlich wurde das Instrument an konvektiven Wolkenseiten aus der bodengebundenen Perspektive als auch an Bord des deutschen Forschungsflugzugs HALO (High Altitude and LOng Range Research Aircraft) erprobt. Um die Ableitungsmethode zu validieren wurden die Ergebnisse mit in-situ Messungen verglichen, welche flugzeug-getragen während der ACRIDICON-CHUVA Kampagne über dem Brasilianischem Regenwald gemacht wurden. Die vorliegende Arbeit belegt die Machbarkeit einer Ableitung von Wolkentröpfchengrößen von Wolkenseiten und stellt damit einen weiteren wichtigen Schritt zur operationellen Anwendung dieser Methode dar.

Abstract

Convective clouds play an essential role for Earth's climate as well as for regional weather events since they have a large influence on the global radiation budget and the global water cycle. In particular, cloud albedo and the formation of precipitation are influenced by aerosol particles within clouds. In order to improve the understanding of processes from aerosol activation, over cloud droplet growth to changes in cloud properties, remote sensing techniques to monitor these microphysical processes throughout the cloud are becoming more and more important.

While passive retrievals for spaceborne observations have become sophisticated and commonplace to infer cloud optical thickness and droplet size from cloud tops, cloud sides have remained largely uncharted territory for passive remote sensing. Faced with the small-scale structure of cloud sides, 'classical' passive remote sensing techniques, like Nakajima-King, are rendered inappropriate. The aim of this work is to test the theoretical and practical feasibility to gain new insights into the vertical evolution of cloud droplet effective radius by using reflected solar radiation from cloud sides. A central aspect of this study was the close analysis of the impact unknown cloud surface geometry has on effective radius retrievals. In order to handle spatially highly resolved measurements from cloud sides, this work therefore rethought the Nakajima-King approach in the context of a unknown cloud surface geometry. Using extensive Monte-Carlo calculations to explore 3D-effects at convective cloud sides, the sensitivity of reflected solar radiation to cloud droplet size was examined. Furthermore, a method was established to resolve ambiguous radiance regions and thus enhance this sensitivity. Influencing factors were identified and masked out like shadows, ground reflections and cloud ice phase. Based on these findings, a statistical approach was used to develop an effective radius retrieval.

Putting the method into practice, the new hyperspectral cloud and sky imager specMACS (Spectrometer of the Munich Aerosol Cloud Scanner) was developed and thoroughly characterized in this work. Additionally, the instrument was applied to convective cloud sides from a ground-based perspective as well as on board the new German research aircraft HALO (High Altitude and LOng Range Research Aircraft). In order to validate this approach, the retrieval was compared to aircraft in situ measurements made during the ACRIDICON-CHUVA experiment conducted over the Brazilian rain forest. The present thesis demonstrates the feasibility to retrieve cloud particle size profiles from cloud sides and thus marks a further important step towards an operational application of this technique.

Contents

CHAPTER 1

Introduction

On average, two thirds of our planet are covered by clouds (*Stubenrauch et al.*, 2013). For centuries, their eye-catching appearance has captured our imagination and curiosity. Composed of liquid water droplets or frozen ice crystals of various sizes and shapes, their particles scatter light into all directions, giving them their bright, white color against the blue sky. Beyond their visual appearance they also play an essential role in Earth's climate. Due to their reflection of solar radiation and their trapping of thermal radiation, clouds became a subject of great scientific interest. The close interactions between clouds and aerosols are still not fully understood, which has been again stressed by the *Intergovernmental Panel on Climate Change* in its *Fifth Assessment Report* (AR5):

> Clouds and aerosols continue to contribute the largest uncertainty to estimates and interpretations of the Earth's changing energy budget.
> (*Boucher et al.*, 2013)

Equally, latent heat release and transport of moisture by clouds are important factors in regional weather events. Numerical models still lack the resolution to represent all effects from the scale of a droplet to that of the entire Earth. Thus, the scientific understanding of the complex interactions and feedbacks between aerosols and clouds is still at an early stage. For that very reason, the ability to monitor and to quantify aerosol and cloud properties and their interactions is an essential step towards a better scientific understanding of their role in Earth's climate.

1.1 State of scientific knowledge

1.1.1 Role of clouds in Earth's climate system

In order to comprehend the far-reaching influence of clouds on Earth's climate system, three basic concepts have become commonplace in atmospheric science. Effects which act on the balance of incoming and outgoing radiation without changes in atmospheric dynamics are called *radiative forcings*. As evident by their bright white color, clouds reflect radiation back into space in the visible spectrum. This enhances the planetary albedo and has a cooling effect of approximately $-50\,W\,m^{-2}$ on surface temperatures. On the other hand, clouds absorb thermal radiation emitted by Earth's surface which would otherwise have escaped into space. The thermal radiation is re-emitted by clouds at a much lower temperature compared to the surface, which has a global warming effect of around $30\,W\,m^{-2}$ (*Loeb et al.*, 2009). In nights with overcast conditions, this *trapping* of thermal radiation by clouds becomes also evident by milder temperatures. The imbalance of solar and thermal effects implies an average net cooling of around $-20\,W\,m^{-2}$ which clouds exert on Earth's radiation balance. Compared with the radiative forcing of CO_2 with $1.6\,W\,m^{-2}$ (*Myhre et al.*, 2013), small changes in one of these effects can have huge ramifications on this balance.

Furthermore, changes in one climate variable can have an influence on other climate variables, which in turn can act back on the original variable. These are *climate feedbacks*, of which the *water vapor feedback* is the most important in Earth's climate. As the most important greenhouse gas, more water vapor leads to higher surface temperatures which in turn lead to more water evaporation. The coupling between cloudiness and surface air temperature is another feedback of this kind which is called *cloud feedback*. According to the current state of scientific knowledge, these cloud feedbacks are likely to be positive. While high clouds are expected to rise in altitude, and thus re-emit less thermal radiation at colder temperatures, overall cloud cover by low clouds is expected to decrease in a warmer climate (*Boucher et al.*, 2013).

While feedbacks occur only through changes in temperature, all further changes, which can occur within weeks or several months, are called *rapid adjustments* in *AR5* by the *IPCC*. Radiative forcing and feedback of clouds strongly depend on their radiative properties which are determined by water content, particle size and particle phase. While the reflection of visible solar radiation is mainly governed by cloud water content, the reflection of near-infrared solar radiation is determined by cloud droplet size (specified by the effective radius). This dependency directly links cloud microphysics, like droplet size, with the radiative forcing of clouds. In turn, cloud droplets only condensate on pre-existing hygroscopic aerosols, called cloud condensation nuclei (CCN), which links cloud microphysics with aerosol concentration. With more cloud condensation nuclei, more cloud droplets can form which in turn scatter more radiation. More clouds droplets do not only change cloud albedo (*Twomey*, 1977) but also affect precipitation-forming processes (*Rosenfeld et al.*, 2008) which have an effect on cloud life time (*Albrecht*, 1989). The following paragraph will take a closer look at these interactions to gain a better insight how natural as well as anthropogenic activities can cause rapid adjustments of clouds.

1.1.2 Aerosol–Cloud Interactions

Atmospheric aerosols are tiny particles or droplets like sea spray, raised dust or secondary particles from gaseous precursors which are suspended in the air. They can originate from natural sources as well as from anthropogenic activities. Since aerosol particles scatter and absorb light, their presence in the lower atmosphere can be observed as *haze*. Additionally, aerosols exert a radiative forcing on Earth's radiation budget which is referred to as the *direct aerosol effect*. Overall, this effect is well understood to have a slight cooling effect on Earth's climate *Boucher et al.* (2013).

Rapid adjustments of clouds to absorbing aerosols are referred to as *semi-direct aerosol effects*. *Ackerman et al.* (2000) suggested a *burn-off* effect, if absorbing aerosols are embedded in clouds, leading to the dissipation of clouds. This influence seems to be small and its impact remains in dispute (*Stier et al.*, 2007). Nevertheless, *Feingold et al.* (2005) observed a decrease in cloud cover due to a reduction in surface fluxes associated with smoke. *Wendisch et al.* (2008) also suggested that absorbing aerosols can have an influence on atmospheric stability an thus on cloud formation. However, the effects of absorbing aerosols on convection are not well understood in general.

The influence of aerosols on cloud microphysics and thus on cloud albedo is a further rapid adjustment of clouds which is also known as *Twomey effect* or *1st indirect aerosol effect*. With liquid water content held fixed and an increase in aerosol particle concentration, more but smaller cloud droplets are formed which scatter light more efficiently and thus increase cloud albedo (*Coakley et al.*, 1987, *Twomey*, 1977). The physical basis of this effect is well understood and agrees well to airborne observations of vertical profiles of cloud droplet concentration and effective radius (*Arabas et al.*, 2009, *Brenguier et al.*, 2000, *Warner*, 1955). However, the individual contributions to cloud albedo, e.g. if rather available condensate than cloud droplet number concentration is influenced, remains a matter of intense debate (*Boers and Mitchell*, 1994, *Brenguier et al.*, 2011, *Feingold et al.*, 1997). For instance, the influence of turbulent strength and mixing of cloudy air with cloud-free air (called *entrainment*) on droplet sizes and water content is still under investigation (*Liu*, 2002, *Lu et al.*, 2008).

Also known as the *Albrecht effect*, a *2nd indirect aerosol effect* on clouds has an influence on their lifetime and convective development. In the classical view of *Albrecht* (1989), higher concentration of CCNs leads to a higher cloud droplet concentration. In turn, this is believed to have an effect on the hydrological cycle and on cloud amount, since it is assumed that cloud droplet concentration plays a crucial role in the development of precipitation (*Gerber*, 1996, *Rosenfeld et al.*, 2012). *Khain et al.* (2005) and *Rosenfeld et al.* (2008) suggested, that smaller cloud droplets delay the formation of ice particles which could intensify convective development by changing the vertical distribution of latent heating. Both influences are illustrated in Figure 1.1 which shows the development of deep

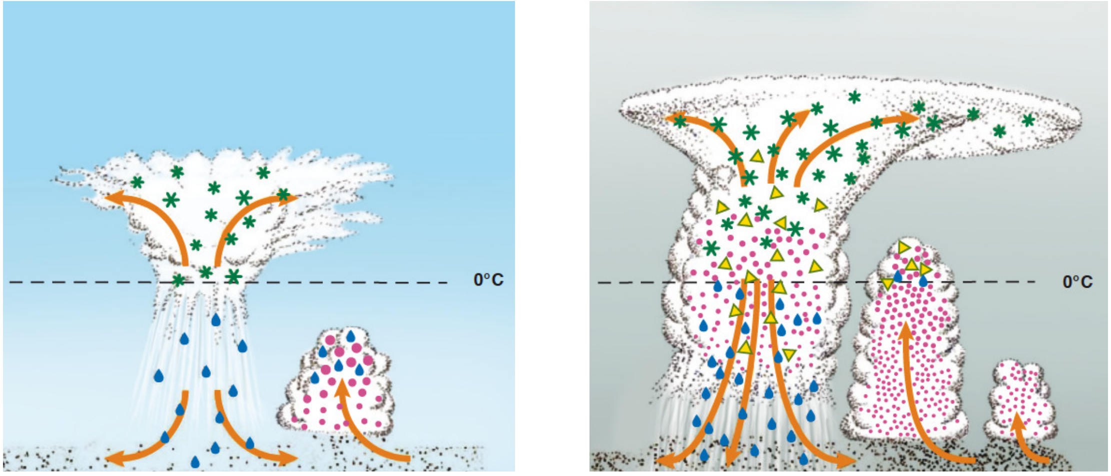

Figure 1.1: Evolution of deep convective clouds developing in the pristine **(left)** and polluted **(right)** atmosphere. As the cloud droplet growth is largely determined by CCN concentration, the smaller cloud droplet size delays the rain out and therefore the cloud dissipation in a polluted atmosphere. (Figure adapted from *Rosenfeld et al.* (2008)).

convective clouds in a pristine (Figure 1.1, left) and in a polluted (Figure 1.1, right) environment. Although these effects are still discussed, various studies found systematic correlations of increased cloud height or increased liquid water content with increased aerosol concentrations (*Christensen and Stephens*, 2011, *Pincus and Baker*, 1994, *Xue et al.*, 2008).

Combined, the *direct aerosol effect* as well as the three mentioned aerosol-cloud interactions are thought to have an overall cooling effect on Earth's climate (*Boucher et al.*, 2013). With anthropogenic emissions of aerosols, like sulfur dioxide (SO_2) and organic carbon, still rising in large parts of the world (*Lu et al.*, 2011), aerosol-cloud interactions have to be thoroughly understood to asses their implications for Earth's climate. For this reasons, a global monitoring of the process from aerosol activation to rainout of large cloud droplets becomes essential in advancing the scientific understanding of climate change.

1.2 Current state of passive remote sensing of clouds

The spectrally resolved measurement of solar radiation is a long standing method in earth science. In the beginning half of the 20th century GORDON DOBSON introduced the method of spectroscopy into the field of atmospheric remote sensing (*Dobson*, 1931). On the basis of passive measurements of the absorption of solar radiation by stratospheric ozone, he determined the depth and variability of the ozone layer. Since then the exploitation of gaseous and particle absorption and scattering has led to the development of ground-based and spaceborne measurement platforms for spectral remote sensing of trace gas profiles and cloud properties.

There exists various methods in the solar spectrum to infer optical properties (e.g. cloud cover, optical thickness and cloud absorption) from observations of cloud tops from above using information about the scattered and absorbed radiation (e.g., *Arking and Childs* (1985), *King* (1981, 1987), *King et al.* (1990), *Plass and Kattawar* (1968)). Phase detection is the first step for every cloud property retrieval. Spectral absorption differences in the near-infrared or brightness temperature differences in the thermal infrared are commonly used to distinguish between liquid water and ice (e.g., *King et al.* (2004), *Nakajima and King* (1990)). Besides optical properties, there also exist various techniques to retrieve microphysical cloud properties like cloud thermodynamic phase and effective particle size (e.g., *Bugliaro et al.* (2011), *Han et al.* (1994), *Nakajima and King* (1990), *Platnick et al.* (2001), *Roebeling et al.* (2006)).

Remote sensing of cloud and aerosol parameters is still mostly done by use of multi-spectral sensors, i.e., using only a limited number of spectral bands. Prominent examples are, e.g., ground-based aerosol retrievals using CIMEL sun-photometers in the Atmospheric Radiation Measurement Program and the Aerosol Robotic Network (AERONET, *Holben et al.* (1998)) or satellite based multichannel techniques following *Hansen and Pollack* (1970) and *Twomey and Cocks* (1989) for remote sensing of cloud properties. Common examples of spaceborne imagers are the Advanced Very High Resolution Radiometer (AVHRR), the Moderate Resolution Imaging Spectroradiometer (MODIS), and the Spinning Enhanced Visible Infrared Imager (SEVIRI).

Systems like the Solar Spectral Flux Radiometer (SSFR, *Pilewskie et al.*, 2003) or the Spectral Modular Airborne Radiation measurement sysTem (SMART, *Wendisch and Mayer*, 2003, *Wendisch et al.*, 2001) were used for cloud remote sensing from ground (*Chiu et al.*, 2012, *Jäkel et al.*, 2013, *McBride et al.*, 2011) or airborne perspective (*Ehrlich et al.*, 2008, *Eichler et al.*, 2009, *Schmidt et al.*, 2007). While most techniques from these two instruments still use only a few channels to derive cloud optical thickness or cloud particle size from solar transmissivity or reflectivity measurements (*Coddington et al.*, 2010, *Kikuchi et al.*, 2006, *McBride et al.*, 2011), some first techniques use spectral slopes for identification of cloud phase (*Ehrlich et al.*, 2009, *Jäkel et al.*, 2013). Only recently *Coddington et al.* (2012) and *LeBlanc et al.* (2015) proposed and systematically tested a range of characteristics of the full spectrum to be used for general ground-based cloud remote sensing. However, the application of spectrally resolved, hyperspectral techniques in cloud and aerosol remote sensing is still in its early stages. All of these methods are based on non-imaging sensors, i.e., only one measurement is taken at a time and one line of measurements is constructed by sensor motion or cloud motion over a ground-based measurement.

Nowadays, most imaging remote sensing of clouds is satellite-based. However, there are concerns about measurement artifacts influencing retrievals of aerosol and cloud properties caused by small-scale cloud inhomogeneity which are unresolved by the coarse spatial resolution of spaceborne platforms (*Marshak et al.*, 2006a, *Varnai and Marshak*, 2007, *Zinner and Mayer*, 2006). The effect of unresolved cloud inhomogeneity is demonstrated in Figure 1.2, where the same cloud side scene is rendered with different spatial resolutions corresponding to different existing imagers. Furthermore, enhanced clear sky reflectance near clouds by radiation scattered by cloud edges can contaminate aerosol retrievals in the vicinity of clouds (*Varnai and Marshak*, 2009, *Wen et al.*, 2007). These problems need to be taken into account in order to observe aerosol-cloud interactions reliably.

Figure 1.2: Influence of spatial resolution Δx of a cloud side as it would be measured **(a)** by the geostationary imager SEVIRI ($\Delta x = 3500\,\mathrm{m}$), **(b)** by its High Resolution Visible (HRV) channel ($\Delta x = 1000\,\mathrm{m}$), **(c)** by the Earth-orbiting imager MODIS ($\Delta x = 250\,\mathrm{m}$) and **(d)** by the *specMACS* instrument ($\Delta x = 70\,\mathrm{m}$) which was developed during this thesis. Original picture: Thunderstorm Off the Coast of Republica de Chile (taken from the International Space Station), ISS015-E-27038, September 7, 2007.

1.3 Scientific objectives and scope of this work

To this end *Marshak et al.* (2006b), *Martins et al.* (2011), *Zinner et al.* (2008) and *Ewald et al.* (2013a) proposed cloud side scanning measurements of convective clouds to observe the basically vertical development of cloud particles. To retrieve particle size and thermodynamic phase they propose to use solar radiation in the near-visible to near-infrared spectral regions reflected by cloud sides. This application is a core goal for the development of the new *spectrometer of the Munich Aerosol Cloud Scanner (specMACS)*. With the help of an imaging spectrometer, the required spatially resolved measurements become possible. Especially the vertical dimension of these observations should reflect many aspects of cloud-aerosol-interaction as well as mixing of cloudy and ambient air (*Martins et al.*, 2011, *Rosenfeld et al.*, 2012). For the same partially cloudy scenes, additional remote measurements of interacting aerosol characteristics (particle type, size, amount) as well as of some gaseous atmospheric components could become accessible by exploitation of the spectral image information.

The Meteorological Institute Munich already hosts a range of instruments for remote measurements of the atmosphere: an aerosol lidar, a millimeter-wave cloud radar, a sun-photometer and multiple Differential Optical Absorption Spectroscopy (DOAS) instruments. This work will expand this suite of remote sensing techniques towards the passive remote sensing of clouds sides using a imaging spectrometer. Figure 1.3 shows the basic measurement concept to infer cloud microphysics from cloud side reflected solar radiation.

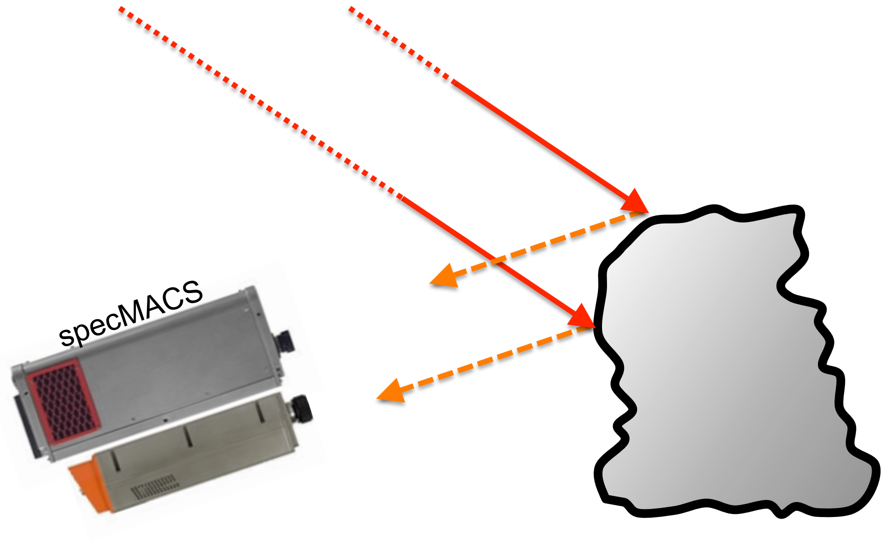

Figure 1.3: The basic measurement concept presented in this work to infer cloud microphysics from cloud side reflected solar radiation, following the approach suggested by *Marshak et al.* (2006b), *Zinner et al.* (2008) and *Martins et al.* (2011).

The present work will introduce a framework for the remote sensing of cloud droplet effective radius profiles from cloud sides based on *Zinner et al.* (2008) and *Ewald et al.* (2013a). This thesis will not only test this framework numerically, but will also present a real-world implementation of the proposed cloud side technique. In the course of this work, following scientific objectives will be addressed:

1. Determine the sensitivity of reflected radiances from cloud sides to cloud droplet radii in the context of a unknown cloud geometry for the ground-based as well as for the airborne perspective.
2. Investigate external influences which can interfere with the proposed cloud side remote sensing technique.
3. Characterize the spectral and radiometric calibration of an imaging spectrometer to investigate the feasibility to measure the reflected radiances with sufficient accuracy.
4. Demonstrate the possibility to retrieve effective radius profiles from cloud sides in real-world applications.

The scope of this work will be limited to the liquid part of convective liquid water clouds, e.g. Cumulus and Cumulus congestus, which exhibit well-developed cloud sides. More complex absorption properties of ice particles will need more detailed studies. Thus, ice phase is excluded in this work.

1.4 Outline of this thesis

This thesis is organized as follows: Chapter 2 will give an introduction into basic concepts and principles of cloud microphysics (Section 2.1) and its interaction with solar radiation (Section 2.4). The following Chapter 3 will then introduce the numerical framework used throughout this work. In Chapter 4, the statistical retrieval of effective radius profiles from cloud sides will be introduced. After the sensitivity of reflected radiances from cloud sides to cloud droplet radii is examined in Section 4.1, the statistical correlation found in extensive Monte Carlo simulations of the radiative transfer in cloud sides is tested for its validity. In order to bring the theoretical concept into real-world application, Chapter 5 introduces and characterizes the newly developed *specMACS* imager as a significant part of this thesis. This part will show if the required radiometric accuracy for the retrieval can be achieved. Finally, the proposed retrieval technique will be put to the test with ground-based and airborne measurements with *specMACS* in Chapter 6 as well as compared with independent in situ measurements of cloud droplet sizes. A discussion of radiometric and retrieval uncertainties follows in Chapter 7, and the summary and outlooks are given in Chapter 8.

CHAPTER 2

Clouds and Atmospheric Radiation

2.1 Liquid water cloud microphysics

This section will give a short introduction into the mechanism of cloud droplet formation and their growth during their ascent in clouds. Furthermore, the most important cloud microphysical properties will be introduced which help to describe the vast number of cloud droplets within each cloud.

2.1.1 Saturated-adiabatic ascent of air

When solar radiation heats up air at the surface, air parcels expand and start to rise. In an *adiabatic expansion* without transfer of heat or matter, the air temperature $T(z)$ decreases with air pressure p along the *dry adiabatic lapse rate* $\Gamma_{d,ad}(z)$:

$$T(z) = T(0) + \Gamma_{d,ad}(z) \tag{2.1}$$

$$e_s(T) = 6.1094 \exp\left(\frac{17.625T}{T + 243.04}\right) \tag{2.2}$$

$$RH = \frac{e}{e_s(T)}. \tag{2.3}$$

With slower water molecules at lower temperatures, the saturation vapor pressure e_s decreases with temperature following the *August-Roche-Magnus* formula (Equation 2.2). The ratio between the actual vapor pressure e and the saturation vapor pressure e_s is called *relative humidity* RH (Equation 2.3). When e_s reaches the vapor pressure e of the parcel ($RH = 100\,\%$), cloud droplets form around CCNs and condensation occurs. As latent heat is released during condensation, the temperature decreases more slowly with height along the *moist adiabatic lapse rate* $\Gamma_{m,ad}(z)$. The mass of water vapor relative to the mass of air is called *mixing* *ratio of water vapor* q_v. It can be derived using the saturated water vapor pressure e_s and the pressure of air p:

$$q_v = 0.622\frac{e_s}{p} \tag{2.4}$$

$$q_l = q_v^s(h_{cb}) - q_v^s(h). \tag{2.5}$$

When $(RH = 100\,\%)$, q_v is called *saturation mixing ratio of water vapor* q_v^s. For liquid water, the *mixing ratio of liquid water* q_l specifies the mass of condensed water vapor relative to the mass of air. During an adiabatic ascent, the *mixing ratio of total water* $q_t = q_v + q_l$ is a conserved quantity. For this reason, q_l can be calculated as the excess water vapor between $q_v^s(h_{cb})$ at cloud base h_{cb} and $q_v^s(h)$ at any height h within the cloud (Equation 2.5).

2.1.2 Cloud droplet growth by condensation

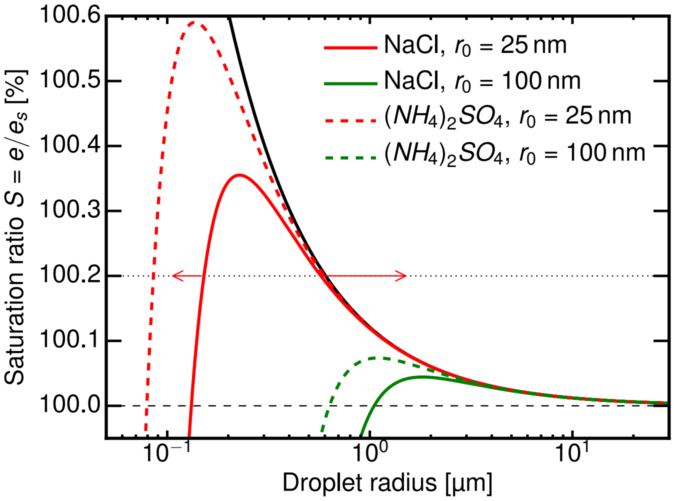

Figure 2.1: Water vapor saturation ratios for droplets which formed around different aerosol particles of different size and composition. With an ambient saturation ratio of $S = 100.2\%$, only droplets formed around CCNs with $r_0 = 100\,\mathrm{nm}$ continue to grow.

Liquid water clouds are composed of tiny water droplets. They form when the water vapor in the air becomes supersaturated. When a number of water molecules form a tiny droplet due to random collision, *surface tension* has to be overcome in order to increase the radius of the droplet. The *vapor pressure of water* e between the vapor and its condensed phase is called *saturation vapor pressure* e_s when as many molecules return to the liquid as escape it. With an increasing curvature of the liquid-vapor interface the water vapor saturation pressure rises (*Kelvin effect*, *Thomson* (1871)). The ratio between ambient water vapor pressure e and e_s is called saturation ratio S or relative humidity, which in Earth's atmosphere rarely exceeds the usual range of $100.2 - 100.8\%$ (*Seinfeld and Pandis*, 2012). Tiny droplets formed by random collisions of water molecules re-evaporate due to the *Kelvin effect* which can be seen in Figure 2.1. For this reason, droplets need *cloud condensation nuclei* (CCN) which get *activated* by water vapor and can grow into cloud droplets. With an initial droplet radius r_0 to start from, the amount of solvent molecules from the CCN further lowers the water vapor pressure due to dilution (*Raoult's Law*, *Raoult* (1887)). In Figure 2.1, saturation ratios for droplets are shown which formed around aerosol particles composed of NaCl (sodium chloride) and $(NH_4)_2SO_4$ (ammonium sulfate) with initial radii of $r_0 = 25\,\mathrm{nm}$ and $r_0 = 100\,\mathrm{nm}$. While saturation ratios differ between solutes due to a different number of ions, droplets around the smaller CCNs (red lines) need a considerably higher saturation ratio S to avoid re-evaporation. Droplets around larger CCNs (green lines) can continue to grow for an ambient saturation ratio of $S = 100.2\%$ until reaching sizes typically found in clouds between $5\,\mu\mathrm{m}$ and $15\,\mu\mathrm{m}$. As the saturation ratio increases, the largest CCNs get activated first, with smaller CCNs following at larger saturation ratios. When aerosol concentration is low and all CCNs have already been activated, the initial cloud droplet concentration is determined shortly after cloud base.

2.1.3 Further growth by coalescence and particle freezing

As the growth of droplet radii by condensation is getting considerably slower for larger droplet volumes, a further process is needed to reach the millimeter size of rain drops. With droplets carried along by convective updrafts, they collide with each other and coalesce to form larger droplets This effect becomes dominant above $r > 15\,\mathrm{um}$. When the droplets get to heavy for weaker updrafts, they fall down in form of rain (*warm rain process*). For stronger updrafts, cloud droplets get lifted into colder regions of the upper troposphere where they begin to freeze.

Pure water droplets do not freeze spontaneously without CCN, unless the ambient temperature falls below $-42\,°\mathrm{C}$ (*Koop*, 2004). For most clouds however, ice crystals can be found shortly after ambient temperature fall below $0\,°\mathrm{C}$. This happens due to the *Bergeron–Findeisen process*, where a freezing nucleus is needed to initiate the freezing process shortly below $0\,°\mathrm{C}$. After a droplet has frozen, the ice crystal particle grows quickly at the expense of other liquid droplets, since saturation vapor pressure over ice is less than over liquid water. Since freezing nuclei are typically much rarer than cloud condensation nuclei, super-cooled cloud droplets and ice crystal particles coexist for a certain time within a mixed-phase layer. If the ice particles get to heavy, they fall down and melt to form rain which is known as *cold rain process*. This is the process that produces precipitation in most locations on Earth.

2.1.4 Cloud droplet size distribution

In an environment with lower CCN concentrations, the available water vapor condenses onto a small number of large droplets. In this case, the condensation process is limited by the number of cloud condensation nuclei. In a polluted environment with higher CCN concentrations, many small cloud droplets can form on an abundant number of aerosol particles. The fact that many small droplets reflect more light than a few large droplets links aerosol concentrations with the cloud radiative effect on the atmospheric energy budget. Due to the diverse radii of aerosol particles, the *cloud droplet size distribution* $n(r)$ is very broad shortly after condensation. As the growth by condensation slows down with radius, the different droplet radii become more uniform with time until they approach a narrow distribution somewhere between 5 and 10 µm. For this reason, the very chaotic ensemble of cloud droplets has typically a very narrow cloud droplet size distribution $n(r)$. This changes when coalescence becomes effective which leads to a continued growth of droplets with an increasing mode and mean cloud droplet radius of $n(r)$ as indicated in Figure 2.2. It is these processes which mainly determine the cloud albedo and the onset of rain and which should therefore be observed throughout the cloud profile.

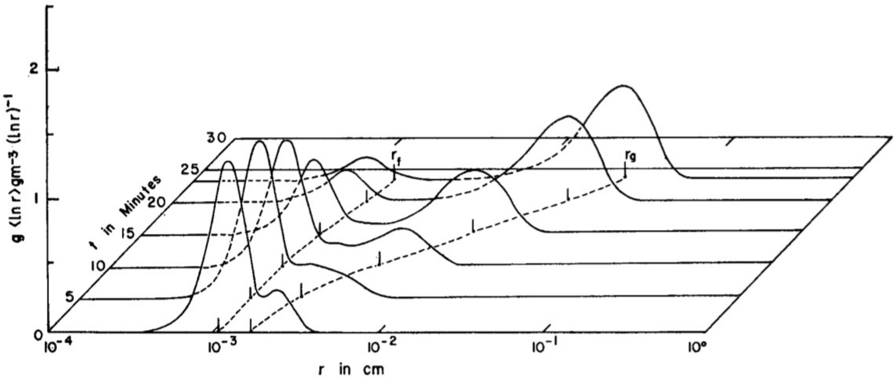

Figure 2.2: Time evolution of a bi-modal cloud droplet distribution with initial modes of $r_1 = 10\,\mu m$ and $r_2 = 20\,\mu m$ as modeled by *Berry and Reinhardt* (1974)

2.1.5 Effective radius

Besides the mode and the mean cloud droplet radius, there exist further moments of $n(r)$ describing the cloud droplet distribution. One commonly used parameter is the *effective radius* which is derived by dividing the 3th moment $r^3\,n(r)$ of the cloud droplet size distribution $n(r)$ with the 2th moment $r^2\,n(r)$:

$$r_{\text{eff}} = \frac{\int_0^\infty r\,\pi r^2\,n(r)dr}{\int_0^\infty \pi r^2\,n(r)\,dr} \quad [\mu m]. \tag{2.6}$$

Cloud droplets in cumulus clouds have typical values for r_{eff} between 4 µm and 15 µm with larger droplets in environments with lower concentration of cloud condensation nuclei (*Brenguier et al.*, 2000). As more water vapor condenses, the cloud droplet effective radius increases with height (*Arabas et al.*, 2009, *Slingo et al.*, 1982, *Stephens and Platt*, 1987, *Warner*, 1969) while its remains fairly constant for a given height in the cloud (*Blyth and Latham*, 1991, *Freud et al.*, 2008, *Gerber*, 2006, *Wang and Rong*, 2009).

As a microphysical cloud property, the effective radius links cloud microphysics with the way how cloud droplets interact with solar radiation. Section 2.5.2 will show how different cloud droplet size distributions have the same optical properties in the solar spectrum, if they have the same effective radius. Due to the weighting, the effective radius r_{eff} is always larger than the *volumetric radius* r_{vol} and for most cloud droplet distributions it is also larger than the most likely radius in $n(r)$. *Martin et al.* (1994) proposed a *correction factor* $k^3 = r_{\text{vol}}/r_{\text{eff}}$ to convert between effective and volumetric radius. This correction factor k depends on the width of the specific cloud droplet size distribution $n(r)$ and varies between 0.67 and 0.8 (*Brenguier et al.*, 2000).

2.1.6 Liquid water content

Another moment of the cloud droplet size distribution is the mass of the droplet ensemble. Most commonly it is defined as total droplet mass in gram per cubic meter, called the *liquid water content* (LWC). It can be derived by integration over $n(r)$ using the volume of the droplets and the density of water ρ_w:

$$\text{LWC} = \frac{4}{3}\pi\,\rho_w \int\limits_0^\infty n(r)\,r^3\,dr \quad [\text{g m}^{-3}]. \tag{2.7}$$

Beside the thermodynamic phase, the effective radius and the liquid water content are the most important microphysical properties which define the optical properties of a cloud in the solar spectrum. If ice particles and cloud droplets are present, the *total water content* TWC is the sum of liquid water content LWC and ice water content IWC:

$$\text{TWC} = \text{LWC} + \text{IWC}, \qquad \gamma = \frac{\text{IWC}}{\text{TWC}}. \tag{2.8}$$

The ratio between IWC and TWC is called ice fraction ratio γ. Normally, LWC increases with cloud height up to the freezing level as cooler air contains less water vapor. Typical LWC values for cumulus clouds range between 0.2 and $1.3\,\text{g m}^{-3}$ and can vary quite significantly at one height (*Warner*, 1955).

2.1.7 Liquid water path

With the liquid water content as a cloud parcel property, the integration of LWC with height yields the *liquid water path* (LWP) which describes the total amount of liquid water within a cloud above a given surface area:

$$\mathrm{LWP} = \int_0^z \mathrm{LWC}(z)\,\mathrm{d}z \quad [\mathrm{g\,m^{-2}}]. \tag{2.9}$$

It is usually given in unit of $\mathrm{g\,m^{-2}}$ and links the liquid water content with the *brightness* of the solar reflection by a cloud. The higher the liquid water path, the more opaque the cloud.

2.1.8 Adiabatic profile of cloud microphysics

Without mixing of sub-saturated surrounding air, the mixing ratio of total water q_t remains constant during an *adiabatic ascent*. The difference between the saturation vapor mixing ratio $q_v^s(h_{cb})$ at cloud base and $q_v^s(h)$ at any height h within the cloud therefore yields the adiabatic liquid water content $LWC_{ad}(h)$:

$$LWC_{ad}(h) = \rho_{air}\,(q_v^s(h_{cb}) - q_v^s(h)), \tag{2.10}$$

$$r_{eff,ad}(h) = k^{-1/3} r_{v,ad} = \left(\frac{LWC_{ad}(h)}{(4/3)\pi\rho_w}\right)^{1/3} (kN_{cb})^{-1/3}. \tag{2.11}$$

In addition, the total droplet number N remains constant throughout the ascent as long as no mixing, evaporation or coalescence is taking place. Accordingly, the profile of a *volumetric adiabatic radius* $r_{v,ad}$ can be derived following Equation 2.11. By using the empirical correction factor k between effective radius r_{eff} and mean volume radius r_v, this leads to the *effective adiabatic radius* $r_{eff,ad}$ (see e.g. *Brenguier et al.* (2000), *Martin et al.* (1994)).

2.1.9 Influence of lateral entrainment on cloud microphysics

The turbulent transport of dry, sub-saturated air into the cloud, illustrated schematically in Figure 2.3, is another essential process for cloud microphysics and cloud dynamics. Since heat and matter is exchanged with the environment, this mixing causes a deviation from the adiabatic profile of cloud microphysics. The process is called *entrainment* and occurs at cloud top and close to the edges of clouds. Hereby, the mixing time is a critical factor in determining the kind of mixing. When the mixing proceeds slowly and at larger scales, larger pockets of dry air get mixed with cloudy air. Consequently, total evaporation of droplets within these dry regions lead to a decrease in total droplet number N_d while droplets in the vicinity remain unaffected (extreme inhomogeneous mixing, *Baker et al.* (1980)).

In contrast, faster mixing with entrainment of smaller filaments of dry air leads to a more homogeneous sub-saturated condition. With all droplets experiencing the same sub-saturated condition, they all shrink by evaporation, shifting the effective radius r_{eff} to smaller values while the total droplet number N_d remains unaffected (homogeneous mixing, *Jensen et al.* (1985)). The cooling by this droplet evaporation leads to a buoyant subsiding shell only a few meters thick, which has been discovered in high frequency in situ measurements (*Katzwinkel et al.*, 2014, *Wang et al.*, 2009) as well as in spatially highly resolved LES simulations (*Heus et al.*, 2009). In general, however, many in situ studies have shown that r_{eff} is largely invariant to LWC at a certain height (*Blyth and Latham*, 1991, *Brenguier et al.*, 2000, *Freud et al.*, 2008).

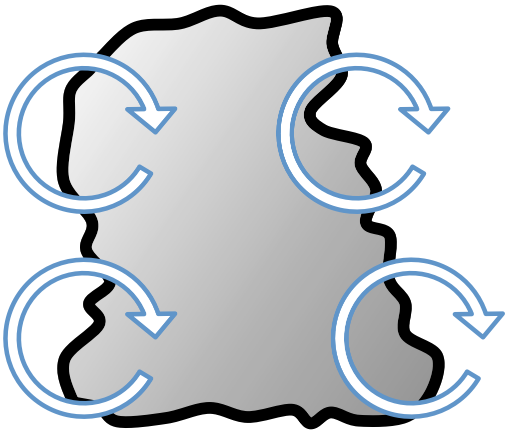

Figure 2.3: Schematic sketch illustrating the turbulent transport of dry, sub-saturated air into the cloud. This mixing of cloudy air with clear air at cloud sides is called *lateral entrainment*.

Following the approach by *Gerber et al.* (2008), the entrainment regime can be determined at each height with the help of the ratio between the measured volumetric cloud droplet radius r_{vol} found at cloud edge with the volumetric cloud droplet radius $r_{\text{v,max}}$ found at cloud core (defined at the location of maximum LWC in each height). During extreme inhomogeneous mixing, cloud droplet sizes would be unaffected (black dashed line in Figure 2.4a), while liquid water content would decrease due to dilution of N_d by total evaporation of all droplets within that air pocket (black dashed line in Figure 2.4b). During homogeneous mixing, cloud droplet sizes would decrease from cloud cores (red drawn line in Figure 2.4a) by evaporation in a homogeneous sub-saturated condition, while the total number N_d of cloud droplets would be unaffected (red drawn line in Figure 2.4b). To get a better understanding how the cloud droplet number, the cloud droplet effective radius and the liquid water path influence the ra-

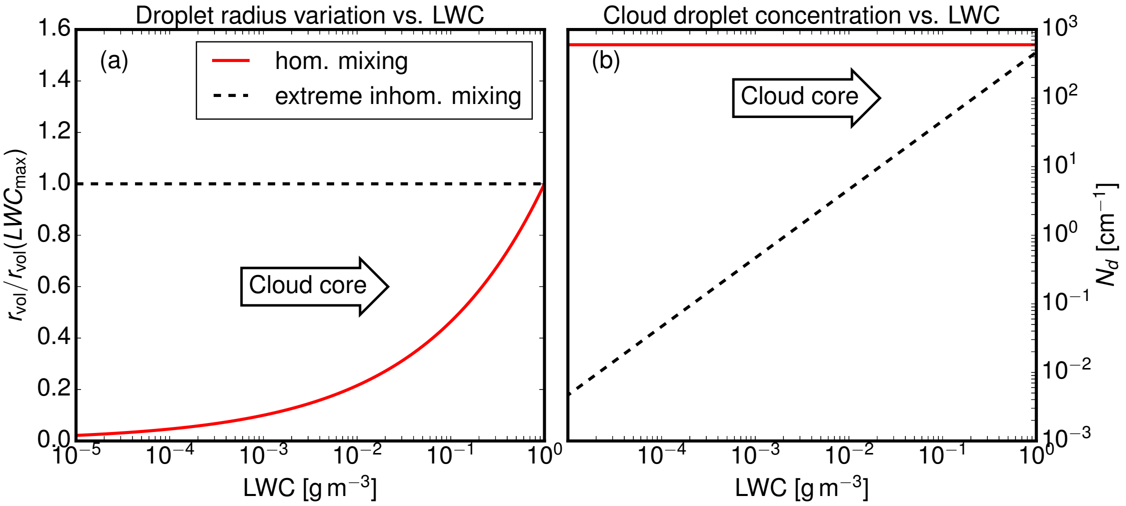

Figure 2.4: **(a)** Deviation of volumetric radius r_{vol} to $r_{v,max}$ found at maximum LWC as a function of LWC at one height in a cloud. **(b)** Cloud droplet number concentrations N_d [cm^{-1}] as a function of LWC at one height in a cloud. The lines indicate values of r_{vol} and N_d that would be found in homogeneous mixing (red drawn) and extreme inhomogeneous mixing (black dashed) regimes.

diative transfer in clouds, the following chapter will give an introduction into atmospheric radiation and its interaction with atmospheric constituents.

2.2 Electromagnetic Theory

Intrinsically tied to the study of particles, the description of particle interactions lies at the heart of physics. Besides the weak nuclear, strong nuclear and gravitational force the electromagnetic force is one of the four fundamental forces. First believed to be caused by two distinct forces, electricity and magnetism are nowadays universally accepted to be a unified model which describes the interaction between charged particles.

The interaction of charged particles with each other are described by the theory of classic electromagnetism. The electric force between charged particles is described by the electric field **E**. With an electric point charge ρ as source the electric field **E** in vacuum is defined by the permittivity of free space ϵ_0 (Equation 2.12a). In contrast the magnetic field **B** is caused by an electric current **j** and can be expressed in numbers using the permeability of free space μ_0 (Equation 2.12b)

$$\nabla \cdot \mathbf{E} = \frac{\rho}{\epsilon_0} \tag{2.12a}$$

$$\nabla \times \mathbf{B} = \mu_0 \mathbf{j} \tag{2.12b}$$

While both fields are caused by electrically charged particles, the magnetic field **B** does not originate from electric charges themselves, but from the electric current **j** of charged particles.

2.2.1 Maxwell Equations

In his famous paper *A Dynamical Theory of the Electromagnetic Field* (*Maxwell*, 1865), James Clark Maxwell was the first who unified the theories of electricity and magnetism in a set of equations known as *Maxwell's equations*. In charge-free vacuum the temporal change of the magnetic field **B** induces a circular electric field **E** around the field lines of **B**. Vice versa a temporal change in **E** causes a magnetic field **B** around the field lines of **E**. In the formulation following Oliver Heaviside (Equation 2.13) *Maxwell's equations* can be used to identify this interaction as the cause of electromagnetic waves:

$$\left.\begin{aligned} \nabla \cdot \mathbf{E} &= 0 \\ \nabla \cdot \mathbf{B} &= 0 \\ \nabla \times \mathbf{E} &= -\frac{\partial \mathbf{B}}{\partial t} \\ \nabla \times \mathbf{B} &= \mu_0 \epsilon_0 \frac{\partial \mathbf{E}}{\partial t} \end{aligned}\right\} \quad \begin{aligned} \frac{\partial^2 \mathbf{E}}{\partial t^2} - c^2 \cdot \nabla^2 \mathbf{E} &= 0 \\ \frac{\partial^2 \mathbf{B}}{\partial t^2} - c^2 \cdot \nabla^2 \mathbf{B} &= 0 \end{aligned} \tag{2.13}$$

When taking the curl of the curl terms in Equation 2.13 on the left and inserting the divergence terms one obtains the electromagnetic wave equations shown in Equation 2.13 on the right. With the **E** and **B** field perpendicular to each other the solution of the wave equation describes an electromagnetic wave travelling with a constant phase velocity v_g.

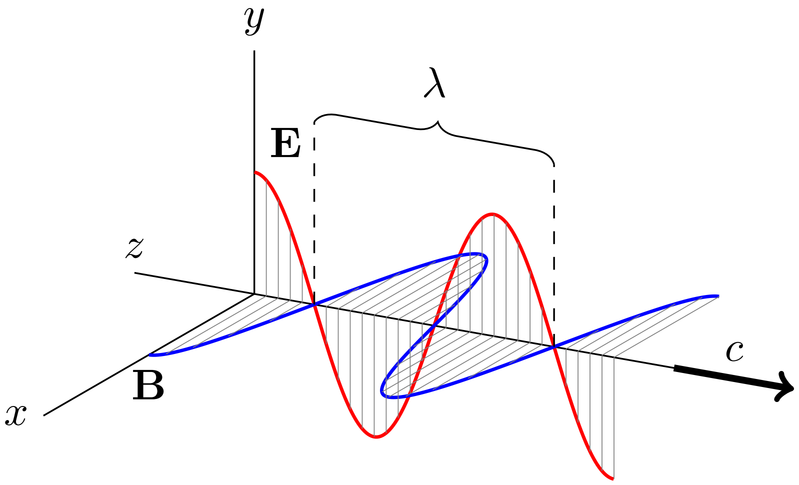

Figure 2.5: **E** and **B** field of an electromagnetic wave propagating along the z-direction

The phase velocity v_g of light in vacuum is defined by the permittivity ϵ_0 and the permittivity μ_0 of free space which are combined in $c = \frac{1}{\sqrt{\epsilon_0 \mu_0}}$. Together with the phase veolcity c, the frequency ν of the electromagnetic wave defines its wavelength $\lambda = \frac{c}{\nu}$. In the Cartesian reference system a solution for the electric field **E** of a plane electromagnetic wave propagating along the z-direction is given by

$$\begin{pmatrix} E_x(z,t) \\ E_y(z,t) \\ 0 \end{pmatrix} = \begin{pmatrix} E_{0x} e^{i(kz-\omega t+\phi_x)} \\ E_{0y} e^{i(kz-\omega t+\phi_y)} \\ 0 \end{pmatrix} = \begin{pmatrix} E_{0x} e^{i\phi_x} \\ E_{0y} e^{i\phi_y} \\ 0 \end{pmatrix} e^{i(kz-\omega t)}. \tag{2.14}$$

Here, equivalent notations of wavelength λ and frequency ν are the wave number $k = \frac{2\pi}{\lambda}$ and the angular frequency $\omega = \frac{2\pi c}{\lambda}$. The remaining vector in Equation 2.14 describes the amplitudes E_{0x} and E_{0y} and phases ϕ_x and ϕ_y of the electric field **E** in the x- and y-direction. The orientation of this vector is also called the *polarization* of the electromagnetic wave. By introducing the theory of waves into the theory of electromagnetism, Maxwell shaped the understanding of the nature of light as an electromagnetic wave.

2.2.2 Photons

Despite the elegance of the wave theory measurements of electromagnetic absorption and emission could not be explained with this idea. Electromagnetic waves can transfer energy to electrons bound in material, just like they are caused by moving electrons, At sufficiently high energies these electrons are ejected from the material in the form of photoelectrons which is known as the *photoelectric effect*. However, measurements have shown that their kinetic energy is independent of the amplitude of the electromagnetic wave. Based on this observation, Albert Einstein deduced that a beam of light has to be quantized into packets of energy E_{ph} where the energy level has to be a function of the wavelength λ:

$$E_{ph} = h\nu, \qquad \text{with} \quad h = 6.626\,069\,57(29) \times 10^{-34}\,\mathrm{J\,s}. \tag{2.15}$$

Here, h denotes the *Planck constant* which links the frequency ν of an electromagnetic wave with the energy packets E_{ph} it consists of. These packets of energy are called *photons*, elementary particles which constitute all forms of electromagnetic radiation. Neglecting polarization these particles are entirely described by their direction of propagation and their energy $E_{ph} = h\nu$. In vacuum the wavelength λ therefore solely determines their energy $E_{ph} = \frac{hc}{\lambda}$. The discovery that light should be regarded as stream of photons solved the puzzling questions raised by the photoelectric effect and by electromagnetic radiation within confined cavities.

2.3 Basics of Radiative Transfer

As humans on the macroscopic scale we do not perceive electromagnetic waves as photons but as beams of light which get emitted, scattered and absorbed by matter. We can only perceive a fraction of the electromagnetic spectrum (390 nm to 700 nm) as visible light. The visible spectrum is followed by the infrared spectrum at lower values of E_{ph}, while the electromagnetic spectrum continues into the ultraviolet and X-Ray region at larger photon energies E_{ph},

2.3.1 Radiation quantities and units

Due to the large number of photons in a light beam, it is convenient to describe the light beam in terms of its transported energy and direction of propagation. The radiated energy ∂Q per unit time ∂t in Equation 2.16a is called **radiant flux** Φ. It is proportional to the square of the amplitude of the electric field $\mathbf{E}$ and increases linearly with the number of photons. When the radiant flux is expressed per unit surface dA as radiance flux density of Φ in Equation 2.16b it is called **irradiance** E.

$$\Phi = \frac{\partial Q}{\partial t} \quad [W] \tag{2.16a}$$

$$E = \frac{\partial \Phi}{\partial A} \quad [W\,m^{-2}] \tag{2.16b}$$

While the radiant flux Φ is normally used to specify the power of an electromagnetic source, the irradiance E describes the electromagnetic flux density at a certain distance to the source. Since the surface area around a source increases with the square of the radius, the irradiance E of a source is inversely proportional to the square of the distance.

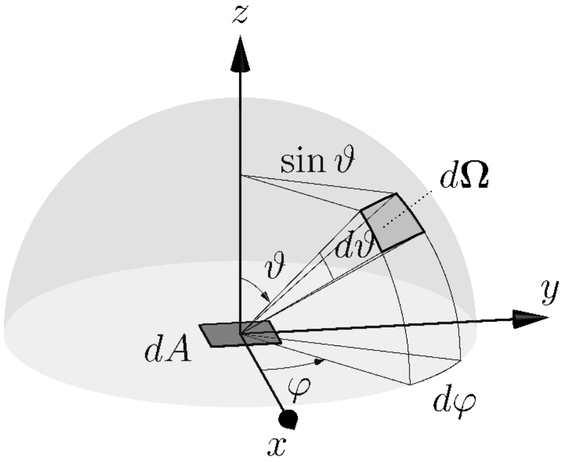

Figure 2.6: In spherical coordinates the radiance L is defined by the azimuth angle φ, the zenith angle ϑ, the solid angle $d\Omega$ and the surface dA for which the radiant flux is described.

Besides its energy, radiation is also defined by its direction of propagation as shown in Figure 2.6. Described by its azimuth φ and zenith angle Θ the radiant flux Φ, emitted or received per unit solid angle $d\boldsymbol{\Omega}$ is given as **radiant intensity** I in watt per steradian. In terms of photons, I specifies the number of photons per second which are received from or emitted into a specific unit solid angle $d\boldsymbol{\Omega}$. When the radiant intensity for dA is related to the projected area $\Delta A = \cos\vartheta dA$ perpendicular to the light propagation, it is called **radiance** L which is introduced in Equation 2.17b. Radiance is measured by imaging instruments and is the radiation quantity that comes closest to the human perception of light. With the unit solid angle $d\boldsymbol{\Omega} = \sin\vartheta d\phi d\vartheta$ as reference, radiant intensity I and radiance L are distance-invariant quantities to describe and measure the radiation of a source. In addition, the spectral distribution of the radiance can be described by the **spectral radiance** L_λ.

$$I = \frac{\partial\Phi}{\partial\boldsymbol{\Omega}} \qquad [W\,sr^{-1}] \qquad (2.17a)$$

$$L = \frac{\partial^2\Phi}{\cos\vartheta\partial A\partial\boldsymbol{\Omega}} \qquad [W\,m^{-2}\,sr^{-1}] \qquad (2.17b)$$

$$L_\lambda = \frac{\partial^3\Phi}{\cos\vartheta\partial A\partial\boldsymbol{\Omega}\partial\lambda} \qquad [W\,m^{-2}\,sr^{-1}\,nm^{-1}] \qquad (2.17c)$$

When the radiance L is integrated over the upper hemisphere, shown for surface dA in Figure 2.6, one obtains the irradiance E for dA. Dividing the irradiance E by $h\nu$ one again gets the number of photons which are passing through surface dA per time ∂t. With its directionality the spectral radiance L_λ fully describes a beam of light if polarization is neglected.

Reflectivity

For the same radiant intensity I, the irradiance E passing through a surface varies with the surface inclination towards the radiation propagation direction. For this reason, the amount of reflected radiation by a surface is significantly determined by the illumination angle to this surface. The spectral *reflectance* R_λ is obtained, when the measured spectral radiance L_λ is related to the incoming irradiance E_0 and the cosine $\cos\vartheta_0$ of the illumination angle:

$$R_\lambda = \frac{\pi L_\lambda}{E_0 \cos\vartheta_0} \tag{2.18}$$

The **spectral reflectance** R_λ (or reflectivity) is commonly used in remote sensing applications, since it describes the reflection of radiation independenly from the incident light source.

2.4 Interaction of Radiation with the Atmosphere

There are various ways how electromagnetic radiation can interact with atomic matter. While atoms can be the source for electromagnetic radiation by *emission* of photons, they also can extinguish photons from the incident beam by absorption or scattering which together is called *extinction*. Like the electron, subatomic particles are bound within the atom in quantum wells formed by the fundamental forces. Electromagnetic waves can interact with these particles elastically by scattering or inelastically by absorption. Using the theory of the driven harmonic oscillator both processes can be understood by discrete electric charges bound within matter (dielectric material) which are set into oscillatory motion by the the incoming electromagnetic wave. Within a dielectric, an electromagnetic wave induces a dielectric polarization density $\mathbf{P}$ by displacing its bounded charges from their equilibrium positions. In case of a harmonic oscillator this polarization depends on the driving frequency which is described by the electric susceptibility $\chi_e(\nu)$. Together with the electric permittivity of free space ϵ_0, P is proportional to the electric field $\mathbf{E}$:

$$\mathbf{P} = \epsilon_0 \chi_e(\nu) \mathbf{E}. \tag{2.19}$$

Hereby, the moving electric charges re-radiate an electromagnetic wave which is phase-shifted with respect to the incident wave due to the harmonic oscillation. Due to the phase-shift in subsequent scattering events, the phase velocity v_p in the dielectric is smaller than the speed of light c in vacuum. The ratio in Equation 2.20 between v_p and c is described by the real part n_r of the complex *index of refraction* n where the electric susceptibility $\chi_e(\nu)$ acts as a squared damping ratio:

$$n = \sqrt{1+\chi_e(\nu)} = n_r + i n_i, \qquad n_r = \frac{c}{v_p}. \tag{2.20}$$

In medium changes of n_r are therefore causing the optical refraction of a plane electromagnetic wave by the change in phase velocity v_p. The dependence of n_r on the frequency ν is called *dispersion* which, for example, explains the refraction of white light containing waves of all frequencies into a color spectrum by a prism.

In the region of natural frequencies of the harmonic oscillator inelastic interactions by absorption of photons becomes possible. Analogous to *dampening* in the case of the harmonic oscillator, the absorption of electromagnetic radiation is determined by the imaginary part n_i of n.

2.4.1 Emission

Most of the light we see and experience in Earth's atmosphere is caused by thermal motion of charged particles. Therefore every body emits *thermal radiation* according to its temperature. According to the second law of thermodynamics bodies within a physically closed system exchange energy until thermal equilibrium is reached. Following this empirical finding, Gustav Robert Kirchhoff concluded that at thermal equilibrium every body has to emit the same amount of energy it absorbs (*Kirchhoff*, 1866). The absorption is specified by the absorptivity of the material which describes the ratio between absorbed and incident radiant flux. The absorptivity α is defined by the ratio of the absorbed and incident radiant flux on a certain material. A body with $\alpha = 1$ absorbs all incoming light and is therefore called a *black body*. To remain in thermal equilibrium a *black body* has to emit the same amount of radiation. The emissivity ε compares the thermal emission of an arbitrary body with the emission of a black body of the same temperature. For the same reason as for the black body, the emissivity ε of an arbitrary body equals its absorptivity α in thermal equilibrium. This finding became known as **Kirchhoff's law of thermal radiation**. As a consequence of Kirchhoff's law, the emitted spectral radiance L_λ is only governed by the spectral absorptivity α_λ and the temperature of the body:

$$\frac{L_\lambda}{\alpha_\lambda} = f(\lambda, T). \tag{2.21}$$

To Kirchhoff, the function $f(\lambda,T)$ was still unknown and it was not until 1900 when the German physicist Max Planck specified this function analytically.

Like many physicist in early 1900, Max Planck was concerned with the description of electromagnetic radiation within confined cavities since it has been widely used as a model of a black body. Satisfying the condition of zero electric field at the walls, there exists an infinite number of stationary waves within a conducting cavity. Seen from the outside, a small hole in this cavity would be a black surface which would absorbed all incident radiation and only emit thermal radiation wave modes from within the cavity. Following the classical law of thermodynamics each wave mode would contain the same energy in thermodynamic equilibrium which leads to a paradox of the classical wave theory. Since there exists an infinite number of wave modes at higher frequencies the energy density within the cavity would be infinite. Max Planck solved this paradox by his assumption that the energy in the cavity wave modes has to be quantized into discrete energy levels E_{ph} which are linked to the frequency ν of the contained electromagnetic wave (Eq.2.15). In thermodynamic equilibrium high energy levels become less likely for wave modes with higher frequencies due to this quantization. As required by Equation 2.21, the spectral radiance of a black body is described by **Planck's law** as a sole function of its temperature T and the observed wavelength λ (*Planck*, 1900):

$$f(\lambda,T) = B_\lambda(T) = \frac{2hc^2}{\lambda^5}\frac{1}{e^{\left(\frac{hc}{\lambda kT}\right)} - 1} \tag{2.22}$$

Here, the Boltzmann constant $k = 1.380 \times 10^{-23}\,\mathrm{J\,K^{-1}}$ links thermal energy with temperature T. The first quotient in Equation 2.22 is part of the **Rayleigh-Jeans law** and specifies the energy density within the cavity as a function of the frequency. Based only on classical wave theory and volumetric reasoning the energy density would diverge at high frequencies due to this term. Planck complemented this term with a quantum mechanical approach by adding a second term in Equation 2.22 which links the quantized wave mode energy levels with the probability of their occurrence according to the Bose-Einstein distribution.

As shown in Figure 2.7, the spectral radiance $B_\lambda(T)$ is solely described and unique for each temperature T and wavelength λ. With its colors illustrated in Figure 2.7, the visible spectrum (390 nm to 700 nm) lies within the spectral radiance distribution emitted by very hot bodies like the sun with a temperature of $T = 5778\,\mathrm{K}$. In contrast, the spectral radiance distribution at terrestrial temperatures has it maximum around $10\,\mu\mathrm{m}$ which is therefore called the *terrestrial spectrum*.

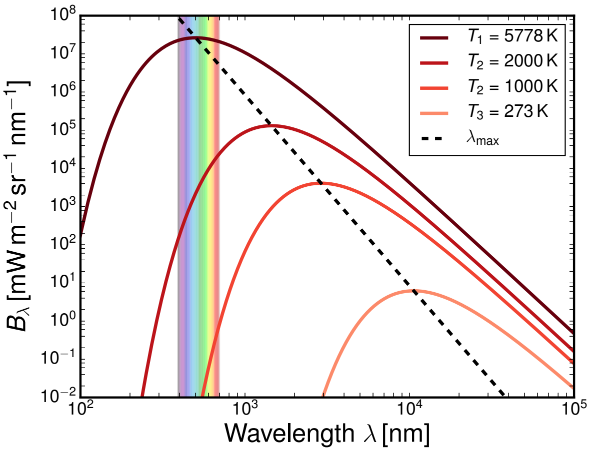

Figure 2.7: Spectral radiance distributions according to Planck's law (Equation 2.22

In 1896, Wilhelm Wien already discovered another (*Wien*, 1896) basic principle of thermal radiation which can be seen in Figure 2.7. When differentiating $B_\lambda(T)$ with respect to λ it becomes obvious that the spectral radiance distribution exhibit an unique maximum λ_{max} for every temperature T. The inverse relationship in Equation 2.23 between the temperature and λ_{max} is known as **Wien's displacement law**:

$$\lambda_{\mathrm{max}} = \frac{2897{,}8\,\mu\mathrm{m\,K}}{T}. \tag{2.23}$$

Moreover, the black body irradiance E_B is a unique function of the temperature and can be obtained when *Planck's law* is integrated over all wavelengths and the upper half-space shown in Figure 2.6. Known as **Stefan-Boltzmann's law**, the black body irradiance E_B can be calculated using the *Stefan-Boltzmann constant* $\sigma = 5.670\,373(21) \times 10^{-8}\,\mathrm{W\,m^{-2}\,K^{-4}}$ and temperature T:

$$E_B = \int_0^\infty \int_\Omega B_\lambda(T) \cos\vartheta \, \sin\vartheta \, d\phi \, d\vartheta \, d\lambda = \sigma T^4. \tag{2.24}$$

2.4.2 Absorption

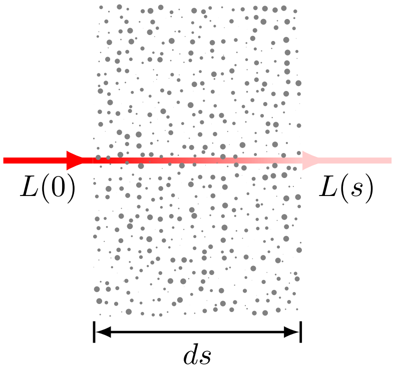

Figure 2.8: Absorption following the Lambert-Beer law.

With light being emitted from matter it can also be absorbed by it. Subatomic particles within atoms take up discrete energy levels which can absorb light of corresponding wavelength, causing narrow absorption lines (*spectral lines*) in continuous light spectra. Moreover, electromagnetic waves can excite various vibration and rotation modes of polarizable molecules. In gaseous or solid matter, multiple of these modes get broadened into whole *absorption bands* where light is absorbed in a wider range of wavelengths. The broadening thereby happens due to collisions with other particles (*pressure broadening*) or by random thermal motion of the particle (*Doppler broadening*).

Each particle can be assigned an effective area for which photons are removed from the incident beam by absorption. This **absorption cross-section** $\sigma_{abs}(r)$ is measured in $[m^2]$. Combined with the particle concentration $n(r)$ in $[m^{-3}]$, the integration over the radius r of all absorption cross-sections $\sigma_{abs}(r)$ yields the **absorption coefficient** k_{abs} in $[m^{-1}]$.

$$dL(ds) = -L(0) \underbrace{\int_0^\infty n(r)\sigma_{abs}(r)dr}_{k_{abs}} \tag{2.25}$$

The amount of radiance $dL(ds)$ absorbed along a thin slab of thickness ds, shown in Figure 2.8, is direct proportional to the original radiance $L(0)$ and the combined absorption cross-sections $\sigma_{abs}(r)$ of all particles within ds. Solving Equation 2.25 for the remaining radiance $L(s)$ and integrating along the distance s leads to:

$$L(s) = L(0) \exp\left(-\int_0^s \int_0^\infty n(r)\sigma_{abs}(r)drds \right). \tag{2.26}$$

This expression is known as **Lambert-Beer's law** which describes the exponential decline of $L(s)$ for a constant absorption coefficient k_{abs}. In Figure 2.9, the imaginary component of the refractive indices of ice and water is shown as a function of wavelength between 0.2 and 3.7 µm. The indices were determined in laboratory measurements by *Warren* (1984) for liquid water and by *Segelstein* (1981) for ice. While water is nearly transparent in the visible wavelength range, the absorption strongly increases with the imaginary refractive index in the

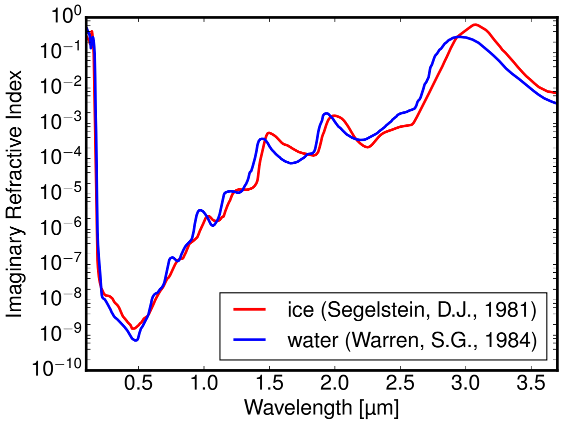

Figure 2.9: Spectral dependence of the imaginary component of the refractive indices of ice and water between 0.2 and 3.7 µm. Data for water was taken from *Warren* (1984), data for ice from *Segelstein* (1981).

near-infrared wavelength region. The differential characteristic between liquid water and ice will be used during phase discrimination which is introduced in Section 2.6.2.

2.4.3 Scattering

In between the emission of a photon and its absorption the direction of its propagation can be changed by scattering. As described in the beginning of this section, scattering can be understood by the interaction of electromagnetic waves with electric point charges, set into oscillatory motion by the electric field of the wave. The re-radiated wave is called the scattered wave. Just like waves on a lake these scattered waves can interfere with each other which gives rise to the different macroscopic phenomena attributed to scattering. The characteristic of these interference is governed by the heterogeneity of the material and the spatial arrangement of its bound electric point charges. When a planar wave front hits a material in which the particles are stationary and arranged in a tightly packed grid with distances below the wavelength λ, the scattered waves exhibit a fixed phase shift. In this *coherent scattering* the fixed phase shift leads to constructive and destructive interference for specific angular directions. Although individually named, *specular reflection* and *optical refraction* are nothing else than coherent scattering at smooth interfaces of different indices of refraction n_r. When the scatterers are distributed more heterogeneous the phase relation between different waves vanishes and the different scattering events become independent This *incoherent scattering* is more isotropic and can be observed as *diffuse reflection* on coarse surfaces or in heterogeneous mixtures of solids in fluids or the atmosphere. Besides the wavelength λ and the index of refraction n_r, the spatial arrangement of the scatterers determines if the classic laws of refraction or laws for single scattering can be applied.

Single scattering by particles

This distinction becomes especially important for the scattering by larger particles, e.g. cloud droplets, where coherent scattering as well as incoherent scattering are at work. While water molecules as oscillating charges within a cloud droplet are tightly packed together compared to the wavelength of visible light, the average distance between cloud droplets is far larger than the wavelength. For this reason the scattering by a single cloud droplet results from the superposition of scattering events by all molecules within the droplet while the scattering by multiple droplets are incoherent single scattering events.

As the particle size increases, the scattered wave of more and more point charges interfere with each other cancelling out more scattering directions. Since the phase relation in the direct forward direction is invariant to the separation of the oscillating point charges the scattering in the forward direction becomes more likely for larger particles. To incorporate this scale dependence the **size parameter** X is used to relate the circumference $2\pi r$ of the particle to the wavelength λ of the electromagnetic wave:

$$X = \frac{2\pi r}{\lambda} \tag{2.27}$$

While the scattering process can be approximated by the radiation of an oscillating dipole at very small values of $X \ll 1$, the scattering by very large particles $(X \gg 1)$ are described by the classic laws of geometric optics.

Shown in Figure 2.10, the angle between the incident direction and the direction of scattering is called the *scattering angle* ϑ_s. The *asymmetry parameter* g specifies the ratio between forward and backward scattering and is given as the average cosine $\langle\cos\vartheta_s\rangle$ of the scattering angle ϑ_s, With $g > 0$, the particle scatters more in the forward direction while $g < 0$ means more backward scattering.

The angular pattern of the scattering by a singular cloud droplet are described by the **phase function** $\mathcal{P}_\lambda(\mathbf{\Omega}' \to \mathbf{\Omega})$. This function specifies the probability that a photon from the incident direction $\mathbf{\Omega}'$ gets scattered into direction $\mathbf{\Omega}$. In order to fulfill the requirement of a probability density function the integral of $\mathcal{P}_\lambda(\mathbf{\Omega} \to \mathbf{\Omega}')$ over all scattering directions $\mathbf{\Omega}'$ is unity:

$$\frac{1}{4\pi}\int_{4\pi} \mathcal{P}_\lambda(\mathbf{\Omega} \to \mathbf{\Omega}')\, d\mathbf{\Omega}' = 1 \tag{2.28}$$

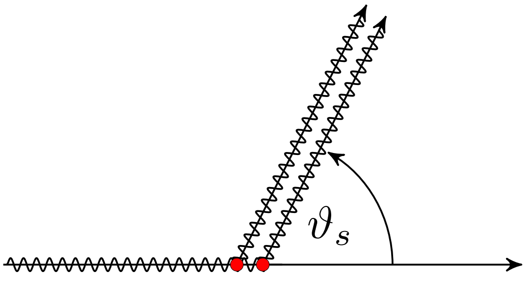

Figure 2.10: Definition of the scattering angle ϑ_s shown for a direction of constructive interference. The red dots are two oscillating point charges.

Each cloud droplet scatters light proportional to its scattering cross-section $\sigma_{sca}(r)$. The scattering efficiency $Q_{sca}(r)$ as ratio between the scattering cross-section $\sigma_{sca}(r)$ and the geometrical cross-section $\sigma_{geo}(r)$, is a convenient factor to connect a droplet size distribution with its corresponding scattering coefficient k_{sca}.

$$Q_{sca}(r) = \frac{\sigma_{sca}(r)}{\pi r^2} \tag{2.29}$$

The probability for a scattering event is given by the effective area which removes photons from the incident beam into any other direction. Each cloud droplet scatters light proportional to its **scattering cross-section** $\sigma_{sca}(r)$. This scattering cross-section $\sigma_{sca}(r)$ is not necessarily connected with the geometric cross-section $\sigma_{geo}(r)$ of the particle. Combined with the phase function $\mathcal{P}$ the *differential scattering cross-section* $\frac{d\sigma_{sca}}{d\Omega}$ describes the angular probability for a scattering event to occur. For multiple individual scatterers the probability for a scattering event is given by the **scattering coefficient** $k_{sca}(r)$ as the sum of the individual scattering cross-sections of n particles:

$$k_{sca}(r) = n\,\sigma_{sca}(r) = n \int\limits_{4\pi} \frac{d\sigma_{sca}}{d\boldsymbol{\Omega}} \mathcal{P}_\lambda\left(\boldsymbol{\Omega} \to \boldsymbol{\Omega}'\right) d\boldsymbol{\Omega}' \tag{2.30}$$

The scattering efficiency $Q_{sca}(r)$ as ratio between the scattering cross-section $\sigma_{sca}(r)$ and the geometrical cross-section $\sigma_{geo}(r)$, is a convenient factor to connect a droplet size distribution with its corresponding scattering coefficient k_{sca}.

$$Q_{sca}(r) = \frac{\sigma_{sca}(r)}{\pi r^2} \tag{2.31}$$

Rayleigh scattering

One prominent example of incoherent scattering is the blue color of the sky. In his famous paper, *Rayleigh* (1899) associated the blue sky color with the scattering of visible light by air molecules much smaller than the wavelength ($X \ll 1$). *Rayleigh's scattering law* describes the scattering by an air molecule with the induced dipole moment $\mathbf{p}$ of a single point charge which is related to the average electric susceptibility $\chi_e(\nu)$ of the medium (compare Equation 2.19). For unpolarized light the induced dipole moment $\mathbf{p}$ can be separated into two orthogonal components parallel $\mathbf{p}_\parallel$ and perpendicular $\mathbf{p}_\perp$ to the plane formed by the incident and scattered direction. Within this plane the perpendicular part $\mathbf{p}_\perp$ of the induced dipole moment creates a radial symmetric electric field which is invariant to the scattering angle ϑ_s. The electric field of the parallel part $\mathbf{p}_\parallel$ decreases with $\sin\vartheta_s$ since no radiation is emitted along the direction of the dipole moment. As the square of the electric field, the angular distribution of the scattered radiant flux has therefore the following form:

$$\mathcal{P}_{R,\perp}(\mu) = 1, \qquad \mathcal{P}_{R,\parallel}(\mu) = \mu^2, \qquad \sigma_{sca} \approx \frac{2\pi^5}{3}\frac{d^6}{\lambda^4}\left(\frac{n^2-1}{n^2+2}\right)^2 . \tag{2.32}$$

The scattering cross-section σ_{sca} of the air molecule can be derived from the steady-state solution of a driven harmonically bound particle with the diameter d and refractive index n. Combined with a suitable normalization, both components $\mathcal{P}_{R,\perp}$ and $\mathcal{P}_{R,\parallel}$ result in the Rayleigh phase function $\mathcal{P}_R$. In combination with the scattering cross-section, $\mathcal{P}_R$ leads to the radiant intensity I_R of light scattered by the molecule:

$$\mathcal{P}_R(\mu) = \frac{3}{4}(1+\mu^2), \qquad I_R(\mu) = I_0\frac{8\pi\alpha^2}{\lambda^4 R^2}(1+\mu^2). \tag{2.33}$$

Illustrated with the blue line in Figure 2.11, the Rayleigh scattering in the forward and backward direction is twice as likely as perpendicular to the incident direction. The wavelength dependence of the scattered intensity can be obtained when the energy loss by re-radiation is included within the theory of the driven harmonic oscillator. RAYLEIGH was the first to give a formula (Equation 2.33) for the angular intensity distribution $I_R(\mu)$. Here, α is the molecular polarizability of the scattering molecule. Inversely to the square of the distance R to the scatterer, the radiant intensity I_R also varies inversely with the fourth power of the wavelength λ^4. For this reason, Rayleigh scattering is weaker in the red and stronger in the blue part of the spectrum which explains the blue color of the sky.

Mie scattering

For objects much larger than the wavelength $(X \gg 1)$, the approach of using singular point charges becomes more complicated. The superposition of their combined emitted electromagnetic waves are described by the *Mie theory*. LUDVIG LORENZ was one of the first physicists who searched and found analytical solutions for the scattering of electromagnetic waves by homogeneous, dielectric spheres. Independently rediscovered by GUSTAV MIE in 1908, both approached the problem of scattering by multiple and interacting dipoles with the method of multipole expansion (*Mie*, 1908). Hereby, the electromagnetic fields, originating from the different dipoles, are expressed in a series expansion in terms of angular functions in spherical coordinates. Satisfying the boundary conditions given by the Maxwell equations, their solution is a sum of the incident and scattered fields which are expressed in vector spherical harmonics. By separation of variables into an angular part, represented by spherical harmonics, and a radial part, represented by *Bessel functions*, the Mie theory gives analytical equations for the coefficients which combined the internal and external fields of the sphere.

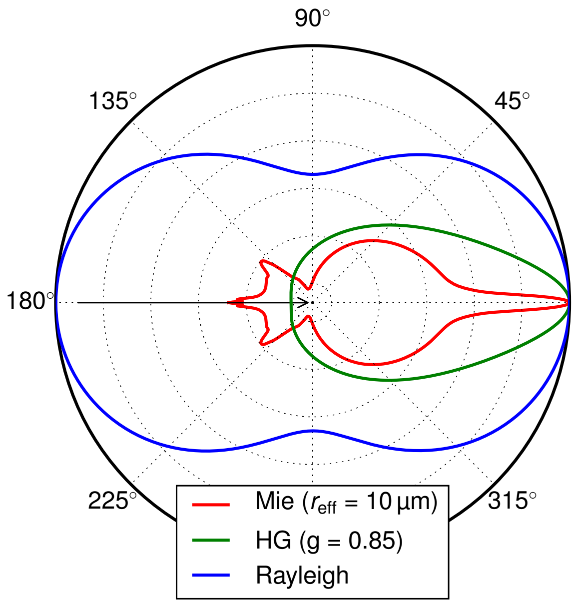

Figure 2.11: Logarithmic plots of various phase functions. Red: Rayleigh, Blue: Mie, Green: Henyey-Greenstein.

As shown in Figure 2.11 (red line), the Mie phase function $\mathcal{P}_{\mathrm{Mie}}(\cos\vartheta_s)$ is a rotationally symmetric function with a wide forward lobe which ends in a very strong and narrow forward peak. The given example is calculated for light with $\lambda = 2100\,\mathrm{nm}$ which is scattered by a water droplet with a radius of $10\,\mu\mathrm{m}$. Besides the forward peak, visible features in the backscatter direction become more pronounced as the droplet size increases or wavelength decreases. Called *glory*, the peaks in the immediate vicinity of the backscatter peak are caused by surface waves propagating around the droplet. The *fog bow* at smaller scattering angles around $\vartheta_s \approx 138°$ transforms into the colorful display of the rainbow for sizes of rain drops. In the limit of geometric optics, the peak of the rainbow can be connected with total internal reflections while its colors can be explained by dispersion happening within the water droplet. An analytical approximation to the Mie phase function is the *Henyey-Greenstein* phase function (*Henyey and Greenstein*, 1941) which is shown by the green line in Figure 2.11.

The sum of absorption and scattering is called *extinction*. The **extinction coefficient** k_{ext} can be derived by adding the absorption and scattering coefficients:

$$k_{\mathrm{ext}} = k_{\mathrm{abs}} + k_{\mathrm{sca}}. \tag{2.34}$$

2.4.4 Radiative transfer equation

With their *birth* by emission, their *life* during scattering and their *death* by absorption, the transport of photons can be described by an *energy conservation formula* known as the **radiative transfer equation** (RTE). With the emission as a photon source $k_{\mathrm{ext}} J_\lambda$ and with extinction as a photon sink $k_{\mathrm{ext}} L_\lambda$, *Chandrasekhar* (1950) described the change ∇L_λ in total spectral radiance as sum of these two terms:

$$-\nabla L_\lambda = k_{\mathrm{ext}} \left(L_\lambda - J_\lambda \right). \tag{2.35}$$

This differential equation describes the change ∇L_λ of incident light from direction (1) while it traverses an infinitesimal distance $d\mathbf{s}$. Hereby, the gains and losses in L_λ can be separated into three processes as illustrated in Figure 2.12. While traversing along ds, extinction of photons from the original beam (0) acts as a sink of L_λ by absorption (1) within the volume $dA\,ds$ or by out-scattering (2). Just as photon are lost by scattering, in-scattering (3) from other directions $\mathbf{\Omega}'$ into the original light beam acts as a source of L_λ. Another source of L_λ is the re-emission (1) of photons within the volume $dA\,ds$. Therefore, the sink term in Equation 2.36 separates into a term described by the scattering coefficient k_{sca} and another term described by the absorption coefficient k_{abs}. The same holds true for the source term, which separates into a part describing the in-scattering J_λ^s and an part describing the emission J_λ^e:

$$-\nabla L_\lambda = k_{sca,\lambda} L_\lambda + k_{abs,\lambda} L_\lambda - k_{sca,\lambda} J_\lambda^s - k_{abs,\lambda} J_\lambda^e \tag{2.36}$$

In Equation 2.36, both scattering terms are governed by the same scattering coefficient k_{sca} while the absorption and the emission term are described together by the absorption coefficient k_{abs} as required by *Kirchhoff's law*.

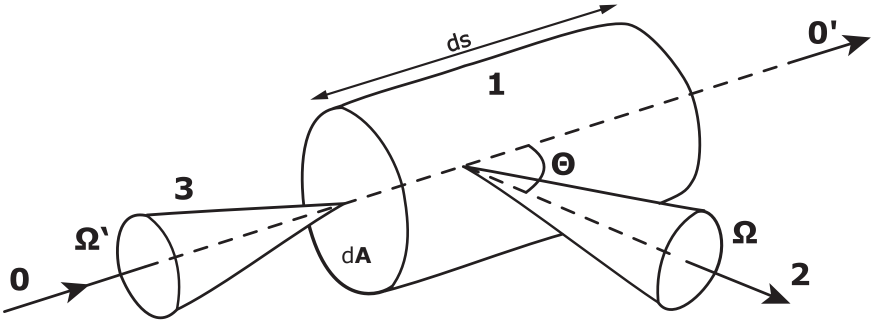

Figure 2.12: Processes in the radiation transfer equation

In order to satisfy conservation of energy, Equation 2.36 has to be integrated over the hemisphere to include the in- and out-scattering terms covering all other directions $\mathbf{\Omega}'$. In the notation of (*Zdunkowski et al.*, 2007), the radiance gained by in-scattering between $\mathbf{\Omega}' \to \mathbf{\Omega}$ is described by Equation 2.37 as a convolution of $L_\lambda(\mathbf{\Omega}')$, originating from $\mathbf{\Omega}'$, and the scattering phase function $\mathcal{P}_\lambda$:

$$k_{sca,\lambda}(\mathbf{\Omega}' \to \mathbf{\Omega}) J_\lambda^s = \frac{k_{sca,\lambda}}{4\pi} \int_{4\pi} \mathcal{P}_\lambda(\mathbf{\Omega}' \to \mathbf{\Omega}) L_\lambda(\mathbf{\Omega}') d\mathbf{\Omega}' \tag{2.37}$$

$$k_{sca,\lambda}(\mathbf{\Omega} \to \mathbf{\Omega}') L_\lambda = \frac{k_{sca,\lambda}}{4\pi} \int_{4\pi} \mathcal{P}_\lambda(\mathbf{\Omega} \to \mathbf{\Omega}') d\mathbf{\Omega}' L_\lambda = k_{sca,\lambda} L_\lambda \tag{2.38}$$

In contrast, the out-scattering $\mathbf{\Omega} \to \mathbf{\Omega}'$ of photons can be described in Equation 2.38 solely by k_{sca} over the integral over the scattering phase function $\mathcal{P}_\lambda$. With the restriction to one-dimensional radiation transport in a layered atmosphere with $\Omega = \cos\vartheta = \mu$, a common form of the RTE is obtained from Equation 2.39 after integration over λ:

$$\underbrace{\boldsymbol{\Omega}\nabla L_\lambda}_{\substack{\text{dL in }\boldsymbol{\Omega}\text{-}\\ \text{direction}}} = \underbrace{-k_{ext,\lambda}L_\lambda}_{\substack{\text{extinction}\\ \text{out of beam}}} + \underbrace{\frac{k_{sca,\lambda}}{4\pi}\int_{4\pi}\mathcal{P}_\lambda(\boldsymbol{\Omega}'\to\boldsymbol{\Omega})L_\lambda(\boldsymbol{\Omega}')d\boldsymbol{\Omega}'}_{\text{scattering into beam}} + \underbrace{k_{abs}J^e_\lambda}_{\text{emission}} \tag{2.39}$$

$$\mu\frac{dL}{dz} = -k_{ext}L + \frac{k_{sca}}{4\pi}\int_{4\pi}\mathcal{P}(\boldsymbol{\Omega}'\to\boldsymbol{\Omega})L(\boldsymbol{\Omega}')d\boldsymbol{\Omega}' + k_{abs}B_{Planck}(T). \tag{2.40}$$

While the RTE forms the basis for many theories in astronomy, in remote sensing and in climate science, an analytic solution for this differential-integral equation has yet to be found. For this reason, the last decades have seen numerous numerical approximations to make predictions for the radiative transport in planetary atmospheres.

2.5 Cloud optical properties

Optical properties of clouds can be obtained when their microphysical properties (Section 2.1) are combined with the way in which light interacts with the atmosphere (Section 2.4). Local cloud optical properties describe the extinction, the scattering and the absorption with coefficients k_{ext}, k_{sca}, k_{abs} and a mean phase function $\overline{\mathcal{P}}$ for a specific cloud volume. Global cloud optical properties influence the transmission and reflection functions of clouds, which can be measured by ground-based or airborne spectrometers (*Kokhanovski*, 2004). Analogous to the liquid water path (Section 2.1.7), these properties are integrated cloud optical properties like the *optical thickness* and a *mean scattering radius* which directly influence the transmission and reflection of clouds. Therefore, optical thickness and mean scattering radius are accessible by remote sensing of cloud reflection (*Hansen and Pollack*, 1970, *Nakajima and King*, 1990, *Twomey and Cocks*, 1989) and are a common way to describe whole cloud ensembles over wide areas.

2.5.1 Optical thickness

An apparent cloud optical property is the vertically integrated extinction. In the visible spectrum, scattering is the dominant contribution to extinction. The vertically integrated extinction therefore significantly influences the amount of scattered radiation and in turn the reflected radiance. Following Lambert-Beer's

Law in Equation 2.26, radiance is deceased to $L(z)$ after passing through a cloud between height $h = 0$ and $h = z$:

$$L(z) = L(0)\ \exp\left(-\int_{0}^{z/\mu} k_{\text{ext}}\,dz\right) = L(0)\ \exp\left(-\tau/\mu\right) \tag{2.41}$$

$$\tau = \int_{0}^{z}\int_{0}^{\infty} n(r)\,\sigma_{\text{ext}}(r)\,dr dz = \int_{0}^{z} k_{\text{ext}}\,dz \tag{2.42}$$

The radiation removed in Equation 2.41 from initial radiance $L(0)$, largely leaves the cloud and can be measured as reflected radiance. In Equation 2.41, the extinction coefficient k_{ext} of a specific layer is determined by integrating the extinction cross-sections $\sigma_{\text{ext}}(r)$ over the droplet size distribution $n(r)$. The result of the vertical integration in Equation 2.42 of the extinction coefficient is called **optical thickness** τ. Generalized to slanted paths of angle μ through the cloud, the **slant optical thickness** τ/μ is the argument of the exponential function in Equation 2.41. At an optical thickness of $\tau/\mu = 1$ within the cloud, the unscattered radiance (direct radiation) is reduced by $^1/_e$.

2.5.2 Mean scattering radius

As introduced in Section 2.1.4, liquid water clouds are condensed water droplets, where their concentration is described by cloud droplet size distributions. To reduce the number of free parameters, cloud droplet size distributions of liquid clouds can be approximated by analytical functions. A commonly used analytical function is the *modified gamma distribution* (MGD). In the form Equation 2.43 following *Deirmendjian* (1969), the modified gamma distribution is defined by the three parameters C, B and α. Equation 2.43 can be rewritten by separating B into the two parameter a and b which determine the location and the width of the modified gamma distribution. Likewise, α can be replaced by the distribution width b. The third parameter C can then be written as a function of parameter a, b and the *total droplet number per unit volume* N which is the sum over the droplet size distribution $n(r)$. With the natural logarithm $\ln\Gamma$ of the Gamma function Γ, the modified gamma distribution is therefore defined by a, b and N:

$$n\left(r\right) = Cr^{\alpha}\exp\left(-Br\right) = Cr^{(1-3b)/b}\exp\left(-\frac{r}{ab}\right) \tag{2.43}$$

$$C = N(ab)^{2b-1/b}\ln\Gamma\left(\frac{1-2b}{b}\right) \tag{2.44}$$

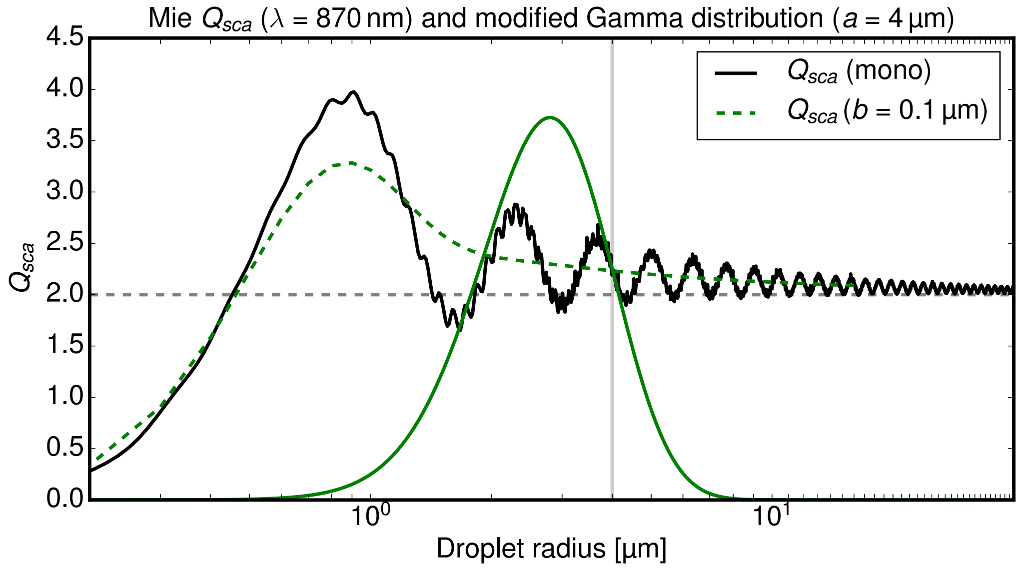

Figure 2.13: Scattering efficiency factor $Q_{sca}(r)$ for monodisperse cloud droplets (black) and for a modified gamma distribution with $a = 4\,\mu m$ and $b = 0.1\,\mu m$.

Looking at the scattering efficiency $Q_{sca}(r)$ as a function of droplet size (Figure 2.13, black line) for $\lambda = 870\,nm$, one can determine the predominant scattering regime. For very small particles, the scattering efficiency $Q_{sca}(r)$ increases with the 4th power of particle size, which is a characteristic of Rayleigh scattering (compare Equation 2.32). For particles that are much larger than the wavelength ($r \gg 870\,nm$), $Q_{sca}(r)$ approach the limit of 2. This limit is a common characteristic of geometric optics and is known as *extinction paradox*. The green line in Figure 2.13 shows a modified gamma distribution for parameters $a = 4\,\mu m$ and $b = 0.1\,\mu m$ (and arbitrary N). Due to the width of the size distribution, the oscillations in $Q_{sca}(r)$ for monodisperse cloud droplets gets smoothed out by the superimposed contributions from droplets in the size distribution.

To facilitate the inversion of measured cloud reflections, different cloud droplets have to be weighted corresponding to their contributions to the scattered radiation. To this end, a *mean radius for scattering* is defined to minimize the number of free parameters describing cloud properties. Following *Hansen and Travis* (1974a), this mean radius for scattering r_{sca} can be obtained by weighting the cloud droplet size distribution $n(r)$ with corresponding scattering cross-section $\sigma_{sca}(r)$. This is done since each cloud droplet scatters light proportional to $\sigma_{sca}(r)$. With the definition in Equation 2.31 of the scattering efficiency $Q_{sca}(r)$, the following expression for r_{sca} can be given:

$$r_{sca} = \frac{\int_0^\infty r\,\sigma_{sca}(r)\,n(r)dr}{\int_0^\infty \sigma_{sca}(r)\,n(r)dr} = \frac{\int_0^\infty r\,\pi r^2 Q_{sca}(r)\,n(r)dr}{\int_0^\infty \pi r^2 Q_{sca}(r)\,n(r)dr} \tag{2.45}$$

When the cloud droplets within the size distribution are much larger than the wavelength, their scattering efficiency $Q_{sca}(r)$ is only slightly dependent on droplet size r. For this reason, Q_{sca} can be cancelled out from the numerator and denominator in Equation 2.45. With this approximation, the mean scattering radius r_{sca} becomes identical with the *effective radius* r_{eff} defined in Section 2.1.5. Thus, the integrated cloud optical property r_{sca} is traced back to the microphysical property r_{eff}. In this thesis, both properties will be mutually used to describe the effective cloud droplet size. With the effective radius as area-weighted mean radius, a second parameter describes the corresponding width of the cloud droplet size distribution. The parameter describing the size distribution width is called *effective variance* v_{eff}:

$$r_{eff} = \frac{\int_0^\infty r\,\pi r^2\, n(r) dr}{\int_0^\infty \pi r^2\, n(r) dr} = \frac{1}{G}\int_0^\infty r\,\pi r^2\, n(r) dr = a \tag{2.46}$$

$$v_{eff} = \frac{1}{G r_{eff}^2}\int_0^\infty (r - r_{eff})^2 \pi r^2\, n(r) dr = b \tag{2.47}$$

The denominator in Equations 2.46 and 2.47 is the geometrical cross-section G in Equation 2.48 integrated for the whole size distribution. As verified by substitution of Equation 2.43 in Equations 2.46 and 2.47 by *Hansen* (1971a), the two parameters a and b describing the modified gamma distribution are identical with the effective radius r_{eff} and the effective variance v_{eff}.

$$G = \int_0^\infty \pi r^2 n(r) dr \tag{2.48}$$

2.6 Retrieval of cloud optical properties

As mentioned in the preceding section, the amount of reflected radiance is significantly influenced by cloud optical thickness. In turn, it is easy to show that optical thickness can be deduced from cloud liquid water content LWC and cloud droplet effective radius r_{eff} *Hansen and Travis* (1974a). Using the definition in Equation 2.42 of τ as the vertically integrated total extinction cross-section $\sigma_{ext}(z)$ and the volumetric relation (Section 2.1.6) between cloud droplet concentration

$n(r)$ and liquid water content $LWC(r)$, following approximation for the optical thickness of plane-parallel, homogeneous clouds can be given:

$$\begin{aligned}\tau &= \int_{z=0}^{h}\int_{0}^{\infty} \sigma_{ext}(r,z)\, n(z,r)\, dr\, dz \\ &= \int_{z=0}^{h}\int_{0}^{\infty} Q_{ext}\pi r^2\, n(z,r)\, dr\, dz \\ &\approx \int_{z=0}^{h} \frac{3\, LWC(z)}{2\rho_w r_{eff}(z)}\, dz\end{aligned} \tag{2.49}$$

Here, the geometric limit assumption $Q_{ext} \approx 2$ was used in combination with monodisperse cloud droplets ($r_{vol} = r_{eff}$). The density of water is denoted by ρ_w. In this common Equation 2.49, the connection between microphysical cloud properties LWC and r_{eff} and the cloud optical property τ becomes already apparent.

2.6.1 Multiple scattering in an absorbing medium

Scattering can be coherent or incoherent, depending on the spatial distribution and distance between the scatterers. The individual scattering events by cloud droplets can be treated independently, since the scattering is incoherent. However, a scattered photon can be scattered again. In clouds this is happening frequently, since there is a huge number ($N \sim 10 \times 10^8\, m^3$) of cloud droplets within a cubic meter. After a photon has left a cloud and is measured, it underwent a high number of scatterings, and thus, a high number of interactions with cloud droplets.

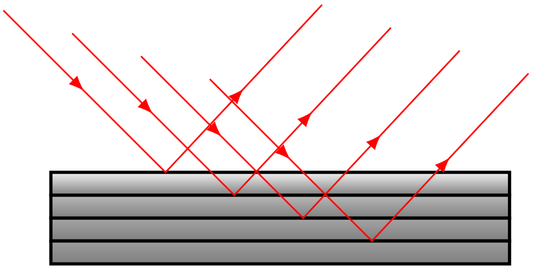

Figure 2.14: Multiple Scattering as reflection on parallel plates

Following the analogy of *Bohren et al.* (2007), the role of multiple scattering in cloud reflection can be understood with the help of multiple scattering by a pile of plates of optical thickness $d\tau$ (see Figure 2.14). When photon scattering is only allowed into two directions (up- and downward), the so called *two-stream equation* describes the steady-state of upward irradiance $E_\uparrow$ and downward irradiance $E_\downarrow$:

$$\frac{d}{d\tau}(E_\downarrow - E_\uparrow) = -(1-\omega_0)(E_\downarrow + E_\uparrow) \tag{2.50}$$

$$\frac{d}{d\tau}(E_\downarrow + E_\uparrow) = -(1-\omega_0 g)(E_\downarrow - E_\uparrow) \tag{2.51}$$

With Equations 2.50 and 2.51 as an analytically solvable variant of the radiative transfer Equation 2.40, the single scattering albedo term $(1-\omega_0)$ describes the probability for absorption in every scattering layer, while the asymmetry parameter g specifies the preferred scattering direction. In a conservative medium, the single scattering albedo is $\omega_0 = 1$ whereby Equation 2.51 becomes a linear function of τ. With suitable boundary conditions ($E_\downarrow(0) = E_0$ and $E_\uparrow(\tau) = 0$), the reflectivity R_τ as ratio between the incident irradiance E_0 and the escaping irradiance $E_\uparrow(0)$ takes the form:

$$R_\tau(\omega_0 = 1) = \frac{E_\uparrow(0)}{E_0} = \frac{\tau(1-g)/2}{1+\tau(1-g)/2}. \tag{2.52}$$

Apparently, the reflectivity R increases asymptotically to $R = 1$ with optical thickness τ. Thus, information about optical thickness τ can be best inferred at non-absorbing wavelengths.

In case of an absorbing medium, the single scattering is $\omega_0 < 1$, which renders the solution to Equations 2.50 and 2.51 a bit more difficult. By differentiating Equations 2.50 and 2.51 with respect to τ, one obtains simple second-order differential equations which can be solved with exponential functions. In the optically thick limit $\tau \to \infty$, *Bohren et al.* (2007) gives Equation 2.53 for the reflectivity R_∞ at an absorbing wavelength:

$$R_\infty(\omega_0 < 1) = \frac{\sqrt{1-\omega_0 g} - \sqrt{1-\omega_0}}{\sqrt{1-\omega_0 g} + \sqrt{1-\omega_0}}. \tag{2.53}$$

In Figure 2.15 on the left, the multiple scattering reflectivity $R_\tau(\omega_0 = 1)$ is shown as function of optical thickness τ and asymmetry parameter g, while Figure 2.15 on the right show the absorbing case $R_\infty(\omega_0 < 1)$ as a function of single scattering albedo ω_0 and asymmetry parameter g. While the reflectivity increases rapidly at small values of τ, it gets more and more saturated when τ becomes large. In case of absorption, already small amounts of absorption have a strong decreasing influence on multiple scattering reflectivity. This can be explained by the fact, that the single scattering albedo of individual scattering events has to be multiplied over the photon path through the medium to yield the probability for a photon to be absorbed at all. For both cases, a larger asymmetry parameter g has an decreasing effect on reflectivity, since photons get scattered deeper into the cloud due to a stronger forward scattering.

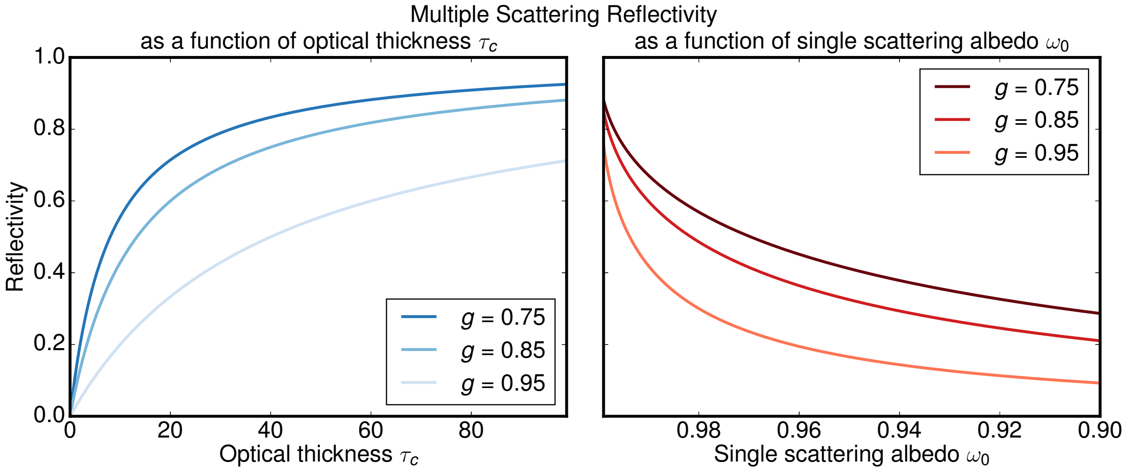

Figure 2.15: Multiple scattering reflectivity R by a pile of plates **(left)** for conservative scattering as function of optical thickness τ and **(right)** for absorbing scattering as a function of single scattering albedo ω_0. The reflectivity was calculated using Equations 2.52 and 2.53 with different values for g.

To transfer this observation to realistic clouds containing droplets of liquid water, the absorption characteristic of water, shown in Figure 2.9, has to be considered in single scattering calculations using Mie theory. In Figure 2.16, the scattering efficiency $Q_{sca}(\lambda)$ and the absorption efficiency $Q_{abs}(\lambda)$ of a water droplet with radius $r = 10\,\mu m$ is plotted as a function of wavelength λ. While Q_{sca} remains in the limit $Q_{sca}(\lambda) \approx 2$ for visible and near-infrared wavelengths, the absorption efficiency $Q_{abs}(\lambda)$ strongly increases in the in the near-infrared spectrum ($\lambda > 800\,nm$). As absorption by water increases with wavelength, the absorption cross-section σ_{abs} increases with radius cubed, since the number of water molecules increases with the volume of the droplet. Combined with the decreasing effect of g on multiple scattering reflectivity, cloud layers with larger, more forward scattering droplets can be distinguished from cloud layers with smaller cloud droplets by using their lower reflectivity in the absorbing near-infrared spectrum. For this discrimination, the two wavelength used in this thesis are marked by the dashed blue line ($\lambda = 0.87\,\mu m$) and the dashed red line ($\lambda = 2.10\,\mu m$) in Figure 2.16.

For realistic clouds, this wavelength-dependent sensitivity for optical thickness ($\lambda = 0.87\,\mu m$) and effective radius ($\lambda = 2.10\,\mu m$) can be shown when solving the complete radiative transfer equation for all scattering directions using $Q_{sca}(\lambda, r)$ and $Q_{abs}(\lambda, r)$. This is shown for clouds with varying optical thickness τ and varying effective radius τ in combination with a realistic solar spectrum (400–2500 nm, *Kurucz* (1994)) using a numerical radiative transfer code (DISORT, *Stamnes et al.* (1988)). In Figure 2.17 on the left, the spectral cloud reflectance is shown for varying optical thickness while the effective radius was held fixed with $r_{eff} = 8\,\mu m$. In turn, Figure 2.17 on the right shows the spectral cloud reflectance

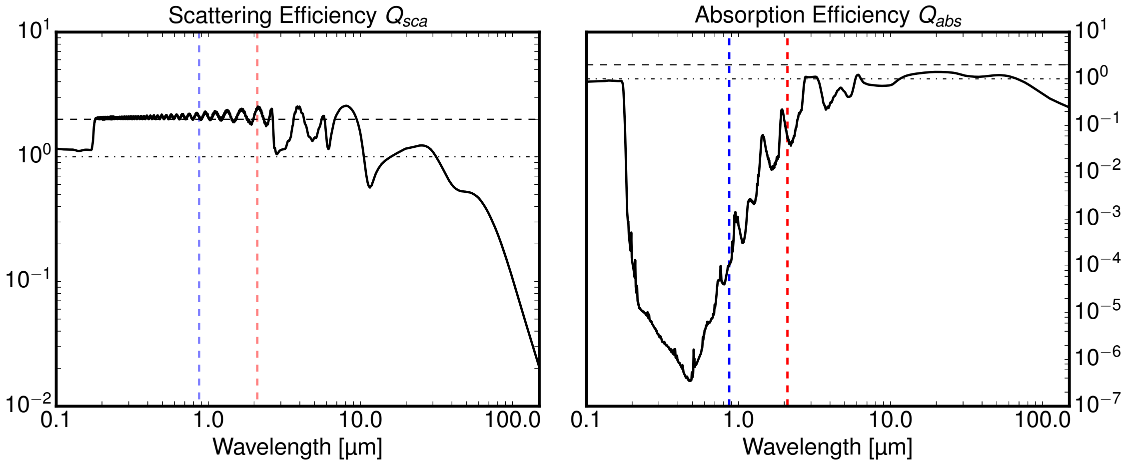

Figure 2.16: Scattering Q_{sca} and absorption Q_{abs} efficiencies for a liquid water droplet with radius $r = 10\,\mu m$.

for varying effective radii while the optical thickness is held constant ($\tau = 30$). In Figure 2.17, cloud reflectance at absorbing wavelengths (dashed red line) is relatively insensitive to larger optical thickness ($\tau > 10$), while it is relatively insensitive to droplet size at non-absorbing wavelengths (dashed blue line). Later on, this will be helpful for separating optical thickness, effective radius and interfering 3D effects in inhomogeneous clouds.

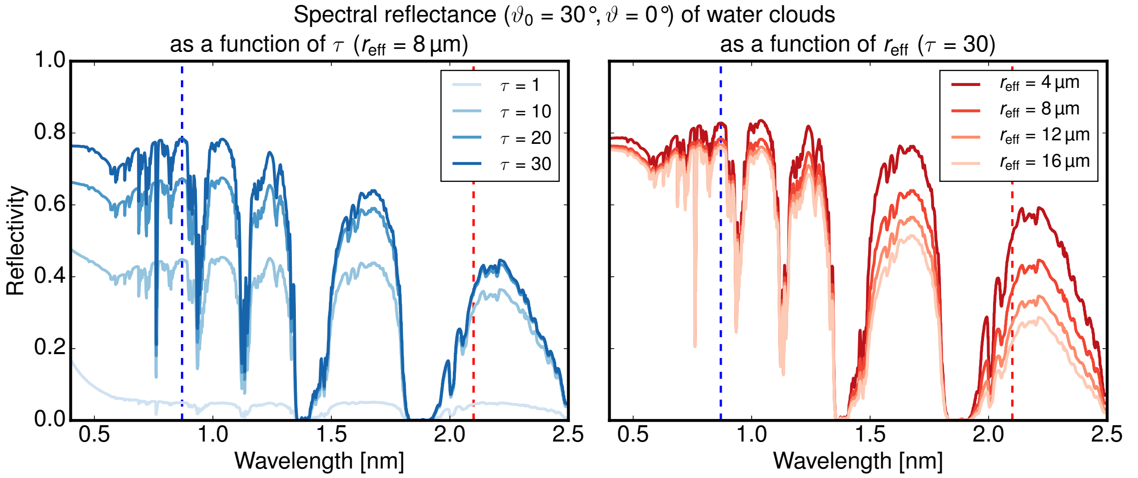

Figure 2.17: Spectral cloud reflectance for **(left)** varying optical thickness and **(right)** varying effective radius. While there is a strong sensitivity on optical thickness at the non-absorbing wavelength $\lambda = 0.87\,\mu m$, the cloud reflectance is sensitive to effective radius at the absorbing wavelength $\lambda = 2.10\,\mu m$).

2.6.2 Retrieval of cloud phase

A further interesting property of clouds is the thermodynamic phase of the particles it is composed of. The cloud phase is of great scientific interest, since the onset of cloud glaciation is a crucial parameter to assess the impact of aerosol-cloud interactions (*Rosenfeld and Lensky*, 1998, *Rosenfeld et al.*, 2008). It is as well as important to remote sensing, since the phase transition from liquid to ice comes with a change in imaginary refractive index. When this change stays undetected, the retrieval of the remaining cloud optical properties, e.g. effective radius and optical thickness, can be severely biased (*Chang and Li*, 2005, *Werner et al.*, 2013, *Yang et al.*, 2003). For this reason, a reliable cloud phase discrimination is mandatory for retrievals of cloud optical properties.

Besides numerous ice detection techniques using measurements of cloud thermal emission (*Baum et al.*, 2000, *Ewald et al.*, 2013b, *Saunders and Kriebel*, 1988), there exist also methods to discriminate cloud phase using measurements of reflected solar radiation. As already shown in Figure 2.9, the imaginary refractive index of liquid water and ice has a different spectral characteristic in the region of the solar spectrum. *Pilewskie and Twomey* (1987) and *Jäkel et al.* (2013) use the different spectral absorption in the wavelength region between 1.55 µm and 1.75 µm to retrieve the cloud phase from measurements of cloud side reflectivity.

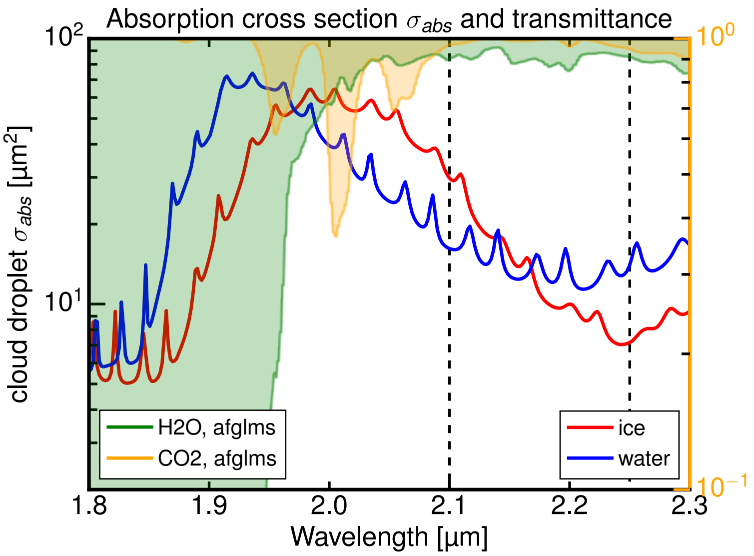

Figure 2.18: Spectral dependence of σ_{abs} for ice particles (red) and liquid droplets (blue) with $r_{\mathrm{eff}} = 10\,\mu\mathrm{m}$ for wavelengths between 1.8 µm and 2.3 µm. The different characteristic of σ_{abs} for ice and water between 2.1 µm and 2.25 µm can be exploited to differentiate between ice and water particles (*Martins et al.*, 2011). The usable wavelength range starts around 2.1 µm, since transmission by water vapor (H_20, green) and carbon dioxide (CO_2, yellow) interferes at shorter wavelengths.

Authors like *Yuan et al.* (2010), *Zinner et al.* (2008) and *Martins et al.* (2011), exploit the differential absorption of ice and water between 2.10 µm and 2.25 µm.

Figure 2.18 shows the spectral dependence of absorption cross-sections σ_{abs} for ice particles (red) and liquid droplets (blue) with $r_{eff} = 10\,\mu m$ for wavelengths between 1.8 µm and 2.3 µm. Additionally, Figure 2.18 shows the spectral direct transmittance of water vapor (H_2O, green) and carbon dioxide (CO_2, yellow) for the standard atmosphere midlatitude summer (afglms) by *Anderson et al.* (1986). To mitigate the influence of molecular absorption by gaseous constituents, the usable wavelength range starts around 2.1 µm. Following observations by *Martins et al.* (2011), the differential absorption reflects into different cloud reflectivities at 2.10 µm and 2.25 µm which leads to a reflectivity ratio $R_{2.1}/R_{2.25}$ of 0.4 for optically thick ice clouds, and around 0.8 for optically thick water clouds. For this reason, *Zinner et al.* (2008) flagged clouds with reflectivity ratios $R_{2.1}/R_{2.25}$ between 0.65 and 0.75 as mixed phase clouds.

2.6.3 Retrieval of optical depth and effective radius

Based on the observation (Figure 2.17) that cloud reflectivity is sensitive to optical thickness at non-absorbing wavelengths and sensitive to effective radius at absorbing wavelengths, various methods have been developed to retrieve these two properties (*Hansen and Pollack*, 1970, *Nakajima and King*, 1990, *Platnick et al.*, 2001, *Twomey and Cocks*, 1982). One of the most common techniques is the retrieval by *Nakajima and King* (1990), which forms the basis in various applications using measurements from airborne and spaceborne platforms (*King et al.*, 1992, 2004, *Martins et al.*, 2011, *Platnick et al.*, 2003, *Vant-Hull et al.*, 2007). As proposed by *Marshak et al.* (2006b), *Zinner et al.* (2008) and *Martins et al.* (2011), this thesis will test the applicability of the Nakajima-King method to spectral radiance measurements of highly structured cloud sides.

Nakajima-King retrieval

The retrieval of Nakajima-King uses the already introduced wavelength combination of a non-absorbing wavelength (0.75 µm) and a absorbing wavelength (2.16 µm). The sensitivity for optical thickness and effective radius becomes evident when cloud reflectance $R_{2.16}$ at 2.16 µm is plotted against cloud reflectance $R_{0.75}$ at 0.75 µm for different optical cloud properties. This is shown by *King et al.* (1992) in Figure 2.19, where the isolines are reflectivities of constant effective radius and constant optical thickness.

Under the assumption of a homogeneous, plane-parallel cloud layer with known illumination and observation geometry, there exists a nearly perfect bijection between optical thickness τ and effective radius r_{eff} pairs and pairs of absorbing $R_{2.10}$ and non-absorbing reflectivities $R_{0.87}$. As already shown in Figure 2.17, the cloud reflection at both wavelengths strongly increases with τ for

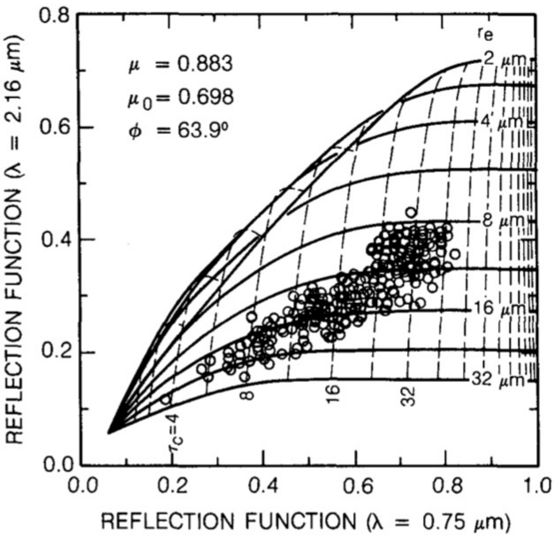

Figure 2.19: Cloud reflection function for $\lambda = 0.75\,\mu\mathrm{m}$ against $\lambda = 2.16\,\mu\mathrm{m}$ for different values of τ and r_{eff} as calculated by King et al. (1992). The superimposed points are reflectance values of marine stratocumulus as measured during the FIRE field campaign

optically thin clouds. With an increasing number of scattering cloud droplets, the cloud extinction increases. In turn, this decreases the probability that a photon passes the cloud unscattered and increases the probability for multiple scattering. In optically thicker clouds, the number of multiple scattering events N per per photon increases linearly with $N \sim \tau$ (Marshak et al., 1995). The separation of effective radius isolines increases non-linearly for higher optical thickness $\tau \gg 1$, since the total probability for absorption of a photon is the product $\prod_{n=1}^{N} 1 - \omega_0$ of absorption occurring during N single scattering events. At a certain optical thickness, the near-infrared reflectance reaches an asymptotic limit which is determined by the cloud droplet effective radius r_{eff}. For even thicker clouds, deep penetrating near-infrared photons, that pass a certain optical depth within the cloud, no longer reach the cloud surface again.

2.6.4 Implications of 3D clouds

The assumption of a homogeneous, plane-parallel cloud layer with known illumination and observation geometry is rarely valid in nature. This has ramifications for the bijective relationship between optical properties and reflected radiances used by the Nakajima-King-technnique. According to Varnai and Marshak (2003), there exists several deviations from the plane-parallel 1D theory which can be categorized into four distinct 3D effects. The eye-catching, high-contrast structure of convective cloud sides is mostly caused by *illumination* and *shadowing* of surfaces at cloud edges turned more towards the sun or facing away from it. If the spatial resolution of a remote sensing instrument is not sufficient to resolve the small scale structure of cloud edges, this radiance variability is averaged into the same pixel leading to a *unresolved cloud variability*. Furthermore, heterogeneous distribution of optical thickness within the cloud leads to *channeling* and *leakage* of light. While optically thinner cloud regions let through more light (channeling), in other, optically thicker cloud parts, this radiation is missing (leakeage). Even with a high spatial resolution, this effect cannot be directly resolved by passive remote sensing since photon paths can not be reconstructed in detail.

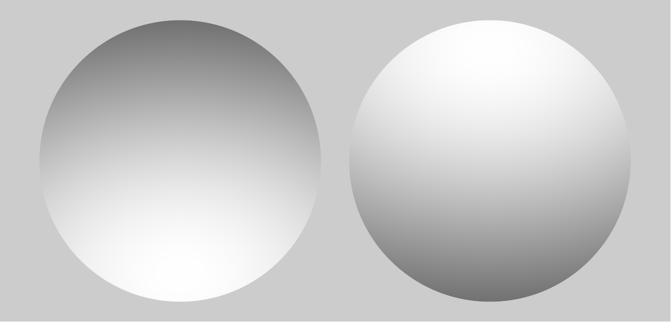

Figure 2.20: Which of these shapes is concave and which convex?

For this very reason, passive remote sensing can not directly access the 3D cloud surface orientation. Figure 2.20 illustrates the problem associated with 2D images of 3D objects with a familiar optical illusions. Only when the illumination direction is known, humans can perceive this very basic shape as either convex or concave. While humans have an remarkable ability to perceive 3D structures from 2D images alone, computer-vision algorithms still face major challanges when faced with translucent materials without specular reflections (*Zhang et al.*, 1999). When brigthness gradients are not entirely caused by shape, but also by changing optical properties of the observed material, their performance has been disappointing across the board (*Todd et al.*, 2014).

Nevertheless, the Nakajima-King-technique depends on the knowledge of the viewing and illumination geometry with respect to the cloud surface in order to model the radiative transfer correctly. However, only the scattering angle between viewing and illumination direction is known if the orientation of the cloud surface is unknown. This underdetermined geometry results in an incorrect assessment of the radiative transfer and therefore to an erroneous retrieval of optical properties. The ramifications of these radiative 3D effects were systematically analyzed for the retrieval of optical thickness by *Varnai and Marshak* (2002a) and for the retrieval of cloud droplet effective radius by *Marshak et al.* (2006a) In their studies, both focused on the spatial resolution and perspective of spaceborne applications. After *Scheirer* (2003) and *Vant-Hull et al.* (2007) discussed the 3D effects for broadband fluxes and for higher spatial resolutions, *Marshak et al.* (2006b) and *Zinner et al.* (2008) assessed the feasibility of a remote sensing of effective radii from clouds sides. Anticipating the sensitivity study in Section 4.1.2, Figure 2.21 illustrates the problem for the 'classical' Nakajima-King-technique posed by highly inhomogeneous cloud sides. Calculated using a 1D radiative transfer code, isolines in this figure represent radiance pairs at $\lambda = 870\,\mathrm{nm}$ and $\lambda = 2100\,\mathrm{nm}$ for liquid water clouds of same

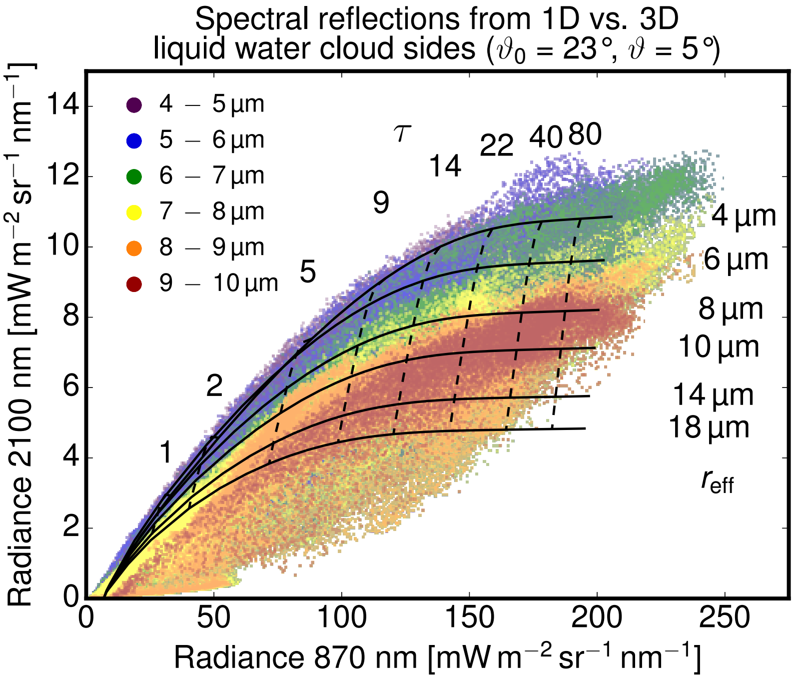

Figure 2.21: The isolines represent radiance pairs for planparallel liquid water clouds of same effective radius r_{eff} and same optical thickness τ which were calculated using a 1D radiative transfer code at $\lambda = 870\,\text{nm}$ and $\lambda = 2100$ nm. Superimposed points show radiance pairs which were simulated for a realistic, threedimensional cloud side under the same illumination using a sophisticated 3D radiative transfer code.

effective radius r_{eff} and same optical thickness τ. The sun and viewing zenith angle of $\vartheta_0 = 23°$ and $\vartheta = 5°$ are chosen to simulate the ground-based perspective onto a cloud wall illuminated by a low sun at $\vartheta_0 = 90° - 23° = 67°$ in the back of the observer. Colored according to the corresponding cloud droplet effective radius, the superimposed points in Figure 2.21 show radiance pairs at $\lambda = 870\,\text{nm}$ and $\lambda = 2100\,\text{nm}$ which were simulated for a realistic cloud side under the same illumination using a sophisticated 3D radiative transfer code. Apparently, 3D radiance pairs of the same effective radius cross the 1D radiative transfer isolines of the same effective radius. In addition, the relation between radiance pairs and optical properties gets blurred and therefore ambiguous. This work will map the ambiguous relation between optical properties and radiances and will investigate the underlying mechanisms responsible.

CHAPTER 3

Numerical prerequisites and data sets

The following chapter introduces numerical prerequisites and data sets, which are used to model and represent the microphysics and the radiative transfer in convective cumulus clouds. This work will follow the approach proposed by *Martins et al.* (2011) and *Zinner et al.* (2008) which use ensemble methods to account for three-dimensional radiative effects on complex-shaped cloud sides. As essential prerequisites, a number of numerical models are needed to represent the dynamics of convective clouds and the related radiative transfer. Along this approach, methods have to be developed to define observables within these models like the surface orientation and the apparent droplet size at cloud boundaries. In order to achieve a sufficiently dense and realistic radiative transfer ensemble, further methods have to be found to select and interpolate between different observation geometries.

3.1 Introduction to the statistical approach

With the high number of possible cloud configurations, the derivation of vertical profiles of cloud microphysics from cloud sides using passive remote sensing is a strongly under-determined problem. In general, the radiance ambiguity of different cloud droplet sizes can be solved by two different approaches. One possibility is the collection of additional information to narrow down the uncertainties by reducing the number of unknown parameters. If additional information is not available or if the combination with passive techniques is not feasible, the ambiguity problem has to be approached in a probabilistic manner. A further benefit of sampling the statistics between cloud microphysics and associated radiances can be a better understanding of uncertainties connected to three-dimensional effects. In statistical analysis the frequency of occurrence of an event is counted to calculate the probability of its occurrence. In this context, an event can be the occurrence of a specific atmospheric state as well as a specific radiance measurement. Among other things like viewing geometry, cloud geometry and cloud microphysics mainly determine the amount of scattered light. Hence, the probability to measure a specific radiance A is directly connected to the occurrence of atmospheric state B, which is likely to produce radiance A.

3.1.1 Bayes' theorem

For the statistical handling of measurements it is essential to understand how *conditional probabilities* are central in putting probabilities of one event into context of another event. *Thomas Bayes* (1702 − 1761) was one of the first to develop analytical expressions to calculate the conditional probability for an event A_i in the case an event B_j has already occurred. These conditional probabilities can be calculated by **Bayes' theorem**:

$$P(A_i|B_j) = \frac{P(B_j|A_i)\,P(A_i)}{P(B_j)} = \frac{P(B_j|A_i)\,P(A_i)}{\int_i P(B_j|A_i)\,P(A_i)}. \tag{3.1}$$

Also known as *posterior*, the conditional probability $P(A_i|B_j)$ for event A_i results from three other probabilities, namely the *likelihood* probability $P(B_j|A_i)$ of event B_j given A_i, the *prior* probability $P(A_i)$ for event A_i and a normalization with the probability $P(B_j)$ of event B_j. With event B_j as evidence of the existence of fact A_i, the likelihood $P(B_j|A_i)$ can be understood as a measure how likely the evidence B_j can be observed after event A_i has occurred. In combination with the prior $P(A_i)$ that event A_i is occurring at all, Equation 3.1 gives the probability that event A_i has occurred after the evidence B_j has been observed. Here, the term is normalized with respect to the probability that evidence B_j is observed at all to ensure that the sum of posteriors equals unity.

3.1.2 Application of Bayes' theorem to remote sensing

In the context of remote sensing, the events A and B correspond to atmospheric states and remote sensing measurements linked to this states. Following *Mosegaard and Tarantola* (1995), the cloud and atmospheric parameters $m^{(1)}, m^{(2)}, ..., m^{(N)}$ describing a specific atmospheric state **i** can be combined into a model state vector $\mathbf{m_i} = \left\{m^{(1)}, m^{(2)}, ..., m^{(N)}\right\}$. Each state vector $\mathbf{m_i}$ can be considered as a point in the model space $\mathcal{M}$ which contains all possible atmospheric states. Hereby, atmospheric parameters can be LWC, r_{eff} or τ, atmospheric states **i** are specific cloud scenes while the model space $\mathcal{M}$ is the set of all cloud scenes which can be generated with the used cloud model. In turn, a set of observations $o^{(1)}, o^{(2)}, ..., o^{(N)}$ can be expressed as observation vector $\mathbf{o_i} = \left\{o^{(1)}, o^{(2)}, ..., o^{(N)}\right\}$ belonging to the observation parameter space $\mathcal{O}$. The observation vector $\mathbf{o_i}$ associated with a atmospheric model state vector $\mathbf{m_i}$ can be simulated by using a numerical forward model f:

$$\mathbf{o_i} = f(\mathbf{m_i}) \tag{3.2}$$

In the case of cloud side remote sensing the forward model f can be a radiative transfer code which reflects our understanding of atmospheric radiation. The relative frequency of modelled observation vectors $\mathbf{o_i}$ for a complete set of states $\mathbf{m_i}$ in $\mathcal{M}$ leads to the likelihood distribution $p(\mathbf{o_i}|\, \mathbf{m_i})$. The likelihood distribution combined with the prior probability $p(\mathbf{m_i})$, which represents the knowledge about $\mathbf{m_i}$ before the observation, leads to the posterior probability $p(\mathbf{m_i}|\mathbf{o_i})$:

$$p(\mathbf{m_i}|\mathbf{o_i}) = \frac{p(\mathbf{o_i}|\, \mathbf{m_i})\, p(\mathbf{m_i})}{\int p(\mathbf{o_i}|\, \mathbf{m_i})\, p(\mathbf{m_i})\, d\mathbf{m_i}} \tag{3.3}$$

$$\langle \mathbf{m_i} \rangle = \int \mathbf{m_i}\, p(\mathbf{m_i}|\, \mathbf{o_i})\, d\mathbf{m_i}. \tag{3.4}$$

After the observation $\mathbf{o_i}$ is taken, the posterior probability represents the knowledge about cloud properties $\mathbf{m_i}$. The denominator in Equation 3.3 ensures that the sum of all posteriors equals unity. To retrieve a mean model state $\langle \mathbf{m_i} \rangle$, the mean of the posterior distribution is calculated by integration over all states in $\mathcal{M}$ in Equation 3.4. While the retrieval of a complete mean model state $\mathbf{m_i}$ would be desirable, the usually smaller number of observations in $\mathbf{o_i}$ underdetermine this inversion problem. Therefore, retrievals commonly try to invert a subset of cloud parameters $m^{(N)}$, e.g. the effective radius r_{eff}, from observations $\mathbf{o_i}$.

For the cloud side application, observations $\mathbf{o_i} = \{L_{0.87}, L_{2.10}\}$ of reflected radiances at absorbing and non-absorbing wavelengths are used to select the associated posterior $p(r_{\text{eff}}|\, L_{0.87}, L_{2.10})$. Following the formulation of *McFarlane et al.* (2002) and *Zinner et al.* (2008), the posterior probability $p(r_{\text{eff}}|\, L_{0.87}, L_{2.10})$ and the retrieved mean cloud droplet effective radius $\langle r_{\text{eff}} \rangle$ for measurements $L_{0.87}$ and $L_{2.10}$ is given by:

$$p(r_{\text{eff}}|\, L_{0.87}, L_{2.10}) = \frac{p_{\text{fwd}}(L_{0.87}, L_{2.10}|\, r_{\text{eff}})\; p_{\text{pr}}(r_{\text{eff}})}{\int p_{\text{fwd}}(L_{0.87}, L_{2.10}|\, r_{\text{eff}})\; p_{\text{pr}}(r_{\text{eff}})\; dr_{\text{eff}}}, \tag{3.5}$$

$$\langle r_{\text{eff}} \rangle = \int r_{\text{eff}}\, p(r_{\text{eff}}|\, L_{0.87}, L_{2.10})\; dr_{\text{eff}}. \tag{3.6}$$

In this thesis, the likelihood function is represented by a numerical forward model $p_{\text{fwd}}(L_{0.87}, L_{2.10}|\, r_{\text{eff}})$ which yields the probability to observe the radiance pair $L_{0.87}, L_{2.10}$ for a present effective radius r_{eff} contained in the cloud model $\mathbf{m_i}$. To obtain a realistic posterior distribution $p(r_{\text{eff}}|\, L_{0.87}, L_{2.10})$, a suitable likelihood function has to be combined with a realistic prior $p_{\text{pr}}(r_{\text{eff}})$, which fits the observed cloud regime. In the following, the framework described here will be referred to as statistical or *Bayesian approach*.

3.1.3 Monte Carlo approximation to the posterior distribution

When the integrand in Equation 3.5 and Equation 3.6 is multidimensional or no analytical expression for the likelihood or prior distribution is available, Monte Carlo sampling from these distributions can be used to approximate the posterior distribution (*Mosegaard and Tarantola*, 1995). In this thesis, the numerical forward model $p_{fwd}(L_{0.87}, L_{2.10}| r_{eff})$ as likelihood function is separated into the MYSTIC radiative transfer code f_{mys} and an observation operator f_{obs}. This is done since the three-dimensional Monte Carlo code MYSTIC $f_{mys}(\mathbf{m_i})$ needs a complete atmospheric state $\mathbf{m_i}$ as input, while the observation operator $f_{obs}(\mathbf{m_i})$ selects the corresponding cloud droplet effective radius r_{eff} for the chosen observation perspective in $\mathbf{m_i}$. In simple terms, the observation operator yields a corresponding image of r_{eff} for the forward simulated cloud side image of $L_{0.87}$ and $L_{2.10}$. In order to approximate the likelihood for radiance measurements $L_{0.87}$ and $L_{2.10}$ for given $\mathbf{m_i}$, the MYSTIC code $f_{mys}(\mathbf{m_i})$ and the observation operator $f_{obs}(\mathbf{m_i})$ are used in the following way. The tuple $(L^{(i)}_{0.87}, L^{(i)}_{2.10}, r^{(i)}_{eff})$ is derived from $f_{mys}(\mathbf{m_i})$ (yielding observations $L^{(i)}_{0.87}$ and $L^{(i)}_{2.10}$) and $f_{obs}(\mathbf{m_i})$ (yielding the specific model parameter r_{eff}) for a specific model state $\mathbf{m_i}$:

$$(L^{(i)}_{0.87}, L^{(i)}_{2.10}, r^{(i)}_{eff}) = (f_{mys}(\mathbf{m_i}), f_{obs}(\mathbf{m_i})), \qquad \text{with: } \mathbf{m_i} \in \mathcal{E}_N, \tag{3.7}$$

$$n(L_{0.87}, L_{2.10}, r_{eff}) = \text{hist}\left\{(L^{(i)}_{0.87}, L^{(i)}_{2.10}, r^{(i)}_{eff}), \ldots, (L^{(N)}_{0.87}, L^{(N)}_{2.10}, r^{(N)}_{eff})\right\}. \tag{3.8}$$

Hereby, the different model states $\mathbf{m_i}$ are drawn from an ensemble $\mathcal{E}_N$ of size N, containing atmospheric states and observation perspectives which are tailored to fit the typical measurement setup. The histogram $n(L_{0.87}, L_{2.10}, r_{eff})$ is obtained by counting (Equation 3.8) the frequency of tuples (Equation 3.7) which combine observations $L^{(i)}_{0.87}, L^{(i)}_{2.10}$ and the corresponding model parameter r_{eff}. With the histogram n as a very simple non-parametric density estimator (*Scott et al.*, 1977), the following relation between histogram n and the joined probability $p(L_{0.87}, L_{2.10}, r_{eff})$ and probability $p(r_{eff})$ can be made:

$$p(L_{0.87}, L_{2.10}, r_{eff}) \propto n(L_{0.87}, L_{2.10}, r_{eff}) \tag{3.9}$$

$$p(r_{eff}) \propto n(r_{eff}) = \sum_{L_{0.87}} \sum_{L_{2.10}} n(L_{0.87}, L_{2.10}, r_{eff}). \tag{3.10}$$

For a successful estimation of these two probabilities, the number of ensemble members N contained in histogram n needs to be large enough. Furthermore, the sampling spread has to match the expected spread of parameter r_{eff} in the model space $\mathcal{M}$. With the likelihood probability $p(L_{0.87}, L_{2.10}| r_{eff})$ as a conditional probability, it can be written as the quotient of the joined probability $p(L_{0.87}, L_{2.10}, r_{eff})$ and $p(r_{eff})$ describing the ensemble of forward calculations contained in n. In this thesis, the likelihood probability $p(L_{0.87}, L_{2.10}| r_{eff})$ is approximated by the histogram $n(L_{0.87}, L_{2.10}, r_{\text{eff}})$ which is normalized with $n(r_{\text{eff}})$ using the relations in Equation 3.9 and Equation 3.10:

$$p(L_{0.87}, L_{2.10}| \, r_{\text{eff}}) = \frac{p(L_{0.87}, L_{2.10}, r_{\text{eff}})}{p(r_{\text{eff}})} \approx \frac{n(L_{0.87}, L_{2.10}, r_{\text{eff}})}{n(r_{\text{eff}})}, \tag{3.11}$$

$$p(r_{\text{eff}}| \, L_{0.87}, L_{2.10}) = \frac{p_{\text{fwd}}(L_{0.87}, L_{2.10}| \, r_{\text{eff}}) \; p_{\text{pr}}(r_{\text{eff}})}{\int p_{\text{fwd}}(L_{0.87}, L_{2.10}| \, r_{\text{eff}}) \; p_{\text{pr}}(r_{\text{eff}}) \; dr_{\text{eff}}}, \tag{3.12}$$

In Equation 3.11, the prior distribution of r_{eff}, contained implicitly in ensemble $\mathcal{E}_N$, is removed by the normalization with the marginal probability $p(r_{\text{eff}})$. In a final step, the thus obtained likelihood probability $p(L_{0.87}, L_{2.10}| \, r_{\text{eff}})$ can be used with an arbitrary prior $p_{\text{pr}}(r_{\text{eff}})$ to obtain the posterior probability $p(r_{\text{eff}}| \, L_{0.87}, L_{2.10})$ given measurements $L_{0.87}$ and $L_{2.10}$. Hereby, the arbitrary prior $p_{\text{pr}}(\mathbf{m_i})$ must be included within the bounds of the implicit prior $p(r_{\text{eff}})$ in $\mathcal{E}_N$. Values of r_{eff} that are not included in $\mathcal{E}_N$ cannot be retrieved since the likelihood probability $p(L_{0.87}, L_{2.10}| \, r_{\text{eff}})$ is not defined for them. To give an example, a uniform prior $p_{\text{pr}}(r_{\text{eff}}) = \text{const.}$ bound between r_{eff} values of 4 µm and 12 µm can be defined. Figure 3.1 shows how such a Monte Carlo approximation (blue histogram) of a posterior distribution (red line) could look like for given radiance measurements $L_{0.87}$ and $L_{2.10}$. Besides an estimated mean effective radius $\langle r_{\text{eff}} \rangle$, the standard deviation of the posterior distribution also yields the uncertainty connected with this estimate.

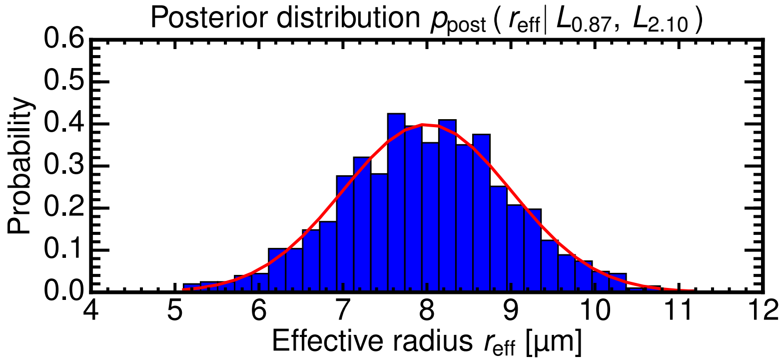

Figure 3.1: Approximation of a posterior pdf (red) by Monte Carlo Sampling (blue).

3.2 Radiative transfer codes and cloud model

In this work the output of one large-eddy model is used for a realistic representation of cumulus clouds while two different radiative transfer models are applied to model reflected solar radiation from clouds.

3.2.1 Radiative transfer codes

The analysis of radiative transfer effects in one-dimensional clouds is done using the *Discrete Ordinates Radiative Transfer Program for a Multi-Layered Plane-Parallel Medium (DISORT2)* (*Stamnes et al.*, 2000). The representation of radiative transfer in realistic cloud ensembles is done using the Monte Carlo approach with the *Monte Carlo code for the physically correct tracing of photons in cloudy atmospheres (MYSTIC)* (*Mayer*, 1998, 2009). Both codes are embedded in the radiative transfer library *libRadtran* (*Mayer and Kylling*, 2005) which provides prerequisites and tools needed for the radiative transfer modelling.

The atmospheric absorption is described by the newly developed representative wavelengths absorption parametrization *(REPTRAN)* (*Gasteiger et al.*, 2014). This parametrization is based on the HITRAN absorption database (*Rothman et al.*, 2005) and provides spectral bands of different resolution ($1\,\mathrm{cm}^{-1}$, $5\,\mathrm{cm}^{-1}$, and $15\,\mathrm{cm}^{-1}$). Calculations have shown that the spectral resolution of $15\,\mathrm{cm}^{-1}$ (e.g. $\Delta\lambda = 1.1\,\mathrm{nm}$ at $870\,\mathrm{nm}$, $\Delta\lambda = 6.6\,\mathrm{nm}$ at $2100\,\mathrm{nm}$) best suits the spectral resolution of common hyperspectral imagers. The extraterrestrial solar spectrum is based on data from *Kurucz* (1994) which is averaged over $1.0\,\mathrm{nm}$. In order to include vertical profiles of gaseous constituents, the standard summer mid-latitude profiles by *Anderson et al.* (1986) are used throughout this work. Pre-computations of the scattering phase function and single scattering albedo are done using the Mie tool *MIEV0* from *Wiscombe and Warren* (1980). The influence of various cloud droplet size distributions on radiative properties were tested (see Sec. 4.1.1) to represent poly-disperse cloud droplet distributions. When not mentioned otherwise, a Gamma size distribution with $\alpha = 7$ was used for the Mie calculations.

One-dimensional radiative transfer model (DISORT)

Introduced by *Stamnes et al.* (1988) and later described by (*Stamnes et al.*, 2000) in detail, *DISORT* is a radiative transfer code to simulate the scattering and emission of electromagnetic radiation in plane-parallel media. The method approaches the problem of solving the radiative transfer Equation 2.40 by solving it for discrete ordinates for which the scattering phase function is expanded in the form of truncated Legendre polynomials. By using the discrete ordinate approach, the integral in Equation 2.40 can be approximated by a quadrature sum which transforms the integro-differential equation into a set of ordinary differential equations. In combination with methods to truncate the highly spiked phase function of large particles (*Wiscombe*, 1977) while maintaining correct intensity values despite low numbers of ordinates (*Nakajima and Tanaka*, 1988), DISORT is a fast and accurate radiative transfer code for one-dimensional problems.

Three-dimensional radiative transfer model (MYSTIC)

For the physically correct tracing of photons in cloudy atmospheres, the Monte Carlo code *MYSTIC* (*Mayer*, 1998, 2009) is used when simulating the radiative transfer in three-dimensional clouds. Like DISORT, it is included in *libRadtran* which provides a common framework to compare and to apply both methods to clouds in a consistent manner. This method circumvents the need to solve the RTE analytically by a numerical simulation of the radiative transfer process. Using the Monte Carlo approach, the radiative transfer in clouds can be regarded as a *Markov chain* of photon collisions with atmospheric particles (*Marchuk et al.*, 1980) which results in either scattering or absorption of photons. VON NEUMANNS *Golden Rule of Sampling* in Equation 3.13 allows to draw random samples x from a probability density distribution $p(x)$ using uniform random numbers ρ:

$$x = P^{-1}(\rho), \qquad P(x) = \int_0^x p(x')dx', \tag{3.13}$$

$$\tau_{\text{ext}} = -\ln(1-\rho), \qquad p_{\text{ext}}(\tau) = \exp(\tau). \tag{3.14}$$

Applying Equation 3.13 to Lambert Beer's law in Equation 3.14, a photon random walk with optical depth steps τ_{ext} can be generated with random numbers $\rho \in [0,1]$. Likewise, scattering and absorption events can be handled as random events corresponding to the phase function and the absorption coefficient of the particle. Tracing huge numbers of photons through three-dimensional fields of atmospheric particles, the radiative transfer in inhomogeneous, complex clouds can be accurately approximated. The high computational costs, however, put a limit to this technique regarding calculations of radiances. With the sun as well as the observer as points in space, very few photon random walks are reaching the observer. Following techniques were used to circumvent this limitation, increasing the photon statistics for the observer position:

- Using the *backward method* in MYSTIC, photons are started at the detector and traced backwards according the reciprocity principle of *von Helmholtz* (1865).
- At each scattering event, the probability for a direct path into the sun is calculated and taken as a valid result, which is known as the *local estimate* method (*Davis et al.*, 1985, *Kunkel and Weinma*, 1976).
- As proposed by *Witt* (1977) and *Meier et al.* (1978), a photon weighting $0 < p_w < 1$ is reduced during absorption instead of termination of the photon, speeding up calculations.

- The photon statistics were further improved using the *Variance Reduction Optimal Option Method (VROOM)* (*Buras and Mayer*, 2011), a collection of various variance reduction techniques.

Careful attention was taken to exclude introduction of any bias by these techniques.

3.2.2 Cumulus cloud model

In order to calculate realistic posterior probability distributions $p(r_{\mathrm{eff}}|\,L_{0.87}, L_{2.10})$, likelihood probabilities, produced by a sophisticated forward model, have to be combined with a realistic prior. While *Marshak et al.* (2006b) used statistical models to obtain this prior of 3D cloud fields, the physical consistency of cloud structures and cloud microphysics are an advantage of the explicit simulation of cloud dynamics and droplet interactions. Following *Zinner et al.* (2008), this work applies the three-dimensional radiative transfer model MYSTIC to realistic cloud fields which were generated with a *large eddy simulation (LES)* model on a cloud resolving scale. While *Zinner et al.* (2008) uses realistic cloud structures combined with a bulk microphysics parametrization, this work extends their approach by including explicit simulations of spectral cloud microphysics.

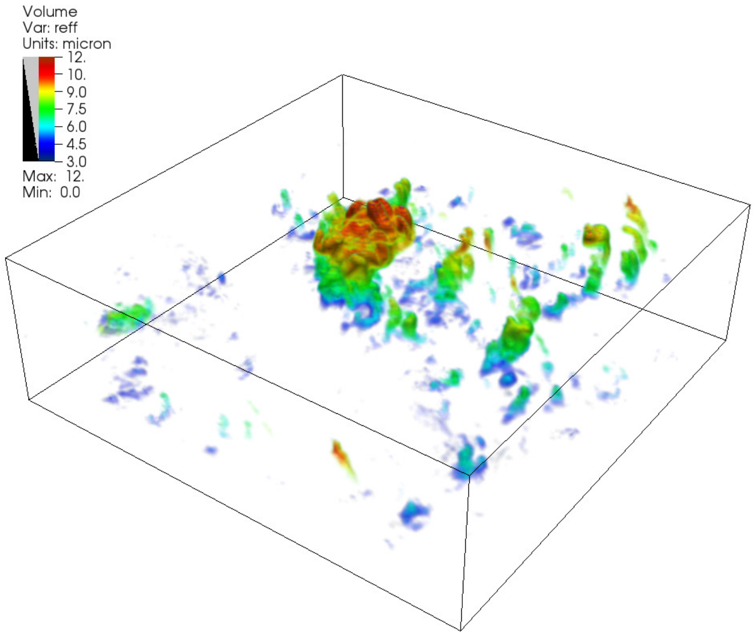

Figure 3.2: Snapshot of the 3D effective radius field for the LES output around 12 h 40 min LT. The growth of cloud droplets with height can clearly be seen in the cloud vertical profile.

Regional Atmospheric Modelling System

In this work large-eddy simulations of trade wind cumulus clouds are used which were done by *Jiang and Li* (2009) using an adapted version of the *Regional Atmospheric Modelling System (RAMS)* (*Jiang et al.*, 2008) which is coupled to a microphysical model developed by *Feingold et al.* (1996). Within *RAMS*, dynamics are handled by a fully non hydrostatic set of equations (*Cotton et al.*, 2003). The LES simulation was compared with other numerical models and independent measurements by *vanZanten et al.* (2011). Despite the high spatial resolution, cloud microphysics are explicitly represented by size-resolved simulations of droplet interactions within each grid box. The cloud droplet distributions cover radii between $1.56\,\mu m$ to $2540\,\mu m$ which are divided into 33 size bins with mass doubling between bins. All warm cloud processes, like collision-coalescence, sedimentation, and condensation/evaporation are handled by the method of moments developed by *Tzivion et al.* (1987). Droplet activation is included by using the calculated supersaturation field and a cloud condensation nuclei concentration of $N_{CCN} = 1000\,cm^{-1}$. The LES simulation (*dx25-1000*) used in this thesis and described by *Jiang and Li* (2009) has a domain size of $6.4 \times 6.4 \times 4\,km$ with a spatial resolution of $10\,m$ in the vertical and a spatial resolution of $25 \times 25\,m$ in the horizontal with periodic boundary conditions. Thermodynamic profiles collected during the Rain In Cumulus over Ocean (RICO) campaign (*Rauber et al.*, 2007) were used as initial forcing. With condensation starting at a cloud base temperature of around $293\,K$ at $600\,m$, the cloud depth of the warm cumuli varies over a large range from $40\,m$ to a maximum of $1700\,m$ (*Jiang and Li*, 2009).

Snapshots of microphysics

In order to sample a representative prior from this cumulus cloud simulation, model outputs were selected over the last 2 hours between $12\,h\ 00\,min$ LT (local time) and $14\,h\ 00\,min$ LT with a time step of $10\,min$. In the following, microphysical moments are derived from the simulated cloud droplet spectra serving as input for the radiative transfer calculations. Using Equations 3.15–3.18, effective radius r_{eff}, liquid water content LWC and total cloud droplet concentration N_d

can be calculated from mass mixing ratios m_i in $\mathrm{g\,kg^{-1}}$ and cloud droplet mixing ratios n_i in $\mathrm{kg^{-1}}$ given for the 33 LES size bins:

$$r_i(x,y,z) = \sqrt[3]{\frac{m_i(x,y,z)}{n_i(x,y,z)} \frac{3}{4\,\pi\,\rho_w}}, \tag{3.15}$$

$$r_{\mathrm{eff}}(x,y,z) = \frac{\sum_{i=1}^{33} r_i^3(x,y,z)\, n_i(x,y,z)\, \Delta r_i}{\sum_{i=1}^{33} r_i^2(x,y,z)\, n_i(x,y,z)\, \Delta r_i}, \tag{3.16}$$

$$\mathrm{LWC}(x,y,z) = \sum_{i=1}^{33} m_i(x,y,z) \rho_{\mathrm{air}}(x,y,z), \tag{3.17}$$

$$N_d(x,y,z) = \sum_{i=1}^{33} n_i(x,y,z) \rho_{\mathrm{air}}(x,y,z). \tag{3.18}$$

As a consequence of the method of moments by *Tzivion et al.* (1987), the bin radius r_i varies around the bin center and has to be calculated in Equation 3.15 using the mass mixing ratio m_i and cloud droplet mixing ratio n_i within each bin. Subsequently the effective radius is derived in Equation 3.16 using r_i. The sum in Equation 3.17 of the product of mass mixing ratios m_i and air density ρ_{air} yields liquid water content just as total cloud droplet concentration N_d results from droplet number mixing ratios n_i in Equation 3.18.

Figure 3.2 shows a snapshot of the 3D effective radius field around 12 h 40 min LT. Here, the growth of cloud droplets with height can clearly be seen in the cloud vertical profile. Figure 3.3a shows the corresponding liquid water path in $\mathrm{g\,m^{-2}}$ and vertical cross-sections of liquid water content in $\mathrm{g\,m^{-3}}$ at $x = 3.5\,\mathrm{km}$ and $y = 2.75\,\mathrm{km}$. In this figure, the full range of LWP and LWC is shown by a logarithmic colormap to highlight their characteristics at cloud edges. With $1067\,\mathrm{g\,m^{-2}}$, the LWP maximum is found co-located with a LWC maximum of over $2\,\mathrm{g\,m^{-3}}$ inside the strongest convective core. Corresponding to Figure 3.3a, optical thickness τ and vertical cross-sections of effective radius r_{eff} are shown in Figure 3.3b. With an overall cloud fraction of 7.6% and a mean optical depth $\tau = 26.5$ for cloudy regions with LWP $> 20\,\mathrm{g\,m^{-2}}$, the maximum optical depth of $\tau = 176$ is found at the convective core as well.

Vertical profiles of cloud micophysics

In the following, statistics of the average microphysical profile combined for all 12 time steps are analyzed to characterize the sampled prior distribution of cloud microphysics. For this analysis, cloud grid boxes are accepted with a liquid water mixing ratio $r_l > 0.01\,\mathrm{g\,kg^{-1}}$ while whole grid columns are assumed cloudy for LWP $> 20\,\mathrm{g\,m^{-2}}$ following the definition by *Jiang and Li* (2009). Figure 3.4 shows contoured frequency by altitude diagrams (CFAD, *Yuter and Houze* (1995)) of

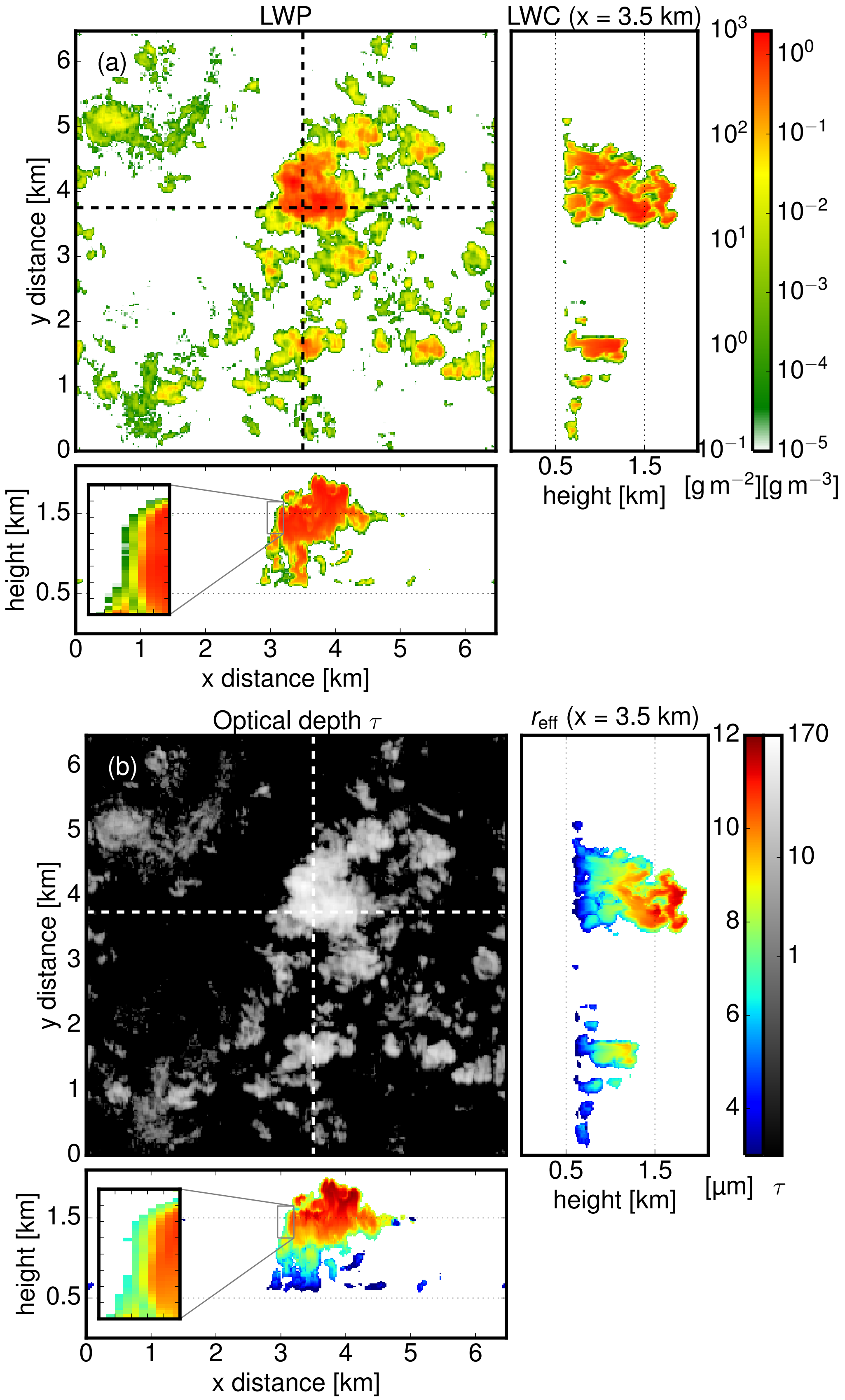

Figure 3.3: (a) Liquid water path in $\mathrm{g\,m^{-2}}$ and vertical cross-sections of liquid water content in $\mathrm{g\,m^{-3}}$ at $x = 3.5\,\mathrm{km}$ and $y = 2.75\,\mathrm{km}$ for the LES cloud field around $12\,\mathrm{h}$ $40\,\mathrm{min}$ LT. **(b)** Corresponding optical thickness τ and vertical cross-sections of effective radius r_{eff} for the same cloud scene. Zoomed cut-outs contain cross-sections of r_{eff} and LWC for a cloud edge region showing signs of lateral entrainment.

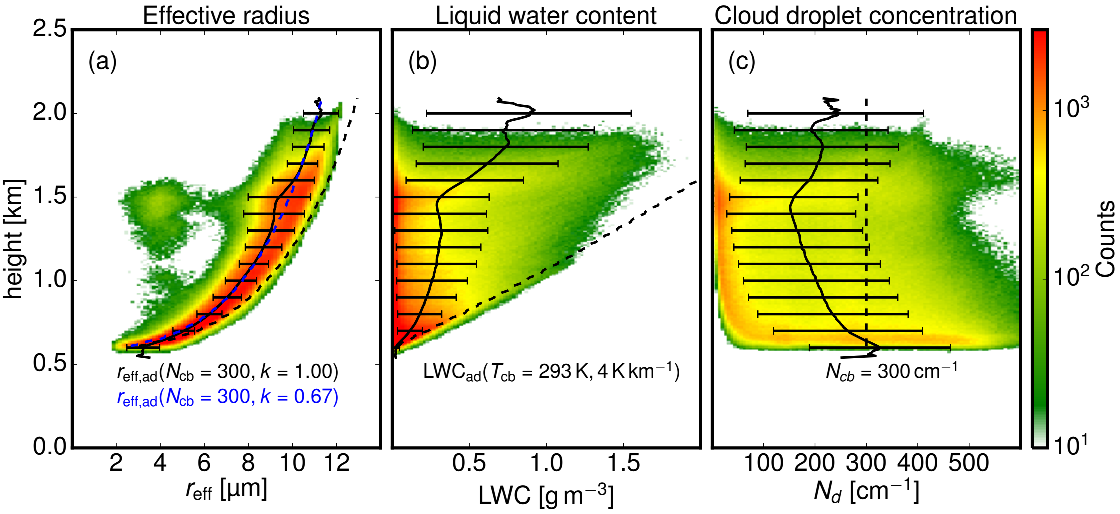

Figure 3.4: Contoured frequency by altitude diagrams (CFADs) of effective radius r_{eff} **(a)**, liquid water content LWC **(b)** and cloud droplet number concentration N_d **(c)**. The respective mean profile (black solid line) and its standard deviation (error bar) are superimposed. The dashed profile is the theoretical adiabatic limit calculated for conditions at cloud base ($T_{\mathrm{cb}} = 293\,\mathrm{K}, N_{\mathrm{cb}} = 325\,\mathrm{cm}^{-1}, 4\,\mathrm{K\,km}^{-1}$).

effective radius r_{eff} (Figure 3.4a), liquid water content LWC (Figure 3.4b) and total cloud droplet number concentration N_d (Figure 3.4c) summarized over all sampled time steps. The respective mean profile (black solid line) and its standard deviation (error bar) are superimposed on each CFAD. While effective radii sharply increase from $3\,\mu\mathrm{m}$ after droplet activation at cloud base to $12\,\mu\mathrm{m}$ at cloud top ($h = 1.7\,\mathrm{km}$) with a small spread, the LWC increases gradually from cloud base to $0.9\,\mathrm{g\,m}^{-3}$ at $h = 1.5\,\mathrm{km}$ with a broad spread of LWC values. Above $1.5\,\mathrm{km}$, convection is capped by a subsidence inversion where cloud liquid water accumulates to values of up to $1.5\,\mathrm{g\,m}^{-3}$. For most clouds, total cloud droplet concentration N_d, in contrast, decreases from up to $500\,\mathrm{cm}^{-1}$ at cloud base to below $100\,\mathrm{cm}^{-1}$ within a few hundred meters. Mean values of N_d also decrease with height from $300\,\mathrm{cm}^{-1}$ down to $150\,\mathrm{cm}^{-1}$ at a height of $1.5\,\mathrm{km}$. Here, the maximum count in the CFAD for N_d is associated with grid boxes at cloud edges while the wide spectrum of N_d can be found within the cloud cores. For comparison, a theoretical adiabatic liquid water content profile is calculated (black dashed line in Figure 3.4b) using the average cloud base temperature $T_{\mathrm{cb}} = 293\,\mathrm{K}$, pressure and a saturated adiabatic lapse rate of $4\,\mathrm{K\,km}^{-1}$ using Equation 2.10. Combined with the initial cloud droplet concentration ($N_{\mathrm{cb}} = 300\,\mathrm{cm}^{-1}$) at cloud base, $r_{\mathrm{eff,ad}}$ for mono-disperse droplets ($k = 1$) gives an upper limit for r_{eff} in Figure 3.4a. A more realistic value of $k = 0.67$ (found for polluted clouds by *Martin et al.* (1994)) compares exceptionally well with the mean profile of r_{eff}. Compared with the adiabatic limit, the existence of entrainment becomes evident in LWC and N_d profiles. While LWC increases along the theoretical adiabatic limit for a few grid boxes, in most grid boxes LWC is close to adiabatic only at cloud base. Together with N_d, LWC decreases to about one fifth of the adiabatic limit shortly above cloud base as described in *Jiang and Li* (2009) and in agreement with in situ measurements by *Warner* (1955). In contrast, r_{eff} follows the adiabatic limit more closely with a mono-modal distribution in accordance with in-situ aircraft observations during the RICO campaign (*Arabas et al.*, 2009).

Analysis of the lateral entrainment influence

The influence of entrainment is strongest at cloud edges with dry air getting mixed with cloudy air. Since the cloud side remote sensing focus exactly on this region, thorough analysis of this process is mandatory. As shown in Section 2.1.9, entrainment can have significant and different effects on droplet size spectra as cloudy air gets sub-saturated. Going back to the example time step at $12\,h\ 40\,min$ LT, Figure 3.3 shows zoomed cut-outs for a cloud edge region in the cross-sections of r_{eff} and LWC. While LWC naturally drops towards cloud edges, r_{eff} drops too; an indication for droplet evaporation taking place. A better insight into this characteristic can be gained when the volumetric cloud droplet radius r_{vol} and N_d are plotted against corresponding LWC values following the approach by *Gerber et al.* (2008) (introduced in Figure 2.4). In Figure 3.5 the result of this comparison, done at each height seperatly, is shown for all selected LES time steps combined. Assuming that lower LWC values can mostly be found at cloud edges, r_{vol} decreases up to 50% going from high LWC within cloud cores towards lower LWC at cloud edges; a further evidence for homogeneous mixing in this model. As explained by *Jiang and Li* (2009) and *Hill et al.* (2009), the observed decrease of r_{vol} at cloud edges is caused by the inherent homogeneous mixing in current models since within each grid cell all drops are exposed to the same sub-adiabatic conditions after entrainment. While the 50% decrease in r_{vol} happens at very low LWC values and therefore in very transparent cloud regions, r_{vol} at optically thicker cloud regions ($LWC > 0.1$) is still 20% lower compared to values found at cloud cores. Since the model microphysics exhibit characteristics of inhomogeneous as well as of homogeneous mixing, the LES output provides a prior for the Bayesian approach which reflects the state of scientific discussion at the moment.

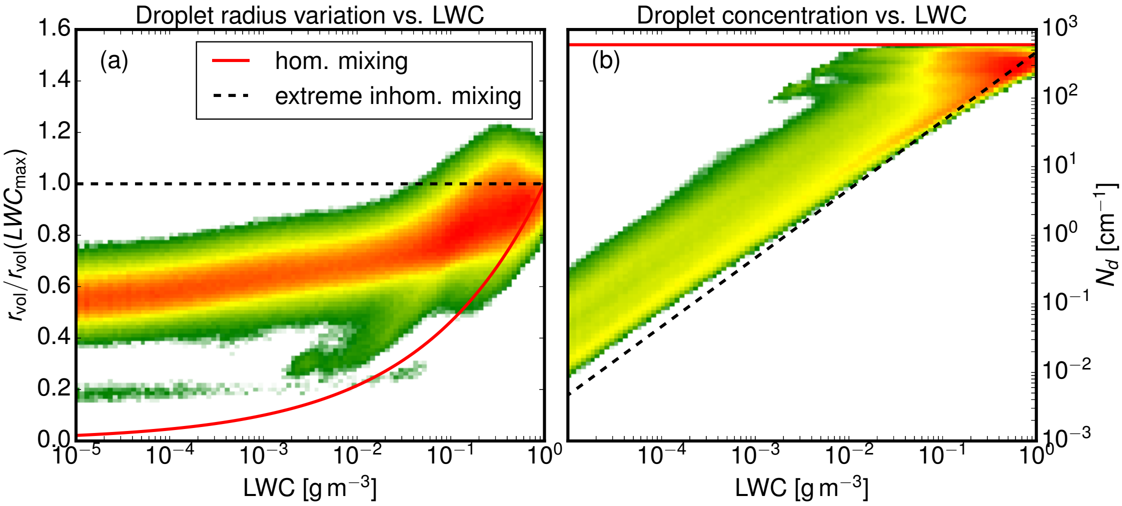

Figure 3.5: **(a)** Deviations of volumetric radii r_{vol} to $r_{v,max}$ found at maximum LWC as a function of LWC. Data is evaluated at each height separately for the selected LES cloud fields. **(b)** Cloud droplet number concentrations N_d [cm^{-1}] as a function of LWC for the selected cloud fields. The lines indicate values of r_{vol} and N_d that would be found in homogeneous mixing (red drawn) and extreme inhomogeneous mixing (black dashed) regimes.

3.3 Defining the cloud surface

With a sideways perspective on model cloud sides so highly heterogeneous, careful attention has to be paid to the photon transport at clouds edges. As *Platnick* (2000) showed, the penetration depth of reflected photons in the visible spectrum lies within some hundred meters while in the near-infrared spectrum the penetration depth is only a few dozen meters. Since the thickness of the subsiding shell mentioned before is in the same order of magnitude as the photon penetration depth, the co-registration of responsible cloud droplet sizes with modelled radiances becomes essential. As already mentioned in Section 3.1.3, during the approximation of the posterior distribution by Monte Carlo sampling, the likelihood distribution $p_{fwd}(L_{0.87}, L_{2.10}|\, r_{eff})$ is separated into the MYSTIC radiative transfer code f_{mys} and an observation term f_{obs}. Since the MYSTIC model needs a complete cloud scene $\mathbf{m_i}$ as input, the term $p_{obs}(\mathbf{m_i})$ selects the grid boxes in $\mathbf{m_i}$ containing r_{eff} to which the reflected radiance pair $(L_{0.87}, L_{2.10})$ is sensitive to. In other words, f_{obs} selects the effective radius which is visible from $\mathbf{m_i}$ given the cloud side observation perspective. Besides the observation perspective, this **apparent effective radius** $\langle r_{eff}\rangle_{app}$ also depends on the observed wavelength since different scattering and absorption coefficients lead to different cloud penetration depths.

$$\langle r_{eff}\rangle_{app} = f_{obs}(\mathbf{m_i}). \tag{3.19}$$

In the following, a technique will be introduced to obtain $\langle r_{\text{eff}} \rangle_{\text{app}}$ during the Monte Carlo tracing of photons which was developed in a preceding master thesis (*Ewald*, 2012).

3.3.1 Determination of the apparent effective radius

In their statistical retrieval approach, *Zinner et al.* (2008) traced along the line of sight of each individual sensor pixel until hitting the first cloudy grid box from which they selected $\langle r_{\text{eff}} \rangle_{\text{app}}$. This method, although very straightforward, has its limitations when it comes to highly structured cloud sides with horizontally inhomogeneous microphysics. By neglecting the penetration depth of photons, reflection from deeper within the cloud are disregarded. The found effective radius $\langle r_{\text{eff}} \rangle_{\text{app}}$ therefore becomes biased towards droplet sizes found directly at cloud edges. However, due to very low LWCs, these grid boxes have only a marginal contribution to the overall reflectance though they stand out in the field of $\langle r_{\text{eff}} \rangle_{\text{app}}$. Both effects are visible in the field of $\langle r_{\text{eff}} \rangle_{\text{app}}$ in Figure 3.7a, where the method by *Zinner et al.* (2008) was applied to the LES output step at 12 h 40 min LT for the ground-based perspective shown in Figure 4.28a. Although the particular cloud in the image center reaches up to an altitude of 1.7 km where droplet sizes $r_{\text{eff}} > 10\,\mu\text{m}$, the values for $\langle r_{\text{eff}} \rangle_{\text{app}}$ stay well below $7\,\mu\text{m}$ in Figure 3.7a.

In order to obtain a better estimate for p_{obs}, a more sophisticated method to determine $\langle r_{\text{eff}} \rangle_{\text{app}}$ has to be devised. As discussed by *Platnick* (2000), there exist analytical as well as statistical methods to consider the contribution of each cloud layer to the apparent effective radius $\langle r_{\text{eff}} \rangle_{\text{app}}$. *Yang et al.* (2003) give an analytically solution to calculate the optical properties of homogeneous mixed-phase clouds. The weighting method by *Platnick* (2000) is designed to determine $\langle r_{\text{eff}} \rangle_{\text{app}}$ for plane-parallel, vertically inhomogeneous clouds. Since these analytical solutions are based on one-dimensional weighting procedures, their application to three-dimensional cloud sides remain difficult. In contrast, the Monte Carlo technique explicitly traces photons as they travel through inhomogeneous cloud layers which can be exploited to calculate $\langle r_{\text{eff}} \rangle_{\text{app}}$. In a previous work, (*Ewald*, 2012) showed that the corresponding apparent effective radius $r_{\text{eff}_{\text{mc},i}}$ for one reflected photon can be derived as a weighted path integral in

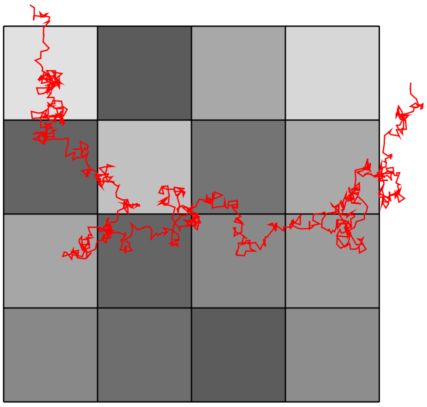

Figure 3.6: Statistical method to determine the effective radius of inhomogeneous clouds along the photon path

Equation 3.20. The optical path length $\lambda_{mc,i}$ for a photon results from the integration of the extinction coefficient k_{ext} of the cloud particles along the geometric path length l in Equation 3.21:

$$r_{eff_{mc,i}} = \frac{\int_0^l k_{ext}(l')\, r_{eff}(l')\, dl'}{\int_0^l k_{ext}(l')\, dl'}, \tag{3.20}$$

$$\lambda_{mc,i} = \int\limits_0^l k_{ext}(l')\, dl'. \tag{3.21}$$

The apparent effective radius $r_{eff_{mc,i}}$ for a photon can be described as a weighted, linear combination (Equation 3.20) of the individual effective radii r_{eff} the photon encounters on its path through the cloud. In Equation 3.20, the effective radii are weighted with the corresponding extinction coefficient k_{ext} of the cloud droplets along the path length in each grid box. Subsequently, the mean over all photons traced for one observation direction leads to the mean optical path length $\langle\lambda\rangle_{mc}$ and the apparent effective radius $\langle r_{eff}\rangle_{mc}$ derived with the Monte Carlo technique:

$$\langle\lambda\rangle_{mc} = \frac{\sum\limits_{i=0}^{photons} p_{w,i}\, \lambda_{mc,i}}{\sum\limits_{i=0}^{photons} p_{w,i}}, \tag{3.22}$$

$$\langle r_{eff}\rangle_{mc} = \frac{\sum\limits_{i=0}^{photons} p_{w,i}\, r_{eff_{mc,i}}}{\sum\limits_{i=0}^{photons} p_{w,i}}. \tag{3.23}$$

In the summations Equations 3.22 and 3.23, the photon weight $p_{w,n}$ is used to account for the different photon path probabilities. As the photon weights $p_{w,n}$ are also used in the calculation of $L_{0.87}$ and $L_{2.10}$, the apparent effective radius $\langle r_{eff}\rangle_{mc}$ can be derived simultaneously. This method was integrated within the MYSTIC Monte Carlo code and will therefore be referred to as the *MYStic method To Infer the Cloud droplet EFFective Radius (MYSTIC REFF)*. For the cloud scene shown in Figure 4.28a, Figure 3.7b shows the apparent effective radius $\langle r_{eff}\rangle_{mc}$ obtained with MYSTIC REFF. Compared with the effective radius found at the cloud edge (Figure 3.7a), $\langle r_{eff}\rangle_{mc}$ appears much smoother. The vertical gradient of $\langle r_{eff}\rangle_{mc}$ also compares better with the vertical gradient of effective radii r_{eff}shown in Figure 3.4b. In *Ewald* (2012) this method was validated with peer-reviewed techniques that determine the relative contribution of different cloud particles on reflected radiances. The comparison with the analytical solution of *Yang et al.* (2003) showed a very good agreement for homogeneous mixed-phase clouds. Here, the deviation of $\langle r_{eff}\rangle_{mc}$ to analytical determined effective radii remained

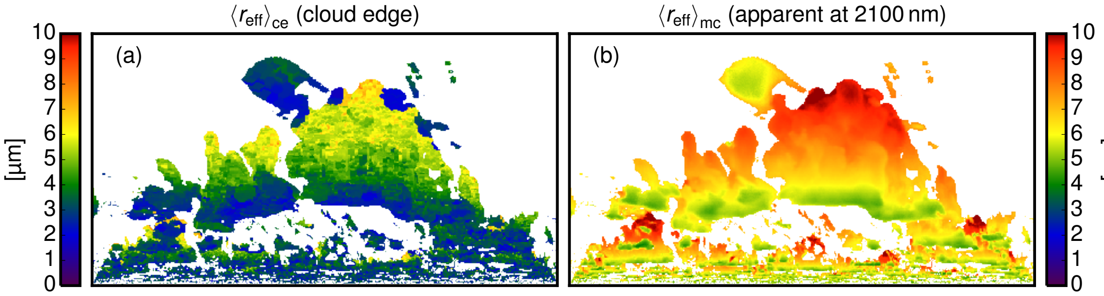

Figure 3.7: **(a)** Effective radii r_{eff} found at the cloud edge for the scene shown in Figure 4.28a, **(b)** Apparent effective radii $\langle r_{\text{eff}}\rangle_{\text{mc}}$ obtained with MYSTIC REFF for the same scene.

within the Monte Carlo noise. Likewise, MYSTIC REFF compares well with the method of *Platnick* (2000) which determines the apparent effective radius for one-dimensional clouds with a vertical effective radius profile.

3.3.2 Determination of the cloud surface in the model

Besides the apparent effective radius, the orientation of the cloud surface is another important factor that affects the solar radiance reflected from cloud sides. Following the definition in Equation 2.17b, the radiance L on a inclined surface dA is directly proportional to the cosine $\cos\vartheta$ of the incidence angle ϑ between illumination direction and surface normal. To investigate the impact of cloud surface orientation in particle size retrievals, *Ewald* (2012) developed a method to obtain the apparent cloud surface orientation in radiative transfer calculations. Since clouds, as heterogeneous collections of water droplets, have no clear boundaries, a general definition of the cloud surface had to be found to determine its orientation towards the sun.

After the first strongly forward-peaked scattering into a cloud, photons loose their initial travel direction. In this isotropic environment, the radiation transport can be described by the diffusion approximation where photon paths are essentially random walks within the scattering medium. In diffusion theory, the random walk of particles gets biased in the presence of a concentration gradient within the scattering medium, leading to a net flow of particles in the direction of lower concentrations as shown mathematically by *Crank* (1979). Following *Davis and Marshak* (2001), this also applies to scattered photons in optically thick media, where a gradient in optical thickness leads to a net transport of photons into the gradient direction towards a lower optical thickness. Since the liquid water content is the most variable factor in Equation 2.42 to calculate optical thickness, a gradient in liquid water content is also the determining factor for photon diffusion. With the isotropic scattering as a random process, the direction into regions of lower cloud droplet concentrations is also the direction with the greatest probability of escape.

Based on this fact, the cloud surface normal $\hat{\mathbf{n}}$ is defined in the following as the gradient $\nabla \mathrm{LWC}(\mathbf{r})$ in liquid water content with $\nabla = \left(\frac{\partial}{\partial x}, \frac{\partial}{\partial y}, \frac{\partial}{\partial y}\right)$ found at location $\mathbf{r}$. More precisely, the cloud surface normal $\hat{\mathbf{n}}$ corresponding to a measured or simulated radiance is defined as the gradient $\nabla \mathrm{LWC}(\mathbf{r})$ at the last scattering within the cloud before the photon reaches the detector. With $\hat{\mathbf{n}}$ as a vector, this approach avoids the arbitrary definition of a cloud boundary. Using the photons to collect $\nabla \mathrm{LWC}(\mathbf{r})$ at their last scattering location during the Monte Carlo ray-tracing, the cloud surface normal $\hat{\mathbf{n}}_{mc,i}$ can be derived simultaneously with the simulated radiance. Just as with the apparent effective radius technique, the mean cloud surface normal $\langle\hat{\mathbf{n}}_{mc}\rangle$ at a certain sensor viewing direction can be derived from a weighted sum (Equation 3.25) using the photon path probabilities $p_{w,i}$.

$$\hat{\mathbf{n}}_{mc,i} = \nabla \mathrm{LWC}(\mathbf{r}), \tag{3.24}$$

$$\langle\hat{\mathbf{n}}_{mc}\rangle = \frac{\sum\limits_{i=0}^{\text{photons}} p_{w,i}\,\hat{\mathbf{n}}_{mc,i}}{\sum\limits_{i=0}^{\text{photons}} p_{w,i}}. \tag{3.25}$$

Using this mean cloud surface normal $\langle\hat{\mathbf{n}}_{mc}\rangle$, one can calculate the local illumination angle and the local viewing angle relative to $\langle\hat{\mathbf{n}}_{mc}\rangle$. Calculated in this way, Figure 3.8a shows the cosine of the relative solar zenith angle $\langle\cos\vartheta_0^*\rangle$ for the ground-based perspective shown in Figure 4.28a. With a solar zenith angle of $\vartheta_0 = 67°$ (with the sun in the back), the illuminated and shadowed cloud parts are clearly discernible by the bright and dark shades.

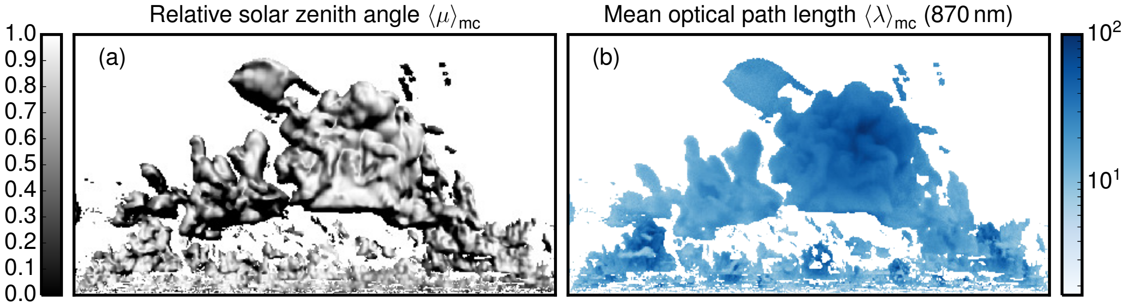

Figure 3.8: (a) Cosine of the local illumination angle $\langle\mu\rangle_{rm}$ on the cloud surfaces for the ground-based perspective shown in Figure 4.28b. **(b)** Mean optical path length $\langle\lambda\rangle_{mc}$ of reflected photons with $\lambda = 870\,\mathrm{nm}$ for the same scene as derived with the MYSTIC REFF method.

CHAPTER 4

Statistical retrieval of effective radius profiles

4.1 Sensitivity studies

This chapter addresses the challenges inherent to the retrieval of cloud droplet size profiles from convective cloud sides. Most of the time, nature is too complex to be fully represented by a mathematical description. Instead, physical theories are used to reduce the complexity and to extract basic principles from observations. In these theories assumptions are used to reduce the number of parameters to obtain a solvable problem. Most passive remote sensing techniques are based on various assumptions about cloud microphysics and about the overall cloud geometry. As described in Section 2.1, present cloud droplet size spectra $n(r)$ are replaced by scalar moments like the effective radius r_{eff} and the liquid water content. Furthermore, most retrievals are based on one-dimensional radiation transfer models. There, the viewing and illumination geometry as well as the cloud surface orientation are well defined and assumed to be known. In contrast, actual clouds, as well as the used LES clouds, are three-dimensional structures with a highly diverse mix of cloud droplet spectra $n(r)$. While the resort to r_{eff} and LWC is a widely accepted and tested approach to model unpolarized light reflected by planetary atmospheres *Hansen and Travis* (1974b), a three-dimensional cloudy atmosphere has remained a major challenge for passive remote sensing techniques (*Cahalan et al.*, 1994, *Fu et al.*, 2000, *Giuseppe and Tompkins*, 2003, *Marshak et al.*, 1998, *Zinner and Mayer*, 2006). As *Vant-Hull et al.* (2007) pointed out, it is in particular the unknown orientation of cloud surfaces towards the sun and the observer that can introduce large uncertainties on retrievals of effective radii. In the following, the sensitivity of reflected radiances to droplet size distributions will be analyzed. As well, the handling of unknown cloud geometries by Nakajima-King-type retrievals *Nakajima and King* (1990) will be tested. If not mentioned otherwise, all following sensitivity calculations were done for cloud droplets only, without considering molecular absorption or molecular scattering. This was done to isolate the investigated sensitivities from effects caused by one-dimensional

DISORT setups, like e.g. enhanced absorption due to longer path lengths or enhanced Rayleigh scattering at oblique viewing geometries.

4.1.1 Influence of the droplet size distribution

As mention in Section 2.1, droplets in clouds are not monodisperse, since collision-coalescence, condensation and evaporation in clouds are highly heterogeneous processes. The turbulent nature of clouds creates regions of higher and lower supersaturation leading to different growth rates throughout the cloud (*Shaw et al.*, 1998). In combination with entrainment, these processes all lead to a broadening of cloud droplet spectra until the onset of rain as summarized by *Beard and Ochs* (1993). The remote sensing of these polydisperse size distributions is a strongly under-determined problem, since many different size distributions lead to the same reflected radiance. This problem is handled by the introduction of the effective radius r_{eff} as described in Section 2.5.2. Ideally, cloud optical properties (optical thickness τ_c and asymmetry parameter g) would be a sole function of effective radius and total cloud droplet concentration N_d. The definition of r_{eff} is based on the assumption of $Q_{sca} = \text{const.}$ (see Section 2.5.2), which is met in the limit of geometric optics where the droplet size r is much larger than the wavelength λ. However, for droplets of the size and smaller than the observed wavelength λ, the scattering coefficient $Q_{sca}(r)$ becomes a function of the droplet size. This violates the assumption made from Equation 2.45 to Equation 2.46, where the mean radius for scattering r_{sca} becomes r_{eff} as long as the scattering efficiency Q_{sca} is invariant to droplet size. As droplets get smaller towards a size parameter of $X \approx 1$, their scattering efficiency Q_{sca} first increases until the Rayleigh scattering regime takes over for $X \ll 1$ where Q_{sca} decreases rapidly. The tail with small droplets of broad cloud droplet spectra $n(r)$can fall within this range, although its effective radius r_{eff} is well above the $X \approx 1$ limit. *Nakajima and King* (1990) analyzed the influence of droplet spectral width on cloud optical properties as a function of r_{eff} (Fig. 3 in their paper). Since they found only a weak sensitivity of cloud optical properties to droplet spectral width for $r_{\text{eff}} > 1\,\mu\text{m}$, they assumed the effective variance ν_{eff} to be fixed in their proposed retrieval method. Likewise, *Hatzianastassiou et al.* (1997) found that the broadening of the droplet spectrum mainly influences reflected radiation by its effect on r_{eff}.

Since the RICO LES output used in this work provides complete cloud droplet spectra, the individual spectra within each grid cell were replaced by modified gamma distributions (see Equation 2.43) of same LWC and r_{eff} but with a constant effective variance $\nu_{\text{eff}} = 7$. This was done to reduce the ill-posed problem of passive remote sensing of cloud microphysics down to two parameters (r_{eff} and LWC) within each grid box in contrast to a full cloud droplet size distribution $n(r)$. In order to validate the assumption that diffuse reflections from clouds are, within certain limits, largely insensitive to the specific shapes of cloud droplet spectra, the sensitivity of cloud optical properties, like Q_{sca} and g, to the spectral

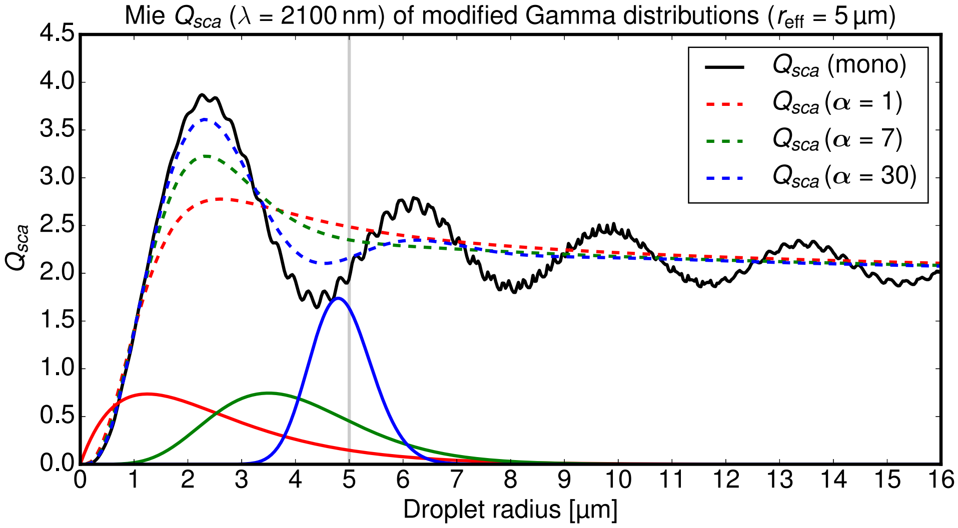

Figure 4.1: Mie scattering efficiency Q_{sca} of monodisperse (black line) cloud droplets as a function of droplet radius. Three modified gamma distributions with the same effective radius $r_{\mathrm{eff}} = 5\,\mu\mathrm{m}$ are shown as drawn lines for different width parameters: $\alpha = 1$ (red), $\alpha = 7$ (green), $\alpha = 30$ (blue). The dashed lines show corresponding Q_{sca} values for the three distributions obtained using the monodisperse Q_{sca} in Equation 4.1.

width (size parameter α) of the modified gamma distribution will be analyzed in the following. For that purpose, mean scattering efficiencies $\langle Q_{\mathrm{sca}} \rangle$ of the investigated droplet distributions were obtained by weighting monodisperse $Q_{\mathrm{sca}}(r)$ values with the size distribution $n(r)$ and the corresponding geometric cross-sections πr^2 of the droplets:

$$\langle Q_{\mathrm{sca}} \rangle = \frac{\int_{r_1}^{r_2} \pi r^2 \, Q_{\mathrm{sca}}(r) \, n(r) \, dr}{\int_{r_1}^{r_2} \pi r^2 \, n(r) \, dr}, \tag{4.1}$$

$$\langle g \rangle = \frac{\int_{r_1}^{r_2} \sigma_{\mathrm{sca}}(r) \, g(r) \, n(r) \, dr}{\int_{r_1}^{r_2} \sigma_{\mathrm{sca}}(r) \, n(r) \, dr}. \tag{4.2}$$

Similarly, the mean asymmetry parameter $\langle g \rangle$ was obtained by weighting monodisperse $g(r)$ values with the corresponding scattering cross-sections $\sigma_{\mathrm{sca}}(r)$ and, again, with the size distribution $n(r)$ of the droplets in Equation 4.2. In Figure 4.1, the scattering efficiency Q_{sca} of monodisperse (black line) cloud droplets at $\lambda = 2.1\,\mu\mathrm{m}$ is shown as a function of the droplet radius. Additionally, the same plot shows three different modified gamma distributions of same effective radius $r_{\mathrm{eff}} = 5\,\mu\mathrm{m}$ but with different width parameters α. Furthermore, the resulting mean scattering efficiencies $\langle Q_{\mathrm{sca}} \rangle$ obtained by Equation 4.1 are shown as dashed lines for the broad (red line), medium (blue line) and narrow (blue line) gamma distributions. While $\langle Q_{\mathrm{sca}} \rangle$ stays nearly the same at large r_{eff} for all three droplet distributions, the values differ when the droplet size becomes comparable with the wavelength $\lambda = 2.1\,\mu\mathrm{m}$. In particular, Q_{sca} exhibits a minimum where r_{eff} is twice as large as the wavelength λ for narrow distributions ($\alpha > 15$). This can be explained with the more asymmetric shape of the broad ($\alpha = 1$) compared to the narrow ($\alpha = 30$) gamma size distribution in this region of strongly fluctuating Q_{sca} between the optical geometric limit and the Rayleigh scattering regime. Since scattering efficiencies $Q_{sca}(r)$ of MGDs become a function of r_{eff} with $r_{\text{eff}} < 6\,\mu\mathrm{m}$, the microphysical effective radius r_{eff} of this droplet spectra no longer relates to the optically relevant mean scattering radius r_{sca}. Due to this split at $\lambda = 2.1\,\mu\mathrm{m}$ between r_{eff} and r_{sca} for small, but realistic values of r_{eff}, the validity of the assumption that reflected radiances are invariant to the width of droplet spectra must be critically scrutinized in this context. To that end, the influence of spectral width α on optical properties $Q_{sca}(r)$ and $g(r)$ as a function of r_{eff} was comprehensively analyzed for wavelengths ($0.87\,\mu\mathrm{m}$, $1.6\,\mu\mathrm{m}$, $2.1\,\mu\mathrm{m}$ and $3.7\,\mu\mathrm{m}$) widely used in passive remote sensing retrievals of r_{eff}. Figures 4.2a–4.2d show the Mie asymmetry parameter g of MGDs as a function of their effective radius r_{eff} and their width parameter α. As already seen for the scattering efficiencies Q_{sca} in Figure 4.1, there also exists a minimum in g around effective radii r_{eff} twice as large as the wavelength λ. Hereby, the minimum in g becomes less pronounced for broader size distributions, since the monotonic g get averaged over a wider range of droplet sizes in Equation 4.2. In Figures 4.2e–4.2h the same is shown for the Mie scattering efficiency Q_{sca} of MGDs. For better visibility, the color scale has been restricted to values of Q_{sca} between 1.8 and 2.8. Although less pronounced, the minimum in g is also seen in Q_{sca} for r_{eff} of twice the wavelength. Moreover, the asymmetric shape of MHDs leads to a variation of Q_{sca} with α for broader ($\alpha < 10$) distributions. Furthermore, the range of r_{eff}, for which Q_{sca} remains largely invariant to r_{eff} as well as α, becomes more limited to larger droplet sizes for larger wavelengths. In conclusion, the chosen spectral width of $\alpha = 7$ is in between the two regimes for smaller distributions ($\alpha > 7$), where the monodisperse features of Q_{sca} become evident, and for broader distributions ($\alpha < 7$), where the asymmetry towards smaller droplets influences $Q_{sca}(r)$.

Although this influence of spectral width on optical properties is by itself interesting, the consequences for reflected radiances are still to be determined. Since the scope of this work are convective water clouds, reflected radiances for optically thick water clouds were calculated as functions of viewing zenith angle ϑ, effective radius r_{eff} and spectral width α using the mean optical properties as input for the radiative transfer model DISORT. To this end, the calculations were done for $1\,\mathrm{km}$ thick water clouds and a fixed LWC of $1.0\,\mathrm{g\,kg^{-1}}$ (which relates to $\tau \approx 300$ for $r_{\text{eff}} = 5\,\mu\mathrm{m}$ and $\tau \approx 100$ for $r_{\text{eff}} = 15\,\mu\mathrm{m}$) to ensure comparability of Q_{sca} for different width parameters α. As LWC values were also left unchanged in the derivation (Equation 3.17) of microphysical properties from the LES output, this analysis presents an error estimate for the assumption of a fixed spectral

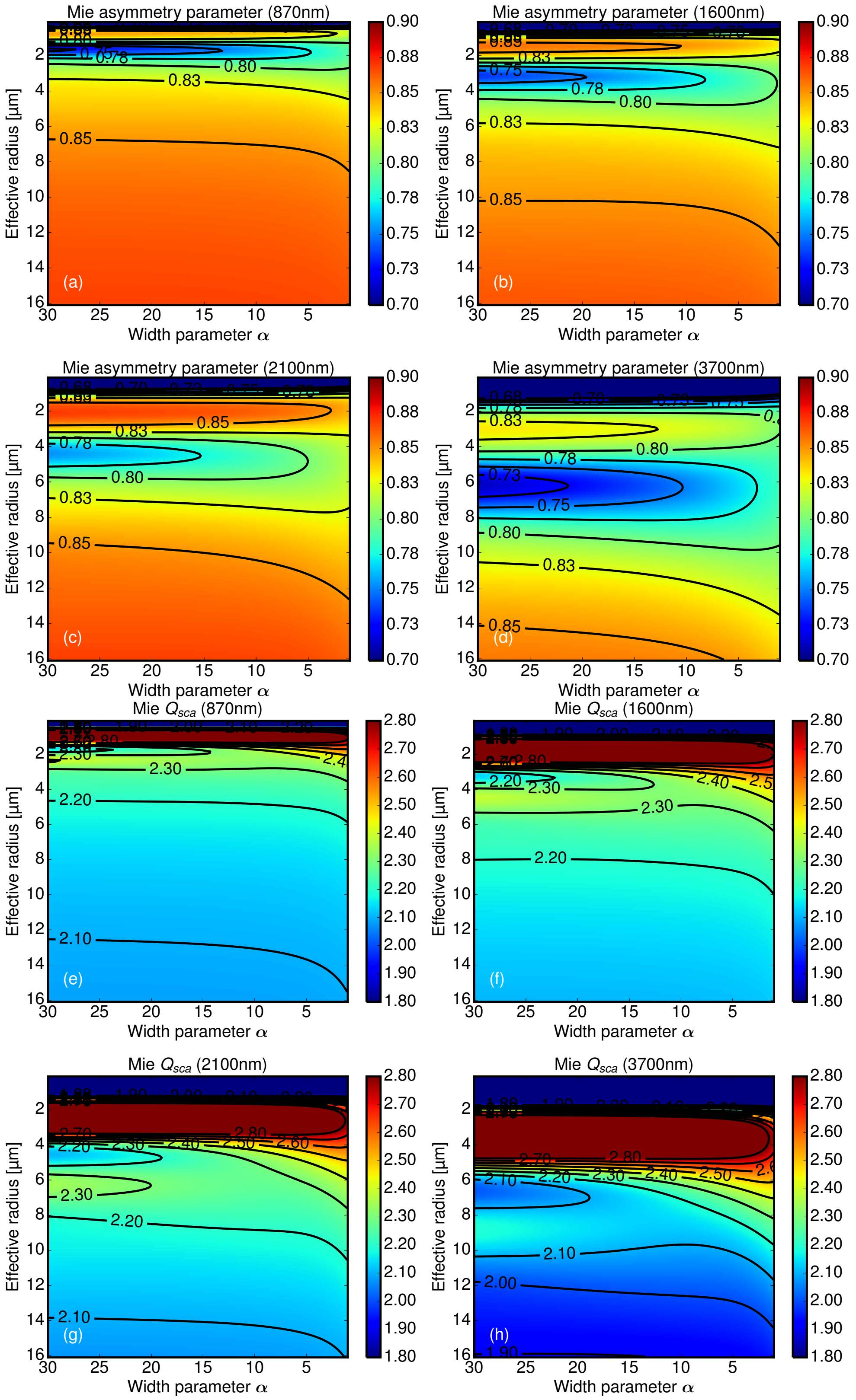

Figure 4.2: (a,b,c,d) Mie asymmetry parameter g of modified gamma distributions (MGD) as a function of their effective radius r_{eff} and their width parameter α for the wavelength 870 nm, 1600 nm, 2100 nm, 3700 nm. **(e,f,g,h)** Mie scattering efficiency Q_{sca} of MGDs as a function of their effective radius r_{eff} and their width parameter α for the wavelength 870 nm, 1600 nm, 2100 nm, 3700 nm.

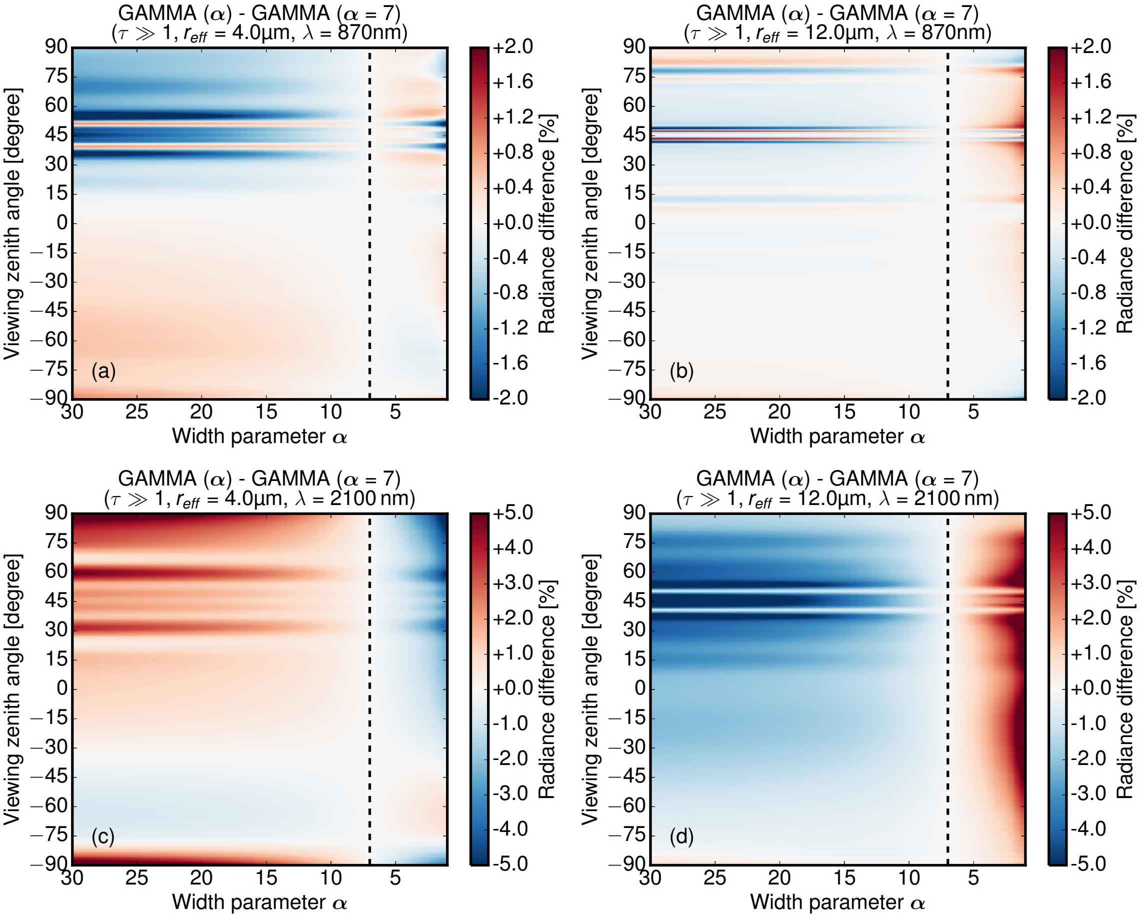

Figure 4.3: Spectral radiance biases that would occur if realistic modified gamma distributions would exhibit another width parameter α than the used $\alpha = 7$. Biases are shown in percent of deviation from optically thick clouds ($\tau \gg 1$) with $\alpha = 7$ as a function of α and viewing zenith angle ϑ with a sun zenith angle of $\vartheta_0 = 45°$). **(a,b)** Radiance biases at 870 nm for clouds with effective radius $r_{\text{eff}} = 4$ and $r_{\text{eff}} = 12$. **(c,d)** The same radiance biases are shown for 2100 nm with $r_{\text{eff}} = 4$ and $r_{\text{eff}} = 12$.

width of $\alpha = 7$. Figure 4.3 shows the radiance biases that would occur if realistic MGDs would exhibit another width parameter α than the used $\alpha = 7$. In this plot the radiance biases are shown as a function of α and the viewing zenith angle with the sun at a zenith angle of $\vartheta_0 = 45°$ for two different effective radii ($r_{\text{eff}} = 4\,\mu\text{m}$ and $r_{\text{eff}} = 12\,\mu\text{m}$) at wavelengths of $\lambda = 870\,\text{nm}$ (Figures 4.3a and 4.3b) and $\lambda = 2.1\,\mu\text{m}$ (Figures 4.3c and 4.3d). In all four cases the largest radiances biases are found near the backscatter geometry in the region of the glory. As a single scattering feature, the glory and its intensity are very sensitive to changes of the mean scattering phase function $\langle \mathcal{P} \rangle$ (*Mayer et al.*, 2004). Albeit constant r_{eff}, different width parameters lead to different $n(r)$ distributions which, in turn, lead to different weightings of monodisperse phase functions in $\langle \mathcal{P} \rangle$. With a maximum

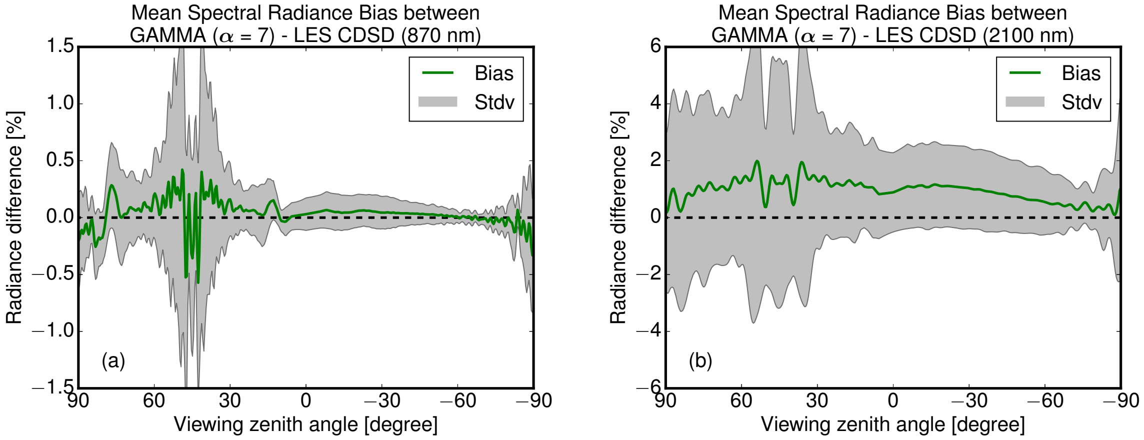

Figure 4.4: Mean spectral radiance bias that occurs between 200 randomly sampled cloud droplet size distributions (CDSD) $n(r)$ from the LES output and modified gamma distributions with a fixed width parameter of $\alpha = 7$. Calculations were done for reflected radiances from a 1 km thick water cloud with effective radii r_{eff} and LWC values from the LES output. **(a)** Mean spectral radiance bias in percent for $\lambda = 870\,\text{nm}$. **(b)** Mean spectral radiance bias in percent for $\lambda = 2.1\,\mu\text{m}$.

positive bias of +7.4% and maximum negative bias of −7.8%, the differences are larger for $\lambda = 2.1\,\mu\text{m}$ when compared to the maximum biases at $\lambda = 870\,\text{nm}$ (+2.0%, −3.3%). The larger biases for $\lambda = 2.1\,\mu\text{m}$ are a direct consequence of r_{eff} being closer at the concerned wavelength (see Figure 4.2g). The sign of the biases depends on the asymmetry of the distribution and the location of r_{eff} along $Q_{sca}(r)$; overlap of $n(r)$ with local minima in $Q_{sca}(r)$ lead to a smaller optical thickness τ, while overlap of $n(r)$ with local maxima in $Q_{sca}(r)$ lead to an optically thicker clouds.

Although the preceding analysis gives a range of potential radiance biases, an investigation of actual occurring radiance biases between realistic cloud droplet size distributions (CDSD) from the LES and MGDs with fixed width parameter is still pending. To that end, the configuration of the preceding analysis was adopted with CDSDs, effective radii r_{eff} and LWC values taken from 200 randomly sampled LES grid boxes with LWC $> 0.1\,\text{g}\,\text{m}^{-3}$. Figure 4.4 shows the mean spectral radiance biases (green line) and its standard deviation (gray area) that occur due to the assumption of MGDs with fixed width parameter $\alpha = 7$ instead of the actual, highly diverse CDSDs from the LES model. The radiance bias for $\lambda = 870\,\text{nm}$ (Figure 4.4a) varies between −0.6% and 0.4% (mean radiance bias 0.04%) with a mean standard deviation of 0.3%, while the radiance bias for $\lambda = 2.1\,\mu\text{m}$ (Figure 4.4b) varies between 0.4% and 3.2% (mean radiance bias 1.4%) with a mean standard deviation of 1.6%. Likewise, the mean biases in upward fluxes are relatively small and positive with 0.05% for $\lambda = 870\,\text{nm}$ and 0.9% for $\lambda = 2.1\,\mu\text{m}$. Even though these biases are already relatively small compared to the extensive simplification from $n(r)$ to the scalar moments r_{eff} and LWC, radiance biases are negligible especially for viewing geometries far away from the backscatter geometry.

4.1.2 Explanation of the cloud geometry effect

As mentioned in the beginning of this chapter, the unknown orientation of cloud surfaces towards the sun and the observer can introduce large uncertainties in microphysical retrievals. With the reduction of complexity by describing cloud microphysics with r_{eff} and LWC, radiances measurements at two wavelengths are used to solve the inversion problem for these two unknown parameters with passive retrievals techniques like *Nakajima and King* (1990). As a prerequisite, these techniques assume that the viewing and illumination incident angle on the cloud surface is known. Since most retrievals are based on one-dimensional radiation transport models, the cloud surface normal $\hat{\mathbf{n}}$ is assumed to point at the zenith. However, the surfaces of convective cloud sides are far from pointing all in the same direction, let alone from pointing all at the zenith. Without additional information about the cloud geometry, the inversion of r_{eff} and LWC from measurements at $\lambda = 870\,\text{nm}$ and $\lambda = 2.1\,\mu\text{m}$ becomes under-determined.

While reflected radiances at non-absorbing wavelengths are essentially influenced by the amount of radiation incident on the cloud surface, the level of these radiances is also used by Nakajima-King-type retrievals to infer the cloud optical thickness τ and thereby the liquid water content. For that reason, the classical framework of Nakajima-King-type retrievals has to be re-evaluated in the context of cloud side remote sensing. In this situation, one possibility can be the limitation to optically thick clouds, since most convective clouds cover larger areas and have higher liquid water contents than small cumuli or cirrus clouds. Figure 4.5 shows the saturation behavior of spectral radiance for water clouds at $\lambda = 870\,\text{nm}$ and $\lambda = 2100\,\text{nm}$ as a function of cloud optical thickness τ_c and effective radius r_{eff}. With the illumination and viewing configuration shown in Figure 4.6b, the DISORT calculations discover at which cloud optical thickness spectral radiances reach their optically thick limit. In the following, the optically thick limit will be defined for τ_c for which spectral radiances have reached 95% of their maximum value. In that way, larger values of τ_c have only a little effect on the cloud radiance with deviations comparable with other uncertainties, e.g. the calibration accuracy.

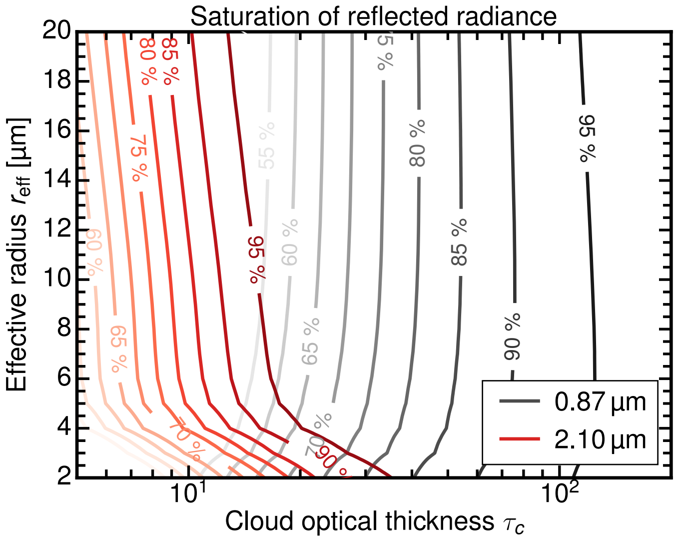

Figure 4.5: Saturation behavior of spectral radiances for water clouds at $\lambda = 870\,\mathrm{nm}$ and $\lambda = 2100\,\mathrm{nm}$ as a function of cloud optical thickness τ_c and effective radius r_{eff}. Calculations were done for the configuration ($\vartheta_0 = 30°, \vartheta_s = 150°$) shown in Figure 4.6b using DISORT to discover the optical thickness limit from which on water clouds are not getting brighter.

In the following, the approach to limit the retrieval to optically thick clouds, for which the cloud surface orientation is unknown, will be tested for feasibility within the retrieval framework of *Nakajima and King* (1990). For ease of understanding, the following angle and vector notation will be used: the normal which defines the cloud surface is $\hat{\mathbf{n}}$, the vector pointing from the sun in the light propagation direction is denoted with $\hat{\mathbf{s}}$ and the vector pointing into the direction of the observer is denoted with $\hat{\mathbf{v}}$. The viewing zenith angle ϑ and the sun zenith angle ϑ_0 are still referenced within the global coordinate system which is defined parallel to the ground surface. Corresponding to these two angles, there exist two additional angles which describe the inclination of $\hat{\mathbf{s}}$ and $\hat{\mathbf{v}}$ on a freely oriented cloud surface. The the local illumination incident angle between the sun vector $\hat{\mathbf{s}}$ and the cloud surface normal $\hat{\mathbf{n}}$ is indicated by ϑ_0^* while the local viewing zenith angle between the viewing vector $\hat{\mathbf{v}}$ and the cloud surface normal $\hat{\mathbf{n}}$ is indicated by ϑ^*. Therefore, angles denoted with a star are always referenced to the cloud surface normal $\hat{\mathbf{n}}$. For simplicity, for now all vectors are assumed to be within a plane spanned by $\hat{\mathbf{s}}$ and $\hat{\mathbf{n}}$ (which is called the **principal plane**). This assumption will be relaxed in the next section.

In contrast to the one-dimensional case, only the scattering angle ϑ_s between $\hat{\mathbf{s}}$ and $\hat{\mathbf{v}}$ is known in addition to radiance measurements from cloud sides. With at least some facts known, the subsequent step will explore, if this information and the assumption of optical thick clouds can help to retrieve cloud droplet sizes. Figure 4.6 shows the basic geometry for cloud side remote sensing with two different viewing geometries but the same illumination angle ϑ_0^*. with a vertical cloud surface with its normal within the principal plane. Figure 4.6 on the left shows a direct backscatter configuration (scattering angle $\vartheta_s = 180°$); a situation which would be more likely for the airborne perspective. On the right, the figure shows the same configuration for a different scattering angle $\vartheta_s = 150°$; a situation more likely for the ground-based perspective.

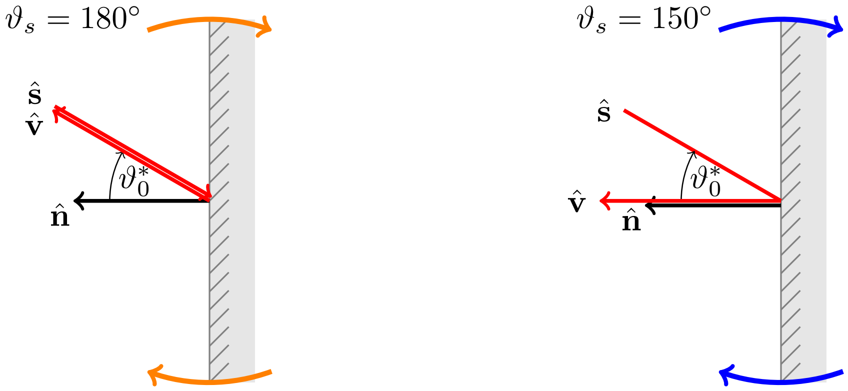

Figure 4.6: Two observation geometries with a scattering angle of $\vartheta_s = 180°$ **(left)** and $\vartheta_s = 150°$ **(right)**. Same cloud surface orientation $\hat{\mathbf{n}}$ (cloud surface normal) and illumination $\hat{\mathbf{s}}$ (solar direction vector) with same solar ϑ_0^* but different viewing zenith angle ϑ^* relative to the cloud surface. Impact of indicated cloud surface rotation on reflected radiances is shown in Figure 4.7

For both cases, Figure 4.7 shows spectral radiances at $\lambda = 870\,\mathrm{nm}$ and $\lambda = 2100\,\mathrm{nm}$ for a clockwise rotation of the cloud surface. The radiative transfer calculations were done with DISORT for an optically thick ($\tau = 500$) water cloud with a fixed r_{eff} of $9\,\mu\mathrm{m}$. To gain insight into the characteristics of reflected solar radiation from cloud sides, molecular absorption and scattering was neglected in this study. The arrows in Figure 4.7 indicate the progression of radiance values, as it could be observed during a cloud surface rotation within the principal plane as shown in Figure 4.6. Immediately striking is the similarity of these lines to the isolines for fixed r_{eff} crossing isolines of different τ in the classic Nakajima-King diagram (Figure 2.19). As already mentioned above, the classic Nakajima-King retrieval uses the radiance in the non-absorbing wavelength to infer the optical thickness τ. Numerous studies *Cahalan et al.* (1994), *Vant-Hull et al.* (2007), *Varnai and Marshak* (2002a), *Zinner and Mayer* (2006) pointed out, that tilted and therefore more shadowed or illuminated cloud sides have a huge impact on the retrieval of optical thickness, especially when using spatially highly resolved cloud images. The radiance similarity of cloud surface rotation and optical thickness variation further underlines the necessity to restrict the retrieval to optically thick clouds when the cloud surface orientation is unknown.

Therefore, the following analysis will determine the remaining information content in $L_{0.87}$ and $L_{2.10}$ about r_{eff} for optically thick clouds with an unknown cloud surface orientation. A difference between the direct backscatter case with a scattering angle of $\vartheta_s = 180°$ and the case with a scattering angle of $\vartheta_s = 150°$ becomes already evident in Figure 4.7. While the spectral radiance first increases at both wavelengths as the illumination and viewing angle becomes smaller, it is only in case of direct backscatter that spectral radiances decrease the same way as they increased when the illumination angle becomes more oblique again. In case of scattering angle $\vartheta_s = 150°$, and as long as the viewing vector $\hat{\mathbf{v}}$ onto the cloud is steeper than the solar angle $\hat{\mathbf{s}}$, spectral radiances at $\lambda = 2100\,\text{nm}$ are lower when compared to the remaining part of the rotation when the viewing angle $\hat{\mathbf{v}}$ onto the cloud is more oblique than the solar angle $\hat{\mathbf{s}}$.

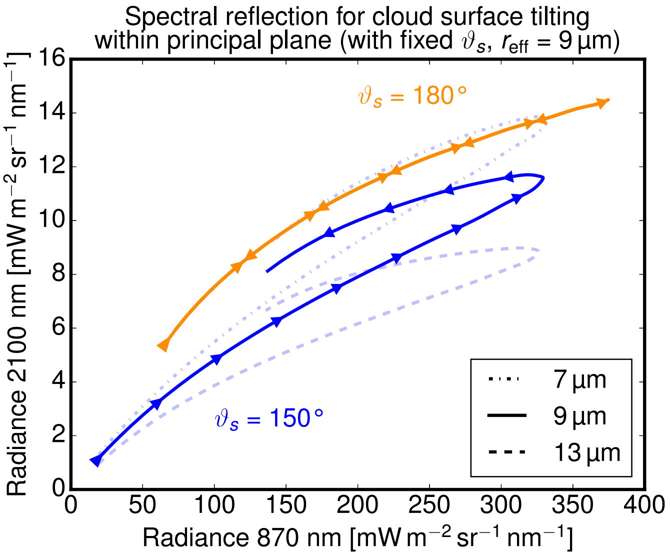

Figure 4.7: Spectral radiances used in Nakajima-King-type retrievals at $\lambda = 870\,\text{nm}$ and $\lambda = 2100\,\text{nm}$ during the rotation of the cloud surface for observation geometries shown in Figure 4.7. Calculations of spectral reflection were done for an optically thick ($\tau = 500$) water cloud with a fixed effective radius $r_{\text{eff}} = 9\,\mu\text{m}$ with a fixed scattering angle of $\vartheta_s = 180°$ (orange line) and $\vartheta_s = 150°$ (blue line).

This radiance behavior under cloud surface rotation within the principal plane leaves a characteristic bow structure visible for scattering angles $\vartheta_s < 180°$ in Figure 4.7. For optically thick clouds with unknown cloud surface orientation, this introduces a further ambiguity between $L_{0.87}$, $L_{2.10}$ and cloud optical properties. For the oblique viewing geometry, radiances for $r_{\text{eff}} = 9\,\mu\text{m}$ within the upper branch of the bow structure coincide with radiance values for $r_{\text{eff}} = 7\,\mu\text{m}$. Nevertheless, towards higher values of $L_{0.87}$ there remain unambiguous regions where radiance pairs ($L_{0.87}$, $L_{2.10}$) of different effective radii do not overlap (compare line for $r_{\text{eff}} = 13\,\text{um}$ in Figure 4.7).

Consequences for the Nakajima-King technique

Up to now, the analysis was limited to cloud surface orientations within the principal plane. The following study will relax this constraint to include all possible cloud surface orientations for which $\hat{\mathbf{s}}$ and $\hat{\mathbf{v}}$ lie within the half sphere defined by $\hat{\mathbf{n}}$; in simple terms to orientations for which the cloud surface is illuminated by the sun and can be viewed from. Furthermore, until now the study was based on one-dimensional radiation transport calculations using DISORT. To check whether the unambiguous regions in Figure 4.7 also exist for realistic, three-dimensional clouds, the Monte Carlo radiative transfer code MYSTIC will be used in the following. A sphere is the ideal geometrical object for this study, because it includes all surface orientations found in real clouds. Moreover, their shape resembles the convex characteristic of freshly formed cumulus clouds. In the plane, which is spanned by the illumination vector $\hat{\mathbf{s}}$ and the viewing vector $\hat{\mathbf{n}}$, the geometry is identical to the one-dimensional consideration within the principal plane in the preceding study. In addition, all cloud surface normals $\hat{\mathbf{n}}$ outside the principal plane are represented. To obtain a spherical model cloud with reasonable microphysics and a smooth cloud surface, an analytical expression of the liquid water content had to found. To include a realistic cloud shell caused by lateral entrainment, the analytical expression of LWC mimics a smooth transition between clear sky and cloudy areas. Accordingly, the expression for $LWC(r)$ is a function of the distance r from the point of origin and includes an exponential term which establishes the transition from clear sky to cloud interior:

$$LWC(r) = LWC_0 \left[1 - \exp\left(3\,\frac{r - r_0}{r_1 - r_0} - 3\right)\right] \; [\mathrm{g\,m^{-3}}] \qquad (4.3)$$

In Equation 4.3, r_0 is the inner sphere radius where LWC values are constant with LWC_0 for $r < r_0$. The second radius r_1 is the outer sphere radius where LWC values drop to zero marking the transition between clear sky and the cloud. This general setup was already used by *Ewald* (2012) to investigate the effect of 3D effects on the retrieval of effective radii. The following study will continue

Figure 4.8: Vertical LWC cross-section and profile (inset) of the spherical cloud used in Figure 4.9 to Figure 4.11.

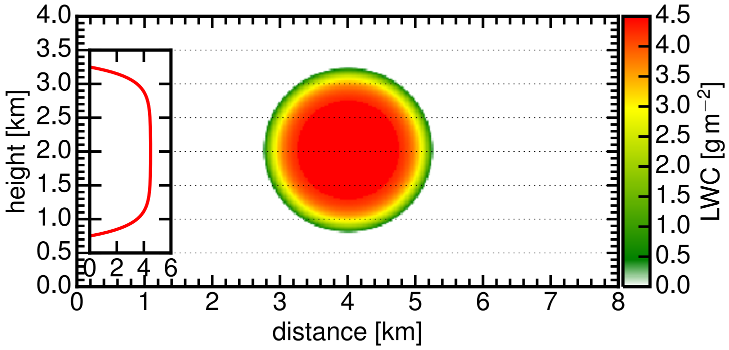

the analysis of *Ewald* (2012) and deepen the understanding of the process which lead to the ambiguity of radiance pairs ($L_{0.87}$, $L_{2.10}$) discovered in the preceding section.

In order to obtain an optically thick cloud with saturated radiances up to the outer regions of the sphere, a very high liquid water content of $LWC_0 = 4.5\,\mathrm{g\,m^{-3}}$ was chosen for the inner sphere with a radius of $r_0 = 750\,\mathrm{m}$. Between the inner radius $r_0 = 750\,\mathrm{m}$ and the outer radius $r_1 = 1250\,\mathrm{m}$ the liquid water content was smoothly phased out within a cloud shell of $500\,\mathrm{m}$ (see inset in Equation 4.3) to create a smooth cloud surface. With its center at $h = 2\,\mathrm{km}$, the cloud reached up to $h = 3.25\,\mathrm{km}$ with a diameter of $h = 2.5\,\mathrm{km}$. In accordance with the one-dimensional study, the effective radius remained constant with $r_{\mathrm{eff}} = 9\,\mathrm{\mu m}$. The spherical cloud was placed in a sufficiently large domain ($8 \times 8 \times 4\,\mathrm{km}$) with a horizontal and vertical grid resolution of $25\,\mathrm{m}$. An overview of the liquid water content field is given in Equation 4.3. With the albedo set to zero, the scene was pictured from above (viewing zenith angle of $\vartheta = 0°$) under varying illumination angles ($\vartheta_0 = 0°, 30°$ and $45°$) and therefore different scattering regimes of $\vartheta_s = 180°, 150°$ and $135°$. The radiative transfer was done with MYSTIC covering the full domain with 320×320 pixel with a spatial resolution of $25\,\mathrm{m}$.

The following Figure 4.9 to Figure 4.11 show the results of the three cases of different illumination regimes in Nakajima-King-type diagrams on the left and as images on the right. While the radiance pairs ($L_{0.87}$, $L_{2.10}$) obtained from the Monte Carlo simulation are shown as scattered points in Figure 4.9 (left), the results from the one-dimensional DISORT simulations are shown like in Figure 4.7 as isolines for different effective radii. The gray isolines in Figure 4.9 on the left mark radiance pairs with same illumination angle ϑ_0^* onto the cloud. On the right, Figure 4.9 shows corresponding images of $L_{0.87}$ and $L_{2.10}$ and the ratio $L_{2.10}/L_{0.87}$. This is done to connect the radiance pairs in the diagram in the left to their spatial origin on the sphere on the right like it is done for the superposed green and red points of same illumination angle $\vartheta_0^* = 30°$.

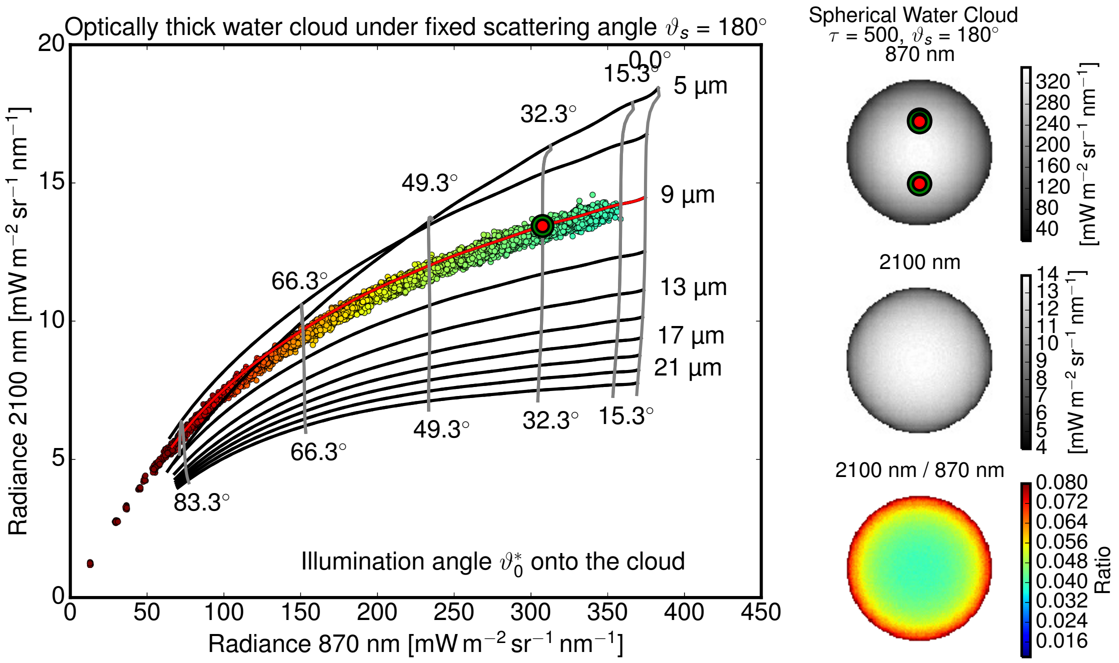

Figure 4.9: **(left)** Spectral radiances at $\lambda = 870\,\mathrm{nm}$ and $\lambda = 2.1\,\mu\mathrm{m}$ for a spherical and optically thick water cloud observed at a fixed scattering angle of $\vartheta_s = 180°$ with the sun in the back. Radiances shown by the black lines were calculated with DISORT with respective fixed r_{eff}. **(right)** Images of $L_{0.87}$ and $L_{2.10}$ for the spherical cloud and their ratio to identify the origin of radiance pairs in the scatter plot on the left.

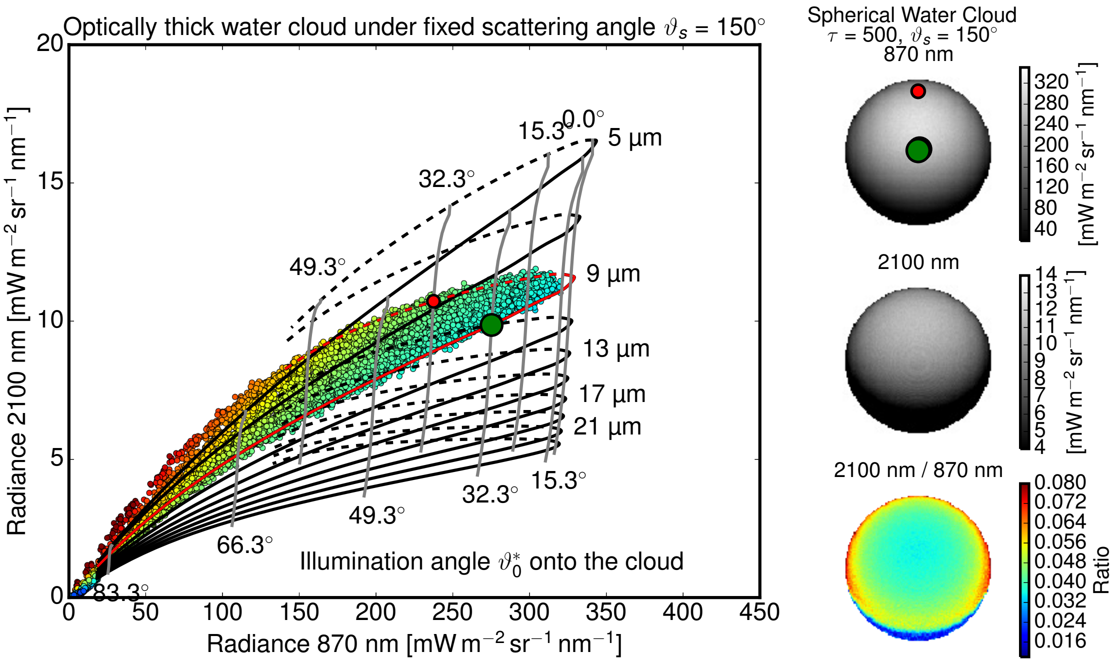

Figure 4.10: Same as Figure 4.9 but for a scattering angle of $\vartheta_s = 150°$

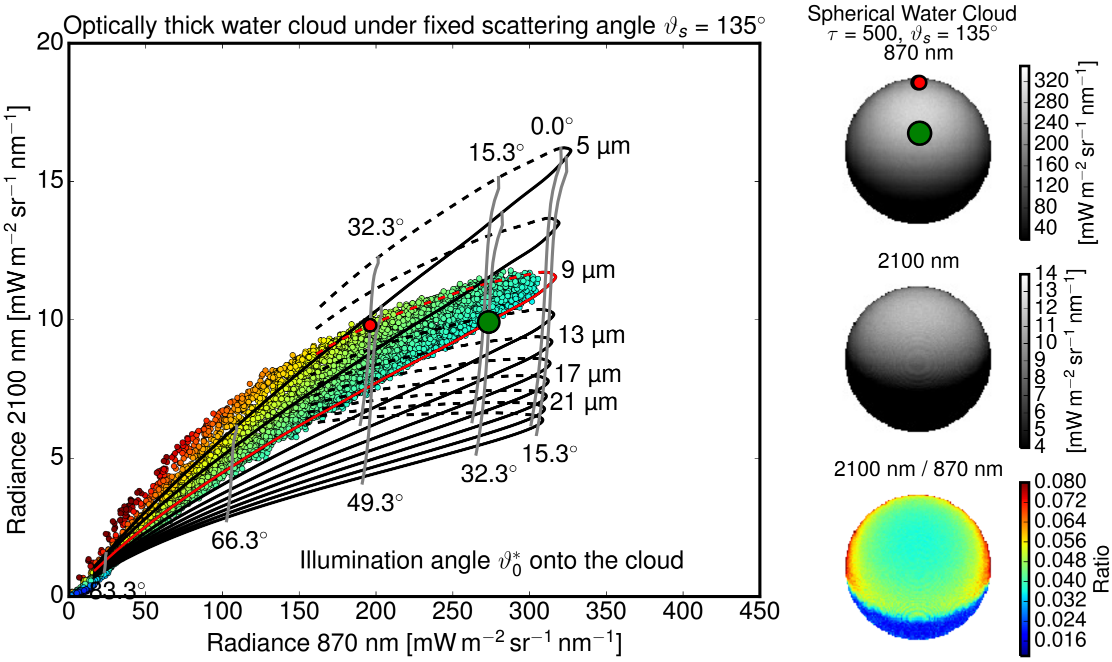

Figure 4.11: Same as Figure 4.9 but for a scattering angle of $\vartheta_s = 135°$

For the direct backscatter geometry in Figure 4.9, the Monte Carlo results for $r_{\text{eff}} = 9\,\mu\text{m}$ match very closely the one-dimensional DISORT results for $r_{\text{eff}} = 9\,\mu\text{m}$.

Due to the symmetric illumination geometry, radiance values also decrease symmetrically with more oblique cloud surfaces. Albeit restricted to airborne or spaceborne platforms, this perspective minimizes the 3D effect on radiance ambiguities caused by unknown cloud surface orientations. The picture changes when the observer leaves the backscatter geometry as shown for a scattering angle of $\vartheta_s = 150°$ in Figure 4.10. As already shown for the one-dimensional case in Figure 4.7, the radiance pairs form a bow-like pattern with higher $L_{2.10}$ values at more oblique surface orientations. In addition to the one-dimensional study, the preceding consideration within the principal plane is now relaxed with cloud surface normals pointing in all directions. It is evident in Figure 4.10 that radiance pairs with cloud surface normals outside the principal plane remain confined by the one-dimensional values within the principal plane, e.g. the Monte Carlo values remain within the bow-like pattern discussed before. Furthermore, the points within the principal plane with the same illumination angle ($\vartheta_0^* = 30°$, red and green dot), leave their superposition seen in Figure 4.9. Where the relative viewing direction is more oblique ($\vartheta^* = 60°$, red dot), the radiance of the absorbing wavelength $L_{2.10}$ is larger compared with its value at the vertically downward-looking direction ($\vartheta^* = 0°$, green dot). Consequently, droplets with $r_{\text{eff}} = 9\,\mu\text{m}$ are wrongly assumed to have an effective radius of $r_{\text{eff}} = 7\,\mu\text{m}$ or even $5\,\mu\text{m}$ when these higher radiances values for $L_{2.10}$ are erroneously attributed to a weaker absorption of smaller cloud droplets. For an even smaller scattering angle of $\vartheta_s = 135°$, the overlap and thus the ambiguity between different effective radii becomes even more apparent (Figure 4.11). While the radiances at the non-absorbing wavelength drops considerably with a more oblique relative viewing geometry ($\vartheta^* = 75°$, red dot), the radiance at the absorbing wavelength remained nearly identical with its value at the very steep viewing geometry ($\vartheta^* = 15°$, green dot).

Ambiguities of reflected radiances

The preceding analysis showed the ramifications of unknown cloud surface geometries on Nakajima-King-type retrievals which have to be considered when applying the technique to three-dimensional clouds. Nevertheless, the reason for the higher radiance values of $L_{2.10}$ at the more oblique viewing angles remains to be discussed. To understand this different behaviour of reflected radiances between absorbing and non-absorbing wavelengths one has to return to the schematic configuration in Figure 4.12 for scattering angle $\vartheta_s = 150°$ for different viewing angles ($\vartheta^* = 0°$ and $60°$) but same illumination angle $\vartheta_0^* = 30°$. The two configurations correspond to the configuration found at the green and red dot in Figure 4.10 for scattering angle $\vartheta_s = 150°$. In order to put the two viewing geometries in context, Figure 4.13 shows the one-dimensional reflected radiance distribution with the same fixed illumination of $\vartheta_0^* = 30°$. Shown for different effective radii, the radiance distribution in Figure 4.13 includes all possible scat-

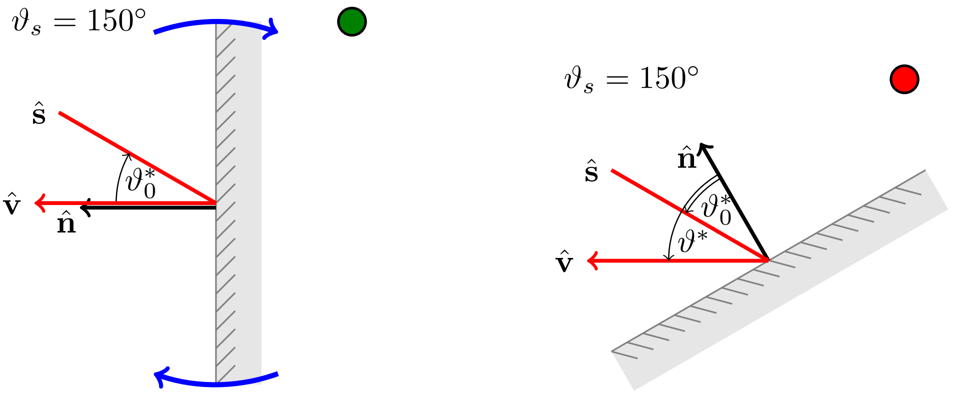

Figure 4.12: Two observation geometries with same scattering angle $\vartheta_s = 150^\circ$ and same illumination angle $\vartheta_0^* = 30^\circ$. **(left)** Viewing direction perpendicular ($\vartheta^* = 0^\circ$) to the cloud surface corresponding to the configuration found at the green dot in Figure 4.10. **(right)** Oblique viewing perspective ($\vartheta^* = 60^\circ$) corresponding to the configuration found at the red dot in Figure 4.10.

tering angles for this illumination. Returning to the fixed scattering angle of $\vartheta_s = 150^\circ$, the two considered configurations in Figure 4.10 and Figure 4.12 are, again, marked with the green and red dot. As visible here as well, the angular characteristic differs between the absorbing and non-absorbing wavelength. For a wide range of scattering angles $\vartheta_s < 180^\circ$, the radiance at the absorbing wavelength remains nearly constant between steep (green dot) and oblique (red dot)

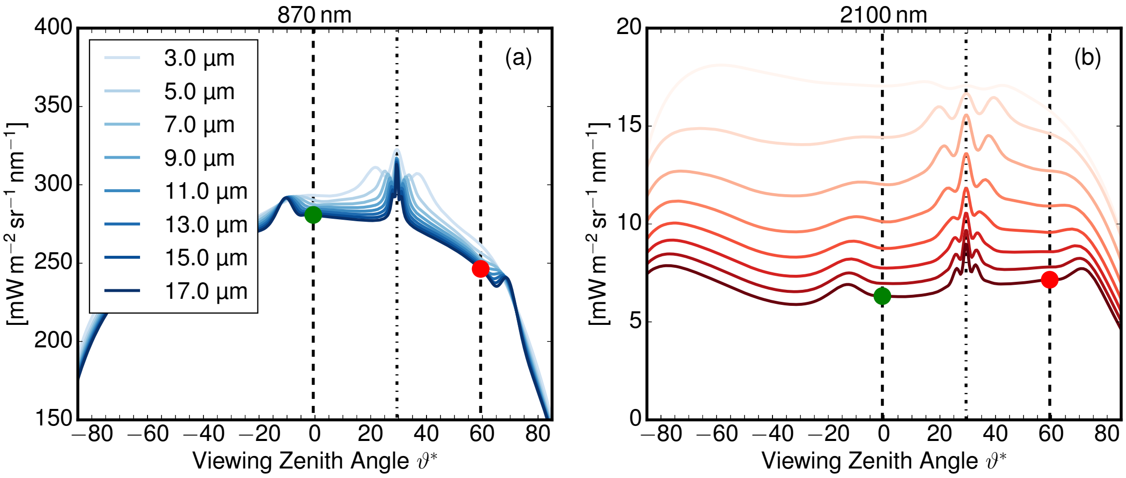

Figure 4.13: Spectral radiances at **(a)** $\lambda = 870\,\mathrm{nm}$ and **(b)** $\lambda = 2.1\,\mu\mathrm{m}$ for an optically thick water cloud for different effective radii as a function of relative viewing angle ϑ^* for a fixed illumination of $\vartheta_0 = 30^\circ$. The green and red dots mark viewing configurations shown in Figure 4.10 and Figure 4.12.

perspective while the radiance at the non-absorbing wavelength is considerably smaller for the oblique perspective. This asymmetric behavior becomes less pronounced for scattering angles near $\vartheta_s = 180°$, when the red and green dots both move towards the backscatter peak in Figure 4.13. For smaller scattering angles $\vartheta_s < 180°$, steeper as well as more oblique relative viewing angles compared to the illumination angle are possible within the same 3D cloud side scene.

The reason behind this different behavior is tied to absorption and the way it is enhanced by multiple scattering. The following will give a deeper insight into this interplay between absorption and scattering for different viewing angles. In Figure 4.14a, the reflectivity R of optically thick water clouds is shown for a relative illumination angle of $\vartheta_0^* = 30°$ as a function of single scattering albedo ω_0 and asymmetry parameter g. Figure 4.14b shows the difference in cloud reflectivity R between the steep configuration with a relative viewing direction of $\vartheta^* = 0°$ (Figure 4.12a, green dot) and the oblique configuration with a viewing direction of $\vartheta^* = 60°$ (Figure 4.12b, green dot). While both parameters can be varied freely using the Henyey-Greenstein phase function, the interdependent pairs of ω_0 and g resulting from Mie theory are shown as dots with colors corresponding to Figure 4.12. In both figures the predominant influence of ω_0 on cloud reflectivity R is evident; after all, this fact is the basis of the Nakajima-King technique. However, the asymmetry parameter g modulates this influence by enhancing the cloud absorption for more asymmetric ($g \to 1$) phase functions For isotropic scattering ($g \to 0$) and strong absorption the reflectivity for oblique viewing angles becomes noticeable larger than for the steep case. As already introduced in the theory Section 2.6.1, this stems from the way in which absorption in combination with asymmetric forward scattering influences the vertical photon distribution within the cloud. More forward scattered photons penetrate deeper into the cloud, which, in turn, reduces the probability to return to the cloud surface as reflected photon in the presence of absorption. Therefore, at absorbing wavelengths, reflected photons originate from shallower regions within the cloud when compared to non-absorbing wavelengths. This is also reflected by the shorter optical path lengths $\lambda_{mc,i}$ at absorbing wavelengths. Reciting the definition (2.17b) of radiance L and reflectivity R, both values relate the amount of radiation, which is emitted by area dA into direction $d\mathbf{\Omega}$, to the projected area $\Delta A = \cos\vartheta dA$ under which dA is seen for viewing angle ϑ. Thus, radiance L is the ratio between the radiant intensity I and the projected area ΔA; under oblique viewing angles the apparent size of dA decreases. Consequently, radiance L is invariant with viewing angle ϑ if and only if the radiant intensity I emitted by dA decreases linearly with $\mu = \cos\vartheta$. Scattering surfaces with this property are called *Lambertian reflector*. Non-lambertian reflection from water clouds, as seen in Figure 4.13, can be traced back to the probability for photons to escape the cloud into direction ϑ. This probability in turn depends on the penetration depth of the photons. In simple terms, photons from deeper within the cloud escape the cloud more steeper than photons escaping from shallower cloud regions. At

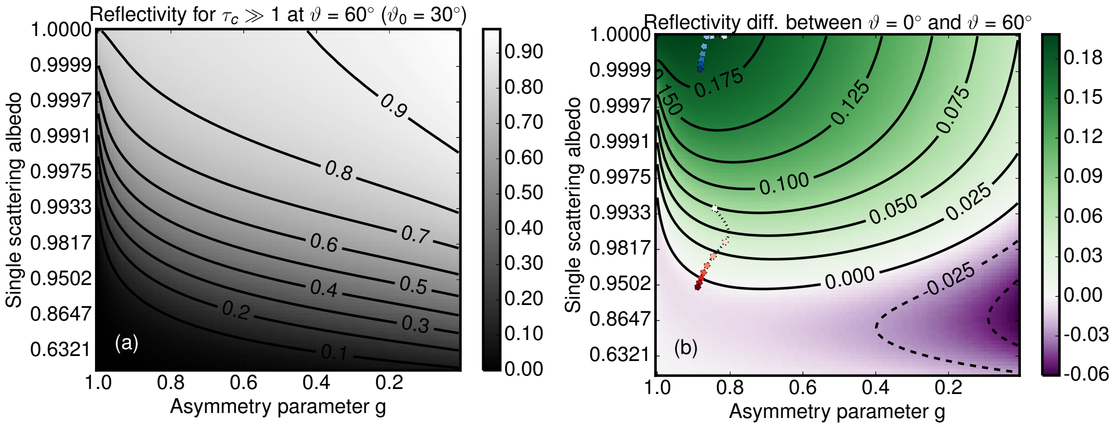

Figure 4.14: **(left)** Reflectivity R of an optically thick cloud as a function of asymmetry parameter g and single scattering albedo ω_0. The calculation were done for a relative viewing angle of $\vartheta^* = 60°$ and a relative illumination angle of $\vartheta_0^* = 30°$ using the Henyey-Greenstein phase function (*Henyey and Greenstein*, 1941). **(right)** Reflectivity difference between a relative viewing angle of $\vartheta^* = 0°$ compared to $\vartheta^* = 60°$. The subset of g and ω_0 valid for Mie scattering is superimposed for different r_{eff} for $\lambda = 870\,\mathrm{nm}$ (blue) and $\lambda = 2.1\,\mu\mathrm{m}$ (red).

non-absorbing wavelengths, more photons escape the cloud from deeper regions. Due to the exponential extinction of light with depth, the escape of these *deep* photons is much more likely along the shortest path and therefore perpendicular to the cloud surface. At absorbing wavelengths, more photons escape the cloud from shallower regions where the escape probability is more isentropic.

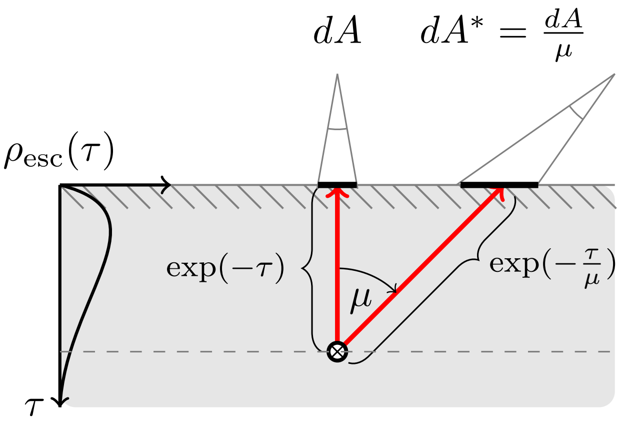

Figure 4.15: The two different photon escape directions for which the contributions to the *perpendicular* radiance and the *slant path* radiance is compared in Equation 4.4 to Equation 4.7.

In the following, this probability is considered for photons escaping a semi-infinite scattering medium from a layer which is located at an optical thickness τ within the cloud (Figure 4.15). For simplicity, the following is considered for isotropic scattering ($g = 0$) or *diffuse photons* which have already lost their initial forward *peaked* direction by multiple scattering. Since escaping photons will not be scattered in between, their escape probability T is given by Lambert-Beer's law using the slanted optical thickness $\tau^* = \frac{\tau}{\mu}$ between this starting layer and the cloud surface. The surface dA^*, for which the escaping photons are observed under a given solid angle $d\boldsymbol{\Omega}$, is obtained by dividing dA by μ. In this configuration, the smaller transmission T^* for the slant path competes with the larger surface dA^* visible for this discrete solid angle. The optical thickness τ_e, for which escaping photons contribute equally to radiance at both angles can be found by solving following equation:

$$dA \cdot T = dA^* \cdot T^* \tag{4.4}$$

$$dA \cdot e^{-\tau_e} = \frac{dA}{\mu} \cdot e^{-\frac{\tau_e}{\mu}} \tag{4.5}$$

For a given viewing angle μ, the optical thickness τ of this layer is then:

$$\tau_e = \frac{\tau_e}{\mu} + \ln \mu \tag{4.6}$$

$$\tau_e = \frac{\ln \mu}{\left(1 - \frac{1}{\mu}\right)} \tag{4.7}$$

Layers deeper in the cloud than τ_e contribute more to the radiance perpendicular to the cloud surface, while layers closer to the surface contribute more to the radiance at the oblique angle. Therefore, it is the photon escape distribution $\rho_{\text{esc}}(\tau)$ which governs the angular radiance distribution of diffuse photons. At absorbing wavelengths, escaping photons stay closer to the cloud surface which is also indicated by their shorter optical path lengths $\lambda_{mc,i}$. Without absorption, photons penetrate deeper into the cloud which favors more perpendicular escape directions. In essence, it is the escape probability combined with the photon distribution that can explain the high radiance values at absorbing wavelengths for oblique viewing geometries.

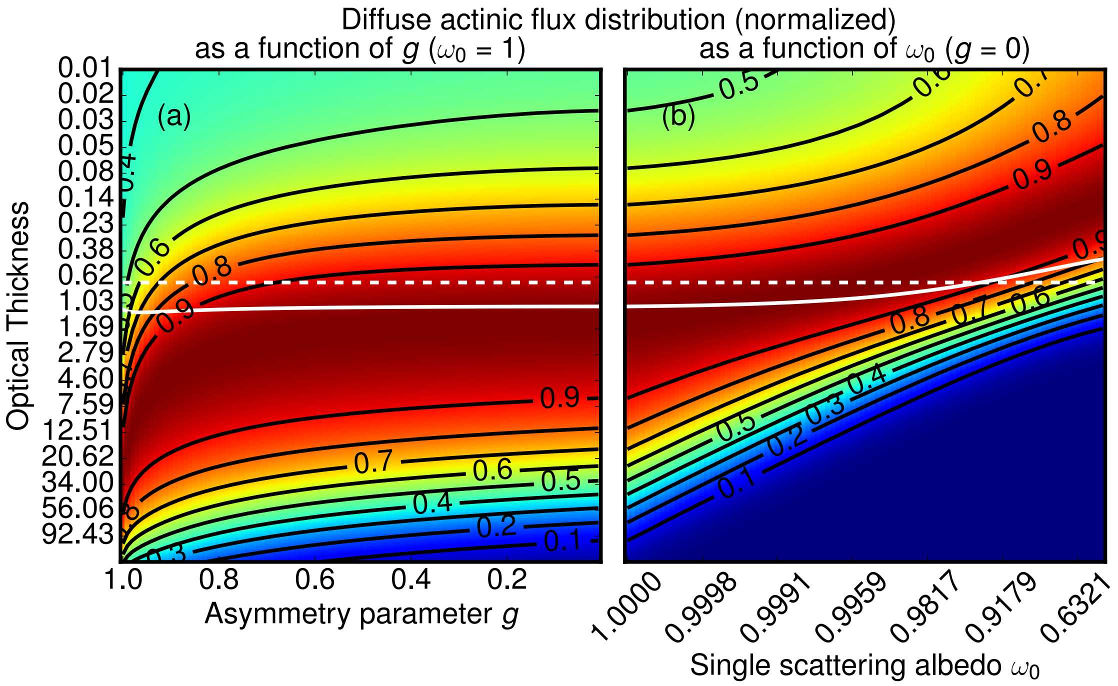

Figure 4.16: Diffuse actinic flux distribution (normalized) as a function of optical thickness within the water cloud examined in Figure 4.14. **(a)** Flux distribution as a function of asymmetry parameter g ($\omega_0 = 1$, conservative case) and **(b)** as a function of single scattering albedo ω_0 ($g = 0$, isotropic case).

This also becomes apparent when analyzing the diffuse actinic flux distribution $F(\tau)$ at absorbing and non-absorbing wavelengths. The photon density $\rho(\tau)$ times the velocity of light yields the photon quantity at a particular point per unit time which is described as actinic flux [photons $m^{-2}\,s^{-1}\,nm^{-1}$]. For the previous cloud configuration, Figure 4.16 shows the actinic flux distribution as a function of optical thickness, asymmetry parameter g (Figure 4.16a) and single scattering albedo ω_0 (Figure 4.16b). Since this analysis is focused on the whereabouts of photons within the cloud without considering absolute photon densities, the diffuse actinic flux is normalized to 1 where the highest diffuse photon density is located.

For isotropic scattering ($g = 0$, Figure 4.16b), photons are diffuse after the first scattering and try to escape uniformly into all directions. In turn, the escape probability only depends on the extinction along the escape path and Equation 4.7 holds. In order to obtain a mean optical thickness $\langle\tau\rangle$ for escaping diffuse photons (Equation 4.8), the normalized actinic flux as photon density $F(\tau)$ is combined with the extinction $\exp(-tau)$ for the different escape locations:

$$\langle\tau\rangle = \frac{\int_0^\infty \tau F(\tau) \exp\left(-\tau\right) d\tau}{\int_0^\infty F(\tau) \exp\left(-\tau\right) d\tau}. \tag{4.8}$$

Applied to the diffuse actinic flux distribution $F(\tau)$ for isotropic scattering ($g = 0$, Figure 4.16b), the white line is the mean optical thickness $\langle\tau\rangle$ for escaping diffuse photons. For the previously discussed case (Figure 4.15) between viewing zenith angles $\vartheta = 0°$ and $\vartheta = 60°$, Equation 4.7 yields $\tau_e \approx 0.69$ as optical thickness for which the escaping radiance should be equal for both viewing zenith angles. As absorption increases, the mean optical thickness $\langle\tau\rangle$ for escaping diffuse photons crosses the $\tau_e \approx 0.69$ limit. For smaller values of ω_0, the radiance at the oblique viewing angle should be larger when compared with the radiance at the steep viewing angle. Comparing this with the calculated reflectivity difference in Figure 4.14, the larger radiances at oblique angles can be recognized in the context of a higher absorption. As this study has shown, photons at absorbing wavelengths stay closer to the cloud surface when compared to the non-absorbing case. In turn, this has a direct influence on the angular cloud reflectance pattern, since photons near the cloud surface contribute more to radiance in the sideways directions when compared to photons escaping from deeper within the cloud. In the context of three-dimensional cloud sides with different cloud surface inclinations, this different angular behavior between cloud reflectivity at $0.87\,\mu\mathrm{m}$ and $2.10\,\mu\mathrm{m}$ leads to the ambiguity pattern in the Nakajima-King plot discussed in Section 4.1.2. The following section will introduce an approach which tries to tackle this problem by using information from surrounding cloud areas.

Additional information from surrounding pixels

The preceding sections focused on the radiance ambiguities that have to be considered when applying Nakajima-King-type retrievals to three-dimensional clouds with unknown cloud surface geometry. The following section will develop a technique to resolve this ambiguities (as much as possible) when no information about the cloud surface orientation is available. In this case, the technique uses information from surrounding pixels to classify the environment of the considered pixel.

The idea to use information from surrounding pixels to arrive at a multi-pixel retrieval of cloud microphysics is becoming increasingly popular. *Varnai and Marshak* (2003) discussed and developed a method to determine how the surrounding of a cloud pixel influences the pixel brightness. First atmospheric retrievals already exploit information from neighboring pixels, e.g. for the retrieval of aerosol properties *Dubovik et al.* (2011) or to retrieve light-absorbing gas plumes *Langmore et al.* (2013). Furthermore, a recent approach by *Martin et al.* (2014) iteratively adjusts a three-dimensional atmosphere to fit multi-angle/multi-pixel measurements.

In this thesis, neighboring pixels are used to separate ambiguous radiances in the Nakajima-King plot. Contrary to a simple global radiance threshold, the method determines if the pixel is surrounded by darker pixels or surrounded by brighter pixels. Additionally, the filter should neglect Monte Carlo or measurement noise between directly adjacent pixels. To this end, a Gaussian band-pass filter is used to classify different illumination regimes in simulated or measured radiance images. As a spatial band-pass filter, it compares the brightness of each pixel with the brightness of other pixels in the periphery. Pixels are classified according to their positive or negative deviation in radiance compared to their surrounding pixels. The band-pass filter consists of two 2D Gaussian functions $H_{LP}(x,y)$ and $H_{HP}(x,y)$ which specify the inner and outer search radius for this comparison. By neglecting directly adjacent pixels, the filter is insensitive to Monte Carlo or measurement noise in the surrounding. With $D(x,y)$ as the distance (Equation 4.9) from the origin pixel, D_H and D_L limit the inner and outer search radius respectively:

$$D(x,y) = \sqrt{x^2+y^2} \tag{4.9}$$

$$H_{LP}(x,y,D_L) = e^{\frac{-D(x,y)^2}{2D_L^2}} \tag{4.10}$$

$$H_{HP}(x,y,D_H) = 1 - e^{\frac{-D(x,y)^2}{2D_H^2}} \tag{4.11}$$

Both functions $H_{LP}(x,y)$ and $H_{HP}(x,y)$ are then combined into the Gaussian Band-pass Kernel $H_{BP}(x,y)$:

$$H_{BP}(x,y,D_L,D_H) = H_{LP}(x,y,D_L) * H_{HP}(x,y,D_H) \tag{4.12}$$

$$g_{class}(x,y,D_L,D_H) = \arctan H_{BP}(x,y,D_L,D_H) \tag{4.13}$$

The Gaussian Band-pass Kernel defined by Equation 4.12 is shown in Figure 4.17. The arcus tangent function is used in Equation 4.13 to obtain the interval bounded gradient classifier $g_{class}(x,y)$.

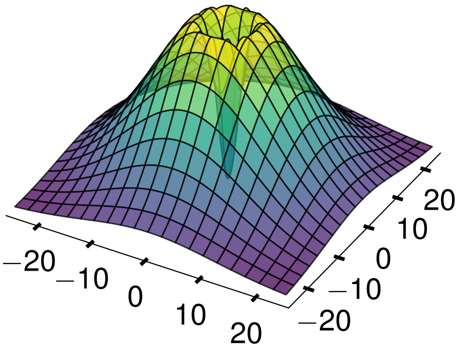

Figure 4.17: Two-dimensional Gaussian Band-pass Filter used to collect information from surrounding pixels

To demonstrate the method, the MYSTIC calculation for the ground-based scene shown in Figure 4.28 was recalculated using the same LES output but with a fixed effective radius of $r_{eff} = 8\,\mu m$. Besides the effects discussed in the previous section, shadows casted, optically thin clouds parts and the varying scattering angle between $\vartheta_s = 165°$ and $\vartheta_s = 165°$ lead to the broad radiance distribution of $L_{0.87}$ and $L_{2.10}$ shown in Figure 4.18a. In Figure 4.18a, an exponential function was fitted to the data points displayed there to determine the positive (blue) or negative (red) deviation $\Delta L_{2.10}$ for each radiance pair. This deviation is taken as a reference for a perfect separation of the ambiguous radiance distribution. A method that would yield the same separation from observable parameters would allow to consider this spread of possible radiance results and allow to mitigate the problem of ambiguous radiances. In Figure 4.19, the spatial position of these points is shown in combination with their radiance deviation colored.

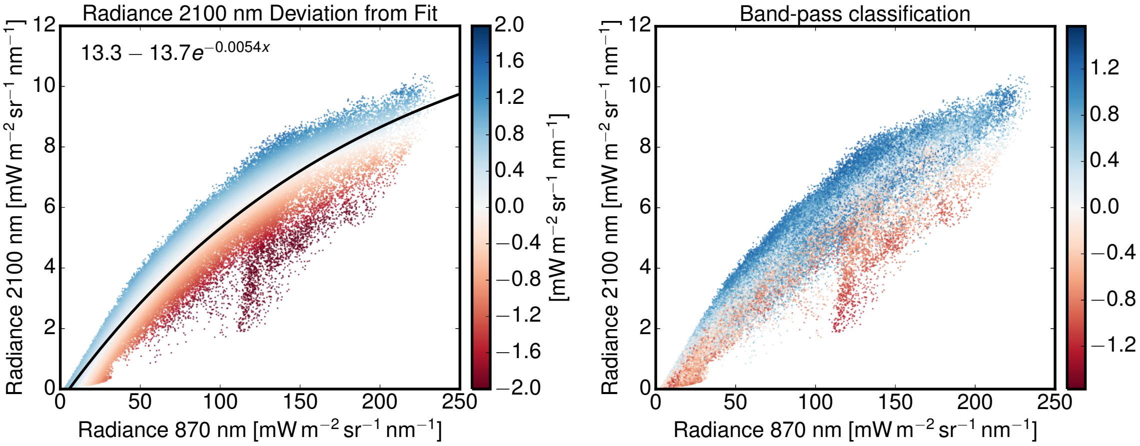

Figure 4.18: **(a)** Nakajima-King plot for the MYSTIC calculation shown in Figure 4.28 but with a fixed effective radius of $r_{\text{eff}} = 8\,\mu\text{m}$. **(b)** Result of the gradient classifier g_{class} applied to the same scene.

In Figure 4.18b, the radiance pairs for the same scene are colored according to the gradient classifier (Equation 4.13). For this cloud side at a distance of 3 km, the inner and outer search radius of the band-pass is set to 15 m and 75 m around the pixel. Converted into an opening angle, the band-pass therefore effectively operates in a region between $D_H = 0.25°$ and $D_L = 1.5°$ around each pixel.

Both dataset are also shown as images in Figure 4.19, where the deviation $\Delta L_{2.10}$ from the fit in the scatter plot is shown as reference on the left (Figure 4.19a) and the result of the gradient classifier on the right (Figure 4.19b).

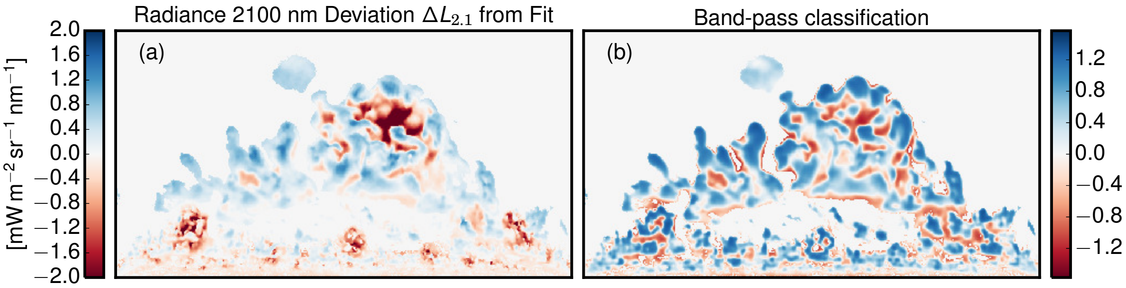

Figure 4.19: **(a)** Deviation $\Delta L_{2.10}$ from the fit in the Nakajima-King plot in Figure 4.18a used as a reference for the **(b)** gradient classifier g_{class} which puts the pixel radiance into context with surrounding pixels.

Apparently, the band-pass classification g_{class} is quite similar to the radiance deviation $\Delta L_{2.10}$ which is responsible for the ambiguous radiance–effective radius relationship. Moreover, it separates the radiance distribution into positive and negative radiance deviations $\Delta L_{2.10}$ at high as well as at low radiance values. With the illumination in the back, the first case is more likely to be associated with a steeper illumination angle compared to the viewing angle, while the latter is more likely to be associated with a more oblique illumination angle compared to the viewing angle. For two pixels with same illumination angle, $g_{\text{class}} > 0$ therefore marks the upper *radiance branch* in Figure 4.7 for $\vartheta_s = 150°$, while $g_{\text{class}} < 0$ marks the lower *radiance branch*. Based on this feature, the band-pass classification g_{class} can be used as a proxy to determine the location of a pixel within the radiance distribution. In that way, smaller effective radii with below average $L_{2.10}$ radiance values can be separated from larger effective radii with above-average $L_{2.10}$ radiance values. Without this classification, the two different effective radii with same radiance pair $(L_{0.87}, L_{2.10})$ would be indistinguishable.

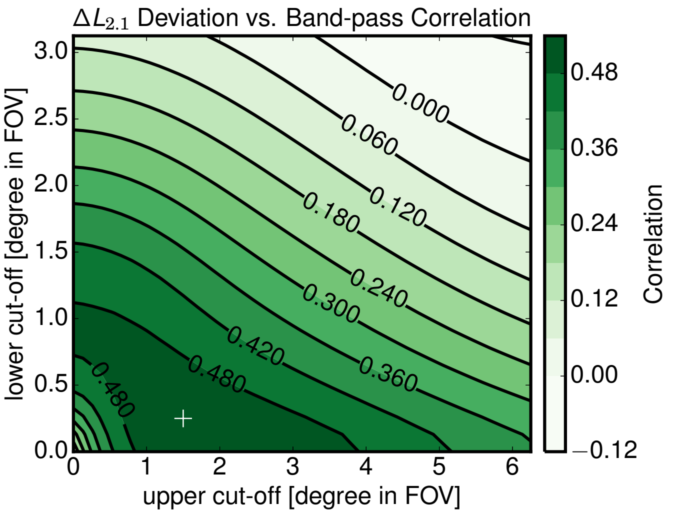

Figure 4.20: Correlation between g_{class} and $\Delta L_{2.10}$ for the scene in Figure 4.19 as a function of the nearby and distant cut-off D_H and D_L in degree.

Albeit its usefulness, this approach is implicitly based on the assumption that the variations in cloud geometry occur on a smaller scale than the variation in cloud microphysics. Excluding sudden changes in cloud phase, this assumption seems reasonable for convective cloud sides where significant variations in cloud microphysics occur on scales larger than 100 m (see discussion of vertical LES profiles in Section 3.2.2). The optimal search region with $D_H = 0.25°$ and $D_L = 1.5°$ was found by correlating the result from g_{class} with the deviation $\Delta L_{2.10}$ while varying the nearby and distant cut-off D_H and D_L. Figure 4.20 shows the correlation coefficient $\rho_{I,G}$ between $\Delta L_{2.10}$ and g_{class} for the scene in Figure 4.19 as a function of D_H and D_L in degree. With a fixed effective radius of $r_{eff} = 8\,\mu m$, the radiance variations in this scene can be solely attributed to changes in cloud geometry. A maximal correlation ($\rho_{I,G} = 0.53$) with $\Delta L_{2.10}$ is found when the gradient classifier g_{class} cuts off at $D_H = 0.25°$ and $D_L = 1.5°$. In the following, the gradient classifier g_{class} is used for the Monte Carlo forward calculation ensemble as well as for real measurements with the *specMACS* instrument.

4.1.3 External influences and their mitigation

Besides the intrinsic sensitivities of reflected solar radiation to cloud optical properties, there are also external influences which interfere with cloud side measurements. Since variations in solar insolation (e.g. due to overlaying cirrus clouds) and variations in aerosol concentration are not dealt with in this thesis, remaining influences are shadows casted on cloud parts, influence of ground albedo and glaciated cloud parts. In order to avoid spurious bias effects on retrieved effective radii, the mitigation of these influences is a necessary first step within the effective radius retrieval.

Exclusion of cloud shadows

One obvious effect on reflected radiances is caused by shadows. Depending on the illumination, cloud parts are in direct shadow if the local solar zenith angle onto the cloud surface ϑ_0' is larger than 90°. On their backside, illuminated cloud parts also cast shadows onto other cloud parts. Without direct illumination, reflected photons from these parts have to originate from previous diffuse scattering events. To exclude the contamination with light from unknown origin, these cloud parts are filtered out before applying the effective radius retrieval.

This diffuse light has usually encountered more absorption compared to the directly reflected light. In this thesis, this is used to define a global threshold to the reflectivity ratio $R_{0.87}/R_{2.10}$, called *shadow index* f_{shad} in the following, to exclude pixel for which light has likely undergone multiple diffuse reflections:

$$f_{\text{shad}} = \frac{R_{0.87}}{R_{2.10}} > 3.5 \qquad \text{(shadowed)} \tag{4.14}$$

An upper threshold for this ratio should separate absorption by large cloud droplets from absorption caused by multiple diffuse reflections. To this end, DISORT calculations were done to determine this threshold for optically thick clouds.

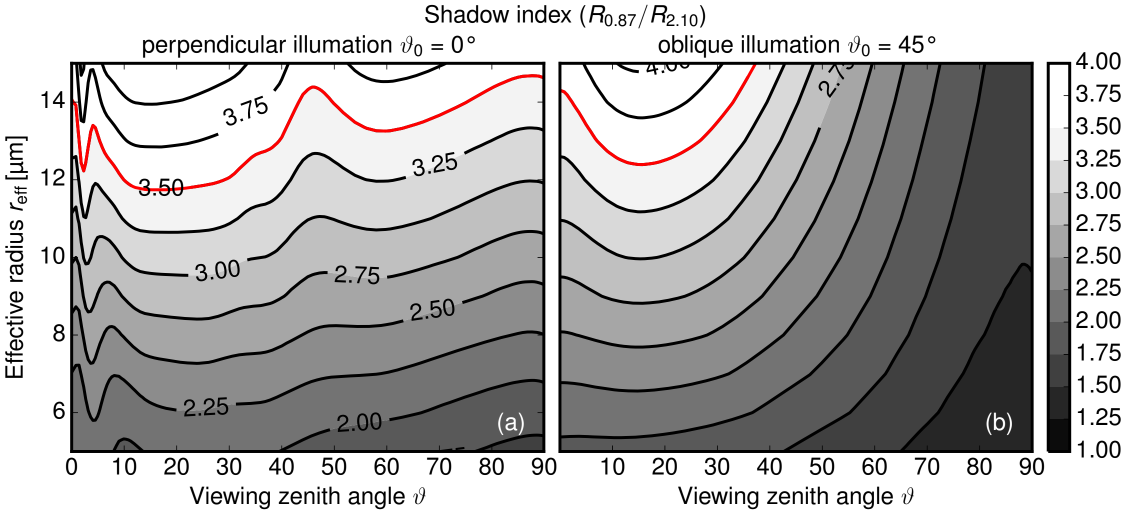

Figure 4.21: Shadow index $R_{0.87}/R_{2.10}$ for an optically thick cloud ($\tau = 500$) as a function of effective radius r_{eff} and viewing zenith angle ϑ **(a)** for perpendicular illumination $\vartheta_0 = 0°$ and **(b)** for oblique illumination $\vartheta_0 = 45°$.

Figure 4.21 shows the ratio $R_{0.87}/R_{2.10}$ as a function of effective radius r_{eff} and viewing zenith angle ϑ. Figure 4.21a shows the shadow index in the case of perpendicular illumination ($\vartheta_0 = 0°$), Figure 4.21b in the case of oblique illumination ($\vartheta_0 = 45°$). While f_{shad} is nearly constant for different viewing zenith angles ϑ under perpendicular illumination, the index becomes a function of ϑ under oblique illumination. However, f_{shad} values are larger for the perpendicular illumination. This allows to choose $f_{\text{shad}} < 3.5$ as filter for shadow-free pixels for effective radii smaller than $r_{\mathrm{eff}} < 12\,\mu\mathrm{m}$. In this thesis, this can be done since the effective radii in the Cumulus cloud model are all smaller than this radius.

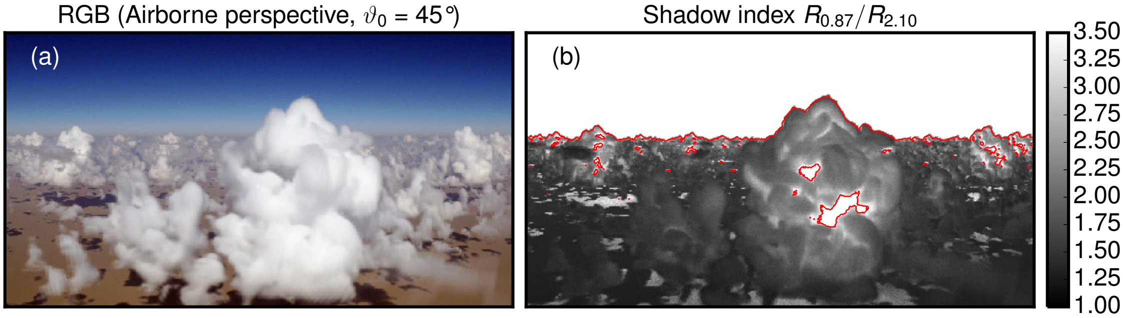

Figure 4.22: **(a)** True-color image of a cloud side scene (12 h 40 min LT) simulated with MYSTIC. **(b)** Shadow index $R_{0.87}/R_{2.10}$ highlighting regions of enhanced cloud absorption caused by multiple diffuse reflections.

Exclusion of ground albedo reflection

Another potential influence on cloud side measurements is caused by light reflected by the ground in front of the observed cloud side as discussed by *Barker and Marshak* (2001). This problem is exacerbated further by the very different spectral behavior between liquid cloud droplets and green vegetation (*Marshak et al.*, 2000). While the cloud optical properties are nearly invariant between $\lambda = 0.65\,\mu\mathrm{m}$ and $\lambda = 0.87\,\mu\mathrm{m}$, the albedo of vegetation increases strongly from 0.1 to 0.5 in that range (*Tucker*, 1979). Figure 4.23a shows an exemplary spectral albedo for an area of $20 \times 20\,\mathrm{km}$ around the Meteorological Institute in Munich. *Hausmann* (2012) derived this spectral albedo by fitting the MODIS white-sky-albedo (*Strahler et al.*, 1999) with a linear combination of spectral albedos of shingle and deciduous from the ASTER spectral library (*Baldridge et al.*, 2009). The *red edge* in this spectral albedo is commonly used to analyze the amount of green vegetation which is indicated by the *Normalized Difference Vegetation Index* (NDVI) (*Rouse et al.*, 1974):

$$f_{\mathrm{NDVI}} = \frac{R_{0.747} - R_{0.672}}{R_{0.747} + R_{0.672}} > 0.1 \tag{4.15}$$

To minimize the influence of Rayleigh scattering and atmospheric aerosol, two very close wavelengths ($\lambda = 0.672\,\mu\mathrm{m}$ and $\lambda = 0.747\,\mu\mathrm{m}$) were chosen to calculate the NDVI in this thesis. In Figure 4.23b, the spectral albedo in Figure 4.23a was used to simulate the NDVI for the already discussed cloud side. Since cloud optical properties are spectrally invariant in this wavelength region, NDVI values larger than zero highlight cloud regions which are influenced by ground albedo reflection.

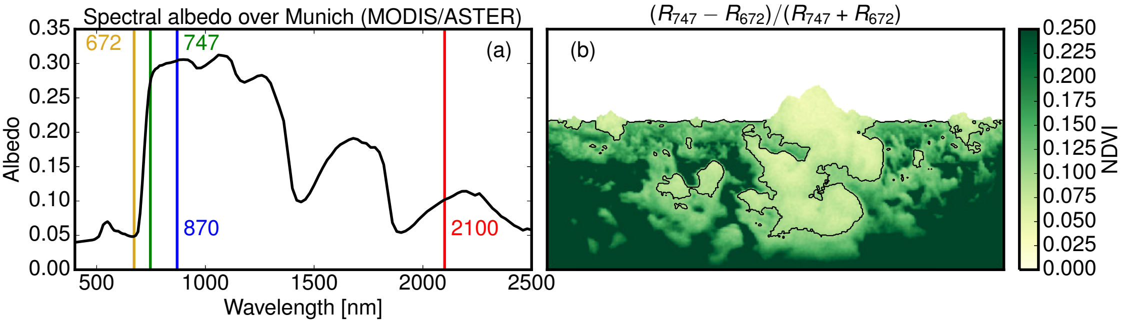

Figure 4.23: **(a)** Spectral surface albedo for Munich (black line) derived by fitting the MODIS white-sky-albedo with ASTER spectral albedos of shingle and deciduous. **(b)** NDVI calculated for the scene shown in Figure 4.22a with $f_{\mathrm{NDVI}} = 0.1$ shown by the black line.

As the albedo of vegetation is quite different for the two wavelengths ($870\,\mu m$ and $2100\,\mu m$) used by the Nakajima-King-technique, ground albedo reflection should be avoided to exclude potential bias in the effective radius retrieval. Turning a disadvantage into an advantage, the red edge can be used to detect and exclude cloud parts contaminated with ground albedo reflection. In this thesis, cloud parts with a NDVI larger than 0.1 were excluded from the retrieval to constrain the bias in $L_{0.87}$ to 5%. This threshold is adapted to the spectral albedo shown in Figure 4.23a. For similar albedo levels, but with less vegetation on the ground, this threshold must be appropriately decreased to still detect the ground albedo influence with the help of the red edge of vegetation.

Determination of cloud phase

The basic principle behind the detection of thermodynamic cloud phase was introduced in Section 2.6.2. Due to the higher absorption at $\lambda = 2.1\,\mu m$ of ice compared to liquid water the ice cloud reflectance is greatly reduced for this wavelength. For this reason, a reliable cloud phase discrimination is mandatory to avoid biases in retrievals of cloud optical properties like effective radius or optical thickness. Since this thesis is focused on liquid water clouds, glaciated cloud parts have to be excluded before the statistical effective radius retrieval can be applied. The ice fraction γ in a mixed phase-cloud is specified by the ratio of ice water content (IWC) to total water content (TWC):

$$\gamma = \frac{\mathrm{IWC}}{\mathrm{TWC}} \tag{4.16}$$

To illustrate the effect of an increase in ice fraction on the apparent effective radius $\langle r_{\mathrm{eff}} \rangle_{\mathrm{mc}}$ and the reflected radiance at $\lambda = 2.1\,\mu m$, the cloud scene shown in Figure 4.22 was modified to include ice particles at cloud top. To this end, the fraction ratio γ was linearly increased from 0 to 1 in a mixed-phase region between

$h = 1\,\mathrm{km}$ to $1.5\,\mathrm{km}$ with liquid cloud droplet with fixed $r_{\mathrm{eff}} = 15\,\mu\mathrm{m}$ at cloud base and ice particles (according to *Baum et al.* (2007)) with fixed $r_{\mathrm{eff}} = 30\,\mu\mathrm{m}$ at cloud top. In Figure 4.24a the increasing apparent effective radius $\langle r_{\mathrm{eff}} \rangle_{\mathrm{mc}}$ with height shows this transition from liquid to ice. Figure 4.24b shows the ratio $R_{2.10}/R_{2.25}$, called *ice index* f_{phase} in the following, where lower values (blue regions) are due to the higher absorption of ice at $\lambda = 2.10\,\mu\mathrm{m}$:

$$f_{\mathrm{phase}} = \frac{R_{2.10}}{R_{2.25}} < 0.75 \tag{4.17}$$

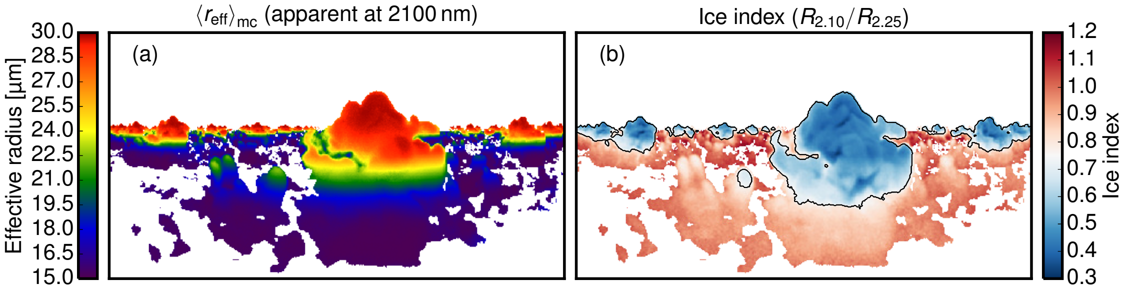

Figure 4.24: Same cloud side scene like in Figure 4.22, but with liquid cloud droplets with fixed $r_{\mathrm{eff}} = 15\,\mu\mathrm{m}$ at cloud base and ice particles with fixed $r_{\mathrm{eff}} = 30\,\mu\mathrm{m}$ at cloud top. In the mixed-phase region between $h = 1\,\mathrm{km}$ to $1.5\,\mathrm{km}$ the ice fraction ratio γ increases linearly from 0 to 1. **(a)** Apparent effective radius obtained with the MYSTIC REFF method **(b)** Ice index ($R_{2.10}/R_{2.25}$) shows the higher absorption of ice at $\lambda = 2.10\,\mu\mathrm{m}$ and the ice threshold f_{phase} by the black line.

In their paper, *Lee et al.* (2006) derived an analytic Equation 4.18 for the mean effective radius r_{em} of a mixed-phase cloud to analyze the influence of a varying ice fraction γ on the Nakajima-King retrieval. In the limit of $Q_{\mathrm{ext}} \approx 2$, the mixed-phase effective radius r_{em} can be written as a sole function of water droplet effective radius r_{ew} and ice particle effective radius r_{ei}, densities of water ρ_w, ice ρ_i and mixed-phase ρ_w and ice fraction γ:

$$r_{\mathrm{em}} = \left[\left(\frac{\gamma}{r_{\mathrm{ei}}\,\rho_i} + \frac{1-\gamma}{r_{\mathrm{ew}}\,\rho_w} \rho_m \right) \right]^{-1} \tag{4.18}$$

To test the threshold $R_{2.1}/R_{2.25} > 0.75$ for liquid water clouds used by *Zinner et al.* (2008), the ratio has been simulated using DISORT for optically thick clouds of varying ice fraction ratio γ observed under different viewing zenith angles ϑ. Figure 4.25a shows the ice index for perpendicular illumination as a function of γ and ϑ, while Figure 4.25b shows the case for an oblique illumination ($\vartheta_0 = 45°$) from the opposite side ($\varphi_0 = 180°$).

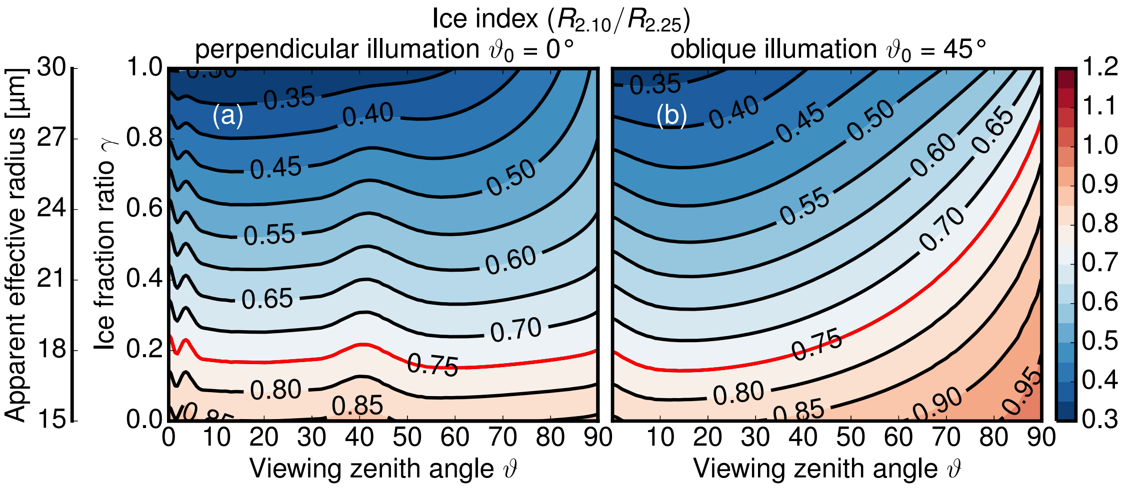

Figure 4.25: Phase index $R_{2.10}/R_{2.25}$ for an optically thick cloud ($\tau = 500$) as a function of ice mixing ratio γ and viewing zenith angle ϑ **(a)** for perpendicular illumination $\vartheta_0 = 0°$ and **(b)** for oblique illumination $\vartheta_0 = 45°$.

While f_{shad} is nearly constant for different viewing zenith angles ϑ under perpendicular illumination, the index becomes a function of ϑ under oblique illumination. With an ice index threshold f_{phase} of 0.75, clouds with an ice fraction ratio $\gamma > 0.2$ for the considered effective radii of $r_{\text{ew}} = 15\,\mu\text{m}$ and $r_{\text{ew}} = 30\,\mu\text{m}$ are filtered out. With a mean apparent effective radius of $\langle r_{\text{eff}} \rangle_{\text{mc}} \approx 16.4\,\mu\text{m}$ for cloud parts in Figure 4.24b classified as liquid ($f_{\text{phase}} < 0.75$), the error in r_{eff} is limited to a mean overestimation of $+1.4\,\mu\text{m}$. However, the dependence of f_{phase} on ϑ suggests that retrieval results have to be considered carefully in the vicinity of mixed-phase cloud parts. For example, a mean apparent effective radius of $\langle r_{\text{eff}} \rangle_{\text{mc}} \approx 18\,\mu\text{m}$ is found in the vicinity of the phase transition region ($f_{\text{phase}} = 0.75$) in Figure 4.24b which is in good agreement with the apparent effective radius in Figure 4.24a. In similar calculations with larger ice particles, this threshold proved to be a quite robust indicator of an ice fraction ratio γ of 0.2. A very strict threshold of $f_{\text{phase}} > 0.85$ would exclude any mixed-phase influence ($\gamma < 0.05$) for the cost of losing a large amount of liquid clouds.

4.2 Implementation of the Monte Carlo ensemble

After the previous sections have discussed the problem of ambiguous radiances on the basis of simple model studies, the following section will expand this analysis to realistic cloud sides of LES cumuli which were discussed in Section 3.2.2. The three-dimensional radiative transfer code MYSTIC will be applied to these LES clouds to obtain simulations of realistic *specMACS* measurements. A whole ensemble of these MYSTIC forward simulations of cloud sides will then be incorporated within the statistical framework introduced in Section 3.1.

Subsequently, the sampled statistics of reflected radiances are analyzed for their sensitivity to the effective cloud droplet radius. Finally, the Monte Carlo sampled posterior distributions $p(r_{\text{eff}}| L_{0.87}, L_{2.10})$ will be used to infer droplet size profiles from convective cloud sides.

As mentioned in the method Section 3.1.1, the posterior $p(r_{\text{eff}}| L_{0.87}, L_{2.10})$ can be derived from Bayes' theorem (Equation 3.1) by solving the easier forward problem $p(L_{0.87}, L_{2.10}|r_{\text{eff}})$ for all values of r_{eff}. Here, the highly complex geometry of convective cloud sides makes high demands on the radiative transfer model. Up to now, this demands are only met by Monte Carlo models like the MYSTIC radiative transfer code.

4.2.1 Selection of suitable cloud sides

A key component of the Bayesian approach is the selection of a suitable sampling strategy to explore the likelihood distribution $p_{\text{fwd}}(L_{0.87}, L_{2.10}| r_{\text{eff}})$. This is especially true, if the sampling of the observation parameter space $\mathcal{O}$, corresponding to model space $\mathcal{M}$, is done with a computational expensive Monte Carlo method. Following *Mosegaard and Tarantola* (1995), the sampling of the model space can be improved when the model space is sampled according to the prior distribution. Compared to a uniform sampling by crude Monte Carlo, measurements $\mathbf{o_i}$ with a high probability are sampled with a higher density. In case of cloud side remote sensing, this can be done by including information about the measurement location and about the most typically selected cloud scenes. To that end, the following will introduce a technique to select suitable locations within the LES model output for which cloud sides are visible from the ground-based perspective. Cloud side measurements are intended for clouds within a few kilometers from the instrument location. With the sun in the back, azimuthal scans of ±45° around the principal plane will be done with the field of view at or slightly above the horizon. To ensure reproducibility, a analytical method was chosen to select observation locations for the Monte Carlo ensemble to sample the likelihood distribution. The concept is based on a convolution of the LES

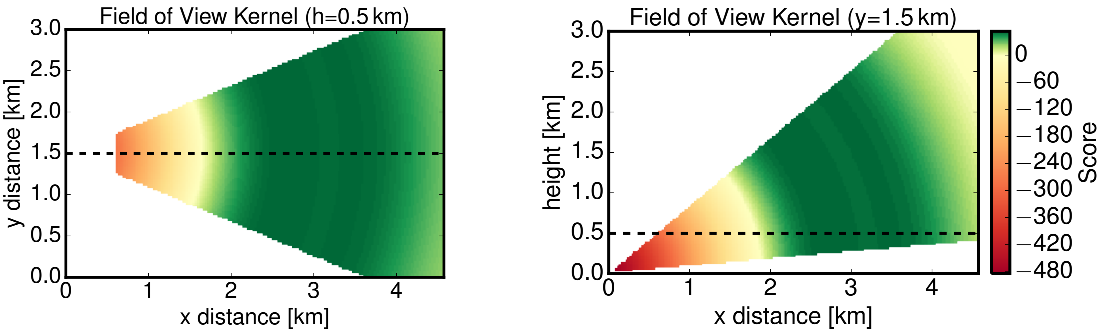

Figure 4.26: Vertical cross-section within the principal plane of the observation kernel. The arbitrary score is positive for regions where clouds are desired.

outputs with a weighting kernel representing a cloud side measurement scan. More precisely, the field of view of a scan is modelled by a kernel k_{FOV} with an azimuthal opening angle of $\Delta\varphi = 45°$ and a zenithal opening angle of $\Delta\vartheta = 40°$, $5°$ above the horizon. As a function of radial distance, the kernel comprises a scalar weighting to curtail the location where clouds are desired. Figure 4.26 shows a vertical cross-section of this kernel. The arbitrary score is negative in the vicinity of the observer to penalize locations where clouds are too close. Between 2 and 4 km with a maximum at 3 km, the weighting score is positive to favor locations with clouds in this region. The weighting is expressed by a spline function which is described by the following points:

Table 4.1: Points which define the spline that describes the arbitrary weighting score as a function of the radial distance from the observer.

Distance [km]	-1.5	0	1.5	2.5	3.0	4.0	8.0
Score	0	-500	0	50	50	0	0

After the kernel is rotated into the desired azimuthal orientation, it is convoluted with the LES field m_{LES} of cloudy grid boxes containing $+1$ for LWC $> 0.01\,\mathrm{g\,m^{-3}}$ and 0 otherwise. The convolution of kernel k_{FOV} with m_{LES} can be expressed as follows:

$$s_{obs}[x,y] = (k_{FOV} * m_{LES})[x,y] = \sum_{j=-\infty}^{\infty} \sum_{i=-\infty}^{\infty} m_{LES}[i,j] \cdot k_{FOV}[x-i, y-j] \qquad (4.19)$$

Numerically, this is done in the Fourier domain to speed up computations. The three-dimensional score field s_{obs} resulting from the convolution is evaluated at ground-level which is shown in Figure 4.27 with colors corresponding to the weighting score in Figure 4.26. For every cloud field and azimuthal orientation, the ground-based observation position $[x,y]_{obs}$ is placed where s_{obs} has its global maximum:

$$[x,y]_{obs} = \underset{1 \leqslant x \leqslant N, 1 \leqslant y \leqslant M}{\operatorname{argmax}} s_{obs}[x,y] \qquad (4.20)$$

In Figure 4.27, the already introduced LES cloud field (12 h 40 min LT) is shown in combination with the corresponding score field s_{obs} obtained for a viewing azimuth of $\phi = 315°$. The observation position is indicated by the yellow dot, where s_{obs} has its global maximum as recognizable by the green color. Also depicted is the field of view towards the largest cloud in the center of the domain. The red region in s_{obs} would be unfavorable for a cloud side perspective since it would be too close to the cloud. For the selected perspective shown in

Figure 4.27, truecolor images are shown in Figure 4.28 simulated with MYSTIC for the ground-based perspective (Figure 4.28a) as well as for an airborne perspective (Figure 4.28b), 1.7 km above the ground-based location.

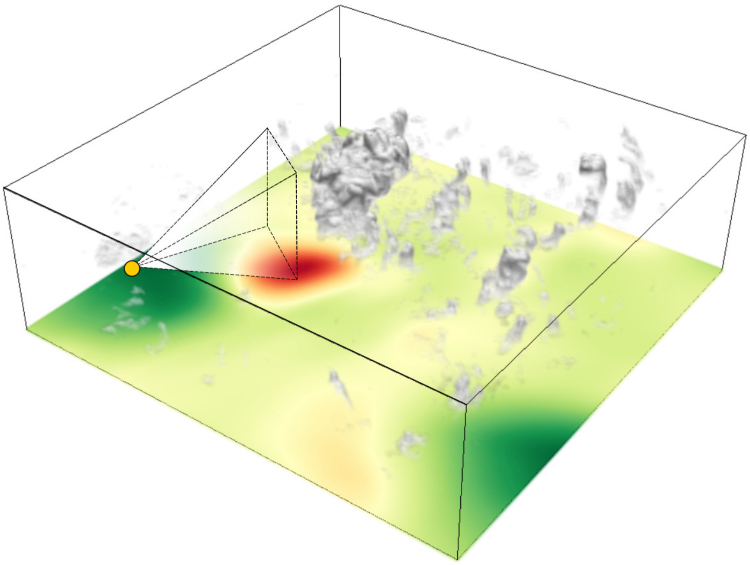

Figure 4.27: Finding the optimal observation location for cloud side measurements. The surface shows the location score derived by convolving the field of view kernel (shown in Figure 4.26) with the LES cloud field (12 h 40 min LT) shown in Figure 3.3

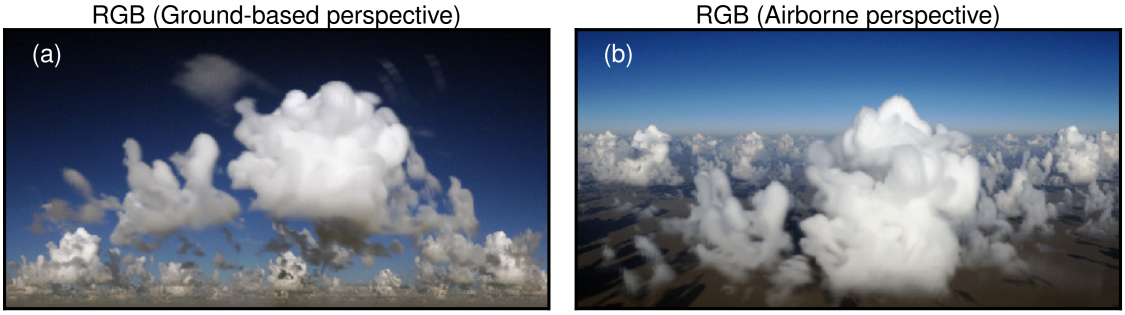

Figure 4.28: **(a)** Truecolor image of a cloud side scene (12 h 40 min LT) simulated with MYSTIC for the ground-based perspective shown in Figure 4.27. **(b)** Truecolor image of the same scene from an airborne perspective, 1.7 km above the ground-based location shown on the left.

4.2.2 Interpolation between illumination conditions

As already mentioned in the preceding sections, the local illumination angle determines the incident irradiance onto the cloud surface which in turn has a huge influence on reflected radiances. Since the Monte Carlo radiative transfer technique is computationally rather expensive only a limited number of illumination directions $\hat{\mathbf{s}}$ can be calculated for one selected cloud scene. However, the angular pattern of the Mie scattering phase function (Section 2.4.3) can be quite variable in the direct backscatter ($\vartheta_s \approx 180°$) or the cloud bow region ($\vartheta_s \approx 138°$). Here, the sparse sampling of illumination directions causes a probleme since the reflection from clouds is usually not a linear function of the illumination angle (*van de Hulst*, 1980). With a steeper illumination angle the reflection from the cloud surface usually becomes brighter, just as the cloud surface is more shadowed for more oblique illumination conditions.

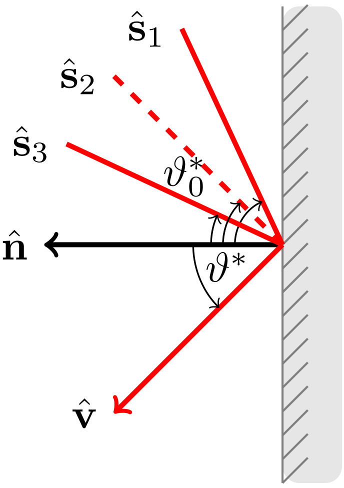

Figure 4.29: Schematic diagram of a cloud side viewing geometry $\hat{\mathbf{n}}$ for two nearby illumination directions $\hat{\mathbf{s}}_1$ and $\hat{\mathbf{s}}_3$. The proposed method interpolates reflected radiances for the new illumination direction $\hat{\mathbf{s}}_2$ in between $\hat{\mathbf{s}}_1$ and $\hat{\mathbf{s}}_3$.

To mitigate the problem of the limited number of Monte Carlo simulations and to enlarge the number of illumination geometries in the radiative transfer ensemble, a method for the interpolation of radiance at an arbitrary illumination geometry by interpolation between known results of explicitly calculated illumination directions is needed. For this task, *Ewald* (2012) developed a interpolation method for the spaceborne perspective with a single viewing direction. This thesis extends the interpolation method to arbitrary viewing geometries in order to be applicable to a airborne or ground-based perspective.

The method is based on the previously introduced determination of the cloud surface normal combined with a precomputed lookup table of the Bidirectional Reflectance Distribution Function (BRDF) of one-dimensional clouds. BRDFs are analytic or tabular expressions which define how light is reflected from a surface as a function of the viewing and the illumination direction. Multiplied by the incident solar irradiance, the BRDF yields the corresponding radiance L_{1D}. With a known viewing and illumination direction as well as a known cloud surface normal, such a lookup table was used to retrieve the differential change δL_{1D} in radiance between the original and a new illumination direction.

The BRDF lookup table was derived from radiative transfer calculations using DISORT by iterating over following parameter combinations:

- the standard summer mid-latitude profile by *Anderson et al.* (1986) was used to include a realistic profile of air pressure and water vapour.
- as 1D RT codes like DISORT are designed to work with vertical layers only, the observer was placed at an altitude of 5 km, looking straight down onto a water cloud layer which was placed between an altitude of 2 and 3 km.
- effective radius of droplets was varied between 4 and 20 km in equidistant steps of 1 km, while optical thickness was varied in 35 steps between 0.05 and 300.
- surface albedo was set to zero,
- solar zenith angles were sampled between 0° and 80°, in equidistant steps of 4°
- viewing zenith angles were sampled between 0° and 80°, in equidistant steps of 4°, while relative azimuth was sampled between 0° and 180° in steps of 10°.
- Using this setup, cloud radiances L_{1D} were calculated with 16 DISORT streams for the wavelengths $\lambda_{NIR} = 870\,\text{nm}$ and $\lambda_{SWIR} = 2100\,\text{nm}$

Starting from this lookup table, the differential change δL_{1D} in radiance between the original and a new illumination direction was calculated as follows.

$$\delta L_{1D}(\hat{\mathbf{s}}_1 \rightarrow \hat{\mathbf{s}}_2, \hat{\mathbf{v}}) = L_{1D}\left(\hat{\mathbf{s}}_2, \hat{\mathbf{v}}, \langle r_{\text{eff}}, \tau\rangle_{mc}\right) - L_{1D}\left(\hat{\mathbf{s}}_1, \hat{\mathbf{v}}, \langle r_{\text{eff}}, \tau\rangle_{mc}\right) \tag{4.21}$$

The differential change δL_{1D} for a change in illumination direction from $\hat{\mathbf{s}}_1$ to $\hat{\mathbf{s}}_2$ was directly obtained from the lookup table as a difference (Equation 4.21) of radiance values for $\hat{\mathbf{s}}_2$ and $\hat{\mathbf{s}}_1$. Besides the known local illumination $\hat{\mathbf{s}}_1$ and local viewing direction $\hat{\mathbf{v}}$, the required cloud optical properties $\langle\tau\rangle_{mc}$ and $\langle r_{\text{eff}}\rangle_{mc}$ were derived with the MYSTIC REFF technique as explained previously (Section 3.3.1). This was done for both wavelengths, except that only $\langle\tau\rangle_{mc}$ for the non-absorbing wavelength was used to determine the cloud optical thickness. As shown by *Marshak et al.* (1995) and *Heidinger and Stephens* (2002) for optically thick clouds ($\tau > 10$), the mean optical path length $\langle\lambda\rangle_{mc}$ of reflected photons scales linearly with cloud optical thickness τ at non-absorbing wavelengths. Since there exists no definition of optical thickness for cloud sides, the mean optical path length $\langle\lambda\rangle_{mc}$ is used here as a best guess for the cloud optical thickness for the lookup in L_{1D}.

This way a lookup of $\delta L_{1D}(\hat{\mathbf{s}}_1 \rightarrow \hat{\mathbf{s}}_2, \hat{\mathbf{v}},)$ is generated. For two identical Monte Carlo scenes with not too different illumination directions $\hat{\mathbf{s}}_1$ and $\hat{\mathbf{s}}_3$ (compare Figure 4.29), all intermediate illumination situations $\hat{\mathbf{s}}_2$ can now be interpolated using it. The tabulated differences δL_{1D} are added to the Monte-Carlo derived radiances L_{3D} to yield the radiance for the intermediate illumination direction $\hat{\mathbf{s}}_2$.

By doing this for $\hat{\mathbf{s}}_1 \to \hat{\mathbf{s}}_2$ as well as for $\hat{\mathbf{s}}_3 \to \hat{\mathbf{s}}_2$, one receives two values (L_{3D} and L^*_{3D}) for $\hat{\mathbf{s}}_2$:

$$L_{3D}(\hat{\mathbf{s}}_2, \hat{\mathbf{v}}) = L_{3D}(\hat{\mathbf{s}}_1, \hat{\mathbf{v}}) + \delta L_{1D}(\hat{\mathbf{s}}_1 \to \hat{\mathbf{s}}_2, \hat{\mathbf{v}}) \tag{4.22}$$

$$L^*_{3D}(\hat{\mathbf{s}}_2, \hat{\mathbf{v}}) = L_{3D}(\hat{\mathbf{s}}_3, \hat{\mathbf{v}}) + \delta L_{1D}(\hat{\mathbf{s}}_3 \to \hat{\mathbf{s}}_2, \hat{\mathbf{v}}) \tag{4.23}$$

Subsequently, both values can be combined in a linear interpolation using the ratio of the angle between $\hat{\mathbf{s}}_1$ and $\hat{\mathbf{s}}_2$ and the angle between $\hat{\mathbf{s}}_1$ and $\hat{\mathbf{s}}_3$ as weight w:

$$w = \frac{\cos^{-1}(\hat{\mathbf{s}}_1, \hat{\mathbf{s}}_2)}{\cos^{-1}(\hat{\mathbf{s}}_1, \hat{\mathbf{s}}_3)} \tag{4.24}$$

Finally, the linear interpolation yields a combined radiance $L_{3D}(\hat{\mathbf{s}}_2, \hat{\mathbf{v}})$ for illumination direction $\hat{\mathbf{s}}_2$:

$$L_{3D}(\hat{\mathbf{s}}_2, \hat{\mathbf{v}}) = (1 - w)\, L_{3D}(\hat{\mathbf{s}}_2, \hat{\mathbf{v}}) + w\, L^*_{3D}(\hat{\mathbf{s}}_2, \hat{\mathbf{v}}). \tag{4.25}$$

By doing so, this method provides a smooth interpolation between two 3D simulated illumination directions $\hat{\mathbf{s}}_1$ and $\hat{\mathbf{s}}_3$ while harnessing the angular pattern contained in the 1D lookup table for additional directions in between.

This technique was validated by *Ewald* (2012) by comparing interpolated scenes with Monte Carlo calculated scenes of the same illumination condition. The analysis revealed that this technique reduced the root-mean-square deviation of the scene for $\hat{\mathbf{s}}_2$ from the Monte Carlo simulation by two-thirds when compared the the results obtained by a simple linear interpolation between the Monte Carlo scenes for $\hat{\mathbf{s}}_1$ and $\hat{\mathbf{s}}_3$. In the following, this method will be called *1D-Assisted Scattering Angle Interpolation* (1D-ASAP).

4.2.3 Ensemble configuration and sampling

In the following, an ensemble of Monte Carlo radiative transfer simulations is created to sample the posterior probability distribution $p(r_{\text{eff}}|\, L_{0.87}, L_{2.10})$. The ensemble of simulated cloud side measurements is set up by using the method to select suitable observation perspectives introduced in Section 4.2.1. During the radiative transfer calculations, the MYSTIC REFF method (Section 3.3.1) determines the apparent effective radius which links the simulated radiances with the corresponding cloud droplet sizes. Furthermore, the 1D-Assisted Scattering Angle Interpolation (1D-ASAP, Section 4.2.2) is used to interpolate calculated scattering angles in the Monte Carlo ensemble. Despite this latter approach and variance reduction methods in the MYSTIC code itself (*Buras and Mayer*, 2011), the time-consuming Monte Carlo technique still limits the number of model runs. For this reason, careful attention is paid to the setup and the sampling of the Monte Carlo ensemble.

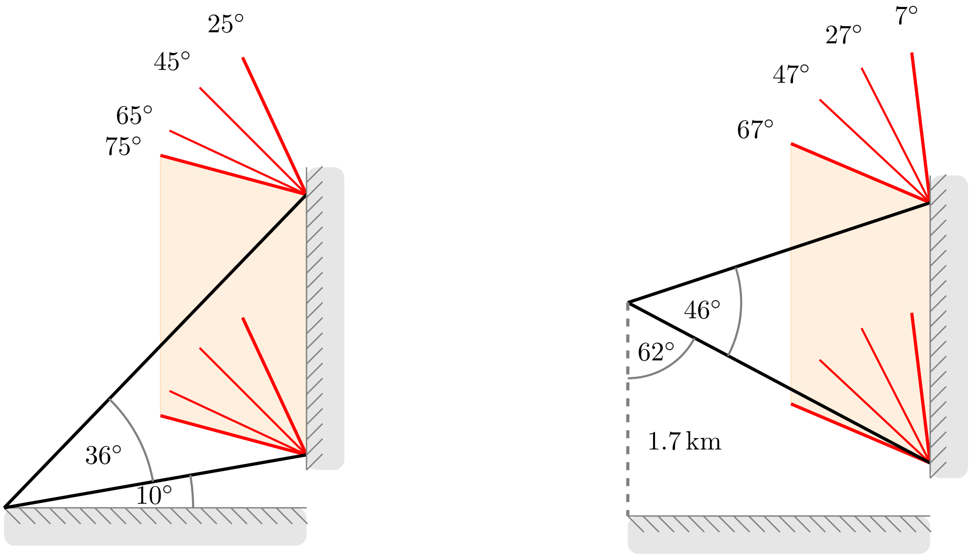

Figure 4.30: (left) Setup of the viewing geometry ($\Delta\vartheta = 36°$, excluding the first 10° above the horizon) and the illumination geometry ($\vartheta_0 = 25, 45, 65$ and 75°) for the ground-based Monte Carlo ensemble. **(right)** Setup of the viewing geometry ($\Delta\vartheta = 46°$, starting 62° from nadir) and the illumination geometry ($\vartheta_0 = 7, 27, 47$ and 67°) for the airborne ($h = 1.7\,\mathrm{km}$) Monte Carlo ensemble. In both cases, the horizontal extent of the field of view is $\Delta\varphi = \pm 45°$ from the principal plane.

Since the retrieval should be able to be applied to ground-based as well as to airborne measurements, two different Monte Carlo ensembles were implemented for both perspectives. Figure 4.30 illustrates the ground-based setup on the left and the airborne setup on the right with a sketched cloud side. For the ground-based ensemble, the field of view was designed with a vertical aperture of 36°. The first 10° above the horizon were excluded from the ensemble since it contained mostly shadowed cloud bases. Illumination geometries typical for middle latitudes were sampled at four solar zenith angles of $\vartheta_0 = 25, 45, 65$ and 75°. With LES cloud tops between 1.5 and 2.0 km, the airborne perspective was set above the ground-based location at an altitude of $h = 1.7\,\mathrm{km}$. Since the airborne campaign was conducted over the Amazonas region, solar zenith angles typical for tropical latitudes were chosen at $\vartheta_0 = 7, 27, 47$ and 67°. To cover viewing directions off principal plane, the field of view was simulated in the range $\Delta\varphi = \pm 45°$ relative to the principal plane.

An entire scan (90° × 46°) was simulated using the MYSTIC *panorama* option. Comprising 720 × 368 pixel, each panorama was calculated with a spatial resolution of 0.125°. For this image setup, solar radiances were calculated at the non-absorbing wavelength $\lambda = 870\,\mathrm{nm}$ ($L_{0.87}$) and the absorbing wavelength $\lambda = 2100\,\mathrm{nm}$ ($L_{0.87}$). As described in Section 3.2.1, the extraterrestrial solar spectrum from *Kurucz* (1994) and the absorption parameterization *(REPTRAN)* by *Gasteiger et al.* (2014) were used in this radiative transfer calculation. Since no significant bias has been found by the width of the cloud droplet size distribution on radiances (see Section 4.1.1), the scattering properties were derived according to the Mie theory for modified gamma size distributions with $\alpha = 7$. For the ensemble, the surface albedo was set to zero since the influence of radiation reflected by vegetation on the ground is masked out in measurements.

Atmospheric aerosol was included by using the continental average mixture from the Optical Properties of Aerosols and Clouds (OPAC) package (*Hess et al.*, 1998). The aerosol optical thickness (AOT) at $550\,\mathrm{nm}$ is around $\tau_a^{550} = 0.15$ for this profile. This aerosol profile is typical for anthropogenically influenced continental areas and contains soot and an increased amount of insoluble (e.g. soil) as well as water-soluble (e.g. sulfates, nitrates and organic) components (*Hess et al.*, 1998).

For each pixel, 2000 photons were started which took roughly one second on a single core of a *Intel Xeon E5-2650* CPU running $2\,\mathrm{GHz}$. Hereby, a compromise had to be found to minimize the Monte Carlo noise and to keep computation time within reasonable limits. The number of 2000 photons, leading to a standard deviation in radiance of about 2%, was chosen to stay below an assumed radiometric uncertainty of ~ 5%.

All 12 RICO LES snapshots between $12\,\mathrm{h}\ 00\,\mathrm{min}$ LT (local time) and $14\,\mathrm{h}\ 00\,\mathrm{min}$ LT with a time step of $10\,\mathrm{min}$ were included in the ground-based as well as in the airborne ensemble. For the 4 azimuth directions $\varphi = 45°$, 135°, 225° and 315°, suitable locations for cloud side observations were determined in each LES snapshot with the field of view kernel convolution method described in Section 4.2.1. In summary, for each ensemble $12 \times 4 = 48$ cloud scenes have been simulated for 4 solar zenith angles and 2 wavelengths with 720×368 pixel, totaling 101,744,640 Monte Carlo pixels. For this number, roughly 2.0×10^{11} photons have been traced on a computing cluster with 300 cores consuming $2.0 \times 10^{8}\,\mathrm{s}$ of CPU time. Increasing the sampling density to 30 solar zenith angles in steps of 2° with the *1D-ASAP* method, 1.5×10^{9} radiance pairs are computed for each ensemble.

4.2.4 Construction of the lookup table

After simulating the cloud side scenes, the radiances for each ensemble were sorted into separate, multidimensional histograms $n(L_{0.87}, L_{2.10}, r_{\mathrm{eff}})$. Following the reasoning of Section 4.1.2, it is in particular the pixel surrounding and the scattering angle ϑ_s which have an influence on the ambiguity in observed radiances. Consequently, radiance are binned into different histograms corresponding to their scattering angle ϑ_s and the result of the gradient classifier g_{class}. Hereby, scattering angles were binned between $\vartheta = 180°$ and 80° in 10 equidistant steps of 10°. Bounded between $-\pi/2$ and $\pi/2$ with the arcus tangent function, the gradient classifier g_{class} is binned in 5 equidistant steps.

At the non-absorbing wavelength $\lambda = 870\,\mathrm{nm}$, radiances up to $290\,\mathrm{mW\,m^{-2}\,sr^{-1}\,nm^{-1}}$ were binned in 58 equidistant steps of $5\,\mathrm{mW\,m^{-2}\,sr^{-1}\,nm^{-1}}$ while the radiances at the absorbing wavelength $\lambda = 2100\,\mathrm{nm}$ were binned up to $18\,\mathrm{mW\,m^{-2}\,sr^{-1}\,nm^{-1}}$ in 90 equidistant steps of $0.2\,\mathrm{mW\,m^{-2}\,sr^{-1}\,nm^{-1}}$. According to their corresponding apparent effective radius, radiances were furthermore binned between $r_{\mathrm{eff}} = 4\,\mu\mathrm{m}$ to $12\,\mu\mathrm{m}$ in equidistant steps of $0.25\,\mu\mathrm{m}$. According to their exact value, radiances were counted in adjoining radiance bins by linear interpolation. In the following, these histograms $n(L_{0.87}, L_{2.10}, r_{\mathrm{eff}})$ will be transformed into lookup tables for the posterior probability $p(r_{\mathrm{eff}}|\, L_{0.87}, L_{2.10})$.

4.2.5 Biased and unbiased priors

The retrieval should not exhibit any trend towards a specific profile. Instead of testing a hypothesis, the retrieval would otherwise only reflect an a-priori knowledge about the vertical profile of cloud microphysics. For this reason, the assumed prior is a key element to be considered in the Monte Carlo sampling of the posterior and the subsequent Bayesian inference. It is important to check its influence and to correct for it when the scientific question demands it. In the case of cloud side remote sensing, two possible priors $p_{\mathrm{pr}}(r_{\mathrm{eff}})$ come to mind:

$$p_{\mathrm{pr}}(r_{\mathrm{eff}}) \propto \begin{cases} \text{(uniform prior)} \quad \text{const.} & (4.26) \\ \text{(LES prior)} \quad n(r_{\mathrm{eff}}) & (4.27) \end{cases}$$

Either one wants to test the hypothesis if there is a distinct profile in cloud droplet size present at all. In particular, the relative frequency of r_{eff} for different scattering angles ϑ_s and gradient classes should be the same. For this problem, the prior probability should be uniform in r_{eff} to avoid the introduction of any bias. Or, one already has a thorough knowledge of the present microphysics and wants to refine his first guess with measurements. In this case, the relative frequency $n(r_{\mathrm{eff}})$ already contained in the LES microphysics seems appropriate.

Another important element of the Bayesian approach is the coverage of the likelihood probability $p(L_{0.87}, L_{2.10}, r_{\mathrm{eff}})$. Naturally, effective radii not included in the ensemble of forward calculations cannot be retrieved using Bayesian inference. Furthermore, it should be kept in mind that sparsely sampled likelihood regions are probably not representative for the whole distribution. This is especially true for the smallest and largest effective radii contained in the LES model.

For this reasons, two different ensembles were created. One, which only includes the already described LES output and a second one where an unbiased coverage of the likelihood probability is pursued. In order to meet the latter objective, the ensemble with the *normal* LES output was complemented with calculations with *flipped* and *fixed* cloud microphysics. Figure 4.31 shows cross-sections of effective radius r_{eff} for the same LES cloud field shown in Figure 3.3 for normal cloud microphysics (Figure 4.31a) and vertically fliped cloud microphysics

(Figure 4.31b). To this end, the cloud optical thickness was held constant while

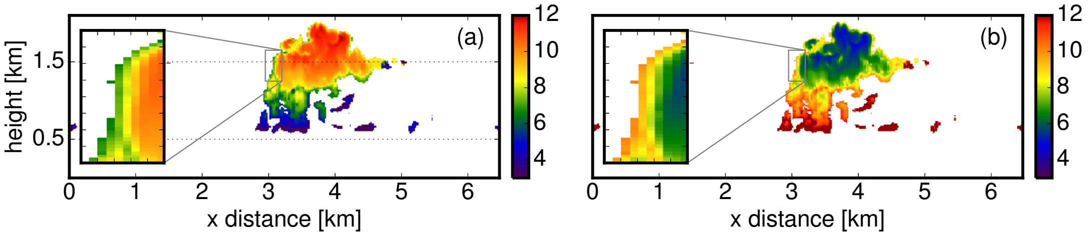

Figure 4.31: Cross-sections of effective radius r_{eff} for the LES cloud field at $x = 3.5\,\text{km}$ for **(a)** the normal cloud profile (also shown in Figure 3.3) and **(b)** the vertically flipped cloud profile.

flipping the effective radius and LWC profile according to Equation 2.49. Albeit creating partly unrealistic LWC profiles, this was done to minimize changes in radiance at non-absorbing wavelengths sensitive to changes in optical thickness. The flipped cloud microphysics were derived by dividing the effective radius range (4 µm to 12 µm) in half at $r_{\text{eff}} = 8\,\mu\text{m}$, where all other effective radii were inverted around this value:

$$r_{\text{eff}}^{\text{flip}} = 8\,\mu\text{m} + (8\,\mu\text{m} - r_{\text{eff}}^{\text{orig}}) \tag{4.28}$$

$$\text{LWC}^{\text{flip}} = \frac{r_{\text{eff}}^{\text{flip}}}{r_{\text{eff}}^{\text{orig}}}\text{LWC}^{\text{orig}} \tag{4.29}$$

Additional, two ensembles were created with a fixed effective radii ($r_{\text{eff}} = 4\,\mu\text{m}$ and $r_{\text{eff}} = 12\,\mu\text{m}$) throughout the whole domain. For the ensemble with uniform prior, the normal, the flipped and both ensembles with fixed effective radius were combined into one histogram. Subsequently, both ensemble histograms were normalized in Equation 3.11 and transformed into their posterior distribution using Equation 3.12. To expand the effective radius range of the posterior distribution, the bins between $4\,\mu\text{m} < r_{\text{eff}} < 6\,\mu\text{m}$ and $10\,\mu\text{m} < r_{\text{eff}} < 12\,\mu\text{m}$ with lower sampling density $n(r_{\text{eff}})$ were replaced by a linear interpolation of the posterior probability for 4 µm and 6 µm, resp. for 10 µm and 12 µm.

The reason to exclude the edge regions in the posterior distribution and replace them with ensembles which sample the boundaries at $r_{\text{eff}} = 4\,\mu\text{m}$ and 12 µm, is shown in Figure 4.32. Figure 4.32a shows the number of pixels $n(r_{\text{eff}})$ contained in a airborne histogram for a scattering angle of $\vartheta_s = 135°$ and a gradient class of $g_{\text{class}} = 4$. Only the original LES ensemble without the boundary ensembles at $r_{\text{eff}} = 4\,\mu\text{m}$ and 12 µm was included in this histogram. Towards the edges of the distribution range, the number of included pixels drops sharply. For this ensemble, Figure 4.32b show the posterior distribution for a fixed radiance $L_{0.87} = 110\,\text{mW}\,\text{m}^{-2}\,\text{sr}^{-1}\,\text{nm}^{-1}$ at the non-absorbing wavelength and variable $L_{2.10}$ radiances at the absorbing wavelength. The same is shown for the ensemble with the uniform prior and with included boundary ensembles at $r_{\mathrm{eff}} = 4\,\mu\mathrm{m}$ and $12\,\mu\mathrm{m}$ in Figure 4.32c. Comparing the posterior distributions in Figure 4.32b and Figure 4.32c, it becomes apparent how the sparser sampling density $n(r_{\mathrm{eff}})$ (hatched area) introduces a bias in the mean effective radii (colored vertical lines) at the edges of the effective radius range. While the posteriors without the boundary ensembles seem to be to low at these edges, the posterior probabilities with the boundary ensembles might be to high near $r_{\mathrm{eff}} = 4\,\mu\mathrm{m}$ and $r_{\mathrm{eff}} = 12\,\mu\mathrm{m}$. This *edge effect* can be attributed to the missing neighborhood of larger (resp. smaller) values for $r_{\mathrm{eff}} = 12\,\mu\mathrm{m}$ and $r_{\mathrm{eff}} = 4\,\mu\mathrm{m}$. When approximating posteriors with solutions on an infinite lattice (in principle, effective radii can have any positive value in $\mathbb{R}$) with solutions for an finite lattice, the boundary sites of the posteriors should be used with caution (*Fishman*, 2003). Nevertheless, the r_{eff} range of the posteriors is enlarged by the interpolation of the boundary cases, while the higher probabilities at the boundaries compensates for the missing distribution part outside the calculated range for r_{eff}.

4.2.6 Radiance and posterior distributions

The following section will present the radiance histograms $n(L_{0.87}, L_{2.10}, r_{\mathrm{eff}})$ and the corresponding posterior distributions $p(r_{\mathrm{eff}}|\, L_{0.87}, L_{2.10})$. Analogous to the likelihood distribution, the first gives the spread of radiances for a given effective radius r_{eff}, while the latter describes the spread of effective radii r_{eff} after the radiances $L_{0.87}$ and $L_{2.10}$ have been measured. Panels on the left side in Figure 4.33 show histograms for the ground-based Monte Carlo ensemble of cloud sides, while on the right histograms for the airborne ensemble are shown. The histograms are shown for the uniform ensemble with flipped and fixed cloud profiles included and for pixels in the scattering angle bin between $\vartheta_s = 130°$ and $140°$ and in the gradient class bin $g_{\mathrm{class}} = 4$ which holds pixels that are brighter as their surroundings. From top to bottom, the effective radius increases from $r_{\mathrm{eff}} = 4\,\mu\mathrm{m}$ on the top, to $r_{\mathrm{eff}} = 9\,\mu\mathrm{m}$ in the center and to $r_{\mathrm{eff}} = 12\,\mu\mathrm{m}$ at the bottom. Furthermore, the one-dimensional DISORT results, discussed in Section 4.1.2, are superimposed as dashed lines. They mark the one-dimensional radiative transfer limit in which reflected radiances from optically thick ($\tau = 500$) water clouds vary for the same effective radius and the same scattering angle for different cloud surface inclinations within the principal plane. The colored dots indicate locations within the histogram for which the posterior distributions are shown in Figure 4.34.

In accordance with the theory of *Nakajima and King* (1990), the radiance at the absorbing-wavelength decreases with increasing droplet size. Moreover, the spread of the radiance from three-dimensional cloud sides can be explained, for the most part, by the one-dimensional DISORT results for different cloud surface inclinations. Since many clouds in the ensemble are optically thinner than in the one-dimensional study, the radiance at the non-absorbing wavelength $870\,\mathrm{nm}$ is not saturated yet. This explains why the Monte Carlo results do not cover the complete one-dimensional sample space spanned by the dashed lines. Even

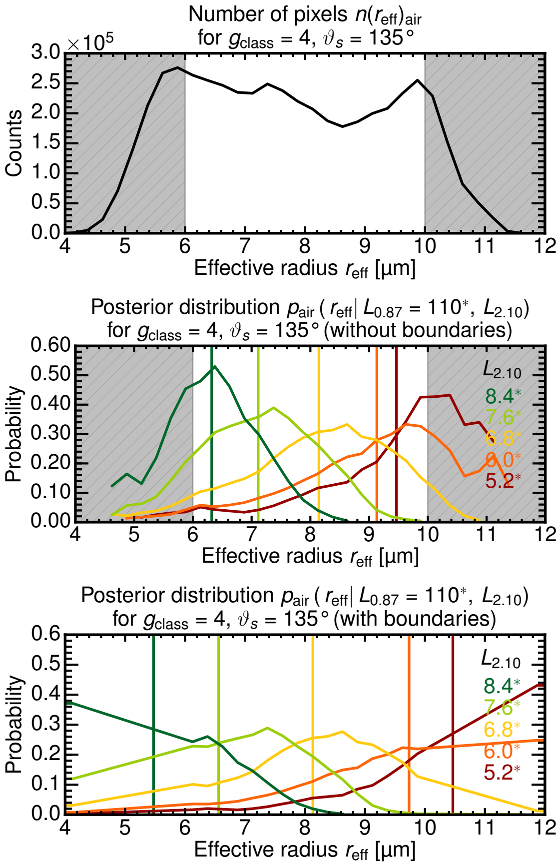

Figure 4.32: **(a)** Number of pixels $n(r_{\text{eff}})$ included in the airborne histogram with the LES prior and without the boundary ensembles at $r_{\text{eff}} = 4\,\mu\text{m}$ and $12\,\mu\text{m}$ for a scattering angle of $\vartheta_s = 135°$ and a gradient class of $g_{\text{class}} = 4$. **(b)** Posterior probability of the same histogram for a fixed radiance $L_{0.87} = 110\,\text{mW}\,\text{m}^{-2}\,\text{sr}^{-1}\,\text{nm}^{-1}$ (unit shortened with *) and variable $L_{2.10}$ radiances. **(c)** Posterior probability for the uniform prior and with included boundary ensembles at $r_{\text{eff}} = 4\,\mu\text{m}$ and $12\,\mu\text{m}$. Here, the sparser sampling density $n(r_{\text{eff}})$ (hatched area) introduces a clear bias in the mean effective radii (colored vertical lines) at the edges of the effective radius range.

though radiance values are a little bit higher for the airborne ensemble, there is no significant difference between the histograms for the ground-based and the airborne ensemble. After normalization of the histograms in Equation 3.11 and after the application of the uniform prior in Section 4.2.5, the posterior probabilities $p(r_{\text{eff}}| L_{0.87}, L_{2.10})$ can be examined. Figure 4.34 shows posterior probabilities as a function of r_{eff} for different radiances $L_{2.10}$ at the absorbing wavelength corresponding to the colored dots in the histogram panels (Figure 4.33). Again, on the left in Figure 4.34 results are shown for the ground-based ensemble, while results on the right are for the airborne ensemble. The vertical lines indicate

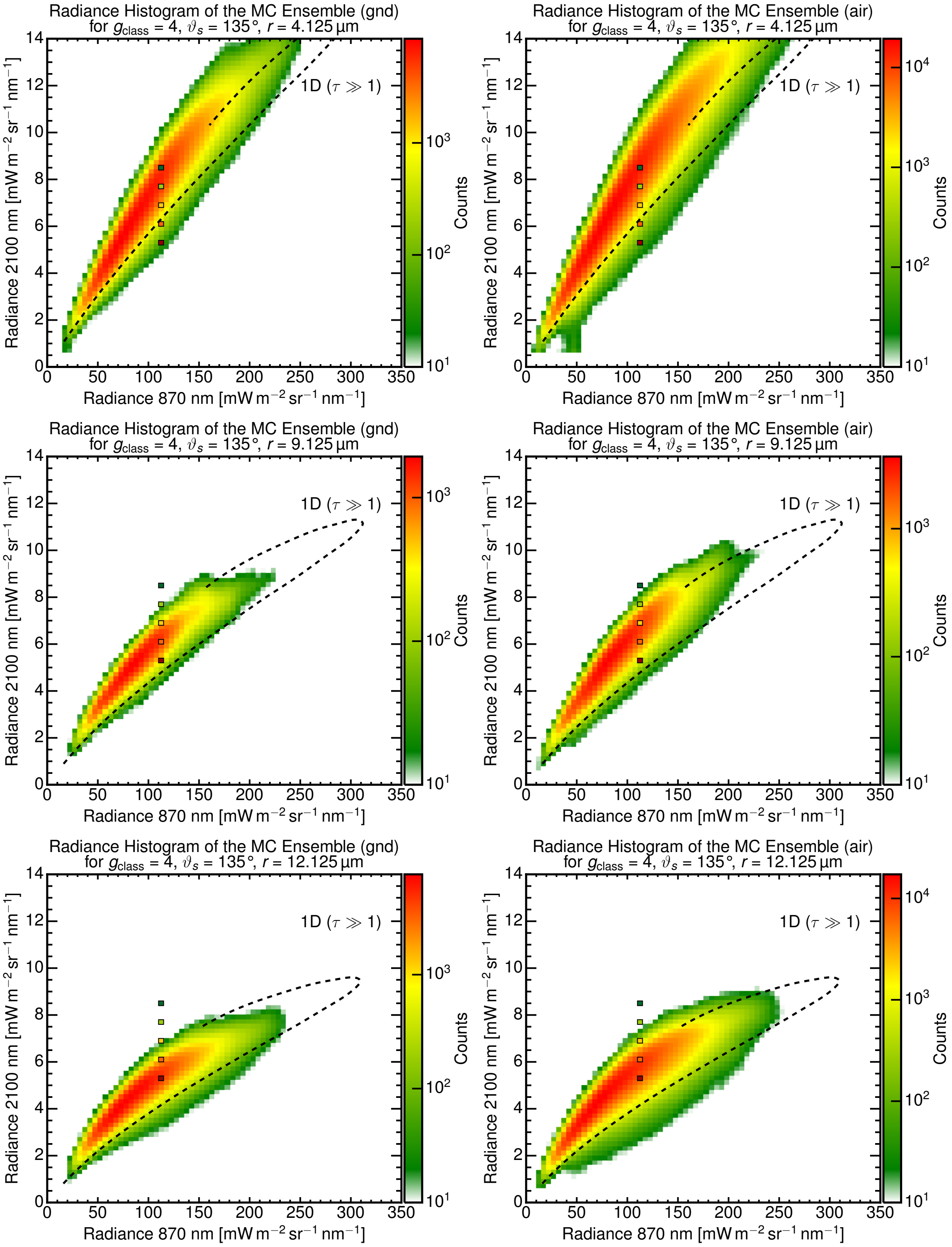

Figure 4.33: Radiance histograms ($\vartheta_s = 135°$, $g_{\mathrm{class}} = 4$) for the ground-based **(left)** and airborne **(right)** Monte Carlo ensemble of cloud sides which illustrate the radiance spread for the effective radius bin of **(top)** $r_{\mathrm{eff}} = 4\,\mu\mathrm{m}$, **(center)** $r_{\mathrm{eff}} = 9\,\mu\mathrm{m}$ and **(bottom)** $r_{\mathrm{eff}} = 12\,\mu\mathrm{m}$. The dashed line shows reflected radiances which were calculated with DISORT (1D RT code) for an optically thick ($\tau = 500$) water cloud with the same effective radius and the same scattering angle for different cloud surface inclinations within the principal plane. The colored dots indicate locations within the histogram for which the posterior distributions are shown in Figure 4.34.

the corresponding mean effective radius for each posterior distribution which were derived using Equation 4.30. The descending order of mean effective radii with ascending radiance $L_{2.10}$ demonstrates the general feasibility to discriminate different effective radii in cloud side measurements. Albeit the relatively large spread in r_{eff}, the measurement of a radiance pair ($L_{0.87}$, $L_{2.10}$) can still narrow down r_{eff} to $\pm 1.5\,\mu\mathrm{m}$ around the most likely value. In comparison, the slightly higher radiance values of the airborne ensemble can also be observed for the posteriors in Figure 4.34. Besides the effective radius and radiance dimension, histograms have also been separated between scattering angles ϑ_s and between gradient classes g_{class}. In order to examine how the posteriors depend on these other parameters, Figure 4.35 shows the posterior for measurements $L_{0.87} = 110\,\mathrm{mW\,m^{-2}\,sr^{-1}\,nm^{-1}}$ and $L_{0.87} = 6\,\mathrm{mW\,m^{-2}\,sr^{-1}\,nm^{-1}}$ for different gradient classes g_{class} on the top, for different scattering angles ϑ_s in the middle and for different solar zenith angles ϑ_0 at the bottom. What stands out most is the large influence of the gradient classifier g_{class}. With every bin in g_{class}, the mean effective radius changes by $\sim 1\,\mu\mathrm{m}$. This strong dependence of $p(r_{\mathrm{eff}}|\,L_{0.87}, L_{2.10})$ on g_{class} suggests that the gradient classifier acts like a filter to exclude cloud regions where the radiance–effective radius relation is too ambiguous. While g_{class} still helps to separate ambiguous radiance distributions, it also acts as local shadow threshold for pixels which were missed by the global threshold used by the shadow mask. Interestingly, the dependence of the posterior on the scattering angle differs between the ground-based and the airborne ensemble. While the mean effective radius of the airborne ensemble posterior decreases by around $1\,\mu\mathrm{m}$ for a decreasing scattering angle from $\vartheta_s = 145°$ to $115°$, the ground-based ensemble mean effective radius seems to be invariant with respect to ϑ_s. The broadening of the radiance distribution for smaller scattering angles found in

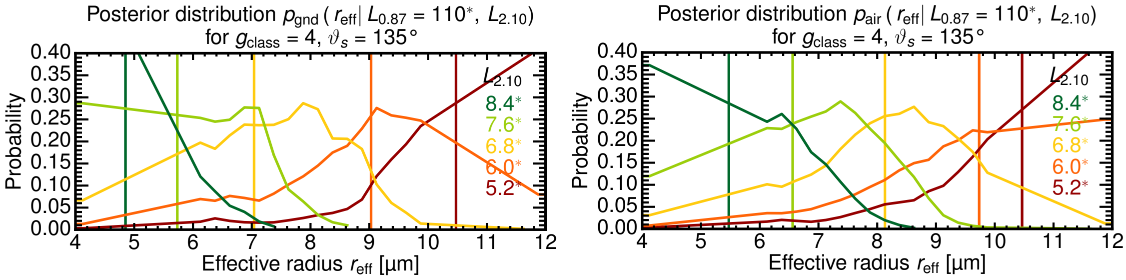

Figure 4.34: (left) Posterior probability ($\vartheta_s = 135°$, $g_{\mathrm{class}} = 4$) for the uniform prior of the ground-based Monte Carlo ensemble for a fixed radiance $L_{0.87} = 110\,\mathrm{mW\,m^{-2}\,sr^{-1}\,nm^{-1}}$ at the non-absorbing wavelength and different $L_{2.10}$ radiances at the absorbing wavelength. **(right)** the same posterior probability for the airborne Monte Carlo ensemble. The vertical lines indicate the corresponding mean effective radius for each posterior distribution. The color of the different posterior distributions corresponds with the dots in the radiance histograms in Figure 4.33.

the spherical cloud study in Section 4.1.2, cannot be found in the ground-based ensemble. The underlying reason has to be connected with the overall cloud shape. Due to their larger height, compared with their width, the RICO LES clouds display more convex, sphere-like surfaces for the airborne perspective while the clouds look more like a wall for the ground-based perspective. With a less uniform distribution of cloud surface inclinations, the scattering angle signature found in the spherical cloud study might be less pronounced. In Figure 4.35 at the bottom, the posterior was tentatively separated for different solar zenith angles ϑ_0 to test for an influence of ϑ_0 on $p(r_{\mathrm{eff}}|\,L_{0.87}, L_{2.10})$. For both ensembles, ground-based as well as airborne, there is no significant posterior probability dependence on solar zenith angle ϑ_0. For this reason, the scattering angle ϑ_s was preferred over the solar zenith angle ϑ_0 as a dimension defining the histograms. In the following, the tabulated set of posterior distributions is used as lookup table for the effective radius retrieval.

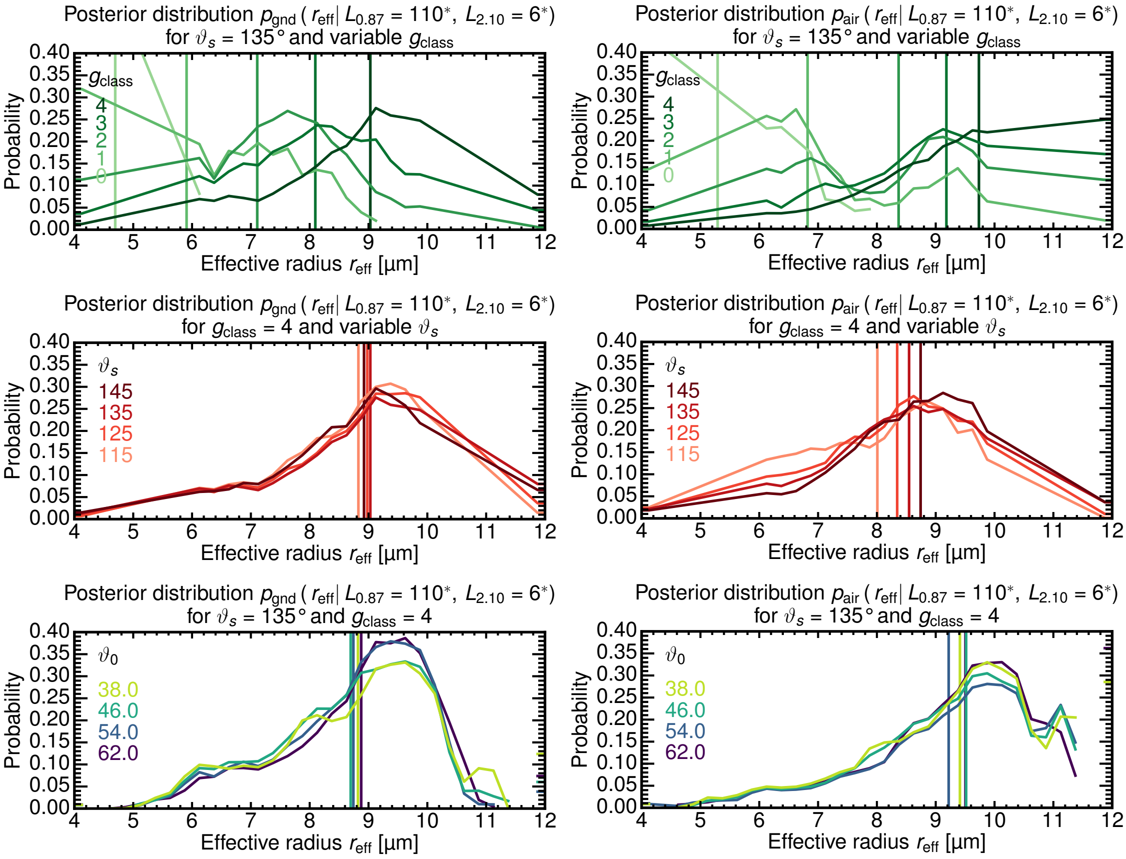

Figure 4.35: Posterior probabilities for the uniform prior of the ground-based **(left)** and airborne **(right)** Monte Carlo ensemble for the fixed radiances $L_{0.87} = 110\,\mathrm{mW\,m^{-2}\,sr^{-1}\,nm^{-1}}$ and $L_{2.10} = 6\,\mathrm{mW\,m^{-2}\,sr^{-1}\,nm^{-1}}$, **(top)** for varying gradient classifier g_{class} bins, **(center)** for varying scattering angles ϑ_s and **(bottom)** for varying solar zenith angles ϑ_0.

4.2.7 Bayesian inference of the effective radius

Based on this lookup table of posterior probabilities $p(r_{\mathrm{eff}}|\, L_{0.87}, L_{2.10})$, the actual retrieval of effective radii can now be introduced. Basically, the process is identical to the creation of the histogram in Section 4.2.4. After a set of spectral radiance pairs $L_{0.87}$ and $L_{2.10}$ has been measured, the band-pass filter (Section 4.1.2) is applied to the $L_{2.10}$ image to derive the gradient classifier g_{class}. Subsequently, the filters describe in Section 4.1.3 exclude cloud shadows, cloud ice-phase and contamination by ground albedo reflection. By using the positional data recorded by the scanning mount or by using the navigational data recorded by the aircraft, corresponding scattering angles can be calculated. With the four parameters, $L_{0.87}$, $L_{2.10}$, g_{class} and ϑ_s, defined for each pixel, the corresponding posterior is retrieved from the lookup table by linear interpolation between posteriors defined at the bin centers of the lookup table. Finally, the mean effective radius $\langle r_{\mathrm{eff}} \rangle$ and the corresponding standard deviation $\sigma(r_{\mathrm{eff}})$ can be derived as first and second moments of the posterior distribution:

$$\langle r_{\mathrm{eff}} \rangle = \int r_{\mathrm{eff}}\; p(r_{\mathrm{eff}}|\, L_{0.87}, L_{2.10})\; dr_{\mathrm{eff}}. \tag{4.30}$$

$$\sigma(r_{\mathrm{eff}}) = \sqrt{\int \left(r_{\mathrm{eff}} - \langle r_{\mathrm{eff}} \rangle\right)^2 p(r_{\mathrm{eff}}|\, L_{0.87}, L_{2.10})\; dr_{\mathrm{eff}}}. \tag{4.31}$$

Throughout this work, this 1-sigma standard deviation $\sigma(r_{\mathrm{eff}})$ will be referred to as the *statistical retrieval uncertainty*.

4.3 Numerical analysis of the retrieval

The next section will examine the stability of the statistical relationship between reflected radiance and cloud droplet size. Hereby, the statistical resilience to unrealistic cloud profiles included in the lookup table remained as an open question. To answer this open question, the statistical retrieval is applied to simulated cloud side measurements for which the underlying effective radius is known. First, this is done for scenes that have already been included in the lookup table. Using scenes with normal, flipped and fixed effective radius profile, the lookup table is tested for an inherent bias towards a specific effective radius profile that could be caused by the chosen forward sampling strategy.

4.3.1 Analysis of the sampling bias

When no prior information about the effective radius profile is assumed (uniform prior $p_{\mathrm{pr}}(r_{\mathrm{eff}})$ for r_{eff}), the retrieval should not exhibit any trend towards a specific profile. This holds especially true for the scenes with fixed effective radius profile. Despite this requirement, it is still possible that a specific microphysical profile can be better detected due to different 3D effects at cloud base compared to 3D effects at cloud top.

for the ground-based perspective

In Figure 4.36, the first test case for the ground-based perspective is shown. For consistency, the LES cloud scene around $12\,\mathrm{h}\ 40\,\mathrm{min}$ LT was used for this study again. In Figures 4.36a and 4.36b, MYSTIC forward results for the normal effective radius profile are shown, while Figures 4.36c and 4.36d show results for the flipped and Figures 4.36e and 4.36f for the fixed profile. In Figure 4.36a and Figure 4.36c, the apparent effective radius $\langle r_{\mathrm{eff}} \rangle_{\mathrm{mc}}$ is shown for the normal and flipped profile. Here, $\langle r_{\mathrm{eff}} \rangle_{\mathrm{mc}}$ is used as a reference for the retrieval and is calculated simultaneously with the radiance fields using the MYSTIC REFF Monte Carlo method. Figures 4.36b, 4.36d and 4.36f on the right show the calculated spectral radiance for $\lambda = 2.1\,\mu\mathrm{m}$. Since the optical thickness was held constant, the spectral radiance for $\lambda = 870\,\mathrm{nm}$ in case of the normal and flipped profile is nearly identical with the spectral radiance in case of the fixed profile shown in Figure 4.36e. The result of the statistical effective radius retrieval for the ground-based cases shown in Figure 4.36 is summarized in Figure 4.37. Here, the retrieved mean effective radius in the right panels (Figures 4.37c, 4.37f and 4.37i) is compared to the true effective radius $\langle r_{\mathrm{eff}} \rangle_{\mathrm{mc}}$ shown in the left panels (Figures 4.37a, 4.37d and 4.37g). The center panels show the mean vertical profile (lines) and its spatial standard deviation (shaded areas) of the true (black) and the retrieved (green) effective radius. Furthermore, the standard deviation $\sigma(r_{\mathrm{eff}})$ provided by the retrieval as error estimate for r_{eff} is shown by the green errorbars. In this comparison, only shadow-free pixel ($R_{0.87}/R_{2.1} > 3.5$) and pixel with $L_{0.87} > 50\,\mathrm{mW\,m^{-2}\,sr^{-1}\,nm^{-1}}$ were included.

Overall, the retrieval reproduces all three profiles quite well. However, there are also great differences (up to $\pm 3\,\mu\mathrm{m}$) for specific cloud regions. For the normal profile as well as for the flipped profile, the retrieved effective radius agrees well with its true value for the upper half of the cloud side. Interestingly, the lower half of the profile is not reproduced very well in both cases. At cloud base, the retrieval overestimated the small r_{eff} values for the normal profile, while it underestimates the large r_{eff} values for the flipped profile; they even seem to be the same in all three cases. Since ground albedo was set to zero, this has to be connected with poor illumination conditions at cloud base. Globally, the retrieval overestimates r_{eff} by $0.29\,\mu\mathrm{m}$ (RMSE: $1.29\,\mu\mathrm{m}$) for the normal profile and underestimates the flipped profile by $-0.73\,\mu\mathrm{m}$ (RMSE: $1.00\,\mu\mathrm{m}$) and the fixed profile by $-0.39\,\mu\mathrm{m}$ (RMSE: $0.72\,\mu\mathrm{m}$). After all, the true effective radius remains within the specified retrieval error estimate given by $\sigma(r_{\mathrm{eff}})$. Although retrieval deviations are, in part, quite large, no major bias is apparent.

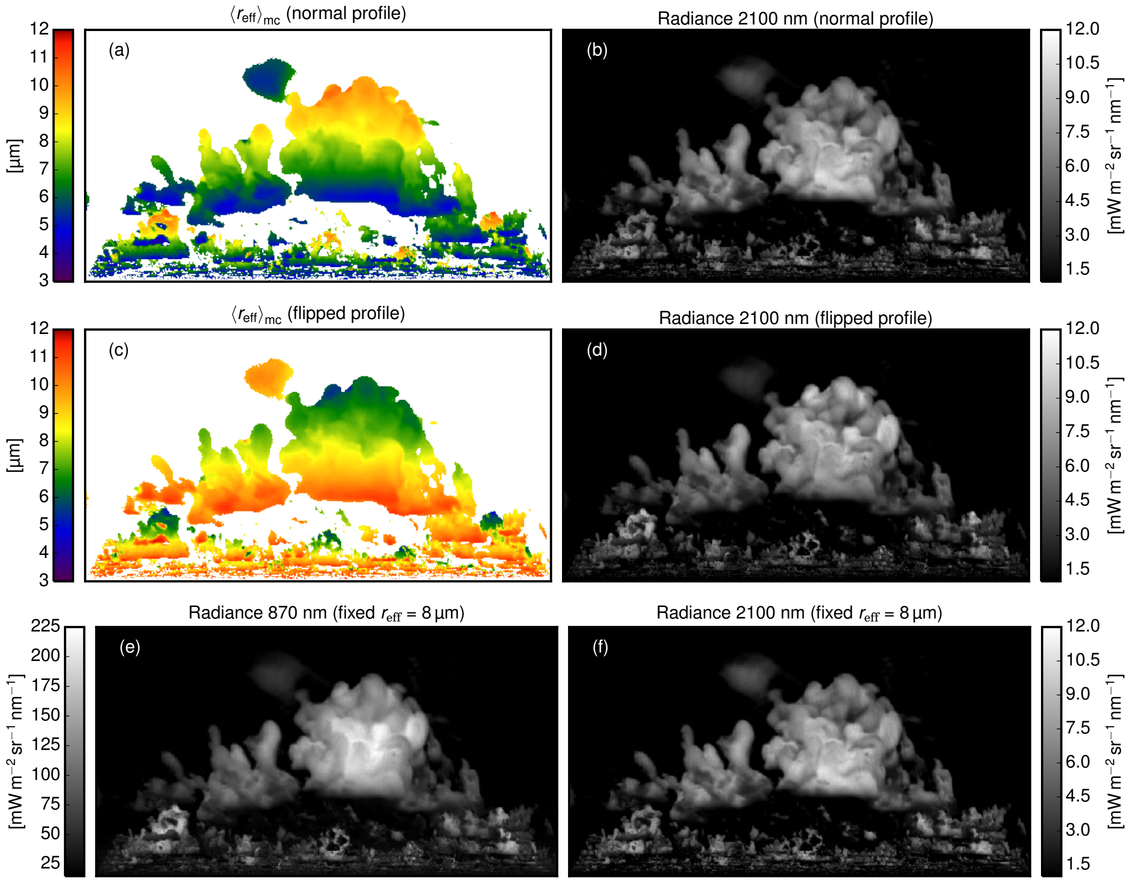

Figure 4.36: Ground-based retrieval test case with normal (top), flipped (center) and fixed (bottom) effective radius profile for the cloud side scene (12 h 40 min LT) shown in Figure 4.28a. **(a)** Apparent effective radius $\langle r_{\text{eff}} \rangle_{\text{mc}}$ for the normal profile, **(b)** Spectral radiance at 2100 nm for the normal profile, **(c)** Apparent effective radius $\langle r_{\text{eff}} \rangle_{\text{mc}}$ for the flipped profile, **(d)** Spectral radiance at 2100 nm for the flipped profile, **(e)** Spectral radiance at 870 nm for the fixed profile (nearly the same for normal and flipped profile), **(f)** Spectral radiance at 2100 nm for the fixed profile.

for the airborne perspective

The second test case is the airborne perspective of the same LES cloud around 12 h 40 min LT, for which the MYSTIC results are shown in Figure 4.38. The setup is identical with the ground-based case described in the previous section, with a normal effective radius profile on top, a flipped profile in the center and a fixed effective radius profile at the bottom in Figure 4.38. A detailed introduction of every plot can therefore be found in the previous section. While the difference in radiance $L_{2.10}$ at 2.1 µm was quite hard to detect by eye for the ground-based

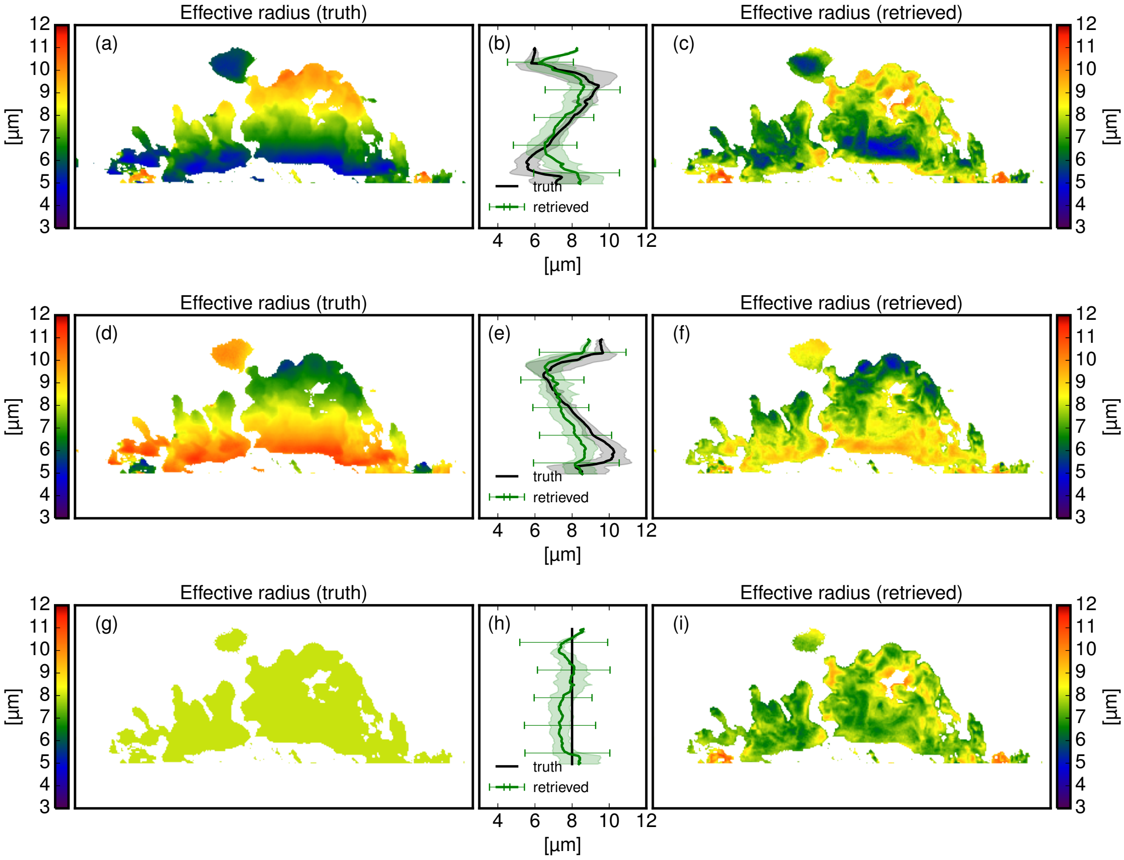

Figure 4.37: Ground-based retrieval comparison between the true effective radius (left) and the retrieved mean effective radius (right) for the normal (top), flipped (center) and fixed (bottom) effective radius profile. **(a)** Apparent effective radius $\langle r_{\mathrm{eff}} \rangle_{\mathrm{mc}}$ for the normal profile, **(b)** Mean and standard deviation of the true (black) and retrieved (green) vertical effective radius profile (normal), **(c)** Retrieved mean effective radius for the normal profile, **(d)** Apparent effective radius $\langle r_{\mathrm{eff}} \rangle_{\mathrm{mc}}$ for the flipped profile, **(e)** Mean and standard deviation of the true (black) and retrieved (green) vertical effective radius profile (flipped), **(f)** Retrieved mean effective radius for the flipped profile, **(g)** Apparent effective radius $\langle r_{\mathrm{eff}} \rangle_{\mathrm{mc}}$ for the fixed profile, **(h)** Mean and standard deviation of the true (black) and retrieved (green) vertical effective radius profile (fixed), **(i)** Retrieved mean effective radius for the fixed profile

perspective, the flipped effective radius profile is somewhat easier to recognize for the airborne perspective between Figure 4.38b and Figure 4.38d.

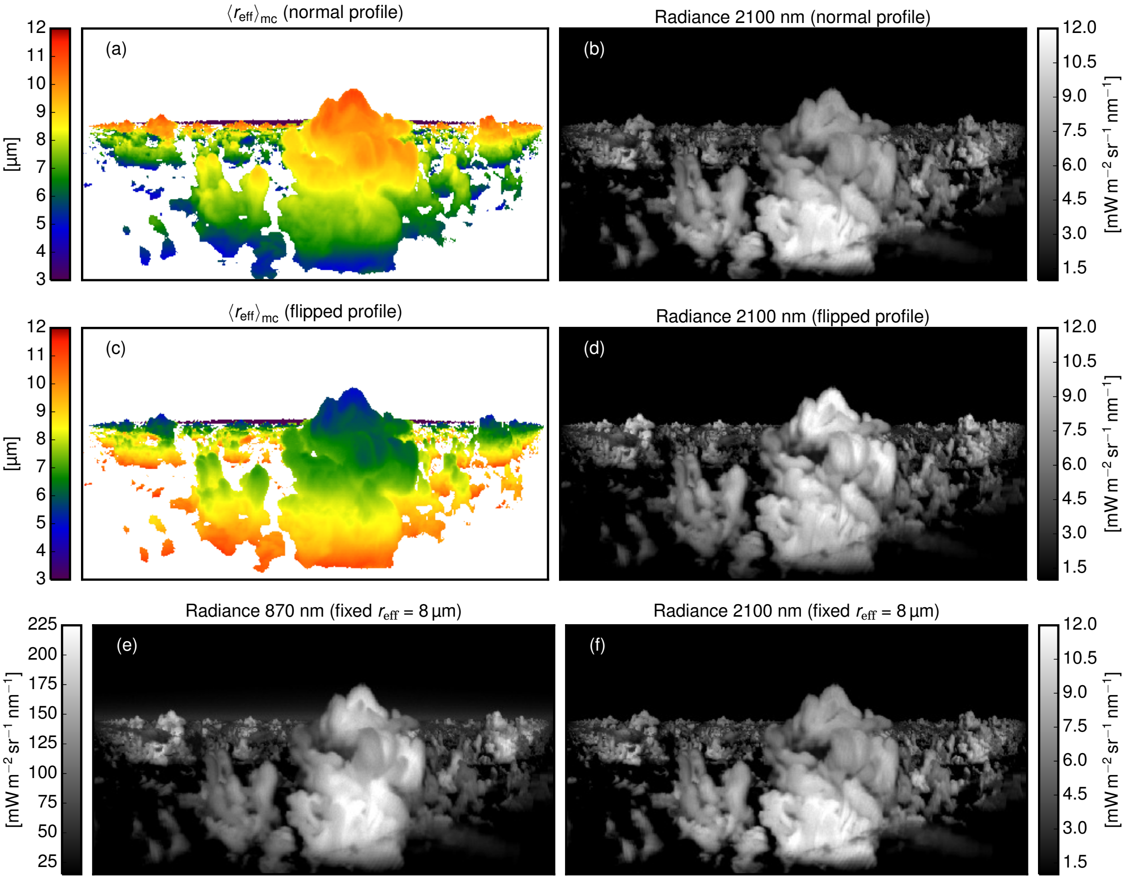

Figure 4.38: Airborne retrieval test case with normal (top), flipped (center) and fixed (bottom) effective radius profile for the cloud side scene (12 h 40 min LT) shown in Figure 4.28b. **(a)** Apparent effective radius $\langle r_{\mathrm{eff}}\rangle_{\mathrm{mc}}$ for the normal profile, **(b)** Spectral radiance at 2100 nm for the normal profile, **(c)** Apparent effective radius $\langle r_{\mathrm{eff}}\rangle_{\mathrm{mc}}$ for the flipped profile, **(d)** Spectral radiance at 2100 nm for the flipped profile, **(e)** Spectral radiance at 870 nm for the fixed profile (nearly the same for normal and flipped profile), **(f)** Spectral radiance at 2100 nm for the fixed profile.

Again, only shadow-free pixel ($R_{0.87}/R_{2.1} < 3.5$) and pixel with $L_{0.87} > 50$ $\mathrm{mW\,m^{-2}\,sr^{-1}\,nm^{-1}}$ were included in the comparison between true and retrieved effective radius shown in Figure 4.39. In contrast to the ground-based perspective, where results for viewing zenith angles between $\vartheta = 90°$ and $100°$ have been filtered out to exclude cloud bases, here, the outermost viewing azimuth angles (20°) were filtered out to exclude very distant clouds created by the continuous boundary condition in the radiative transfer code. In general, the results resemble the results for the ground-based perspective. In the lower half of the cloud side near cloud base, the retrieval underestimates the large droplets of the flipped profile by up to 1 µm. However, the retrieval seems to perform slightly better for the airborne perspective, especially for the normal profile where droplets increase with altitude. This is also reflected by the smaller biases when averaged over the complete scene. Globally, the retrieval overestimates r_{eff} by 0.22 µm (RMSE: 1.18 µm) for the normal profile and underestimates the flipped profile by −0.16 µm (RMSE: 1.08 µm) and the fixed profile by −0.16 µm (RMSE: 0.91 µm).

Altogether, the statistical relationship between reflected radiance and cloud

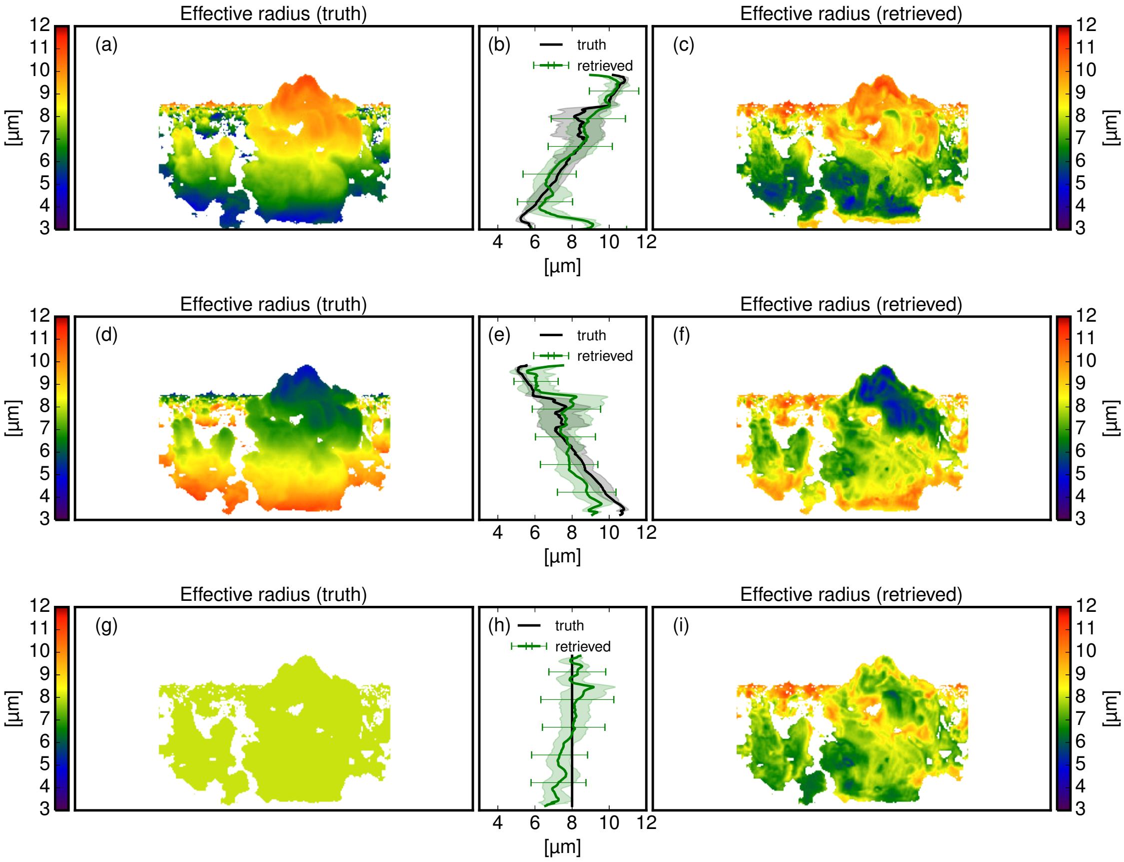

Figure 4.39: Airborne retrieval comparison between the true effective radius (left) and the retrieved mean effective radius (right) for the normal (top), flipped (center) and fixed (bottom) effective radius profile. **(a)** Apparent effective radius $\langle r_{\text{eff}} \rangle_{\text{mc}}$ for the normal profile, **(b)** Mean and standard deviation of the true (black) and retrieved (green) vertical effective radius profile (normal), **(c)** Retrieved mean effective radius for the normal profile, **(d)** Apparent effective radius $\langle r_{\text{eff}} \rangle_{\text{mc}}$ for the flipped profile, **(e)** Mean and standard deviation of the true (black) and retrieved (green) vertical effective radius profile (flipped), **(f)** Retrieved mean effective radius for the flipped profile, **(g)** Apparent effective radius $\langle r_{\text{eff}} \rangle_{\text{mc}}$ for the fixed profile, **(h)** Mean and standard deviation of the true (black) and retrieved (green) vertical effective radius profile (fixed), **(i)** Retrieved mean effective radius for the fixed profile

droplet size seems stable enough to be used for highly complex cloud sides. Moreover, these first results indicate that the retrieval seems to be resilient to unrealistic cloud profiles included in its lookup table. Although the retrieval showed problems to retrieve the flipped profile, no substantial bias towards a specific effective radius profile could be detected. Since these results were only obtained for a single cloud side scene, the following section will investigate these findings for a representative number of scenes.

4.3.2 Statistic stability of the Monte Carlo ensemble

The following section will examine the statistic stability of the Monte Carlo ensemble for a larger set of cloud side scenes. In a first step, the retrieval will again be tested for perspectives which are already included in the lookup table. This is done to test the retrieval for biases and to obtain a robust measure of correlation between the retrieval and the cloud side scenes it is composed of. By comparing this correlation with the correlation for cloud side scenes that are not included in the lookup table, this analysis will also be used to detect a potential over-fitting. There is the risk that the lookup table only reflects 3D effects that are specific for the included cloud side scenes. Rather, the principal goal should be a general representation of the statistical relationship between reflected radiance and cloud droplet size. To find out if this is the case, the retrieval is also applied to cloud scenes that are not included in the lookup table.

Statistic stability for perspectives included in the ensemble

During the statistical investigation of the retrieval bias and its correlation with the true effective radius, 9 cloud side perspectives were randomly chosen from the forward calculation ensemble. The corresponding time slots, viewing azimuths φ and solar zenith angles ϑ_0 can be found in the Appendix in Table A.1. For each of these 9 perspectives, all three cloud effective radius profiles were tested (normal, flipped and fixed profile). Here, the same filter thresholds as in the previous section were chosen (shadow-free: $R_{0.87}/R_{2.1} < 3.5$, cloud filter $L_{0.87} > 50\,\mathrm{mW\,m^{-2}\,sr^{-1}\,nm^{-1}}$, excluded cloud bases between $\vartheta = 90°$ and $100°$) before the statistical retrieval was applied to all 10 cloud side scenes. Additionally, only retrieval results with an error estimate $\sigma(r_{\mathrm{eff}})$ of less than $2\,\mu\mathrm{m}$ were included in this comparison.

For the included perspectives, correlation plots between the true and the retrieved effective radius are shown in Figure 4.40. The left panels show the correlation for the ground-base cases for the normal (Figure 4.40a) and the flipped profile (Figure 4.40c) with around 243,000 pixel, while the right panels show the correlation for the airborne cases for the normal (Figure 4.40b) and the flipped profile (Figure 4.40d) with around 358,000 pixel. The retrieved effective radius for both normal profile cases show a correlation coefficient of 0.80 for the ground-based and 0.79 for the airborne perspective. In both cases, the linear regression shows a slight underestimation of the effective radius range with a slope of 0.87 in case of the ground-base perspective and a slope of 0.90 in case of the airborne perspective. In contrast, the correlation is poorer in case of the flipped profiles. For the ground-based perspective in Figure 4.40c, the correlation coefficient is 0.56 between the retrieved and the true effective radius. With a correlation coefficient of 0.68, the airborne retrieval results resemble the true effective radius slightly better. This different performance is also reflected by the slope of the linear regression. The ground-based retrieval underestimates the flipped effective radius profile quite strongly with a slope of 0.56, while the airborne retrieval performs quite well with a regression slope of 0.82.

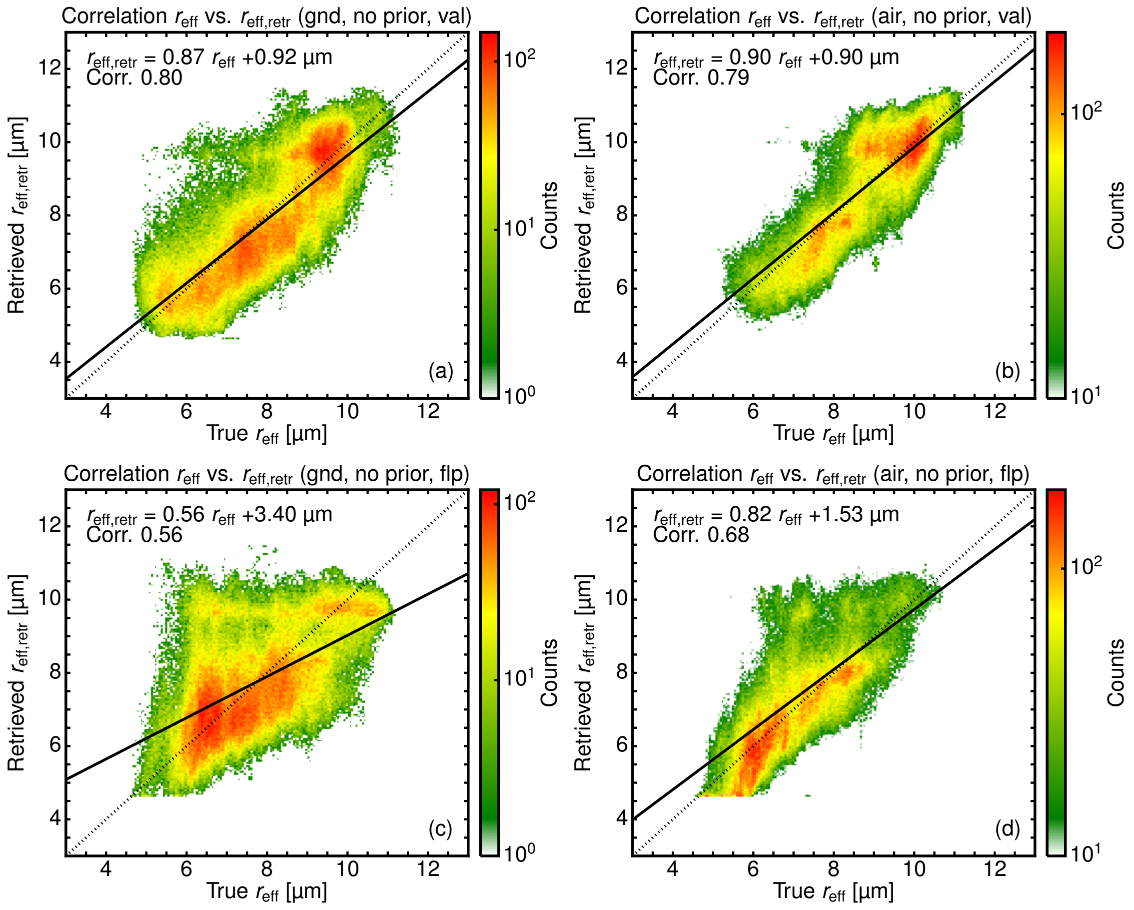

Figure 4.40: 2D histograms and linear regressions to determine the correlation between the true effective radius r_{eff} and the retrieved effective radius $r_{eff,retr}$, **(a)** for the ground-based perspective and **(b)** for the airborne perspective for the included cases with normal effective radius profile; **(c)** for the ground-based perspective and **(d)** for the airborne perspective for the included cases with flipped effective radius profile.

In case of the fixed effective radius profile, the deviation ($r_{eff,retr}$ - apparent $\langle r_{eff}\rangle_{mc}$) of the statistical retrieval is shown in histograms in Figure 4.41. For the ground-based test scenes with around 233,000 pixel, the retrieval deviation shows two distinct modes. The retrieval underestimates the effective radius slightly with most likely values between 0 µm and −1 µm. A second maximum is found where the retrieval overestimates r_{eff} with values between 1 µm and 2 µm. In combination, there is only a slight overestimation of 0.13 µm with a larger standard deviation of 1.17 µm. A further investigation showed that the overestimation peak is connected with and found around undetected cloud shadows. A scene-wise optimization of the shadow filter greatly reduced these overestimations at the cost of losing a universal shadow threshold. With 344,000 pixel, the retrieval deviations for the airborne cases show a very similar behavior, with a slight overestimation of 0.10 µm and a standard deviation of 1.17 µm.

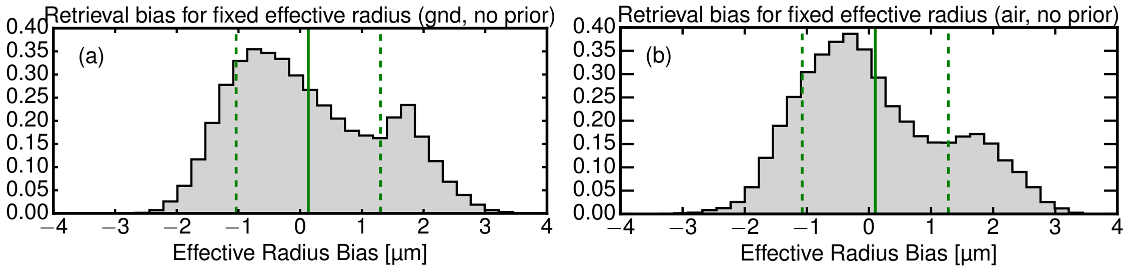

Figure 4.41: Retrieval deviations (retrieved $r_{eff,retr}$ - true r_{eff}) for the 9 cloud sides with fixed effective radius profile **(a)** for the ground-based perspective and **(b)** for the airborne perspective. The green line shows the average bias in retrieved effective radius $r_{eff,retr}$, the green dashed lines the root mean square error for $r_{eff,retr}$.

Overall, the analysis showed no significant difference in retrieval performance between the ground-based and the airborne perspective. The only difference was found for the flipped effective radius profiles where the correlation between the retrieved and the true effective radius was higher for the airborne perspective.

Statistic stability for perspectives not included in the ensemble

The last section tested the statistical retrieval for bias and investigated its statistic stability by using cloud side scenes that were already used during the lookup table creation. In the following section, the retrieval will be checked for potential overfitting by applying the retrieval to unknown cloud side scenes that were not used during the lookup table creation. To that end, five new cloud side perspectives were selected for which suitable cloud side observation locations (x, y) were determined using the field of view kernel convolution method described in Section 4.2.1. While the forward ensemble contains viewing azimuths of 45°, 135°, 225° and 315°, these new cloud side perspectives were chosen for new viewing azimuths of 0°, 90°, 180° and 270°. The corresponding time slots, viewing azimuths φ and solar zenith angles ϑ_0 can be found in Table A.2. Since the retrieval bias was already tested in the last section, only normal effective radius profiles were used this time.

Figure 4.42 shows one of these new cloud side scenes (12 h 40 min LT, $\varphi = 0°$, $\vartheta_0 = 65°$) with Figures 4.42a and 4.42b for the ground-based perspective and Figures 4.42c and 4.42d for the airborne perspective. Figure 4.43 compares the result of the statistical retrieval with the true effective radius for the scene shown in Figure 4.42. Again, the retrieved mean effective radius is shown in the right panels (Figures 4.43c and 4.43f) which is compared to the true effective radius shown in the left panels (Figures 4.39a and 4.43d). The center panels (Figures 4.43b and 4.43e) show mean vertical profiles (lines) and their spatial standard deviation (shaded areas) for the true (black) and the retrieved (green) effective radius. Both, the ground-based retrieval (Figure 4.43b) and the airborne retrieval (Figure 4.43e) detect the effective radius profile quite well as the true values for r_{eff} remain within the retrieval error estimate $\sigma(r_{\mathrm{eff}})$ shown by the green errorbars. For the whole scene, the retrieval overestimates r_{eff} by 0.03 µm (RMSE: 1.06 µm) for the ground-based case (Figure 4.43c) and by 0.07 µm (RMSE: 0.92 µm) for the airborne case (Figure 4.43f).

The comparison for all cloud sides, that were not included in the lookup table, is shown in Figure 4.44. For the ground-based cases, around 77,000 pixel went into the 2D histogram (Figure 4.44a), showing a correlation coefficient of 0.76

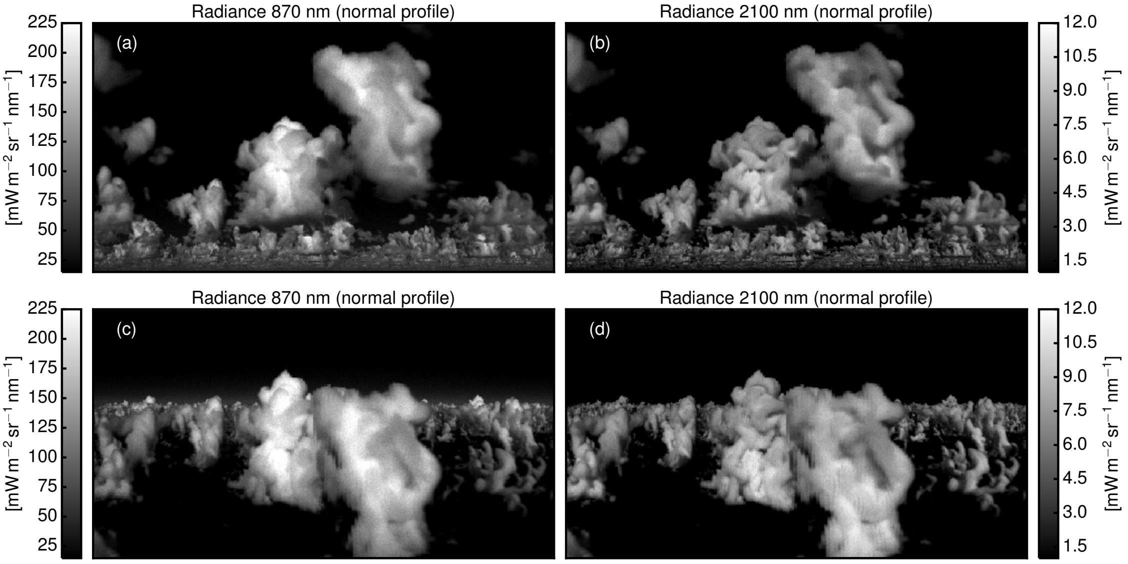

Figure 4.42: Ground-based (a,b) and airborne (c,d) retrieval test case with normal effective radius profile for a cloud side scene that was not included in the forward ensemble. **(a)** Spectral radiance at 870 nm and **(b)** at 2100 nm for the ground-base perspective, **(c)** Spectral radiance at 870 nm and **(d)** at 2100 nm for the airborne perspective

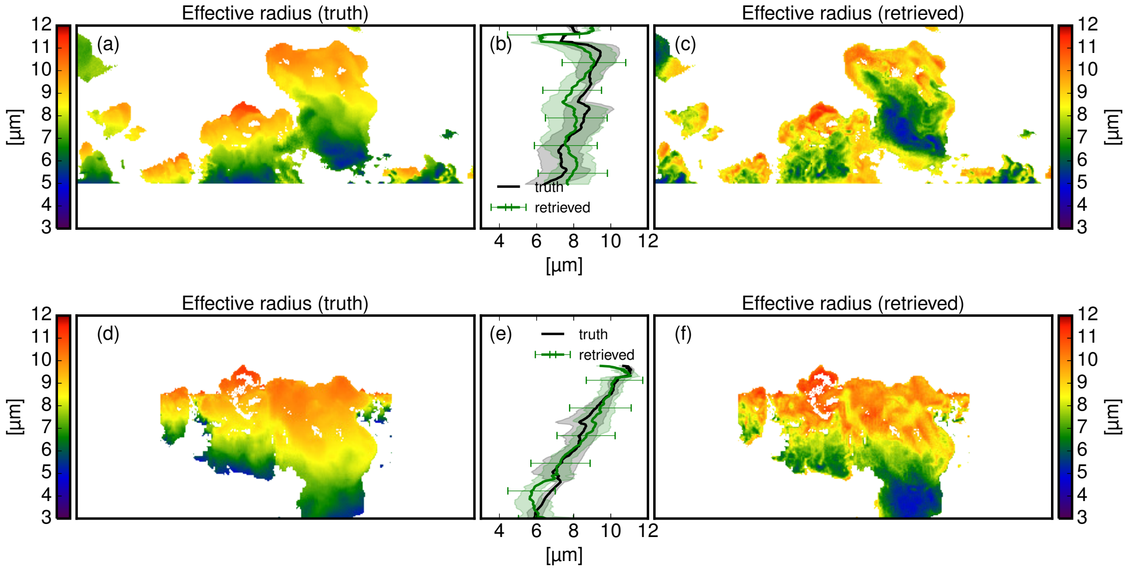

Figure 4.43: Retrieval comparison between the true effective radius (left) and the retrieved mean effective radius (right) for the cloud scene shown in Figure 4.42 that was not included in the forward ensemble, **(a)** Apparent effective radius $\langle r_{\text{eff}} \rangle_{mc}$ for the ground-base perspective, **(b)** Mean and standard deviation of the true (black) and retrieved (green) vertical effective radius profile, **(c)** Retrieved mean effective radius for the ground-base perspective, **(d)** Apparent effective radius $\langle r_{\text{eff}} \rangle_{mc}$ for the airborne perspective, **(e)** Mean and standard deviation of the true (black) and retrieved (green) vertical effective radius profile, **(f)** Retrieved mean effective radius for the airborne perspective.

between the retrieved $r_{\text{eff,retr}}$ and the true effective radius r_{eff}. The correlation for the airborne cases is even better with 0.78, where around 339,000 pixel are compared in Figure 4.44b.

For both perspectives, the statistical retrieval reliably detected the present effective radius profile without introducing any significant bias. With nearly the same correlation coefficient, the retrieval performance remains the same when faced with unknown cloud side scenes. It can therefore be concluded that the retrieval is not trained only for the included cloud side scenes. Rather, is represents the statistical relationship between reflected radiance and cloud droplet size for this cloud ensemble.

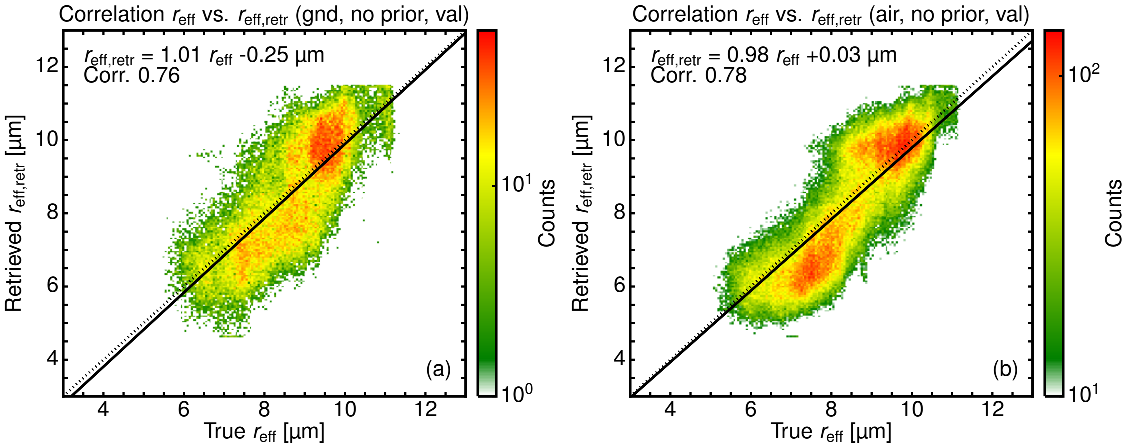

Figure 4.44: 2D histograms and linear regressions to determine the correlation between the true effective radius r_{eff} and the retrieved effective radius $r_{eff,retr}$, **(a)** for the ground-based perspective and **(b)** for the airborne perspective for the not included cases with normal effective radius profile.

CHAPTER 5

Design and characterization of specMACS

The previous chapter discussed uncertainties and influences which affect the sensitivity of solar reflectance from cloud sides to effective droplet radii. To measure the spectrally-resolved radiance from cloud sides a new instrument will be introduce in the following. As no suitable instrument was available so far, the setup and characterization of this new instrument is a significant part of this thesis. In particular, this chapter will investigate the radiometric accuracy of this measurement concept. The radiometric uncertainties should be substantially lower compared to the ambiguities in the radiative transfer to preserve the remaining sensitivity on cloud droplet size.

The following Sections 5.1–5.5 were submitted to be published in the scientific journal *Atmospheric Measurement Techniques (AMT)*. It has already been published in the *Atmospheric Measurement Techniques Discussions (AMTD)* with the title *Design and characterization of specMACS, a multipurpose hyperspectral cloud and sky imager* (Ewald et al., 2015). This work was done in close cooperation with following co-authors: T. Koelling, A. Baumgartner, T. Zinner, and B. Mayer.

5.1 The hyperspectral imager specMACS

The new spectrometer of the Munich Aerosol Cloud Scanner (specMACS) is a multipurpose hyperspectral cloud and sky imager designated, but not limited, to investigations of cloud-aerosol interactions in Earth's atmosphere. With its high spectral and spatial resolution, the instrument is designed to measure solar radiation in the visible and shortwave infrared region that is reflected from, or transmitted through clouds and aerosol layers. It is based on two hyperspectral cameras that measure in the solar spectral range between 400–2500 nm with a spectral bandwidth between 2.5–12.0 nm. During the thesis project, the instrument was operated in ground-based campaigns as well as aboard the German High Altitude LOng Range (HALO) research aircraft, e.g. during the ACRIDICON-CHUVA campaign in Brazil during summer 2014.

This section describes the *specMACS* instrument hardware and software design and characterizes the instrument performance. During the laboratory characterization of the instrument the radiometric response as well as the spatial and spectral resolution was assessed. Since the instrument is primarily intended for retrievals of atmospheric quantities by inversion of radiative models using measured radiances, a focus is placed on the determination of its radiometric response. Radiometric characterization was possible for both spectrometers with an absolute accuracy of 3 % at their respective central wavelength regions. First measurements are presented which demonstrate the application possibilities. They show that key demands are met regarding the radiometric and spectral accuracy which are required for the intended remote sensing technique.

5.1.1 Motivation

There exist some imaging spectroscopy instruments for the ground-based or airborne remote sensing perspective. In the visible wavelength range, one of the earliest instruments was the Compact Airborne Spectrographic Imager (CASI, *Babey and Anger* (1989)) with 288 spectral channels (2.5 nm resolution). Over the years, CASI measurements were used in various applications in atmospheric sciences. Naming only a few, *Wendling et al.* (2002) investigated aerosol-radiance interactions, *Mayer et al.* (2004) determined water cloud droplet size distributions using the backscatter glory and *Zinner and Mayer* (2006) assessed retrieval biases due to inhomogeneity of stratocumulus clouds. Further cloud remote sensing applications were done with the AisaEAGLE instrument from SPECIM, which covers the spectral range between 400–970 nm with a spectral resolution of 2.9 nm. From the ground-based perspective, *Schäfer et al.* (2013) retrieved cirrus optical thickness and ice crystal shape, while *Bierwirth et al.* (2013) and *Schäfer et al.* (2015) used the instrument to retrieve optical thickness and effective radius of Arctic boundary-layer clouds from the airborne nadir perspective. The Airborne Visible/InfraRed Imaging Spectrometer (AVIRIS, *Green et al.* (1998)) extended the measurement range into the shortwave infrared spectrum with 224 spectral channels (10 nm resolution) between 400–2500 nm. *Gao et al.* (1993) used it to detect cirrus clouds using the information in the near-infrared, while *Thompson et al.* (2015) used the higher spectral resolution (5 nm) with 600 spectral channels of AVIRIS-NG for the remote detection of methane. A further imaging spectroscopy instrument is the Airborne Prism EXperiment (APEX) imaging spectrometer (*Itten et al.*, 2008, *Schaepman et al.*, 2015) with 532 spectral channels and a spectral resolution between 0.9–12.3 nm. Exploiting this high spectral resolution, *Popp* *et al.* (2012) used APEX for high-resolution remote sensing of NO2. With 1056 spectral channels in the 400–2500 nm spectral region, the *specMACS* instrument continues the development of atmospheric radiation measurements towards imaging spectroscopy.

As commercially available spectral imagers for measurements in the solar visible and near-infrared spectrum become more and more affordable they become more frequently used nowadays. For airborne remote sensing of land surfaces a few, still costly commercial solutions are available at the moment. Based on spectral off-the-shelf camera systems, the Meteorological Institute of the University of Munich decided to tailor a system to its specific needs. In the following this new hyperspectral imaging instrument for atmospheric measurements on ground-based and airborne platforms with a spectral coverage of 400–2500 nm will be introduced and characterized in detail. On the basis of some first applications the scientific data obtained with the *specMACS* instrument will be introduced.

5.1.2 Accuracy considerations

The complexity of cloud geometry and three-dimensional radiative effects related to it pose a great challenge to cloud side remote sensing. Various studies of *Marshak et al.* (2006a), *Varnai and Marshak* (2002b) and *Zinner and Mayer* (2006) quantified the impact of three-dimensional radiative effects on particle size retrievals based on 1D radiation transfer simulations like *Nakajima and King* (1990) and found an overestimation of effective radius by up to 2 µm (*Cornet et al.*, 2005) with a standard deviation of 1.5 µm (*Bréon and Doutriaux-Boucher*, 2005). Especially for spatially highly resolved cloud side measurements (<100 m) standard deviations to the true effective radius can be 20 % and more (*Zinner and Mayer*, 2006).

The proposed retrieval method by *Martins et al.* (2011) and *Zinner et al.* (2008) tries to account for this uncertainty by means of a statistical retrieval based on fully 3-D radiative transfer simulations. For optically thick liquid water clouds an uncertainty in effective radius of 2 µm relates roughly to a radiance uncertainty of 20 % at the near-infrared wavelength 2100 nm used in the retrieval of (*Nakajima and King*, 1990). To limit the uncertainty in microphysical retrievals due to sensor characteristics, we aim for an absolute radiometric calibration uncertainty well below the retrieval uncertainty.

Spectral accuracy requirements are not too strict for current microphysical cloud retrievals, as no sharp absorption line is evaluated. However, the solar spectrum itself exhibits many narrow absorption lines. For this reason, the spectral accuracy should be comparable or better than the spectral bandwidth of the instrument. The radiometric accuracy can be compromised if resolved absorption lines are spectrally misaligned. Furthermore, measurements of accurate and highly resolved spectra are invaluable for the application of novel retrieval techniques since various spectral atmospheric and soil features become exploitable. High spectral resolution measurements are needed in the VNIR spectral range where many narrow absorption features are located, e.g., for photon path analysis using the optical depth of the oxygen A-band or for the detection of surface albedo influence on the basis of known spectral vegetation features. Conceivable use of the spectral data to estimate the oxygen A-band depth tightens spectral accuracy requirements to a few nanometer or less (*Fischer and Grassl*, 1991). As shown by *Heidinger and Stephens* (2000), the retrieval of the total column optical depth of the oxygen A-band is limited by the spectral resolution of the instrument.

This work is based on previous work which developed hyperspectral instruments and their calibration. The general principle of measurement and the specific implementation of the used hyperspectral instrument was developed and described in detail by *Aikio* (2001). *Jørgensen* (2002) examined this design and described necessary steps in its calibration, potential error sources and their mitigation. The overall approach to the calibration is based on the work of *Lenhard et al.* (2015) and was carried out in close cooperation with the Remote Sensing Technology Institute (IMF) of the German Aerospace Center (DLR).

This section is organized as follows: Section 5.2 first introduces the new *specMACS* instrument and its measurement principle. Next, all necessary technical amendments and software developments are introduced that make *specMACS* a versatile and accurate cloud remote sensing instrument usable for airborne push-broom applications as well as for ground-based cloud side or hemispheric scan. In Section 5.3 the methods used during characterization and calibration of the instrument are introduced and described. Following each subsection, detailed results of the radiometric and spectral sensor characterization are given and discussed. Finally application examples are shown, presenting the first airborne deployment of the instrument on-board HALO, the German high-altitude long range research aircraft (Section 5.4). Cloud side measurements were collected through a customized side window of the aircraft during the Brazilian-German ACRIDICON-CHUVA campaign in autumn 2014.

5.2 Measurement principle and instrument design

The spectrometer of the Munich Aerosol Cloud Scanner (*specMACS*) is an imaging spectrometer system for the measurement of solar radiation in the 400–2500 nm wavelength range, which is based on two hyperspectral cameras. It is designed for remote sensing of cloud and aerosol optical properties and atmospheric trace gases. The emphasis is on the development of new ground-based retrieval methods of clouds as well as on the understanding of 3-D radiative effects in existing retrieval methods. Key properties of the two imaging spectrometers that were determined in this work are given in Table 5.1. The instrument was developed at the Meteorological Institute of the Ludwig Maximilians University and is usually operated on the roof platform of the institute.

Figure 5.1: *specMACS* VNIR and SWIR sensors on scanning mount. The stray light protection is prominently visible in front of the sensors.

Table 5.1: Properties of the two SPECIM imaging spectrometers employed in *specMACS* for so-called visible near-infrared and shortwave infrared spectral ranges as characterized in this work. Here, FOV means the field of view of the complete spatial line, while IFOV denotes the instantaneous field of view of single pixels, which determines the spatial resolution along and across track.

	VNIR	SWIR
Detector	SiO2 CMOS	HgCdTe CMOS
Spectral range	417–1016 nm	1015–2496 nm
Spectral bandwidth	typ. 2.5–4 nm	typ. 7.5–12 nm
FOV	32.7 °	35.5 °
IFOV (across track)	typ. 1.4 mrad	typ. 3.8 mrad
IFOV (along track)	typ. 2.0 mrad	typ. 1.8 mrad
Spatial Pixels	1312	320
Spectral Channels	800	256
Radiometric quantization	12 bit	14 bit
Usable dynamic range	9.5 bit	typ. 11–11.6 bit
Max. frame rate	145 Hz	103 Hz
Temp. Control	uncooled	200 K

5.2.1 Instrument concept

The instrument comprises two commercially available hyperspectral line spectrometers built by SPECIM (Specim Spectral Imaging Ltd., Oulu, Finland.). Combined, these hyperspectral cameras simultaneously acquire light spectra between

400–2500 nm for one spatial dimension. The measurement principle is based on the diffraction of a light beam by a Volume Phase Holographic (VPH) Transmission Grating after one spatial dimension has been filtered by an entrance slit (≈ 30 µm for both spectrometers) as shown in Figure 5.2. After the grating, the spatial variations of the radiant flux are captured on one dimension of an CMOS active pixel sensor (APS) (*Fossum*, 1997) while the spectral variations are registered on the other dimension. An order blocking filter (OBF) is mounted just in front of the APS to prevent spectral overlap of different diffraction orders. A detailed description of the measurement principle and the specific implementation of the used hyperspectral instrument can be found in *Aikio* (2001).

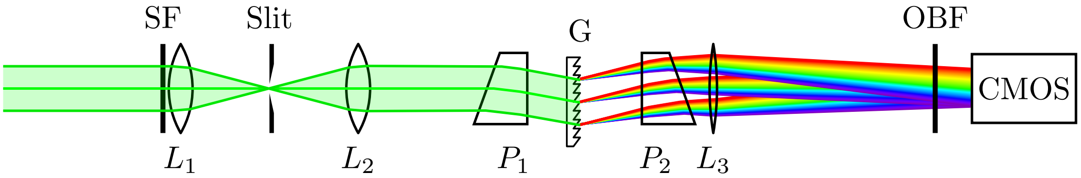

Figure 5.2: Optical concept of hyperspectral imagers. Sketch of the light path entering the instrument as it first gets spatially filtered by a slit and subsequently separated by a holographic grating: SF ~ Spectral Flattening Filter, L_1 ~ Front optics, L_2 ~ Collimator, P_1 ~ Entry Prism, G ~ Volume Phase Holographic Transmission Grating, P_2 ~ Exit Prism, L_3 ~ Focuser, OBF ~ Order Blocking Filter, CMOS ~ Imaging Sensor.

5.2.2 VNIR spectrometer

The spectral camera PFD (SPECIM SP-PFD-CL-65-V10E) is used for the coverage of the visible and near-infrared wavelength range (400–1000 nm) (which in the following is referred to as the visible near-infrared, VNIR). It is equipped with a 18.5 mm f/2.4 front lens (OLE18.5). Inside the spectrograph (ImSpector V10E) the entrance slit, the collimating optics, the PGP-element and the focusing optics are firmly connected together. Its linear dispersion is specified with 97.5 nm mm^{-1}. In front of the sensor region corresponding to longer wavelengths originating from first order $m = -1$ diffraction an order blocking filter (SPECIM OBF 570) is placed to prevent light of shorter wavelengths from second order $m = -2$ diffraction to reach the sensor. The sensor is based on a camera (MV1-D1312-160) from Photonfocus, which is built around the monochrome, uncooled CMOS active pixel sensor (A1312). This sensor is backside-illuminated to increase its low-light performance. It provides a resolution of 1312 × 800 pixels with a pixel distance on chip (pixel pitch) of 8 µm × 8 µm and an active optical area of 10.48 mm × 8.64 mm. The field of view (FOV) along the spatial line is 32.7°, while the instantaneous field of view (IFOV) for a single pixel is 1.37 mrad across and 2.00 mrad along the spatial line. The entrance slit width of 30 µm limits the average spectral resolution to 3.1 nm with an average spectral sampling of 0.8 nm.

Due to noise, the usable dynamic range for a single frame of the VNIR camera is approximately 9.5 bit. Further parameters can be found in Table 5.1.

5.2.3 SWIR spectrometer

For the wavelength region between 1000–2500 nm the SWIR spectrometer (SPECIM SP-SWIR-LVDS-100-N25E) is used (which in the following is referred to as the shortwave infrared, SWIR). It is equipped with a 15 mm f/2.1 front optic lens (OLES15). Since the solar radiance decreases strongly from 1000 to 2500 nm the usable dynamic range over the complete wavelength range would be very limited. A spectral flattening filter (Hebo RC 01, SPECIM) is therefore placed in front of the lens to attenuate the shorter wavelengths and thereby improve the overall use of the dynamic range of the sensor for solar radiation. This filter has an additional special coating to block the wavelength range from 800–960 nm since the SWIR sensor is sensitive from 800 nm onwards and since these wavelengths cannot be filtered by an order sorting filter. The linear dispersion of its spectrograph (ImSpector N25E) is specified with 208 nm mm^{-1}. Similar to the VNIR, an order blocking filter (OBF 1400) is placed in front of the SWIR sensor to prevent spectral overlap from different diffraction orders. The SWIR spectrometer uses the MARS SW 320 × 256 sensor from SOFRADIR with a pixel pitch of 30 µm. The HgCdTe-based detector is thermoelectrically cooled to 200 K to reduce the level of dark current noise. The FOV along the spatial line is 35.5 ° while the IFOV is 3.79 mrad across the spatial line and 1.82 mrad along the spatial line. The entrance slit width of 30 µm limits the average spectral resolution to 10.3 nm with an average spectral sampling of 6.8 nm. Due to the strongly varying dark signal, the noise-limited usable dynamic range for a single frame of the SWIR camera varies in the range of 11–11.6 bit, depending on integration time and environment conditions. More detailed information is given in Section 5.3.1. Further parameters are listed in Table 5.1

5.2.4 Stray light protection

Both, the VNIR and the SWIR sensor are affected by stray light, however the effects on the SWIR sensor are typically a few times larger than on the VNIR. In Figure 5.3, the effect of stray light and its mitigation is shown using a prototype of the actual stray light protector. To mitigate the effects of stray light permanently, a system of shielding baffles which are placed in front of the cameras optics (Figure 5.4) was designed. The stray light protector was built of aluminium which was sandblasted, anodized and painted with NEXTEL Velvet Black paint. According to *Dury et al.* (2007), the regular and diffuse single scattering reflectance of this coating is typically less than 5 % in the whole spectral range of both spectrometers. Simulations showed that these baffles attenuate incident light that originates from angles more than 15 ° outside the FOV by at least 2–3 orders of

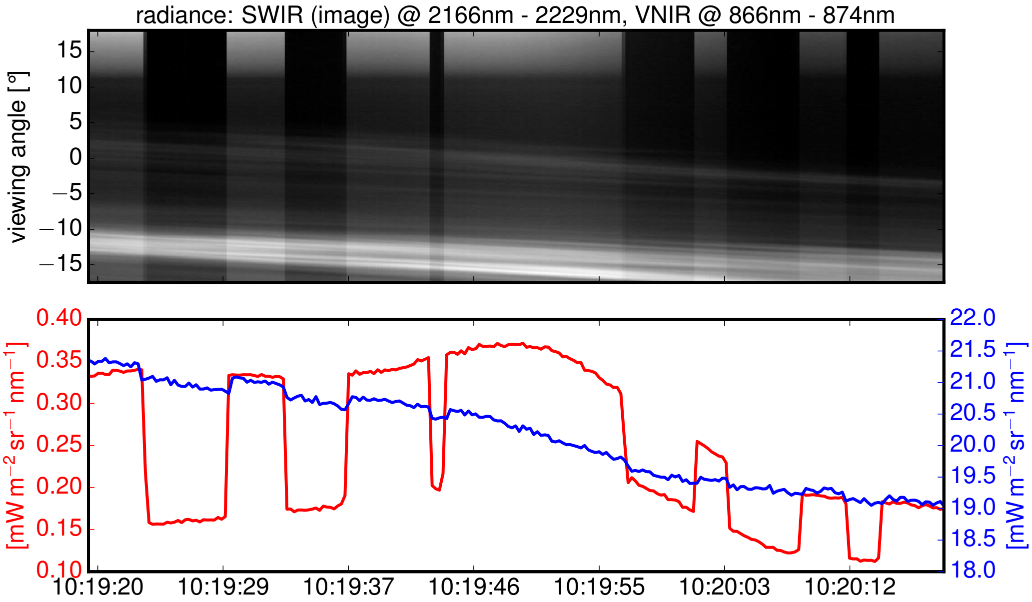

Figure 5.3: The top image shows a zenith pointing scene as captured with the SWIR camera. During the capture, stray light has been repeatedly shielded from the sensors with a prototype of the now permanently installed stray light protection. Due to the faint cloud cover, the radiance from inside the nominal field of view is very small and the stray light effect becomes very obvious. The lower plot shows the radiance averaged over the full field of view of the SWIR and VNIR sensors in blue and red respectively. On both sensors, a stray light effect and its mitigation is visible, however the effect on the VNIR is much less pronounced.

magnitude. After implementing the stray light protection, no visible evidence of stray light was found during ground measurements with the sun outside the FOV by more than 15 °.

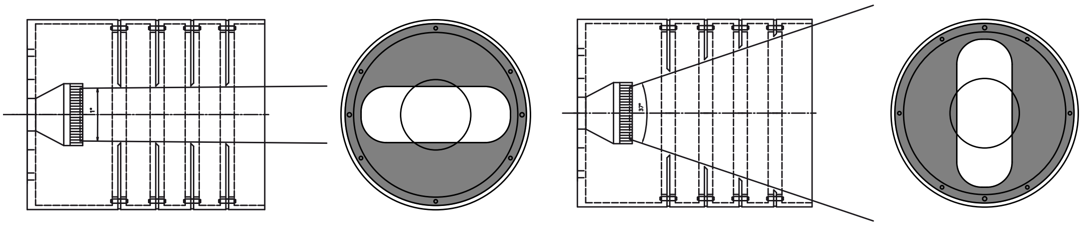

Figure 5.4: Design of stray light protection. Left: cut along spectral axis, right: cut along the spatial axis. The baffles have a length of 160 mm and a diagonal of 125 mm.

5.2.5 Instrument automation

The *specMACS* hyperspectral imager is a multipurpose measurement system, which produces data at a rate of up to $300\,\mathrm{MiB\,s^{-1}}$ and which must be stored reliably on disk. Furthermore, the system must be autonomous. This applies in particular to an airborne deployment with limited operator availability.

During ground-based scans or unsupervised airborne operation the integration time t_{int} has to be be adjusted to avoid over- as well as underexposure. Furthermore, frequent dark frame measurements are necessary since the dark current signal of the SWIR sensor varies strongly with integration time and ambient air temperature. For this reasons, a control software automatically sets integration time and controls dark frame measurements, potentially resulting in additional (non-instantaneous) 5.6 bit of dynamic range for each sensor. Details of the automated control software are described in detail in Appendix A.2.

In order to control and repeat complex measurement tasks, the CAMPaign ASsistant (CAMPAS) was developed. It is a domain specific scripting language combined with a communication library which has access to all system components. Using CAMPAS the user can define measurement tasks like a hemispherical scan through step-by-step instructions These instructions control the behavior of the sensors, the scanning mount and all other system components combined. The CAMPAS system furthermore provides simple access to various dynamic coordinates (e.g. sun position or the current position of other instruments). Thus a general task can be written once and repeated many times, which increases comparability of results.

5.3 Characterization and calibration methods

There are three essential characteristics which define the overall performance of imaging spectrometers. First, the radiometric response of the instrument has to be known to obtain absolute radiometric measurements. Secondly, a precise knowledge about the spectral projection onto the sensor is required for a correct radiometric registration. Concluding, information about the spatial projection and its geometric distortions are required to asses the spatial image quality and its resolution. In contrast to the stable sensor characteristics, faster varying data, like sensors settings, orientation and dark signal need to be captured during measurement. Using this information, measured raw data can be converted into physical units during the calibration procedure. A guideline through the whole process and the involved quantities is given by the calibration flow chart in Figure 5.5. The process follows *Lenhard et al.* (2015) closely and is extended by a nonlinearity correction regarding integration time explained in Section 5.3.1. The following subsections will cover each of the displayed steps.

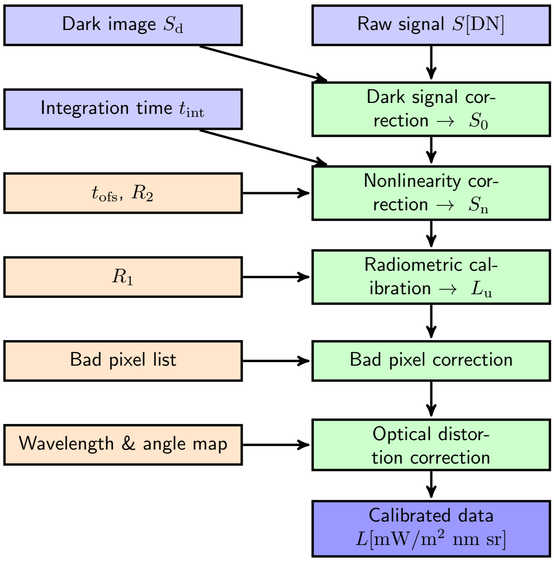

Figure 5.5: Schematic calibration using the newly developed nonlinearity correction. Light blue boxes are measured data, orange boxes are characterization data, green boxes are calibration steps and dark blue is the calibrated data.

In the following, all variables are given as pixel-wise properties when not mentioned otherwise. Temporal averaged properties of the sensor will be identified with angle brackets while spatial averages will be indicated with an overbar. The laboratory characterization of the *specMACS* sensors was performed at the Calibration Home Base (CHB) (*Gege et al.*, 2009) of the Remote Sensing Technology Institute of the German Aerospace Center.

5.3.1 Radiometric characterization

The sensors consist of independent pixels of which each acts as a radiance sensor for its specific spectral and spatial section of the full image. For this reason, pixel sensors are subject to inter-pixel variations caused by imperfections in the sensor material and electronics. These variations are almost constant in time but become evident on uncorrected images as visible noise pattern. This pattern is generally called fixed pattern noise (FPN) and can be mitigated through calibration using characterized parameters determined in the following sections. Long term variations of the FPN can be covered through periodic recharacterization of the sensor.

Each pixel outputs the measured signal as a digital number (DN). To obtain an absolute radiometric value the sensor has to be calibrated since its signal is subject to influences other than the impinging light. The sensor signal S can be modeled as a sum of a radiometric signal S_0 containing only radiance information, S_d which describes the dark signal of the sensor and the noise $\mathcal{N}$ of the sensor:

$$S = S_0 + S_d + \mathcal{N} \tag{5.1}$$

In the following, subsections dark signal S_d, radiometric signal S_0 and noise $\mathcal{N}$ will be independently examined. In the remaining subsections optical performance like angular and spectral bandwidth as well as keystone effects will be discussed.

Dark signal

Inherent to all electronic imaging sensors is the dark signal S_d. It is a pixel dependent offset and its variation between pixels is often described as dark signal non-uniformity. The total signal S is composed of the photoelectric signal S_0, a dark signal S_d and the remaining noise $\mathcal{N}$ (Equation 5.1). When the shutter is closed and the photoelectric signal S_0 becomes zero by definition, an averaged dark frame $\langle S_d \rangle$ with very small remaining noise (as $\langle \mathcal{N} \rangle \rightarrow 0$) can directly be measured:

$$\langle S \rangle = \langle S_0 + S_d + \mathcal{N} \rangle = \langle S_d \rangle + \langle \mathcal{N} \rangle \approx \langle S_d \rangle \tag{5.2}$$

The dark signal S_d is further composed of the dark current signal $S_{dc} = s_{dc} t_{int}$ and a readout offset S_{read}:

$$S_d = s_{dc} t_{int} + S_{read} \tag{5.3}$$

The dark current s_{dc} originates from thermally generated electrons and holes within the semiconductor material. Since the electrons are randomly generated over time, the dark current signal S_{dc} increases linearly with s_{dc} and integration time t_{int}. The remaining offset S_{read} is caused by the readout process and is therefore independent from t_{int}.

The dark signal $S_d(t_0)$ of an illuminated frame at time t_0 is estimated through linear interpolation of averaged dark frames $\langle S_d(t_{-1}) \rangle$ and $\langle S_d(t_1) \rangle$ measured at t_{-1} before and t_1 after the image frame:

$$\langle S_d^*(t_0) \rangle = (1 - w) \langle S_d(t_{-1}) \rangle + w \langle S_d(t_1) \rangle \qquad \text{with:} \quad w = \frac{t_0 - t_{-1}}{t_1 - t_{-1}} \tag{5.4}$$

The photoelectric signal $S_0(t_0)$ (including the remaining noise $\mathcal{N}$) can then be estimated using the interpolated dark frame $\langle S_d^*(t_0) \rangle$:

$$S_0(t_0) + \mathcal{N} = S(t_0) - S_d(t_0) \approx S(t_0) - \langle S_d^*(t_0) \rangle. \tag{5.5}$$

Hereby, the linear interpolation leads to a dark signal uncertainty

$$\sigma_d(t_0) = \sqrt{\sigma_d^2(t_{0-})(1 - w) + \sigma_d^2(t_{0+}) w}. \tag{5.6}$$

This uncertainty results from standard deviations $\sigma_d(t_{+1})$ and $\sigma_d(t_{-1})$ of the individual dark signal averages at t_{-1} and t_1 in combination with an upper estimate for the dark signal drift $\Delta\overline{S_d}$ projected forward from t_{-1} and backward from t_1 to time t_0:

$$\begin{aligned} 2\sigma_d^2(t_{0-}) &= 2\sigma_d^2(t_{-1}) + \left(\Delta\overline{S_d}(t_0 - t_{-1})\right)^2 \\ 2\sigma_d^2(t_{0+}) &= 2\sigma_d^2(t_1) \quad + \left(\Delta\overline{S_d}(t_1 - t_0)\right)^2 \end{aligned}$$

To specify this uncertainty for actual measurements, the following analysis will investigate the dark signal characteristic, e.g. the maximal dark signal drift, of both sensors.

The dark signal analysis was done under controlled laboratory conditions during calibration within the CHB facility as well as on one flight during the ACRIDICON-CHUVA campaign. In order to suppress the noise during lab analysis, 500 consecutive dark frames were averaged. Dark frames were measured for 9 different integration times while ambient air temperatures were held constant by air-conditioning. During the measurements the temperature in the VNIR casing remained stable at 312.0 K. Since the SWIR camera is not equipped with a temperature sensor the VNIR temperature has been used as a proxy.

For the analysis during the flight only 30 consecutive dark frames were averaged to minimize gaps between radiometric measurements. Analysis of mean dark signal levels $\overline{S_d}$ in flight over all pixels was done for both spectrometers using integration times t_{int} of 5, 8, and 12 ms. During the 6 h flight the ambient air temperature was gradually changing due to the cabin air-conditioning system. This led to fluctuating VNIR casing temperatures between 312.4 and 320.6 K.

The analysis of the dark signal shows clear differences between the sensors used for the VNIR and the SWIR spectrometer. Figure 5.6 (right) shows mean dark signal levels $\overline{S_d}$ in available digital number range when averaging over 30 dark frames as measured during a flight of the aircraft campaign ACRIDICON-CHUVA. The green curve shows the readings from a temperature sensor located within the casing of the VNIR spectrometer. While the level of $\overline{S_d}$ for the SWIR depends on integration time t_{int} as well as on temperature, the level of $\overline{S_d}$ for the VNIR appears to be independent from t_{int} and temperature. Maximal dark current drifts $\Delta\overline{S_d}$ of 30 DN/min were found for the SWIR, while $\Delta\overline{S_d}$ remained below 6 DN/min for the VNIR. In the following, these values will be used as upper estimate in the calculation of the 2σ error of the dark signal in Equation 5.6.

A more in-depth analysis of the dark signal behavior is shown in Figure 5.6 (left) where measurements of S_d in a controlled lab environment (CHB) are compared with measurements of S_d during the flight. The slope of the regression line reflects the dependence of $\overline{S_d}$ on t_{int} while the shaded area shows the influence of temperature on this relationship. In Figure 5.6 (left) the non-uniformity of S_d is shown by error bars, which is only significant for the SWIR. With temperature

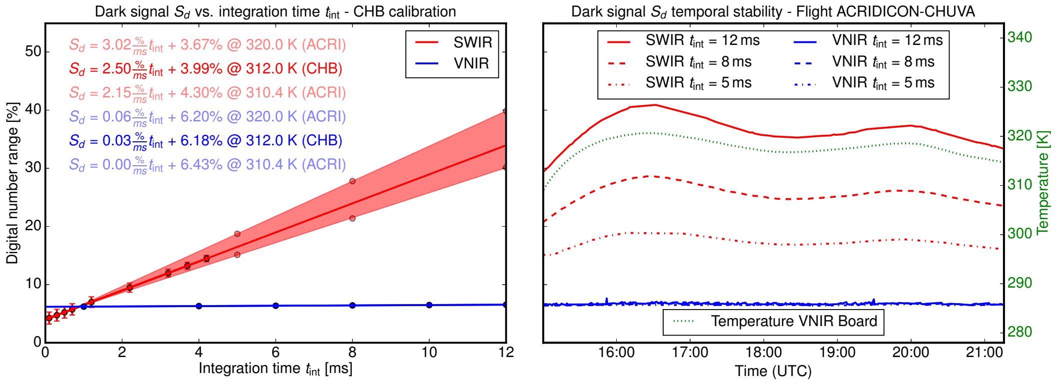

Figure 5.6: (left) Mean dark signal levels $\overline{S_d}$ in DN as a function of integration time t_{int} when averaging over 500 dark frames as observed during the CHB calibration. (right) $\overline{S_d}$ when averaging over 30 dark frames as observed on one flight AC14 (21 September 2014) during the ACRIDICON-CHUVA campaign. The blue lines show $\overline{S_d}$ for the VNIR, red lines for the SWIR spectrometer while the different linestyles denote different integration times. The green curve shows the temperature as measured within the VNIR casing. In both plots the dependence of $\overline{S_d}$ from temperature and integration time becomes clearly visible for the SWIR, while $\overline{S_d}$ remains constant for the VNIR.

increasing from 310.4 to 320.0 K the number of thermally generated electrons per second increases from 352 DN ms^{-1} to 494.0 DN ms^{-1} for the SWIR sensor. In this temperature range the VNIR sensor shows only a marginal influence on dark signal levels. In contrast, a considerable amount of dynamic range is lost to the dark signal for the SWIR.

For the VNIR, there is mainly a fixed dark signal offset independent of t_{int}. Since thermally generated electrons do not play an important role in dark signal generation within the VNIR sensor the independence of S_d from t_{int} and temperature is evident. In order to push the dark signal below the photoelectric signal the HgCdTe-based detector of the SWIR spectrometer has to be cooled down to 200 K. Although the SWIR sensor is equipped with a thermoelectric cooler the dark signal S_d in Figure 5.6 is obviously still influenced by air temperature fluctuations.

Additionally, dark signal offsets S_{read} exhibit a slight dependence on temperature in both spectrometers. The offsets S_{read} between both sensors differ fundamentally with respect to their pixel-wise distribution and the fixed pattern noise they are creating. Figure 5.7 shows the noticeable uneven fixed pattern noise FPN^{SWIR} of the SWIR sensor. While FPN^{VNIR} appears smooth with $\sigma_{FPN}^{VNIR} = 9.4$ DN the spatial distribution of FPN^{SWIR} is very uneven with $\sigma_{FPN}^{VNIR} = 173.8$ DN. Bad pixels that were excluded in this analysis are also shown.

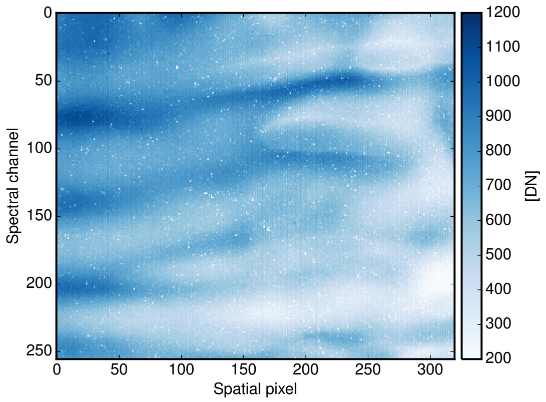

Figure 5.7: Extrapolated fixed pattern noise $\mathrm{FPN}_{\mathrm{SWIR}}$ in time at integration time $t_{\mathrm{int}} = 0\,\mathrm{s}$ for the SWIR spectrometer. The measurements were done with closed shutter at multiple integration times and reduced to $t_{\mathrm{int}} = 0\,\mathrm{s}$ by linear regression.

Nonlinear radiometric response

The photoelectric signal $\tilde{S_0}$ from a perfectly linear sensor with response R should scale linearly with the set integration time t_{set} and radiance L:

$$\tilde{S_0} = RLt_{\mathrm{set}} = s_n t_{\mathrm{set}} \tag{5.7}$$

Accordingly, there exists an unambiguous normalized signal $s_n = RL$ independent from camera settings for each radiance value L. However, measurements of constant radiance levels originating from a large integrating sphere (*LIS*) with various integration times (see Table 5.2) have shown deviations from this idealized linear model. This deviation between the idealized signal $\tilde{S_0}$ and the actually observed signal S_0 is called photo response non-linearity. Figure 5.8a and Figure 5.8b show the found deviations of the VNIR and SWIR from the idealized linear model (Equation 5.7). Here, the photoelectric signal S_0 of the same stabilized light source (*LIS*) should become invariant after normalization with the set integration time t_{set}. The fit of the original VNIR signal s_n (gray line, Figure 5.8a) shows a photo response non-linearity, which is visible at higher signal levels by lower DN for $t_{\mathrm{set}} = 12.0\,\mathrm{ms}$ compared with $t_{\mathrm{set}} = 2\,\mathrm{ms}$. By contrast, the fit of the original SWIR signal s_n (gray line, Figure 5.8b) is almost linear but is insufficiently normalized when using the set integration time t_{set}. To obtain absolute radiance values, the photoelectric signal S_0 has to be linearized first before the absolute radiometric response can be applied. In the following, the different deviations of both sensors from the linear model (Equation 5.7) will be analyzed in detail.

We identified two effects which together explain the observed nonlinearities very well. According to *Janesick* (2007), the diode capacitance of CMOS detectors can increase significantly as charge collects. Thereby, the sensor specific conver-

Table 5.2: Integration times [ms] used for nonlinearity measurements with the large integrating sphere.

VNIR	1.0	2.0	4.0	6.0	8.0
	10.0	12.0	14.0	16.0	
SWIR	0.1	0.3	0.5	0.7	1.2
	2.2	3.2	3.7	4.2	

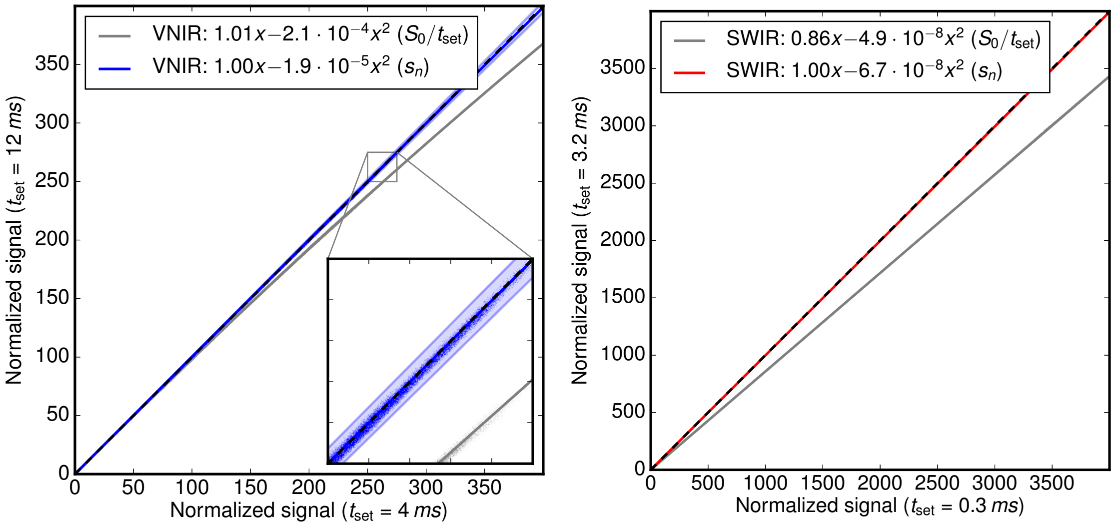

Figure 5.8: **(a)** Normalized signal s_n (gray line) of the stabilized light source (*LIS*), measured with the VNIR using two different integration times $t_{\mathrm{set}} = 4\,\mathrm{ms}$ and $t_{\mathrm{set}} = 12.0\,\mathrm{ms}$. The blue line shows the signal after the nonlinearity correction with the remaining nonlinearity uncertainty shown as blue filled area. The dotted line represents the response of a perfectly linear sensor following Equation 5.7. **(b)** Normalized signals s_n (gray line) of the stabilized light source (*LIS*), measured with the SWIR using two different integration times $t_{\mathrm{set}} = 0.3\,\mathrm{ms}$ and $t_{\mathrm{set}} = 3.2\,\mathrm{ms}$. The red line shows the signal after normalization using the corrected integration time $t_{\mathrm{set}} + 0.055\,\mathrm{ms}$. In both cases the dotted lines represents the response of a perfectly linear sensor following Equation 5.7.

sion gain k [DN] becomes a function of the number N of received photoelectrons. For higher signal levels this causes a nonlinear relationship between incoming radiance L and the photoelectric signal S_0. We considered this nonlinearity by adding a quadratic term to Equation 5.7, which leads to the form in Equation 5.8. Furthermore we found a small mismatch between the set integration time t_{set} and the actual integration time t_{int}. For this reason, an offset term t_{ofs} was added to be fitted in the model in Equation 5.8. The improved model which describes the observed photoelectric signal S_0 then reads:

$$S_0 = s_n(t_{set} + t_{ofs}) + \gamma\left(s_n(t_{set} + t_{ofs})\right)^2 \tag{5.8}$$

Here, γ is the nonlinearity of S_0 in DN^{-1} and t_{ofs} is the offset between actual and reported integration time. The model can be inverted to yield the normalized signal s_n from measured signal S, dark signal S_d and t_{set} when γ and t_{ofs} are known:

$$s_n = \frac{\sqrt{4\gamma(S - S_d) + 1} - 1}{2\gamma(t_{set} + t_{ofs})} \xrightarrow{\gamma \to 0} \frac{S - S_d}{t_{set} + t_{ofs}} \tag{5.9}$$

This nonlinear model converges to the linear model in Equation 5.7 for $\gamma \to 0$ and $t_{ofs} \to 0$.

Using the integration times in Table 5.2 and the model described in Section 5.3.1, the parameters γ and t_{ofs} were determined for every pixel. This was done for measurements taken on the large integrating sphere at the CHB facility on 3 July 2014 by regression of measured S_0 on Equation 5.8 using the least squares method. Since solar radiances are naturally very strong signals the model in Equation 5.8 was not designed to model effects at very low signal levels. For this reason the fit was only done for pixels with signal levels higher than 2 % of the maximum signal level. Mean and standard deviation of γ and t_{ofs} over the sensor are shown in Table 5.3. The fact that γ and t_{ofs} do not vary much across pixels allows to use a single value for each of them on the whole sensor for simplicity. As the agreement between the presented model and all measurements was very good, a possible further dependence of the model parameters on other parameters has been discarded.

For the VNIR camera the nonlinearity causes a deviation of 9 % from the linear model at maximum signal level while the SWIR camera does not exhibit a noticeable nonlinearity. In contrast t_{ofs} of the VNIR camera is negligible with 0.001 ms while the SWIR offset 0.055 ms lies within the same order of magnitude as the shortest possible integration time of 0.1 ms.

By using the found parameters γ and t_{ofs} in the nonlinear model (Equation 5.9), the linearized signal s_n of the VNIR is shown by the blue line in Figure 5.8a, while s_n of the SWIR is shown by the red line in Figure 5.8b. After the nonlinearity correction, the VNIR signal s_n better follows the linear model. Likewise, the corrected SWIR signal s_n now seems sufficiently normalized by using the additional integration time offset t_{ofs}.

The uncertainty in γ and t_{ofs} leads to a remaining nonlinearity uncertainty σ_{nonlin}. The maximum error due to this uncertainty was estimated by using the error boundaries of both parameters in Equation 5.9. Only the uncertainty in γ for the VNIR is of significance which is shown by the blue filled area in Figure 5.8a.

During this analysis, some alternative nonlinearity models have been tested in place of the existing nonlinearity parameterization, which is assumed to be a

Table 5.3: Nonlinearity γ and integration time offset t_{ofs} determined by fitting measurements to the model described in Equation 5.8.

sensor	γ [DN^{-1}]	t_{ofs} [ms]
VNIR	$(-2.3 \pm 0.3)10^{-5}$	-0.001 ± 0.01
SWIR	0	$+0.055 \pm 0.001$

function of total collected radiative energy ($\propto L \cdot t_{int} \propto s_n \cdot t_{int}$). A simpler model, considering only a quadratic term in t_{int}, was not able to provide similarly good results as the model presented above. Some combinations of quadratic or higher order terms in the form of $s_n^a \cdot t_{int}^b$ have also been tried, assuming equal nonlinear response of all pixels of one sensor and exploiting the intensity variations between pixels as introduced by the spectrograph. As the assumption of equal nonlinear response for all pixels has been found to hold true for the finally chosen model and neither of the alternate models showed better results, they have also been discarded. This behavior suggests, but is no evidence, that the signal is actually a nonlinear function of the total collected radiative energy and neither in t_{int} nor L alone.

Absolute radiometric response

After nonlinearity correction the normalized signal s_n in [DN ms^{-1}] can be converted into absolute radiance values L in [mWm^{-2}nm^{-1}sr^{-1}]. Using the absolute radiometric response R in [DN ms^{-1}mW^{-1}m^{2}nm sr], this can be described by

$$L = R^{-1} \cdot s_n. \tag{5.10}$$

R is different for each pixel and thereby also covers the correction of inter-pixel variations of the sensor response, also called photo response non-uniformity (PRNU). The absolute radiometric response R is determined once during a radiometric calibration with a known radiance standard.

In this work the absolute radiometric response R was characterized using the absolute RAdiance STAndard (*RASTA*) (*Schwarzmaier et al.*, 2012) of the IMF at DLR-EOC which was characterized with absolute radiance standards operated by the *PTB* (Physikalisch-Technische Bundesanstalt), the German National Metrology*specMACS* Institute. As the *RASTA* does not cover the full field of view of the sensors, a large integrating sphere (*LIS*) was additionally used as an isotropic light source. As determined by *Baumgartner* (2013), the output stability of the *LIS* is better than $\sigma = 0.02\,\%$ for a duration of 330 seconds.

To transfer the absolute radiance standard from the *RASTA* to the *LIS*, measurements of both light sources were performed in fast succession with pixels in the geometric center of the *specMACS* FOV. The absolute calibration of the *RASTA* can then be transferred to the *LIS* by using the ratio between the normalized signals $s_{n;LIS}$ and $s_{n;RASTA}$ measured at the integrating sphere and the absolute standard:

$$L_{LIS} = L_{RASTA} \cdot \frac{L_{LIS}}{L_{RASTA}} = L_{RASTA} \cdot \frac{s_{n;LIS}}{s_{n;RASTA}} \tag{5.11}$$

Simultaneously the calibration transfer was done with a second, independent spectrometer (SVC HR-1024i) to validate the transfer with the *specMACS* instrument. In Figure 5.9 the spectral radiance of the large integrating sphere is shown as it was transferred from the *RASTA* standard using Equation 5.11.

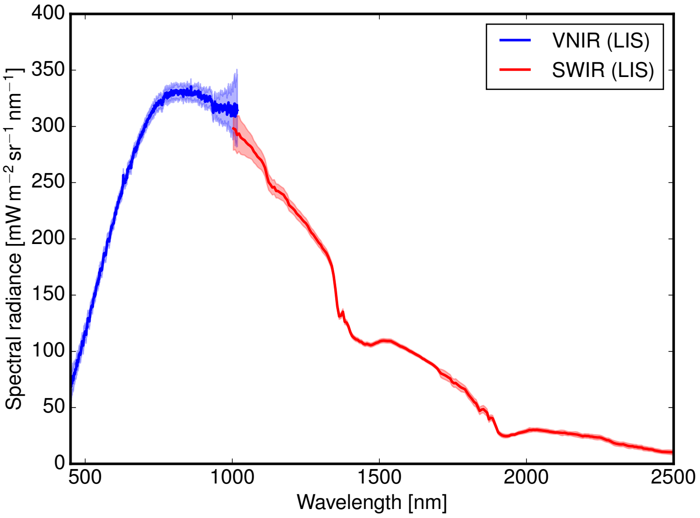

Figure 5.9: Reconstructed spectral radiance on top the large integrating sphere during the respective radiometric characterization. The absolute radiometric values were transferred from the *RASTA* base standard using the *specMACS* VNIR and SWIR sensors. The 2σ-uncertainty associated with the radiometric calibration is shown by the filled area.

With the *LIS* illuminating the complete FOV of the instrument the conversion from normalized signals to absolute radiances (R in Equation 5.10) is calculated for each pixel.

The absolute radiometric response R of the VNIR and the SWIR sensors are presented in Figure 5.10. Both sensors show strongly reduced sensitivity at the upper and lower boundaries of the spectrum, which is expected due to the nature of the material dependent band-gap and the transmissivity of the optical system. The VNIR sensor shows an etalon fringe pattern (seen in Figure 5.10(left) along the spectral dimension) typical for backside-illuminated sensors (*Marques Vatus and Magnan*, 2004), whereas the front-illuminated SWIR sensor does not exhibit significant patterns. The discrepancy between the found absolute radiometric responses R and the ones given by the manufacturer does not exceed more than 10 %.

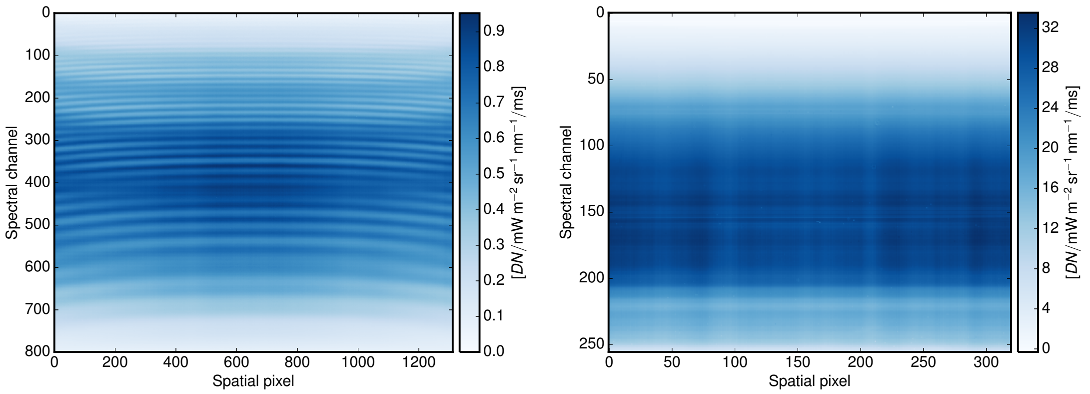

Figure 5.10: Absolute radiometric response R in [DN ms^{-1}mW^{-1}m^{2}nm sr] for the VNIR (left) and SWIR (right) spectrometer. The radiometric response shows a strong dependence with wavelength for both sensors, which is expected due to a material dependent band-gap and the specific transmissivity of the optical system. The VNIR sensor shows an etalon fringe pattern typical for backside-illuminated sensors.

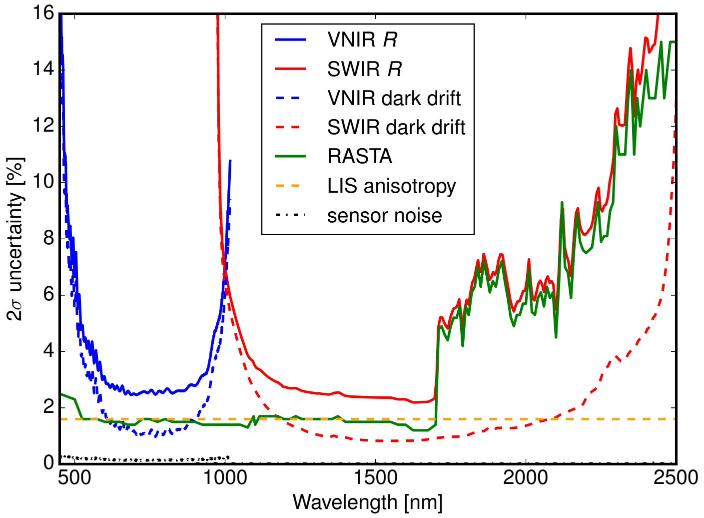

Figure 5.11: Main contributions to the 2σ-uncertainty of the absolute radiometric response R. The uncertainties resulting from sensor noise and dark current drift are exemplary shown for the *RASTA* measurements. Due to the lower radiance of the *RASTA*, other noise and drift components contribute less to the total error.

Using the nominal accuracies of the reference light sources and signal statistics derived from the sensors during characterization measurements, an error budget for the absolute radiometric response R was calculated and is shown as 2σ uncertainty in Figure 5.11. The uncertainty in the absolute radiometric calibration of the *RASTA* was given by the *PTB* and is indicated by the green line in Figure 5.11.

At longer wavelengths the nominal uncertainty of the *RASTA* increases, which can be traced back to the accuracy of the reference radiometers used during the *RASTA* characterization at the *PTB*. The uncertainty due to inhomogeneities of the *LIS* is given to be ±1.6 % (*Baumgartner*, 2013). Another source of uncertainty arises from the drift of the dark signal S_d over time and from the noise $\mathcal{N}$ of the signal S, which is shown as blue (VNIR) and red (SWIR) dashed lines. The drift per minute was assumed to be 10 DN for the SWIR and 3 DN for the VNIR as found in the dark signal analysis (Section 5.3.1). The noise was calculated for 100 averaged dark frames and 500 averaged illuminated frames resulting in $\sigma_{\langle S \rangle} = 0.5\,\mathrm{DN}$. At the *RASTA* and the *LIS* the 2σ uncertainty due to the dark signal drift and noise accounts to around 1 % for the VNIR and 3 % for the SWIR for wavelengths in the center of both spectra. While the dark signal drift and noise level stays constant with wavelength the radiometric sensitivity and therefore the signal S decreases towards the edges of the spectra. This results in a sharp increase of the relative uncertainty towards spectral regions with low radiometric sensitivity. In particular towards the edges of the spectra, the drift of the dark signal S_d contributes the most to the overall radiometric uncertainty. Altogether this error budget is a very conservative estimate for an individual measurement with a single pixel without any averaging. For relative measurements some of these uncertainties cancel out e.g. the *LIS* inhomogeneity and the *RASTA* uncertainty during a window transmissivity characterization presented in Section 5.4.2.

Noise

The noise $\mathcal{N}$ is composed of dark current noise $\mathcal{N}_{\mathrm{dc}}$, read noise $\mathcal{N}_{\mathrm{read}}$ and photon shot noise $\mathcal{N}_{\mathrm{shot}}$. Their joint standard deviation $\sigma_{\mathcal{N}}$ is calculated using the individual standard deviations σ_{shot}, σ_{dc} and σ_{read}:

$$\sigma_{\mathcal{N}} = \sqrt{\sigma_{\mathrm{shot}}^2 + \sigma_{\mathrm{dc}}^2 + \sigma_{\mathrm{read}}^2} = \sqrt{k^2 N + \sigma_d^2}. \tag{5.12}$$

Since photons arrive randomly in time the number N of photoelectrons measured during a fixed time interval is distributed according to the Poisson distribution. Following the Poisson statistics the standard deviation σ_N of a distribution with the expectation value N is proportional to $\sqrt{N}$. For this reason the photon shot variance σ_{shot}^2 scales linearly with the number of incoming photoelectrons N and the squared conversion gain k^2 [DN²] (Equation 5.12). For a sensor with linear response, the relation $S_0 \propto N$ holds. A deviation from this relationship can be an indication for a nonlinear relationship between the number N of photoelectrons and the photoelectric signal S_0 or is caused by a non-Poisson noise source.

Similar to the dark signal S_d in S, a dark noise $\mathcal{N}_d$ remains in $\mathcal{N}$ without illumination. It is comprised of dark current noise $\mathcal{N}_{\mathrm{dc}}$ and readout noise $\mathcal{N}_{\mathrm{read}}$. The dark current noise is caused by statistical variation of thermally generated electrons. Pixel readout and analog to digital conversion is further subject to electronic readout noise, which is independent from integration time.

For this analysis, $\sigma_{\mathcal{N}}$ is calculated as the pixel-wise standard deviation of 500 consecutive frames which were obtained during the nonlinearity measurements with varying integration times as listed in Table 5.2. Here, the noise standard deviation $\sigma_{\mathcal{N}}$ and mean, darkcurrent-corrected signal level $\langle S_0 \rangle$ are calculated individually for each pixel, since both sensors cannot be homogeneously illuminated due to the spectrographic diffraction grating, As noise $\mathcal{N}$ describes unbiased temporal variations of the signal around its expectation value, its temporal mean vanishes: $\langle \mathcal{N} \rangle \approx 0$.

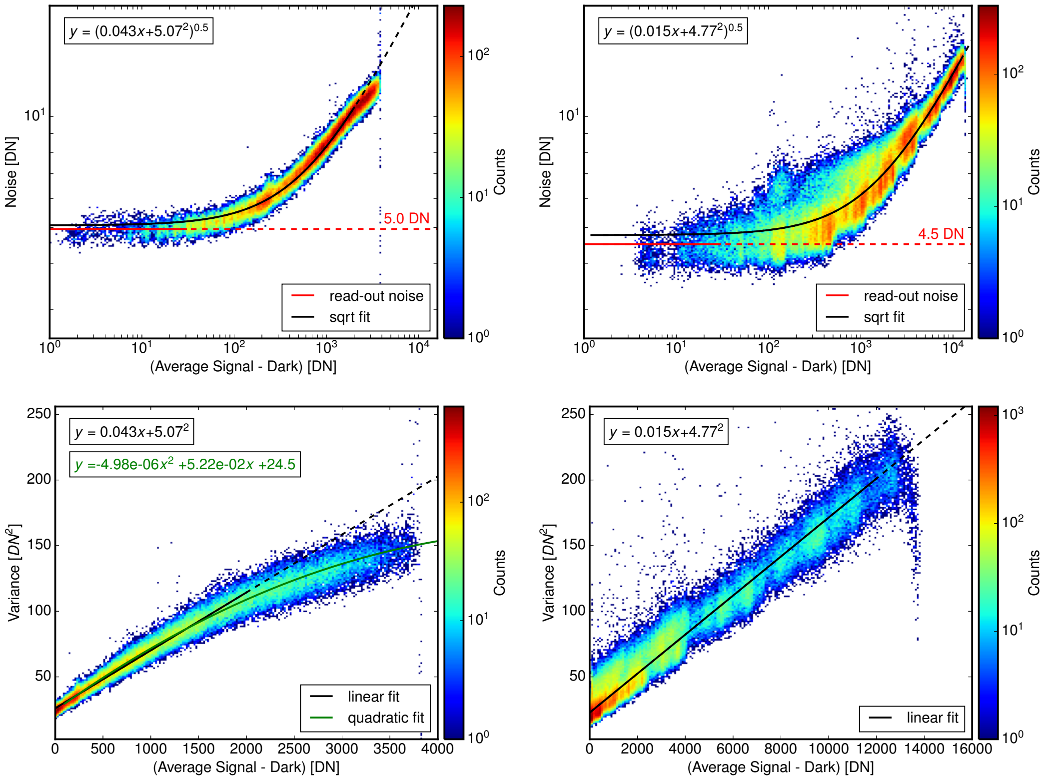

Figure 5.12: Noise characteristics for the (left) VNIR and (right) SWIR spectrometer. (top) The noise $\sigma_{\mathcal{N}}$ (standard deviation of S) is shown against the mean, darkcurrent-corrected signal level $\langle S_0 \rangle$. (bottom) Noise variance $\sigma_{\mathcal{N}}^2$ against $\langle S_0 \rangle$ for both spectrometers.

Figure 5.12 shows the results of the noise analysis. For each pixel and each integration time, the mean and standard deviation was calculated and accumulated in the shown 2-D histograms. The noise characteristics of the VNIR are shown on the left while results for the SWIR are shown on the right. On top in Figure 5.12 the pixel-wise standard deviation $\sigma_{\mathcal{N}}$ is plotted against the mean, darkcurrent-corrected signal level $\langle S_0 \rangle$ on a log-log scale. On the bottom, the same is done with the pixel-wise variance $\sigma_{\mathcal{N}}^2$ on a linear scale.

With the classic Photon Transfer Curve (PTC) (*Janesick*, 2007) the noise characteristics can be used to determine many important camera parameters. When the signal noise standard deviation $\sigma_{\mathcal{N}}$ is plotted against the mean, darkcurrent-corrected signal level $\langle S_0 \rangle$ on a log-log scale, like it is done in Figure 5.12, different noise regimes become apparent. The dark noise at integration time $t_{\text{int}} = 0\,\text{s}$ at the lower end of $\langle S_0 \rangle$ is dominated by read-out noise with standard deviation σ_{read}. With increasing mean signal level $\langle S_0 \rangle$ photon shot noise becomes dominant with σ_{shot}. Due to the Poisson-like distribution the photon shot noise variance σ^2_{shot} should scale linearly with mean signal level. Deviations from this linear relationship can provide an indication of a nonlinear radiometric response (*Bohndiek et al.*, 2008) or a charge sharing mechanism between pixels (*Downing et al.*, 2006, *Stefanov*, 2014).

At low values of $\langle S_0 \rangle$ the signal-independent read-out noise becomes apparent. The read-out noise for $t_{\text{int}} = 0\,\text{s}$ is derived as the y-intercept of a constant fit on $\sigma_{\mathcal{N}}$ for $\langle S_0 \rangle < 30\,\text{DN}$. By doing this, the noise associated with the readout channel was found to be 5.0 DN for the VNIR and 4.5 DN for the SWIR spectrometer. For larger values of $\langle S_0 \rangle$ the noise begins to increase.

When the standard deviation $\sigma_{\mathcal{N}}$ is fitted with the square root model following Equation 5.12, the noise characteristics can be further investigated. At first glance, the noise standard deviation of the VNIR sensor is in accordance with the noise model described by Equation 5.12 with a constant conversion gain $k = 0.043\,[\text{DN}]$. For values of S_0 between 0–2000 DN it follows the function

$$\sigma_{\mathcal{N}} = \sqrt{0.043 S_0 + 5.07^2}\ [\text{DN}]. \tag{5.13}$$

For larger values the noise variance $\sigma^2_{\mathcal{N}}$ no longer scales linearly with $\langle S_0 \rangle$ but remains below the fit in Equation 5.13. As seen in Figure 5.12 bottom left, the VNIR noise can no longer be explained by a Poisson noise model (Equation 5.12) with a constant conversion gain $k\,[\text{DN}]$. This noise characteristic can be an indication for two different mechanisms at work. Either $k\,[\text{DN}]$ varies with signal level S_0, which would cause a photon response nonlinearity or a charge sharing is occurring between pixels which would violate the Poisson assumption. A more in-depth analysis of the noise showed a small autocorrelation within pixels of the same spatial sensor row, which would suggest the latter. But as the photon response nonlinearity analysis in Section 5.3.1 has shown, radiometric nonlinearity has to be considered as a possible explanation.

In contrast the SWIR noise standard deviation $\sigma_{\mathcal{N}}$ shown in Figure 5.12, top right compares much better to the Poisson model. Between 0–12 000 DN, which is only limited by the subtracted dark signal, it fits the following form:

$$\sigma_{\mathcal{N}} = \sqrt{0.015 S_0 + 4.77^2}\ [\text{DN}] \tag{5.14}$$

At larger values of $\langle S_0 \rangle$ the noise variance σ_N^2 remains linear with $k = 0.015\,[\mathrm{DN}]$ until saturation is reached. For both sensors no wavelength dependence in noise was found.

Polarization sensitivity

All optical components can exhibit polarization dependent loss, which in effect makes the signal sensitive to polarization. This polarization sensitivity has an influence on the absolute radiometric response R when parts of the measured light are linearly polarized. The polarization sensitivity can be examined by splitting the instrument response virtually into a polarization insensitive part with partial response O and a fully polarization sensitive part with partial response $2A$, such that $R = A + O$ for unpolarized light. In line with Malus' Law the polarization dependent normalized photoelectric signal $s_n^P(\phi)$ of incoming radiance L, with a degree of polarization p, measured with such an instrument is given by

$$
\begin{aligned}
s_n^P(\phi) &= 2A \cdot L_{\parallel} + O \cdot L && (5.15)\\
&= 2A \left(p \ \cos^2(\phi - \phi_0) + \frac{1-p}{2} \right) \cdot L + O \cdot L && (5.16)
\end{aligned}
$$

Here, $L_{\parallel}$ denotes the incoming radiation parallel to the sensors polarization direction, ϕ the polarization orientation with respect to the entrance slit and ϕ_0 the polarization orientation for which $s_n^P(\phi)$ is maximal.

To investigate the polarization influence, a wide-band wire grid polarizer (99.9% degree of polarization between 400 – 2500 nm) mounted in a rotation stage was placed between the large integrating sphere and the *specMACS* instrument. Following *Lenhard et al.* (2015), measurements of the photoelectric signal $s_n^P(\phi)$ were done while rotating the polarizer between 0° and 180° with respect to the entrance slit in steps of 15°. For fully polarized light ($p = 1$) of intensity L, Figure 5.13 shows the polarization sensitive behavior of $s_n^P(\phi)$ for one VNIR pixel (spatial: 400, spectral: 600) while rotating the wire grid polarizer (red crosses). While the maximum of $s_n^P(\phi)$ can be found for polarization orientations parallel to ϕ_0, the maximum signal loss due to the polarization sensitivity occurs orthogonal to ϕ_0

In the following, the polarization sensitivity P is defined as the increase of the signal between unpolarized light ($p = 0$) and light fully polarized in the most sensitive direction of the sensor ($p = 1, \phi = \phi_0$), while the total radiance of the light source remains unchanged. The polarization sensitivity P reads as follows:

$$
P = \frac{A}{A+O} \cdot 100\,\% \tag{5.17}
$$

A natural light source has an unknown degree p and orientation ϕ of polarization. Nonetheless, the maximum error in the normalized signal s_n due

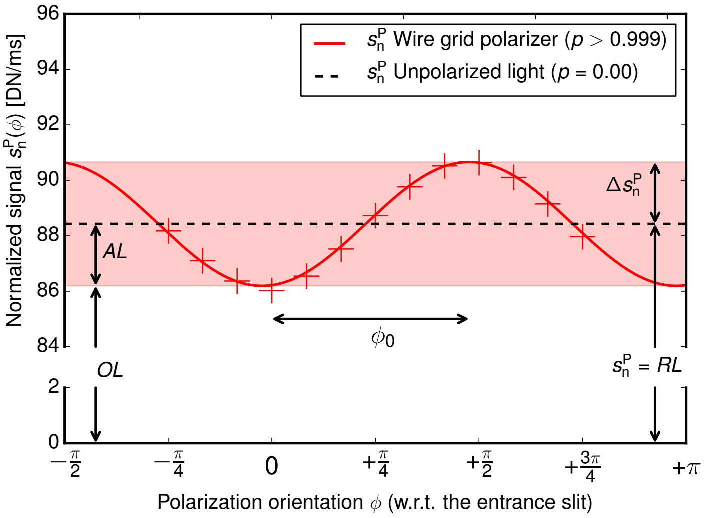

Figure 5.13: Polarization dependent normalized photoelectric signal $s_n^P(\phi)$ for one VNIR pixel (spatial: 400, spectral: 600) while rotating the polarizer between $-45°$ and $135°$ with respect to the entrance slit in steps of $15°$. The polarization sensitivity P and its orientation ϕ_0 is found by fitting the measurements with the model in Section 5.3.1.

to polarization can be given for an estimated maximum degree of polarization $p_{max} \leqslant 1$. Note that this estimate is always possible in the form of $p_{max} = 1$ for a completely unknown light source. Following Section 5.3.1, any signal s_n^P measured from an incoming radiance L with maximum degree of polarization p_{max} can be constrained for the following bounds (which are illustrated by the red shaded region in Figure 5.13):

$$((1 - p_{max})\,A + O)\,L \leqslant s_n^P \leqslant ((1 + p_{max})\,A + O)\,L \qquad (5.18)$$

Ideally, the signal would be independent from ϕ, following the linear model $s_n = RL$. In particular, this holds true for s_n^P for unpolarized light ($p_{max} = 0$), as it was the case during the radiometric characterization. It follows that the error Δs_n for an unknown degree $p > 0$ and orientation ϕ of polarization is given by $\Delta s_n = |s_n - s_n^P|$. An upper bound of the error Δs_n due to polarization can then be estimated by using $s_n = RL$, $R = A + O$ and Equation 5.18:

$$\Delta s_n \leqslant \max\left(|RL - ((1 \pm p_{max})\,A + O)\,L|\right) = p_{max}AL \qquad (5.19)$$

Furthermore, an upper bound for the relative uncertainty due to polarization can be estimated using the polarization sensitivity P by estimating L through s_n^P using Equation 5.18 again and inserting Equation 5.17 after solving for A:

$$\frac{\Delta s_n}{s_n^P} \leqslant \frac{p_{\max} A}{(1 - p_{\max})A + O} = \frac{p_{\max} P}{1 - p_{\max} P} \tag{5.20}$$

In the field, radiation is never fully polarized. The polarization of sunlight reflected by water clouds is well below 5 % for most viewing geometries. It only reaches values of up to 15 % in the rainbow region of optically very thin clouds (*Hansen*, 1971b). In contrast, Rayleigh scattering can be strongly polarized, depending on the scattering angle. If strongly polarized light must be assumed, the calibrated radiance has to be handled with care and provided with corresponding uncertainty estimates following Equation 5.20. For sensor regions with a small polarization sensitivity P, the relative radiometric error due to polarization scales linearly with the light polarization p.

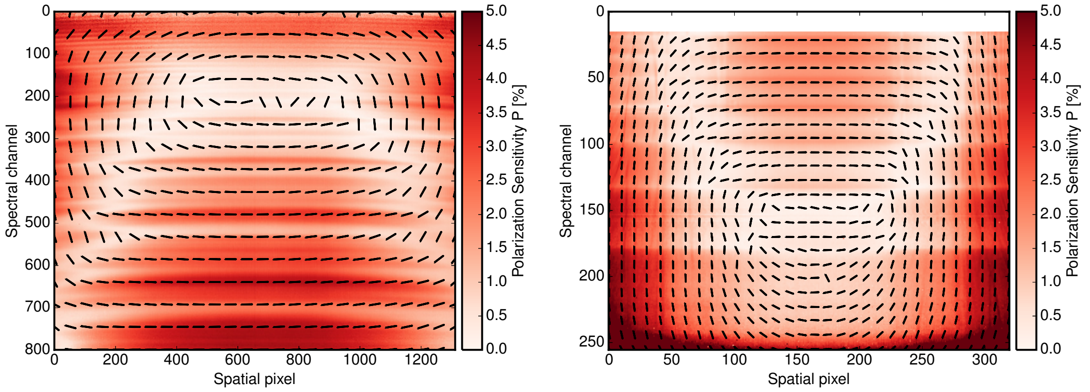

Figure 5.14: Results of the polarization sensitivity characterization for the VNIR (left) and the SWIR (right). The colormap shows the polarization sensitivity P for all pixels as determined with Equation 5.17. With the entrance slit oriented horizontally to this figure, the black solid lines indicate the polarization orientation for which the signal becomes minimal.

The polarization sensitivity P and the angular offset ϕ_0 were found by fitting the measurements to Section 5.3.1. In Figure 5.14, the characterization results for P and ϕ_0 are shown as color and black lines respectively. Here, the black solid lines indicate the polarization orientation for which the signal becomes minimal. The polarization sensitivity P can be observed to increase from 1% to 5% towards larger wavelengths for both cameras, resulting in a maximum error of 5.3 % for fully polarized light. While P is higher in the center of the VNIR FOV, it increases towards the edges for the SWIR. Furthermore very high values for P (>5 %) can be observed at both wavelength cutoffs of the SWIR, where the radiometric sensitivity becomes very small. Due to the very low radiometric sensitivity of the SWIR the region of shortest wavelengths were excluded in this analysis. Despite the slightly different definition, the values of P agree well with *Lenhard et al.* (2015) and *Hyvarinen et al.* (1998) and can be explained by the polarization caused at the entrance slit and the holographic transmission grating.

Overall radiometric uncertainty budget

To specify the total radiometric uncertainty for every measurement, the following section will give a bottom-up calculation of the propagation of radiometric errors. As it has already been done during the estimation of the total dark signal uncertainty, maximum errors (Δ) are being used as approximation of 2σ errors, when no standard deviation is available.

First, the absolute error contributions to the photoelectric signal S_0 are combined:

$$2\sigma_{S_0} = \sqrt{(2\sigma_d(t_0))^2 + (2\sigma_{\mathcal{N}}(S_0))^2} \tag{5.21}$$

Here, $\sigma_d(t_0)$ denotes the estimated standard deviation of the dark signal (following Equation 5.6) and $\sigma_{\mathcal{N}}(S_0)$ is the estimate of the instantaneous noise of the signal (derived from the photon transfer curve). Subsequently, the relative error of the normalized signal is obtained by combining the relative errors of the photoelectric signal σ_{S_0} with the estimated remaining nonlinearity uncertainty σ_{nonlin} and the polarization uncertainty Δs_n:

$$\frac{2\sigma_{s_n}}{s_n} = \sqrt{\left(\frac{2\sigma_{S_0}}{S_0}\right)^2 + \left(\frac{2\sigma_{\text{nonlin}}}{s_n}\right)^2 + \left(\frac{\Delta s_n}{s_n^P}\right)^2} \tag{5.22}$$

Lastly, radiometric calibration additionally adds the uncertainty $\frac{\sigma_R}{R}$ of the sensor response:

$$\frac{2\sigma_L}{L} = \sqrt{\left(\frac{2\sigma_{s_n}}{s_n}\right)^2 + \left(\frac{2\sigma_R}{R}\right)^2} \tag{5.23}$$

An example of typical total uncertainty values for real measurements is given later in the application section (Section 5.5).

5.3.2 Spatial and spectral characterization

Besides the radiometric characterization of the spectrometer its spatial and spectral projection onto the detector are of great importance for the scientific application. The radiance contribution for a single pixel from different solid angles is described by two line spread functions (LSF), the across- and along-track LSFs. The spectral responsivity for every pixel is described by a spectral response function (SRF). Moreover some of the pixels of the detector yield unreliable (dead pixel) or biased (hot pixel) measurements, which should be marked and classified as “bad”.

Bad pixel correction

Bad pixels are pixels which do not behave according to the instrument model assumed by the calibration procedure. As already argued by *Lenhard et al.* (2015), bad pixel characterization of an assembled hyperspectral sensor is not straight forward as a uniform illumination of the sensor chip is not achievable due to the dispersing element. It was decided to manually observe measured data and keep track of pixels which behave very different from surrounding pixels in a list associated with the calibration files. For the VNIR sensor, there existed no previous knowledge about bad pixels. For the SWIR sensor, the manufacturer provided list of bad pixels was included. Currently one bad pixel is known for the VNIR sensor and 264 randomly distributed bad pixels are known for the SWIR sensor.

Bad pixel correction or the replacement of invalid pixel values by interpolated values is needed if further processing algorithms cannot handle invalid pixels in the resulting dataset. Depending on the goal of the proceeding analysis, different interpolation schemes may be appropriate. Currently, bad pixel correction is implemented based on the list of bad pixels provided by the calibration file and a user defined strategy how interpolation rules should be derived from the bad pixel list. The primarily used strategy is to perform a linear interpolation from spatially adjacent good pixels over a single or a group of bad pixels in order to keep spectral features intact.

Response function

Figure 5.15 shows a measured line spread function of the VNIR spectrometer and a spectral response function of the SWIR spectrometer. Due to asymmetric distortions of the LSFs of both sensors and the SRFs of the SWIR sensor a fit with a Gaussian function G would yield distorted estimates of center and resolution. For this reason, the process to retrieve the center and the resolution respectively bandwidth of the response functions is twofold: First, a third order B-spline F is fitted to the measurements to determined the center of a response function as the median x_c of F. Then, the resolution Δx is centered around x_c and determined by the area under the normalized spline fit F, which is equal to the area (0.7610) under a Gaussian function $G(x)$ between its full width half maximum FWHM. This way a measure of the response function width is provided in analogy to the full width half maximum of a Gaussian shaped function. Consequently, the resolution is derived by optimizing the symmetric integration limits $\Delta x/2$ to satisfy Equation 5.24:

$$\frac{\int_{x_c-\Delta x/2}^{x_c+\Delta x/2} F(x)\,dx}{\int_{-\infty}^{\infty} F(x)\,dx} = \frac{\int_{-\mathrm{FWHM}/2}^{\mathrm{FWHM}/2} G(x)\,dx}{\int_{-\infty}^{\infty} G(x)\,dx} = 0.7610 \tag{5.24}$$

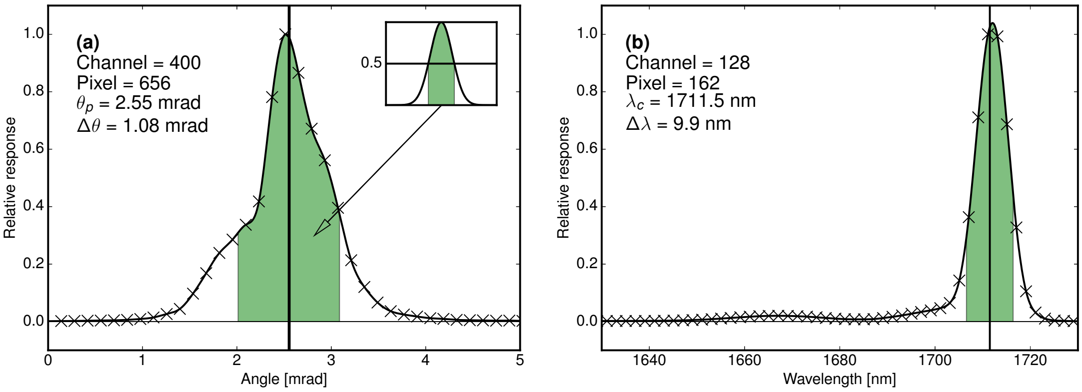

Figure 5.15: **(a)** LSF of spectral channel 400 for spatial pixel 656 of the VNIR sensor. The vertical line denotes the median viewing angle θ_c, the width of the filled area the angular resolution $\Delta\theta$. **(b)** SRF of spectral channel 128 for spatial pixel 162 of the SWIR sensor. The vertical line denotes the median wavelength λ_c, the width of the filled area the wavelength bandwidth $\Delta\lambda$. For both plots the crosses are the measurements, and the curve is a spline fitted to these data points.

The basic idea to transfer the FWHM concept to asymmetric response functions is also illustrated by the inset in Figure 5.15. Using this technique the angular resolution $\Delta\theta$ and the spectral bandwidth $\Delta\lambda$ are determined. In the following, the terms *along track* and *across track* denote directions perpendicular and parallel to the spatial line respectively.

Spatial characterization

Every pixel of the sensor arrays has its own set of LSFs, which are described by the viewing angle θ_c and the angular resolution $\Delta\theta$. The viewing angles θ_c of one spatial pixel along the spectral axis are ideally the same. Any deviation is commonly called keystone, which is expressed as the maximum difference of the viewing angles of one spatial pixel. The width of LSFs $\Delta\theta$ across- and along-track determines the sharpness of the spatial image.

The geometric and spectral characterizations were done analogous to *Gege et al.* (2009) and *Baumgartner et al.* (2012). The measurement setup consists of a narrow slit with a width of 0.05 mm, illuminated by a Quartz Tungsten Halogen lamp and positioned at the focal plane of a reflective collimator with a focal length of 750 mm. This results in a collimated beam with a divergence of 0.07 mrad that is guided via a folding mirror onto the aperture of the spectrometer. Through linear movement and simultaneous rotation of the folding mirror, different spatial pixels can be illuminated. The collimated beam is large enough to fill the aperture of the spectrometer.

The across-track LSFs are measured by using a slit which is imaged perpendicular to the entrance slit of the spectrograph. The angular scan for the selected pixels is accomplished by changing the illumination angle via the folding mirror over a range of 0.7 rad. For the VNIR this scan is done in increments of 0.14 mrad covering the entire FOV. In case of the SWIR instrument, the scan is performed in increments of 0.35 mrad.

The along-track LSFs are measured at 7 angles that are evenly distributed over the FOVs of the instruments. They are measured by using a slit that is imaged parallel to the entrance slit of the spectrograph. The incidence angle of the collimated beam on the spectrometer aperture is changed by a along-track translation of the illuminated slit in the focal plane of the collimator. For the measurement of the selected spatial pixels of the VNIR, the along-track LSF is scanned over a range of 6.06 mrad in increments of 0.3 mrad, and for the SWIR over a range of 5.9 mrad in increments of 0.15 mrad.

To retrieve the viewing angles and angular resolutions from the measurements, the measurements were interpolated using splines as described in Section 5.3.2. The geometric along track values of pixels that are not measured directly are inferred by interpolation of the viewing angles and angular resolution in between the measured spatial pixels. For the interpolation a second order polynomial fit to the measured spatial pixel is used. The order of the polynomial functions is selected so that higher order polynomials do not reduce the residuals significantly more. The keystone distortion of one spatial line is defined as the largest difference of across-track viewing angles along the spectral axis.

A typical LSF for the VNIR sensor is shown in Figure 5.15a. As previously discussed in Section 5.3.2, the LSFs cannot be accurately approximated with Gaussian functions. Therefore splines were fitted to the measurements to compute the viewing angles θ_c and the angular resolution $\Delta\theta$ of both spectrometers related to the usual FWHM values for a Gaussian shaped sensitivity. The characterization results for both sensors are shown in Figure 5.16 and in Table 5.4. Due to low sensitivity some channels of the sensors could not be evaluated accurately. Therefore, the first 30 channels of the VNIR and the first 17 channels of the SWIR sensor are not taken into account. Figure 5.16a and c show the deviations of the across track viewing angles θ_c relative to spectral channel 400 for the VNIR and to spectral channel 128 for the SWIR sensor. Ripples in Figure 5.16a and b are caused by the etalon effect in the VNIR. For both spectrometer the strongest keystone distortion occurs at longer wavelengths while its mean value of 0.30 mrad in the VNIR and 0.50 mrad in the SWIR remain well below the angular resolution of the sensors.

Figure 5.16b and d show the across track angular resolution $\Delta\theta$ of the sensors. The area with the smallest $\Delta\theta$ and therefore sharpest pixel is stretched across the sensor FOV. At longer wavelengths and lower pixel numbers the VNIR image projection gets rather blurry. Besides the achromatism this behavior could be explained by an slightly misaligned entrance slit with respect to the entrance optics. Considering the mean ratio of 3.15 between angular resolution and sampling and the fact that only parts of the image appear sharp the VNIR shows a

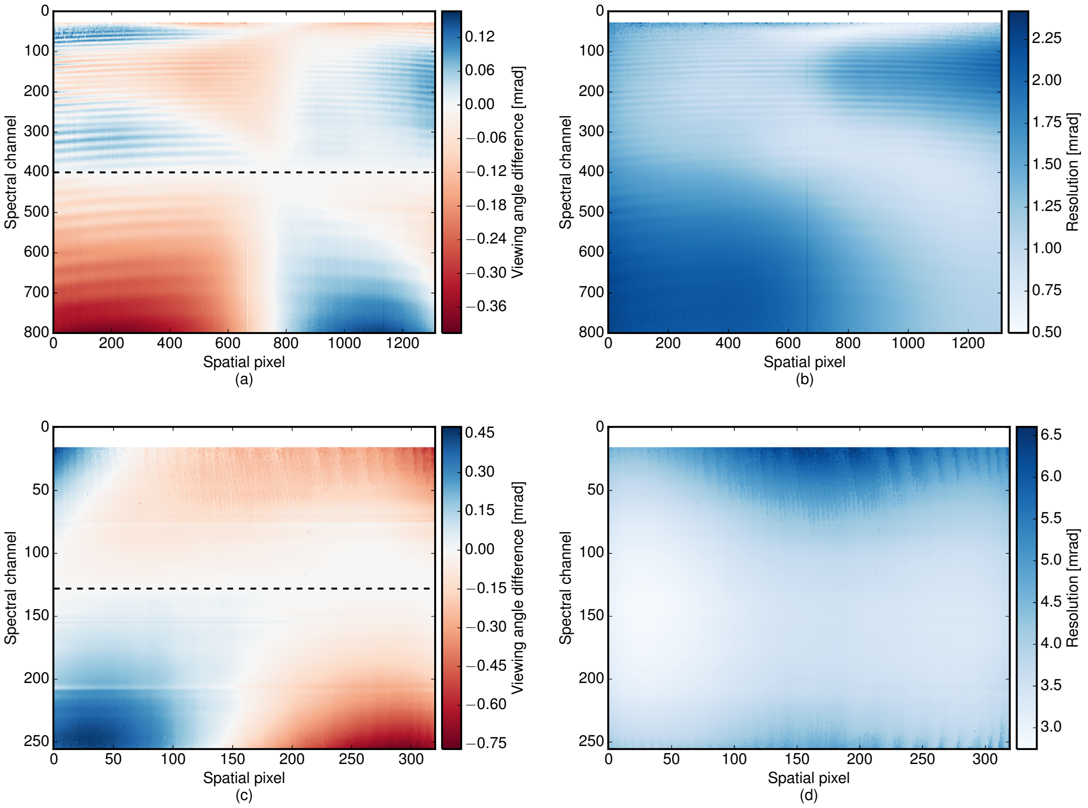

Figure 5.16: Spatial characterization results of the VNIR **(top)** and SWIR **(bottom)** sensor. **(a)** and **(c)** show the difference of the viewing angle of each pixel to those of channel 400 (VNIR) and channel 128 (SWIR) respectively. **(b)** and **(d)** show the angular resolution. White areas indicate channels which are excluded from evaluation due to their low sensitivity.

reduced focusability. The sharpest SWIR image projection is approximately at the center in wavelength but asymmetric in lower pixel numbers as it can be seen in Figure 5.16d. With a mean angular oversampling of 1.95 the SWIR optics produce a sharper image on the detector. However, the angular sampling (1.94 mrad) and resolution (3.79 mrad) is far coarser than for the VNIR (0.44 and 1.37 mrad). The deviations in along track viewing angles θ_c and along track angular resolutions $\Delta\theta$ are not shown here since their values are similar to their across track values. Both along track properties exhibit an even more symmetrical distribution over the sensors.

Table 5.4: Summary of the geometric across-track properties of the *specMACS* VNIR sensor (left) (excluding the first 30 channels) and for the SWIR sensor (right) (excluding the first 17 channels).

	VNIR		SWIR	
Parameter	Avg.	Min–Max	Avg.	Min–Max
Total FOV (°)	32.7	–	35.5	–
Angular Sampling (mrad)	0.44	0.37–0.53	1.94	1.73–2.07
Angular Resolution (mrad)	1.37	0.50–2.89	3.79	2.75–6.60
Angular Resolution (mrad)*	2.00	1.12–2.79	1.82	1.70–2.22
Angular Oversampling	3.15	1.17–5.81	1.95	1.45–3.36
Keystone (mrad)	0.30	0.06–0.54	0.50	0.27–0.77
Keystone (pixel)	0.71	0.13–1.23	0.26	0.13–0.41

$*$ along-track property

Spectral characterization

For one spectral channel the SRF center and its width can vary over the FOV of the instrument, i.e. every single pixel of the sensor array has its individual SRF, similar to the LSFs. The deviation of the center wavelength λ_c within a spatial line is commonly described as spectral smile while the SRF width gives the spectral bandwidth $\Delta\lambda$. In the following, the spectral smile will be given as the deviation of λ_c with respect to the center pixel within each spatial line.

To measure the SRF, a collimated beam of nearly monochromatic light from a monochromator is used. The collimated beam is guided into the spectrometer's aperture by the previously discussed folding mirror that allows for the illumination of a selectable spatial pixel. A detailed sketch of the calibration setup can be found in *Gege et al.* (2009) in Fig. 7. To guarantee that the spectrometer aperture and IFOV are completely illuminated, the beam cross-section is larger than the aperture and the beam divergence is larger than the IFOV of the spectrometer. The monochromator has an absolute uncertainty of ±0.1 nm for wavelengths below 1000 nm, and ±0.2 nm for longer wavelengths. The spectral bandwidth is set to 0.65 nm for the measurement of the VNIR and 1.3 nm for the measurement of the SWIR. Computations indicate that the chosen bandwidth of the monochromator has only very little influence on the measured bandwidths as long as the monochromator bandwidth is smaller than the measured bandwidth and its SRF is known. With a Gaussian monochromator SRF well below the specified spectrometer bandwidth both requirements are met. For the measurement of the SRFs of the VNIR, the wavelength of the monochromator is scanned from 400 to 1030 nm in steps of 1 nm, and for the SWIR, from 940 to 2550 nm in steps of 2 nm.

Due to time constraints, these measurements are only feasible for a small subset of all spatial pixels: For both sensors, the SRFs are measured at seven angles evenly distributed over their across-track FOV.

The spectral properties of the other pixels are inferred by fitting the center wavelengths and bandwidths with a second order polynomial. This procedure assumes that the properties of the optical system do not vary rapidly on the scale of the detector array. This assumption holds for the *specMACS* imaging spectrometers, which was validated using spectral line lamps. The spectral smile for each spatial pixel is computed as the difference between its wavelength and the wavelength of the center pixel within the same spectral channel.

The measurement setup is described in more detail in *Gege et al.* (2009) and details about the data analysis as well as a validation of the approach for another hyperspectral camera can be found in *Baumgartner et al.* (2012).

A measured SRF of the SWIR sensor can be seen in Figure 5.15b. The figure shows an asymmetric response with a second peak at shorter wavelengths. The results of the spectral characterization can be seen in Figure 5.17 and Table 5.5. As for the geometric characterization some channels are not evaluated. The first 36 channels of the VNIR and the first 17 channels of the SWIR sensor are skipped due to low sensitivity in these regions.

Figure 5.17a and c illustrate the smile distortion. For the VNIR sensor, the magnitude of the average spectral smile is between 0.1 and 1.1 nm. For the SWIR sensor, the magnitude of the average spectral smile is on the order of 1.1 nm, ranging from 0.1 to 4.1 nm. Note that the sign of the smile curve changes between the bottom half and the top half of both detector arrays.

Figure 5.17b and d show the spectral bandwidth of each detector element It is about 3.1 nm in average for the VNIR sensor, and degrades to 6.0 nm at the spatial edges of the detector array. For the SWIR sensor, spectral bandwidth is about 10.3 nm at the center of the detector array, and increases up to 19.6 nm at the spatial edges of the array. For the VNIR, spectral oversampling is 4.03, which allows the spectral sampling to be reduced by half without losing information. In contrast the average SWIR spectral oversampling is only around 1.64.

The ripple features in the plots of Figure 5.17a and b are caused by the etalon effect.

Optical distortion correction

Optical distortion correction can be performed through interpolation of the dataset onto a regular grid. As the adequate grid depends on the particular application and as interpolation for every pixel is lossy in terms of information content, this interpolation step should be performed during spatial rectification of the image. Hereby the optical characterization for each instrument is combined with the location information for each frame, which is then stored together with the radiometric signal from each pixel. Subsequently this meta data can be used in the transformation onto the final target coordinate system.

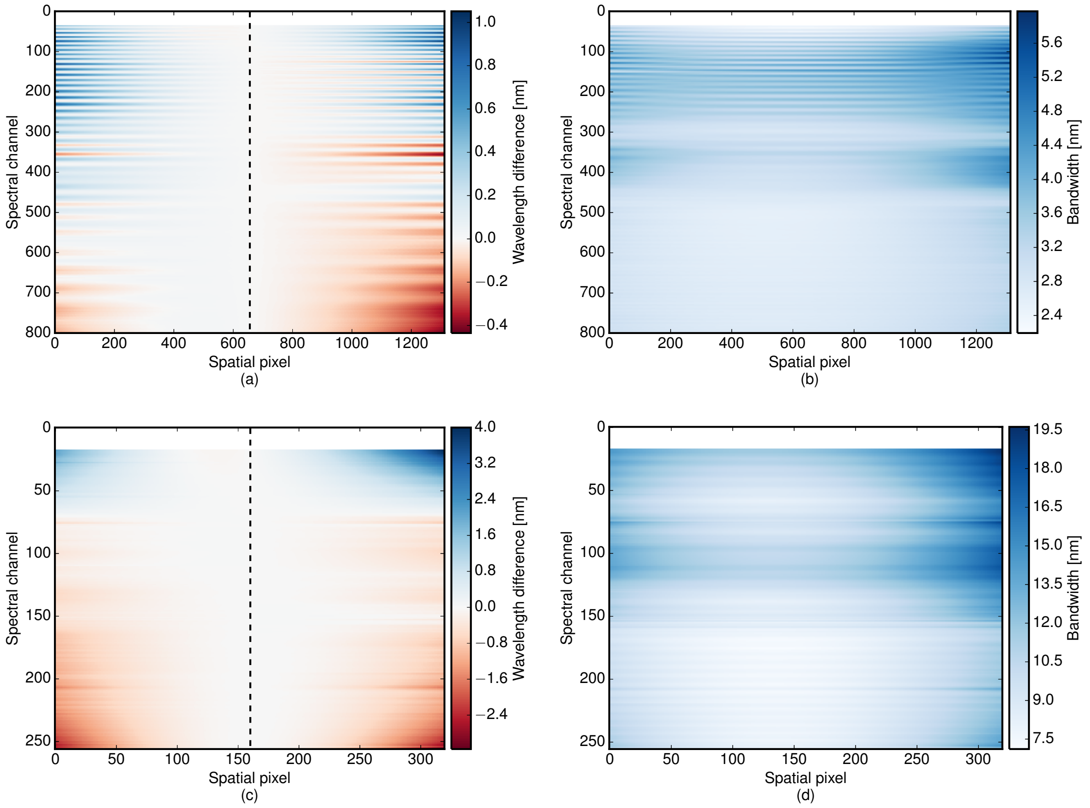

Figure 5.17: Spectral characterization results of the VNIR **(top)** and SWIR **(bottom)** sensor. **(a)** and **(c)** show the difference of the wavelength of each channel to those of pixel 656 (VNIR) and pixel 160 (SWIR) respectively. **(b)** and **(d)** show the bandwidth. White areas indicate channels which are excluded from evaluation due to their low sensitivity.

Table 5.5: Summary of the spectral properties of the *specMACS* VNIR (left) and SWIR (right) sensor. For this analysis, the first 36 channels were excluded for the VNIR, while excluding the first 18 channels in case of the SWIR.

	VNIR		SWIR	
Parameter	Avg.	Min–Max	Avg.	Min–Max
Spectral Range (nm)	–	421.3–1017.5	–	1017.8–2505.5
Spectral Sampling (nm)	0.8	0.6–1.0	6.3	5.2–6.9
Spectral Bandwidth (nm)	3.1	2.2–6.0	10.3	7.1–19.6
Spectral Oversampling	4.03	3.08–7.82	1.64	1.15–3.10
Spectral Smile (nm)	0.3	0.1–1.1	1.1	0.1–4.1
Spectral Smile (pixel)	0.38	0.07–1.40	0.18	0.02–0.65

5.4 Ground-based and airborne deployment

First deployments of the *specMACS* instrument were the ground-based measurement campaign HOPE in Melpitz, Germany in September 2013 and the aircraft campaign ACRIDICON CHUVA in the Amazon region around Manaus, Brazil in September 2014 (*Wendisch et al.*, submitted). While *specMACS* was put on a scanning mount during the ground-based campaign, the instrument was installed on the German research aircraft HALO (High Altitude LOng range aircraft, *Krautstrunk and Giez*, 2012) during the ACRIDICON CHUVA campaign.

5.4.1 Ground-based setup

For ground based measurements, *specMACS* is mounted on a scanning mount (MESU-OPTICS Mesu-Mount 200) with two rotating axes (vertical and horizontal). This allows the instrument to be pointed anywhere in the upper hemisphere and to perform precise and repeatable automated scans. The scanning mount is equipped with a customized closed loop motor controller (based on a ROBOTEQ Inc., SDC2130). It is equipped with an optical relative position encoder, which allows to control the full turn of each axis in 10 000 steps resulting in a relative positioning accuracy of the angle of about two steps, which is accordingly 0.072° and thereby in the same order as the sensors IFOV.

5.4.2 Airborne setup

For airborne measurements, *specMACS* was mounted into a HALO Rack looking sideways with vertical spatial axis in cooperation with enviscope GmbH. For this task, a specifically designed window for the HALO side view port had to be developed to ensure a high transmissivity over the whole spectral range of *specMACS* (Figure 5.18). Into two vertical apertures inside the side view port two 2 cm thick purified quartz glass panes (Herasil 102, Haereus) were embedded. To address the problem of window icing, a fan was installed below the window, which constantly blows warm cabin air onto the inner window surface.

The cameras' field of view was titled 5 ° downward with respect to the horizontal axis of the airplane. After matching both cameras field of views, a combined usable field of view of 21 ° below to 11 ° above the lateral axis is available.

During the airborne operation the across-track pixel size for clouds in a distance of 5 km is around 2.2 m for the VNIR and 9.7 m for the SWIR in accordance with their respective angular sampling. In order to obtain a comparable spatial along-track resolution the frame rate is set to 30 fps. With a maximum ground speed of 800 km h^{-1} the pixel size for clouds in this distance becomes 2.2 × 7.4 m for the VNIR and 9.7 × 7.4 m for the SWIR. Internal storage was designed large enough to enable continuous measurements for at least 2 flights of 8 h duration.

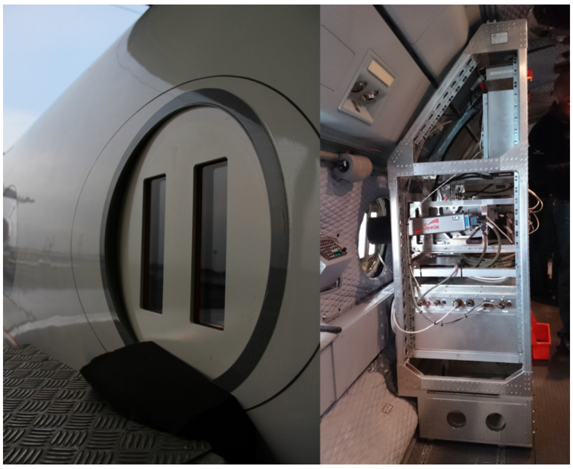

Figure 5.18: *specMACS* mounted on the HALO aircraft equipped with the SideView-Port.

Since the instrument was fixed in one of the measurement racks of HALO, the captured data has to rectified during post processing to correct for the airplane movements. The spatial rectification can be done using inertial navigation systems (INS) provided by the BAsic HALO Measurement And Sensor System (BAHAMAS) (*Krautstrunk and Giez*, 2012) or by the Spectral Modular Airborne Radiation measurement sysTem (SMART) (*Wendisch et al.*, 2001) whose subsystems offer both a 100 Hz data stream of accurate position information.

Window transmission

The transmission of the quartz glass windows were characterized radiometrically and spectrally on the CHB Large Integrating Sphere by comparing *specMACS* measurements of the sphere with and without the windows in the optical path. The angular dependence of the window transmission was further characterized at three different angles between the optical axis of the sensors and the window (0° = perpendicular to the optical axis, 11.8° = angle as mounted on HALO, 15.5° = steepest angle possible with the chosen experimental setup). Note that the transmission

$$T = \frac{L_{\mathrm{Win}}}{L} = \frac{R^{-1} s_{n;\mathrm{Win}}}{R^{-1} s_n} = \frac{s_{n;\mathrm{Win}}}{s_n} \tag{5.25}$$

can be calculated based on the darkcurrent and nonlinearity corrected signals alone and without using the characterization of the absolute radiometric response. In addition to the laboratory characterization and transmission values as specified by the manufacturer, theoretical reflection losses of the window surface including internal reflections were calculated using refractive indices from the glass data sheet (varying from 1.4703 to 1.4280 in our wavelength range) and Snell's and Fresnel's laws for comparison.

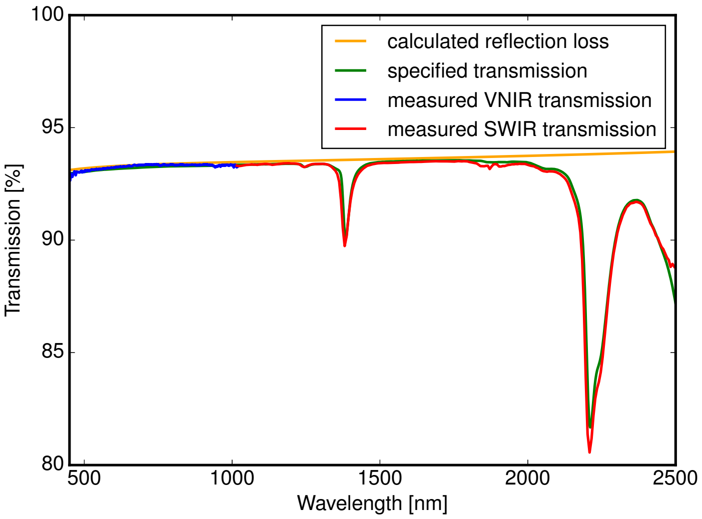

Figure 5.19: Spectral transmission and calculated reflection loss of the HALO SideViewPort.

The spectral transmission of the SideViewPort is shown in Figure 5.19. As expected, the theoretical reflection loss calculation yields an upper estimate for the actual transmission because of the missing absorption. The low discrepancy between specification and measurement and the close match of the overlapping region between both sensors show the high relative accuracy of the sensors and indicate that the nonlinearity correction works as intended. The two absorption bands in the spectrum show the expected strong IR-absorption of remaining OH species in fused quartz glass.

Significant spatial variation of the window transmission has not been observed, however small reflections of the sensors optical systems with an intensity of up to 0.5 % of the direct transmission were found.

5.5 Application and radiometric uncertainty

In Figure 5.20 examples of reflected solar spectra which were measured with the *specMACS* instrument on flight AC10 (12 September 2014) during the ACRIDICON-CHUVA campaign are shown. The shaded regions show the overall radiometric 2σ uncertainty, which was estimated using Equation 5.23. Hereby, a fully polarized signal ($p = 1$) was assumed to obtain an upper estimate of the radiometric uncertainty. At the edges of the spectra, at the transition between VNIR and SWIR around 1000 nm and within the water vapor absorption bands, the overall radiometric uncertainty reaches values of up to 50 % due to low signal levels. Around 1.3 µm, 1.6 µm and 2.1 µm, the radiometric uncertainty remains below

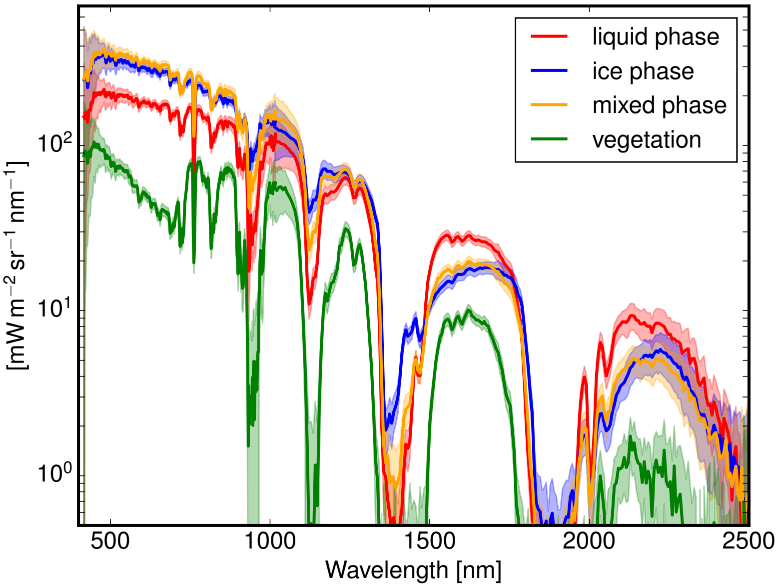

Figure 5.20: Reflected solar spectra measured with *specMACS* onboard HALO during the ACRIDICON-CHUVA campaign in Brazil.

10 % for well illuminated scenes. In the visible and near-infrared, the error even remains well below 5 %.

The locations of the spectra shown in Figure 5.20 are indicated in Figure 5.21 by points with corresponding color. While below 1000 nm the spectral radiance from the ice cloud (blue line) is higher than that from the liquid water cloud (red line) the spectral radiance from the liquid water cloud is higher at longer wavelengths. The lower radiance of the ice cloud at longer wavelengths can be explained by the higher absorption coefficient of ice and with the usually larger size of ice particles. Due to a higher absorption the ice cloud phase can also be distinguished from the liquid cloud phase by their different spectral slope between 1500–1700 nm (*Ehrlich et al.*, 2008) and 2100–2200 nm (*Martins et al.*, 2011). With a spectral slope in between the ice and liquid phase the spectrum of a cloud region with mixed phase is shown in orange. At a lower spectral radiance and with its distinct jump between 680–730 nm, the *near infrared edge* of vegetation on the ground (green line), is easy to recognize due to the spectral signature of chlorophyll.

Figure 5.21a shows the true-color image corresponding to Figure 5.20 that was rendered using spectral radiance data from the VNIR camera. Calibrated radiances at 2200 and 2100 nm are shown below in Figure 5.21b and c. Since the ice absorption is stronger at 2100 nm compared to 2200 nm the cloud ice phase becomes visible as evident drop in radiance at 2200 nm.

Corresponding to the shaded regions in Figure 5.20, Figure 5.22 shows the spatial distribution of the overall radiometric 2σ uncertainty for the same scene

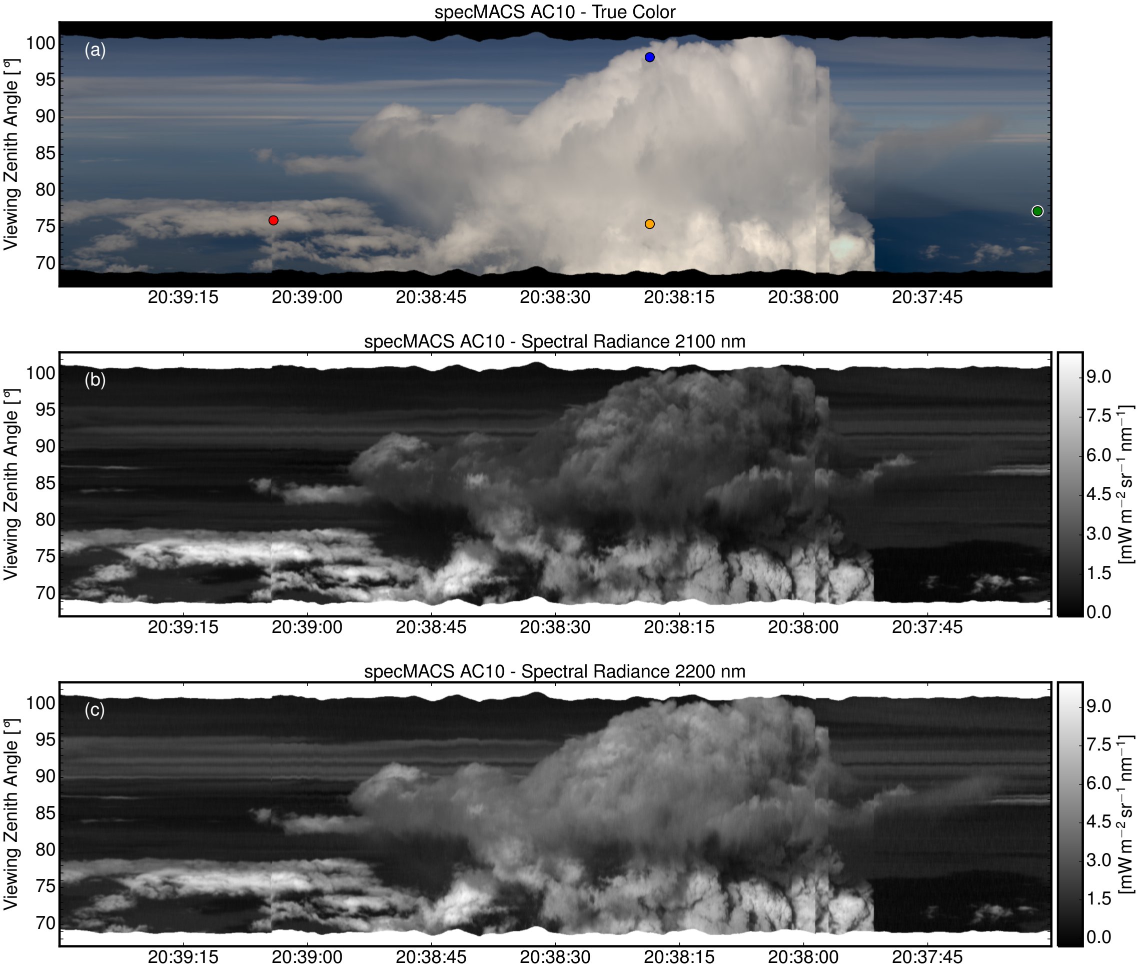

Figure 5.21: Spectral measurements of cloud sides taken with *specMACS* onboard HALO during ACRIDICON-CHUVA campaign in Brazil. **(a)** True-color RGB calculated from the hyperspectral image, **(b)** Spectral radiance image at 2100 nm, **(c)** Spectral radiance image at 2200 nm. The ice phase is clearly visible as a distinct drop of the spectral radiances from panel **(c)** at 2200 nm to panel **(b)** at 2100 nm. The drop in radiance can be explained by the stronger ice absorption coefficient at 2100 nm compared to 2200 nm.

at the near-infrared wavelength 870 nm (Figure 5.22a) and the shortwave infrared wavelength 2100 nm (Figure 5.22b). At 870 nm, the radiometric error is very low (¡5 %) for well illuminated clouds and ground regions. Shaded ground and clear-sky regions exhibit larger radiometric uncertainty of up to 10 %. Due to a lower sensor sensitivity, the same radiometric uncertainty is given for well illuminated cloud scenes at 2100 nm. Here, radiances from shaded cloud and ground regions can only be determined with a very large uncertainty of 20 % or more. In the SWIR spectral range, the limiting factor to radiometric accuracy is the unknown dark signal drift between dark frame measurements.

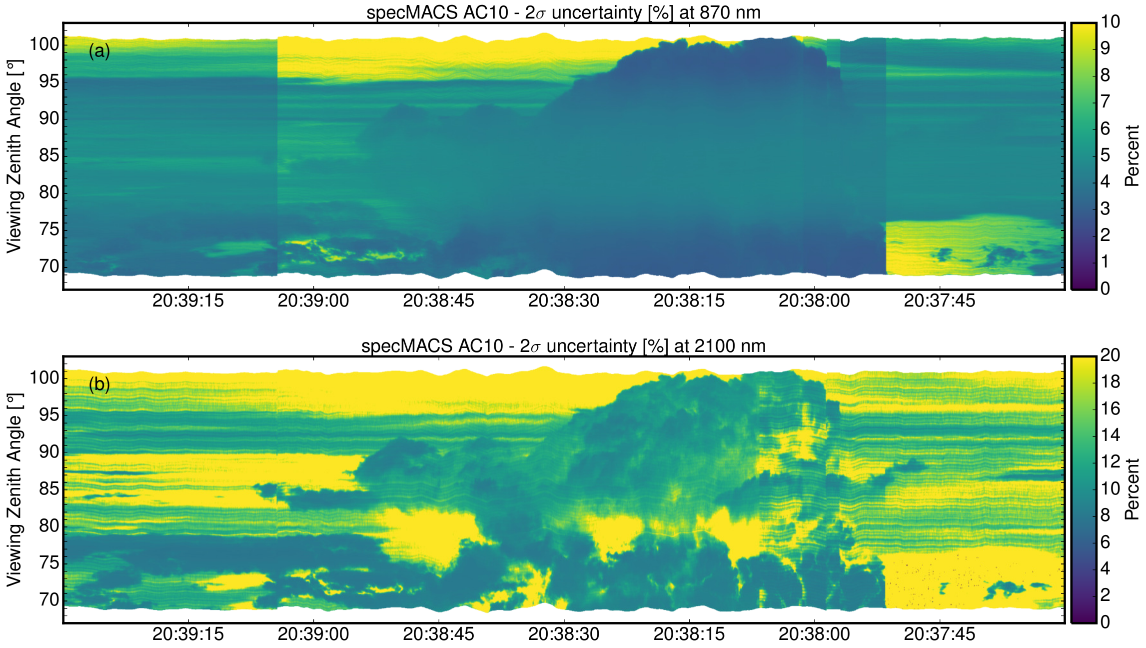

Figure 5.22: Relative uncertanties (2σ) in percent for the spectral measurements of cloud sides shown in Figure 5.21 **(a)** at 870 nm and **(b)** at 2100 nm.

CHAPTER 6

Application to cloud side measurements

After the statistical retrieval has been introduced and thoroughly tested in Section 4.2, it will now be taken to the field to be tested on real-world case studies. For that purpose, the algorithm will be applied to measurements of solar radiance reflected from cloud sides that were acquired with the *specMACS* instrument during two field campaigns. By that way, the implementation (Section 4.2) and the numerical analysis (Section 4.3) of the retrieval will be put to the test and verified. Furthermore, the proposed retrieval approach will be validated with independent in situ observations. During the airborne field campaign, *specMACS* remote sensing measurements have been made simultaneously with corresponding in situ measurements of cloud microphysics. The comparison with these in situ measurements will test the validity of the proposed retrieval approach.

6.1 Ground-based application

6.1.1 Shallow cumulus during the HOPE-Melpitz campaign

One of the first ground-based deployments of *specMACS* was during the Observational Prototype Experiment (HOPE) within the German-wide research initiative *High Definition Clouds and Precipitation for Climate Prediction* (HD(CP)2). The HOPE measurement campaign took place in September 2013 near Melpitz, Germany. An exemplary dataset is given in Figure 6.1 which was captured on the Melpitz measurement site (51.5258° N, 12.9278° E) on the 13th September 2013 between $09:29:04$ and $09:30:22$ UTC. According to the nearest quality-assured AERONET station in Leipzig (data courtesy of Albert Ansmann, TROPOS), the aerosol optical thickness τ_a^{550} for $550\,\mathrm{nm}$ at 09:37:00 UTC was 0.24 ($\tau_a^{550} = 0.19$ averaged over the day) and therefore slighly higher than in the Monte Carlo ensemble with $\tau_a^{550} = 0.15$. The first panel (Figure 6.1a) shows a true-color image that was rendered using spectral radiance data from the VNIR camera. The image was captured by moving the scanning mount anti-clockwise starting from a northward pointing direction ($\phi = 2°\,\mathrm{N}$ to $\phi = 210°\,W$). At the time of this

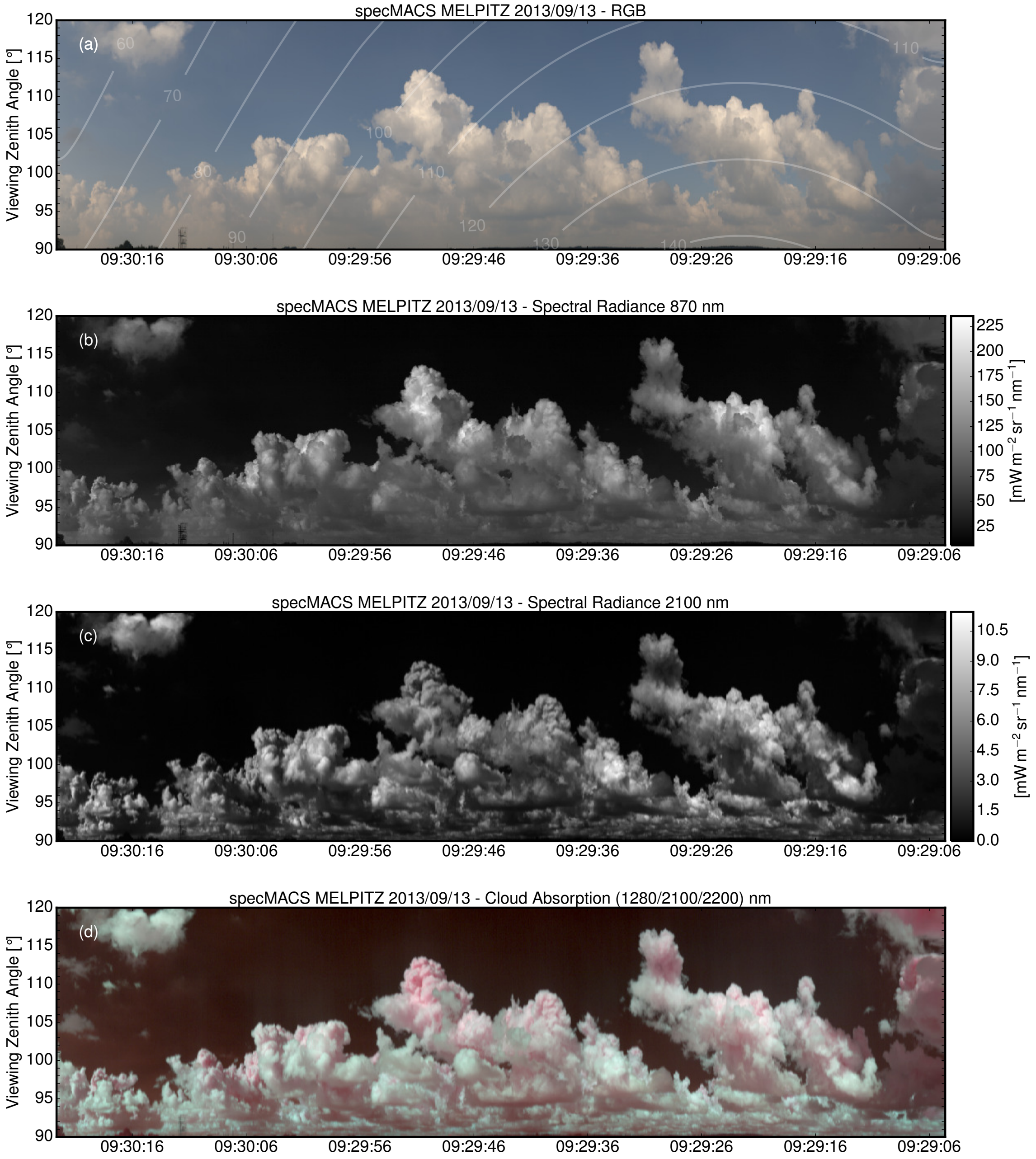

Figure 6.1: **(a)** True-color image between $9\,\mathrm{h}\,29\,\mathrm{min}\,6\,\mathrm{s}$ and $9\,\mathrm{h}\,30\,\mathrm{min}\,20\,\mathrm{s}$ UTC as measured on the 13th September 2013 during the HOPE-Melpitz campaign. Superimposed are isolines of same scattering angle ϑ_s. **(b)** Calibrated spectral radiances at $\lambda = 870\,\mathrm{nm}$ and **(c)** at $\lambda = 2100\,\mathrm{nm}$ in $\mathrm{m}W\,\mathrm{m}^{-2}\,\mathrm{sr}^{-1}\,\mathrm{nm}^{-1}$. While clouds appear much smoother at $\lambda = 870\,\mathrm{nm}$ due to radiative smoothing, darker cloud tops at $\lambda = 2100\,\mathrm{nm}$ could be an indication for larger cloud droplets. **(d)** The increasing absorption by larger cloud droplets between $\lambda = 1280\,\mathrm{nm}$, $2100\,\mathrm{nm}$ and $2200\,\mathrm{nm}$ is visible by the "'rose"' color in this false color composite.

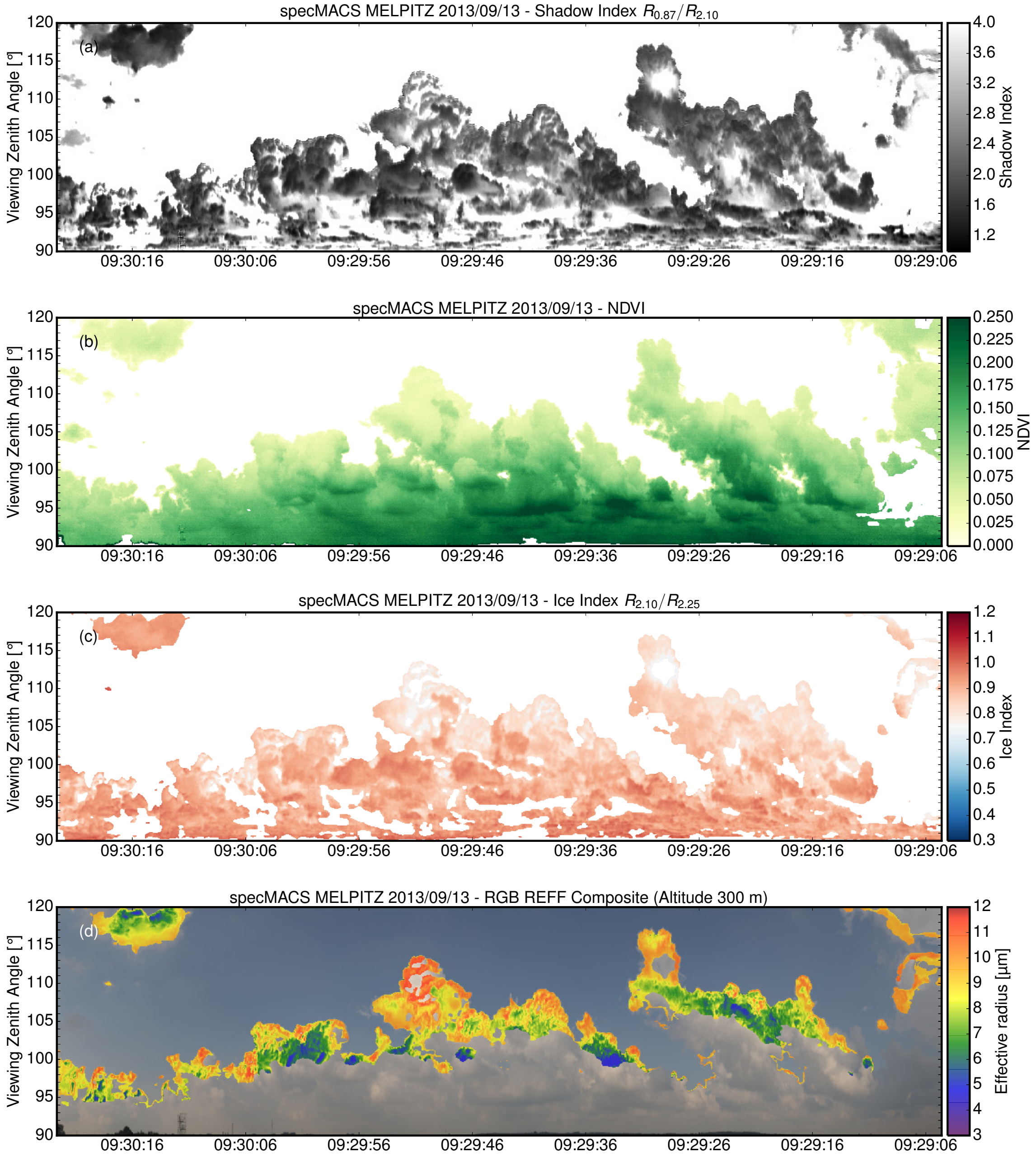

Figure 6.2: Retrieval results between 9 h 29 min 6 s and 9 h 30 min 20 s UTC as derived for the 13th September 2013 during the HOPE-Melpitz campaign, Germany. **(a)** Reflectance ratio $R_{0.87}/R_{2.10}$ between 870 µm and 2.10 µm is used as shadow mask ($R_{0.87}/R_{2.10} > 3.5$) **(b)** Contamination of radiances with vegetation albedo specified by the NDVI between 672 nm and 747 nm. **(c)** Reflectance ratio $R_{2.10}/R_{2.25}$ between 2.10 µm and 2.25 µm used as cloud phase indication (ice: $R_{2.10}/R_{2.25} < 0.75$). **(d)** Mean effective radius r_{eff} in µm as retrieved with the statistical approach described in this thesis.

scan the sun was at an azimuth of $\phi = 149.6°$ and a zenith angle of $\phi = 48.0°$. In Figure 6.1a, corresponding scattering angles towards the sun are shown as isolines. The next two panels show calibrated radiances for the same scene as they were measured with the VNIR spectrometer at 870 nm (Figure 6.1b) and with the SWIR spectrometer at 2100 nm (Figure 6.1c). The more rough appearance of clouds at 2100 nm can be attributed to shorter photon pathlengths due to a higher absorption by cloud droplets at this wavelength. Due to radiative smoothing clouds appear much smoother at $\lambda = 870\,\mathrm{nm}$ when compared to the their rough appearance at $\lambda = 2100\,\mathrm{nm}$. Furthermore, the slightly lower radiance from cloud tops at 2100 nm could be an indication for larger cloud droplets. On the next page, the first three panels in Figure 6.2 show index masks to filter out unwanted influences which were discussed in Section 4.1.3. The first panel (Figure 6.2a) shows the shadow index f_{shad} which is basically the reflectivity ratio $R_{0.87}/R_{2.10}$. An upper global threshold of $f_{\mathrm{shad}} > 3.5$ is used to exclude pixel for which light has likely undergone multiple diffuse reflections The next panel (Figure 6.2b) gives values for f_{NDVI} corresponding to the measured cloud side scene. This normalized reflectivity difference between $\lambda = 0.747\,\mu\mathrm{m}$ and $\lambda = 0.672\,\mu\mathrm{m}$ indicates cloud side regions which are influenced by ground-reflected radiation. Due to the ground-based perspective, very large regions around the cloud bases are masked out by the NDVI threshold $f_{\mathrm{NDVI}} > 0.1$. The high values for f_{NDVI} are furthermore a direct consequence of the relatively low sun elevation at this early time of the day. In this way, cloud sides are illuminated by diffuse reflection from a larger ground region between observer and cloud. As expected on the basis of the low cloud height, the ice index in the third panel (Figure 6.2c) indicates only liquid water clouds. At last, the fourth panel (Figure 6.2d) gives first results of the effective radius retrieval.

Due to very structured cloud sides and some unfiltered cloud shadows, the retrieved effective radii vary quite strongly. However, an overall tendency towards larger droplet sizes with height is evident. The lowest cloud regions not filtered by the NDVI mask show values of r_{eff} of around $5\,\mu\mathrm{m}$. Above these cloud regions, higher effective radius values of around $6\,\mu\mathrm{m}$ to $8\,\mu\mathrm{m}$ are detected. For the highest cloud regions in the center of the image, r_{eff} values of up to $10\,\mu\mathrm{m}$ to $11\,\mu\mathrm{m}$ are reached.

Preliminary results of in situ measurements done with the Airborne Cloud Turbulence Observation System (ACTOS, *Siebert et al.* (2006)) for the same cloud scene showed effective radii between $5\,\mu\mathrm{m}$ to $6\,\mu\mathrm{m}$ at an altitude of $h \approx 1400\,\mathrm{m}$ (personal communication with Holger Siebert). Here, the helicopter-borne in situ measurement platform ACTOS was flying through the upper third of this cloud scene, corresponding to regions were the retrieval suggested droplet radii around $8\,\mu\mathrm{m}$. This would suggest an overestimation of effective radii of around $\Delta r_{\mathrm{eff}} = 2\,\mu\mathrm{m}$ by the retrieval. Subsequent studies with quality-assured ACTOS data could help to validate this ground-based observation. Nevertheless, this comparison already fits into a trend also discovered in the now following validation of airborne measurements.

6.2 Airborne validation

6.2.1 The ACRIDICON-CHUVA campaign on HALO

During September 2014, the combined measurement campaign ACRIDICON-CHUVA took place over the Amazonian rainforest near Manaus, Brazil. The German-led campaign focused on *Aerosol, Cloud, Precipitation, and Radiation Interactions and Dynamics of Convective Cloud Systems* (ACRIDICON) which used the German High Altitude LOng Range (HALO) research aircraft as airborne platform. It "aimed at the elucidation and quantitation of aerosol-cloud-precipitation interactions and their dynamic and radiative effects in convective cloud systems by combination of in situ aircraft observations with remote sensing" (*Wendisch et al.*, submitted). On board the HALO aircraft, the *specMACS* instrument covered the remote sensing of cloud sides, while the *Cloud and Aerosol Spectrometer with Depolarization (CAS-DPOL)* measured in situ cloud droplet size distributions. The *CAS-DPOL* instrument is able to differentiate water droplets from ice crystals in mixed phase clouds (*Baumgardner et al.*, 2011) and was operated by the *German Aerospace Center* (DLR) with *Tina Jurkat* as instrument principal investigator.

6.2.2 Warm cumulus clouds (AC17)

The first presented airborne case study was measured on flight AC17 (27th September 2014) during the ACRIDICON-CHUVA campaign over the Amazonian rainforest in Brazil. The main objective was the characterization of clouds forming over forested and deforested areas to assess the influence of deforestation on cloud microphysics, e.g. effective radius and cloud droplet concentration. After the take-off from Brigadeiro Eduardo Gomes–Manaus International Airport around $14\,\mathrm{h}\ 2\,\mathrm{min}$ UTC, the HALO aircraft headed south to probe clouds over freshly deforested areas in the municipality of Novo Progresso, Pará. Figure 6.3a shows a false color RGB of a VIIRS satellite overpass between $17\,\mathrm{h}\ 38\,\mathrm{min}\ 0\,\mathrm{s}$ and $17\,\mathrm{h}\ 43\,\mathrm{min}\ 0\,\mathrm{s}$ for this region. In Figure 6.3a, the HALO flight track is superimposed with time indicated by color (from blue to red). The HALO position during the VIIRS overpass is marked with the black arrow, where Figure 6.3b shows a zoomed cut-out of cloud top brightness temperatures which were derived from VIIRS measurements at $\lambda = 11.45\,\mu\mathrm{m}$. With the *specMACS* instrument pointing starboard, all VIIRS cloud top temperatures were above $270\,\mathrm{K}$, suggesting that only liquid-phase clouds were present. Figure 6.5 shows *specMACS* measurements that were taken during the overpass shown in Figure 6.3b between $17\,\mathrm{h}\ 38\,\mathrm{min}\ 30\,\mathrm{s}$ and $17\,\mathrm{h}\ 42\,\mathrm{min}\ 30\,\mathrm{s}$ UTC at an altitude of around $3200\,\mathrm{m}$ above mean sea level (amsl). Figure 6.5a shows a true-color image which was derived from VNIR spectra with superimposed isolines of scattering angles ϑ_s. Around $17\,\mathrm{h}\ 41\,\mathrm{min}\ 0\,\mathrm{s}$ UTC, the aircraft executed a sidestep maneuver to sample in situ measurements during a cloud penetration. For the same scene, calibrated spectral radiances

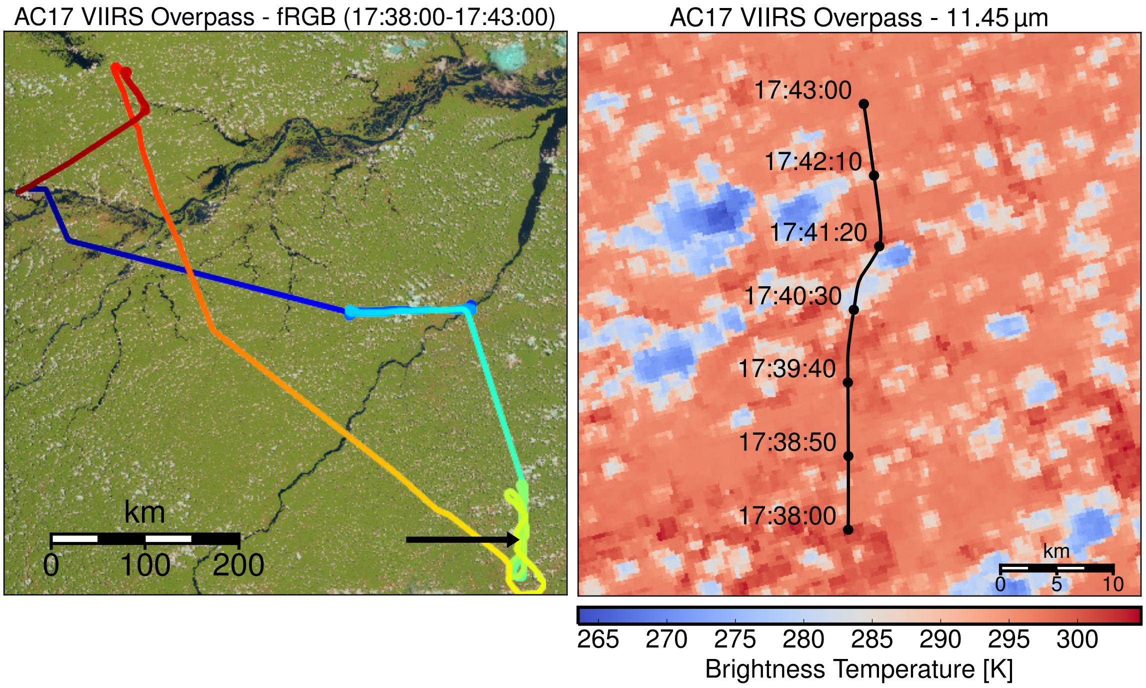

Figure 6.3: (a) False color RGB of the VIIRS satellite overpass between between 17 h 38 min 0 s and 17 h 43 min 0 s during the *specMACS* measurement shown in Figure 6.5. Superimposed is the flight track of the HALO aircraft with time progressing from blue to red. The black arrow annotates the position of the HALO aircraft during the VIIRS overpass. **(b)** Zoomed cut-out of the brightness temperatures of cloud tops as measured by VIIRS at $\lambda = 11.45\,\mu\mathrm{m}$ during the *specMACS* measurement shown in Figure 6.5.

in $\mathrm{mW\,m^{-2}\,sr^{-1}\,nm^{-1}}$are shown in Figure 6.5b at $\lambda = 870\,\mathrm{nm}$ and Figure 6.5c at $\lambda = 2100\,\mathrm{nm}$. Besides the ground albedo, the different appearance of clouds catches the eye when comparing radiances at the non-absorbing and the absorbing wavelength. Furthermore, the slightly darker cloud tops at $\lambda = 2100\,\mathrm{nm}$ could be an indication for larger cloud droplets. This enhanced absorption by cloud droplets becomes more noticeable in Figure 6.5c, where spectral radiances are combined into a false color composite with $1280\,\mathrm{nm}$ (divided by 7) for the red channel, $2100\,\mathrm{nm}$ for the green channel and $2200\,\mathrm{nm}$ for the blue channel. With a higher absorption by clouds (e.g. due to larger cloud droplets), values for the blue ($2200\,\mathrm{nm}$) and, in particular, the green ($2100\,\mathrm{nm}$) channel are lower which results in a ”‘rose”’ color. With the spectral radiances at $870\,\mathrm{nm}$ (Figure 6.5b) and $2100\,\mathrm{nm}$ (Figure 6.5c) as input, Figure 6.6 shows the result of the statistical effective radius retrieval and corresponding indices to filter out unwanted influences. Like in the ground-based case, the first panel (Figure 6.6a) shows the shadow index. In the second panel (Figure 6.6b), the NDVI indicates cloud side regions which are influenced by reflected light from the ground. Since the sun was in the back of the instrument and the aircraft flew over a very wooded area of the Amazonian rain forest, the ground albedo influence cannot be neglected for cloud base regions. The ice index in the next panel (Figure 6.6c) indicates only liquid water clouds which confirms the spaceborne observation of VIIRS brightness temperatures. Finally, the last panel (Figure 6.6d) presents the results of the effective radius retrieval. While the values of r_{eff} vary quite strongly due to unfiltered shadows and very structured cloud sides, a general trend of r_{eff} with altitude is visible. For the very shallow clouds, the retrieval yields very small effective radii between $4\,\mu m$ and $5\,\mu m$ with some cloud parts even outside the lookup table. In horizontal direction at the same altitude $h \approx 3200\,m$ of the aircraft, cloud droplets are larger with r_{eff} between $8\,\mu m$ and $9\,\mu m$. At higher altitudes $h > 3200\,m$, even larger cloud droplets with values of up to $r_{\mathrm{eff}} = 11\,\mu m$ are suggested by the retrieval.

To compare the results of the statistical retrieval with in situ observations of the cloud droplet size distribution, measurements of the *CAS-DPOL* in situ probe were analyzed in Figure 6.4. During the *specMACS* measurement, the HALO aircraft performed a cloud profile measurement starting around $16\,h\ 45\,min$. With the first flight leg at cloud base at $1900\,m$, further cloud penetrations followed at flight legs at $2500\,m$, $3200\,m$ and $3800\,m$. To exclude clear sky or only partly cloudy sections, $1\,Hz$ *CAS-DPOL* r_{eff} measurements were filtered for LWC $> 0.1\,\mu m$. Caused by several wild fires, very high aerosol particle concentrations of around $2300\,cm^{-1}$ were measured below cloud base. Correspondingly, the mean effective radii were quite small with $4.7\,\mu m$ at cloud base, $5.7\,\mu m$ at $2500\,m$, $6.3\,\mu m$ at $3200\,m$ and $7.1\,\mu m$ at $3800\,m$. A last measurement nearly a hour later, showed a mean effective radius of $8.8\,\mu m$ at an altitude of $4500\,m$. Within each height, r_{eff} varied with a standard deviation of up to $0.6\,\mu m$ while the mean water content increased from $0.3\,g\,m^{-3}$ at cloud base to $1.6\,g\,m^{-3}$ at cloud top.

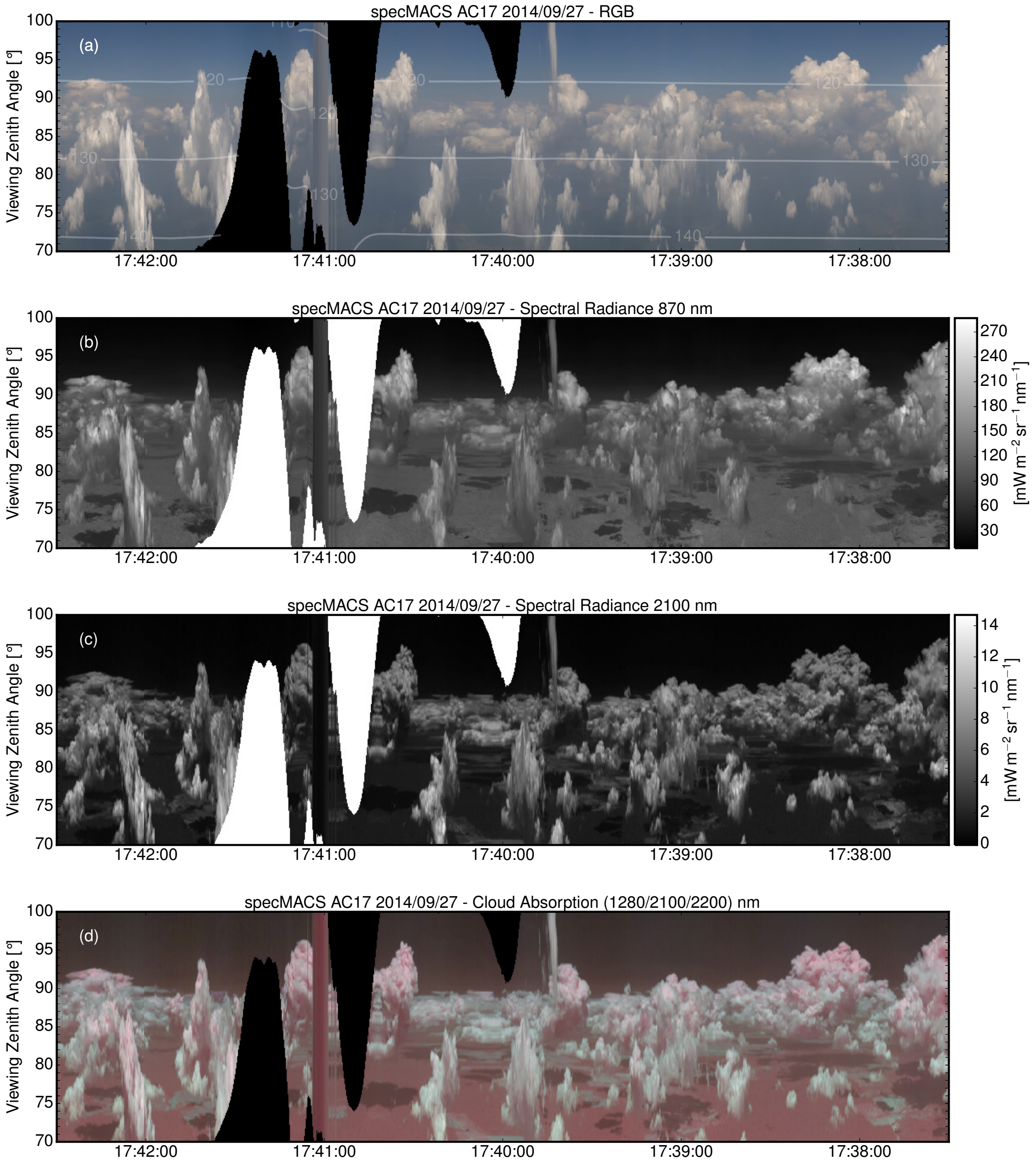

Figure 6.5: **(a)** True-color image between 17 h 38 min 30 s and 17 h 42 min 30 s UTC as measured on flight AC17 during the ACRIDICON-CHUVA 2014 campaign, Brazil. Superimposed are isolines of same scattering angle ϑ_s. **(b)** Calibrated spectral radiances at $\lambda = 870\,\mathrm{nm}$ and **(c)** at $\lambda = 2100\,\mathrm{nm}$ in $\mathrm{mW\,m^{-2}\,sr^{-1}\,nm^{-1}}$. While clouds appear much smoother at $\lambda = 870\,\mathrm{nm}$ due to radiative smoothing, darker cloud tops at $\lambda = 2100\,\mathrm{nm}$ could be an indication for larger cloud droplets. **(d)** The increasing absorption by larger cloud droplets between $\lambda = 1280\,\mathrm{nm}$, $2100\,\mathrm{nm}$ and $2200\,\mathrm{nm}$ is visible by the ″'rose″' color in this false color composite.

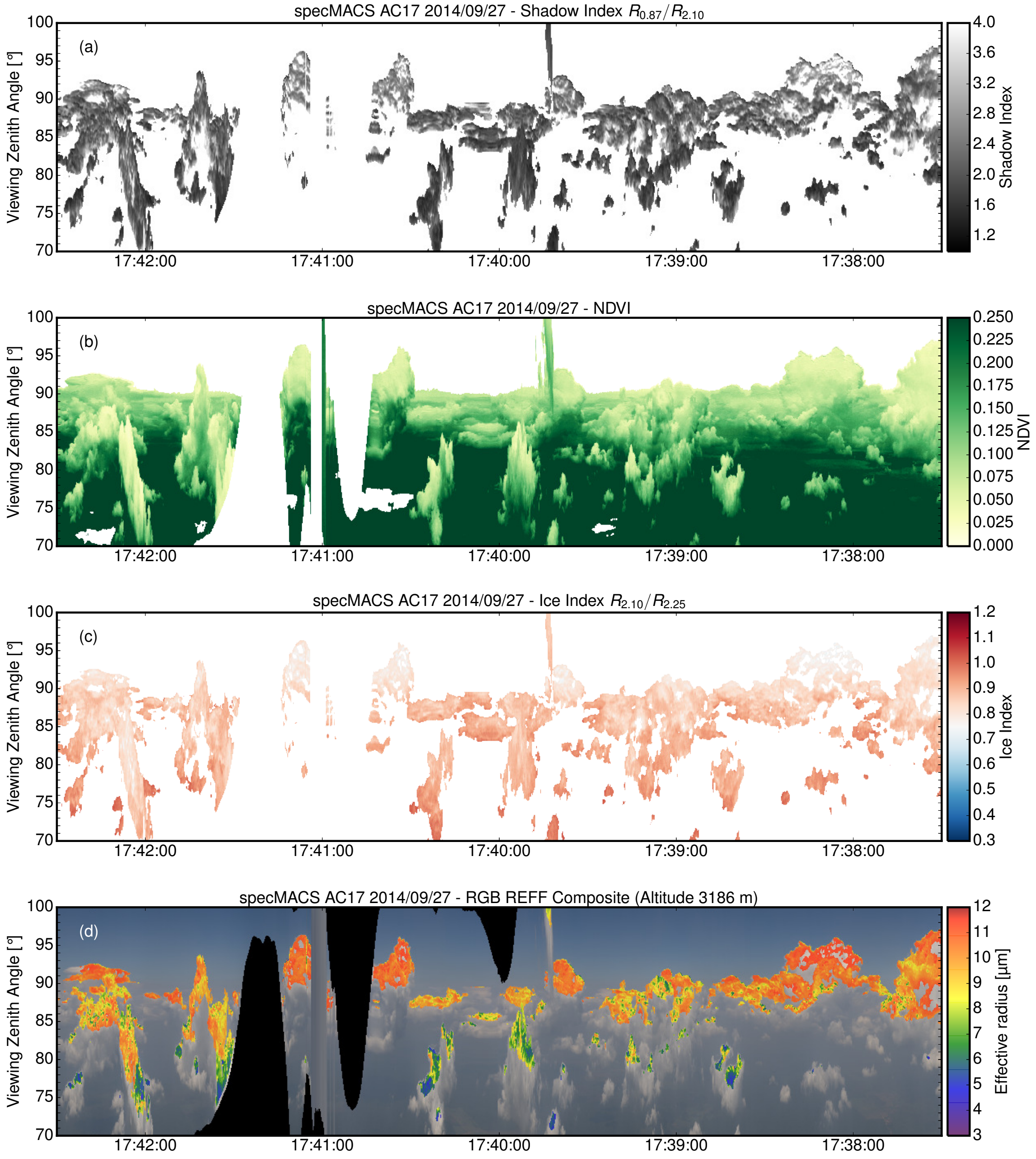

Figure 6.6: Retrieval results between 17 h 38 min 30 s and 17 h 42 min 30 s UTC as derived for flight AC17 during the ACRIDICON-CHUVA 2014 campaign, Brazil. **(a)** Reflectance ratio $R_{0.87}/R_{2.10}$ between 870 µm and 2.10 µm is used as shadow mask ($R_{0.87}/R_{2.10} > 3.5$) **(b)** Contamination of radiances with vegetation albedo specified by the NDVI between 672 nm and 747 nm. **(c)** Reflectance ratio $R_{2.10}/R_{2.25}$ between 2.10 µm and 2.25 µm used as cloud phase indication (ice: $R_{2.10}/R_{2.25} < 0.75$). **(d)** Mean effective radius r_{eff} in µm as retrieved with the statistical approach described in this thesis.

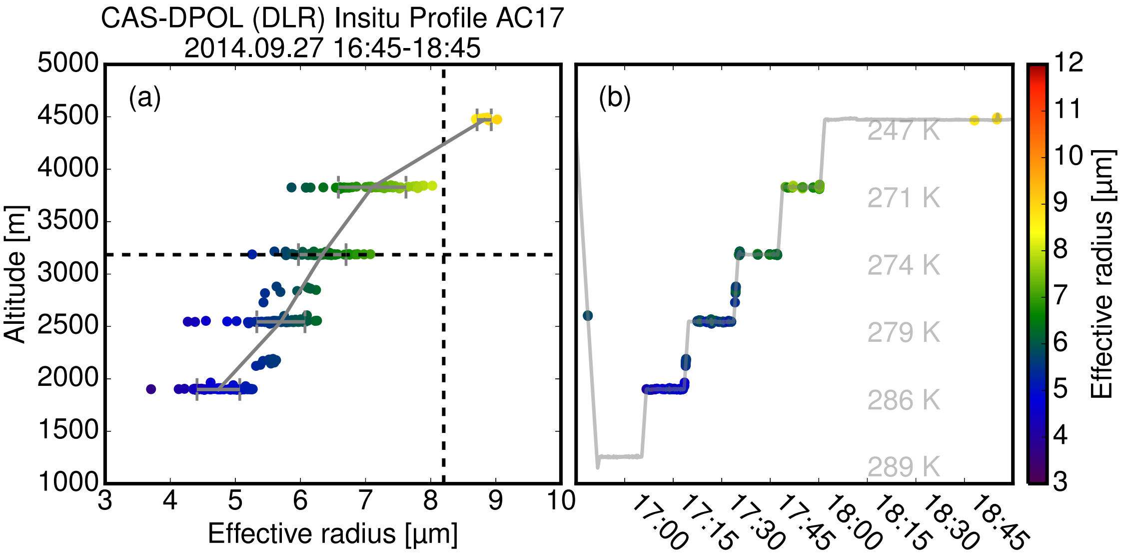

Figure 6.4: **(a)** Profile of effective cloud droplet radii as measured by the *CAS-DPOL* in situ probe for the cloud ensemble shown in Figure 6.5a. Dashed lines indicate the flight altitude and the mean effective radius (in situ) during the remote sensing retrieval of r_{eff} shown in Figure 6.6d. **(b)** Flight profile with effective radii during the cloud probing which was performed between 16 h 45 min and 18 h 45 min UTC (data courtesy of Tina Jurkat, DLR).

At the same altitude ($h = 3200\,\text{m}$) of the *specMACS* measurement, the in situ effective radii of 6.3 µm is smaller by around $\Delta r_{\text{eff}} = 2\,\mu\text{m}$ compared to the retrieved effective radii of around 8.5 µm at the horizontal viewing direction ($\vartheta = 90°$). This overestimation is in line with the observations made for the ground-based perspective. Although results cannot be compared directly for the other heights due to the missing high assignment of *specMACS* measurements, the retrieved profile of increasing r_{eff} with height and the range of retrieved r_{eff} between 4 µm to 9 µm matches the characteristic of the in situ profile quite well.

6.2.3 Deep convection with mixed-phase region (AC13)

The second airborne case study was also measured during the ACRIDICON-CHUVA campaign on flight AC13 (19th September 2014). This time, the main objective was the sampling of cloud profiles around the larger area of Alta Floresta in the state of Mato Grosso and a subsequent sampling of old convective outflows during the return flight to Manaus. Figure 6.7a shows a false color composite of a VIIRS satellite overpass between 16 h 49 min 38 s and 16 h 55 min 52 s UTC for this region. In Figure 6.7b, brightness temperatures measured at $\lambda = 11.45\,\mu\text{m}$ are shown in combination with the HALO flight track for this *specMACS* cloud side case study. Although the satellite overpass was two hours earlier, cloud top temperatures already reach down to 250 K, making onset of icing very likely. Two hours after the satellite overpass, between 18 h 49 min 00 s and 18 h 50 min 30 s UTC, the cloud side measurement shown in Figure 6.8 was made. The true-color image (Figure 6.8a) shows the *specMACS* scan which was acquired at an altitude of around 5400 m during the left turn indicated by the black arrow in Figure 6.7b. In Figure 6.8b and Figure 6.8c shows calibrated radiances at $\lambda = 870\,\mathrm{nm}$ and $\lambda = 2100\,\mathrm{nm}$. At the absorbing wavelength $\lambda = 2100\,\mathrm{nm}$, the absorbing ice clouds stand out as apparent difference to the first case study. This enhanced absorption by ice becomes also evident in Figure 6.8d, where the cloud absorption is indicated by the ”‘rose”’ color due to lower values for the blue (2200 nm) and the green (2100 nm) channel. The enhanced ice absorption is misinterpreted as shadow by the shadow index (Figure 6.9a), which is sensitive due to the use of the 2.1 µm wavelength. Since the effective radius retrieval is only focused on water clouds, this problem should not interfere with the results of the retrieval. It should, however, be noted that the shadow index only works for liquid water clouds; subsequent studies of ice clouds have to use a different technique to exclude shadowed cloud parts. Compared to the first case study, the influence of ground albedo reflection was less as it can be seen by lower

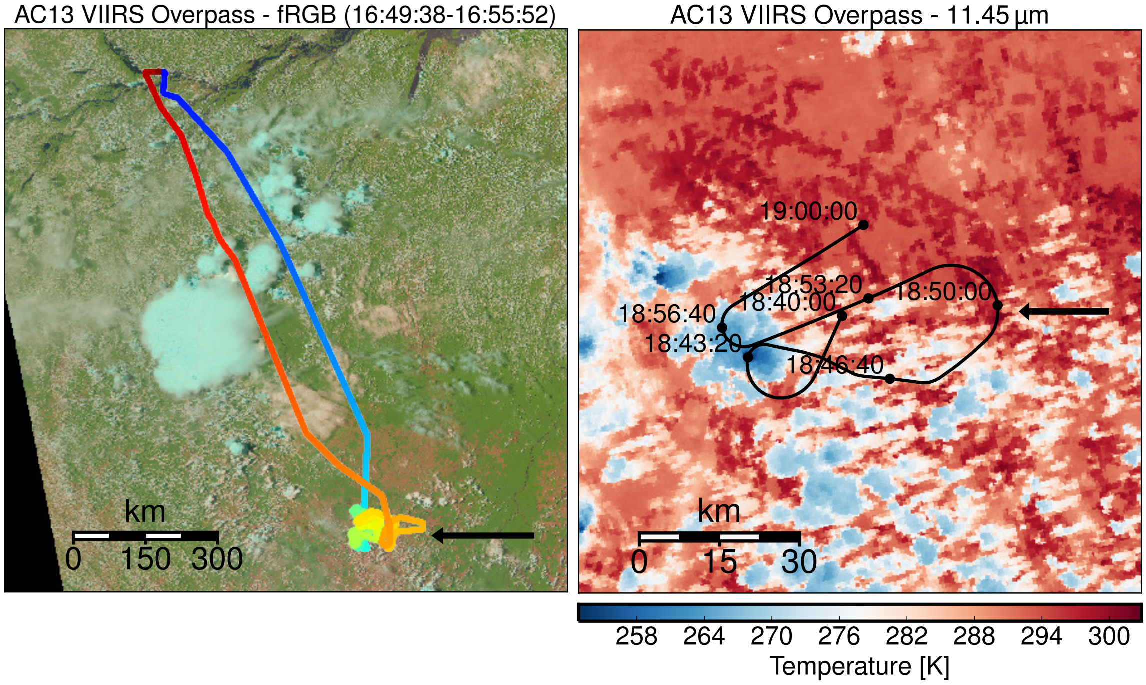

Figure 6.7: **(a)** False color composite of the VIIRS satellite overpass between between 16 h 49 min 38 s and 16 h 55 min 52 s UTC during the *specMACS* measurement shown in Figure 6.8. Superimposed is the flight track of the HALO aircraft with time progressing from blue to red. **(b)** Zoomed cut-out of the region for which two hours later cloud sides were measured with *specMACS*.

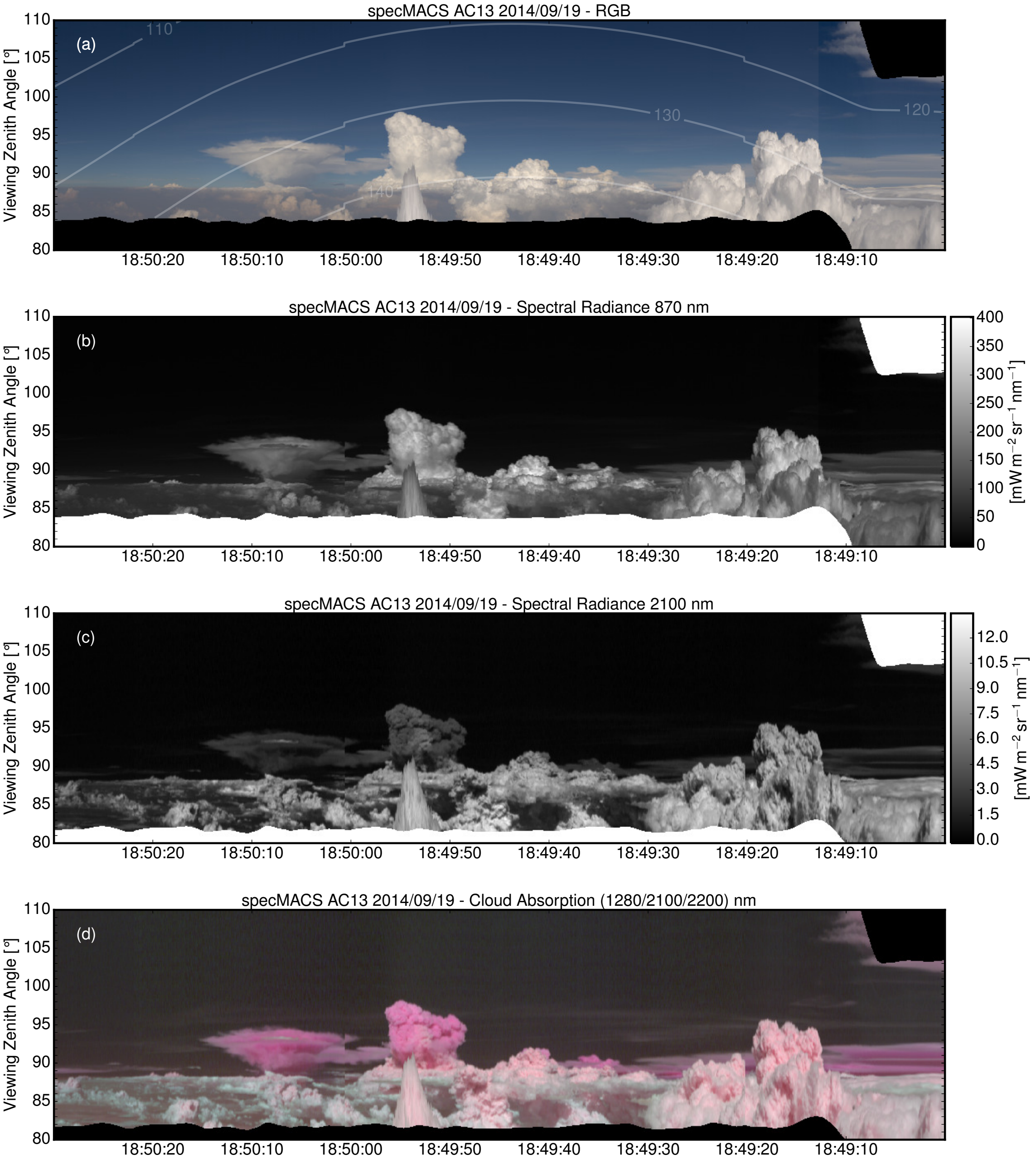

Figure 6.8: **(a)** True-color image between 18 h 49 min 0 s and 18 h 50 min 30 s UTC as measured on flight AC13 during the ACRIDICON-CHUVA 2014 campaign, Brazil. Superimposed are isolines of same scattering angle ϑ_s. **(b)** Calibrated spectral radiances at $\lambda = 870\,\mathrm{nm}$ and **(c)** at $\lambda = 2100\,\mathrm{nm}$ in $\mathrm{mW\,m^{-2}\,sr^{-1}\,nm^{-1}}$. While clouds appear much smoother at $\lambda = 870\,\mathrm{nm}$ due to radiative smoothing, darker cloud tops at $\lambda = 2100\,\mathrm{nm}$ could be an indication for larger cloud droplets. **(d)** The increasing absorption by larger cloud droplets between $\lambda = 1280\,\mathrm{nm}$, $2100\,\mathrm{nm}$ and $2200\,\mathrm{nm}$ is visible by the "'rose"' color in this false color composite.

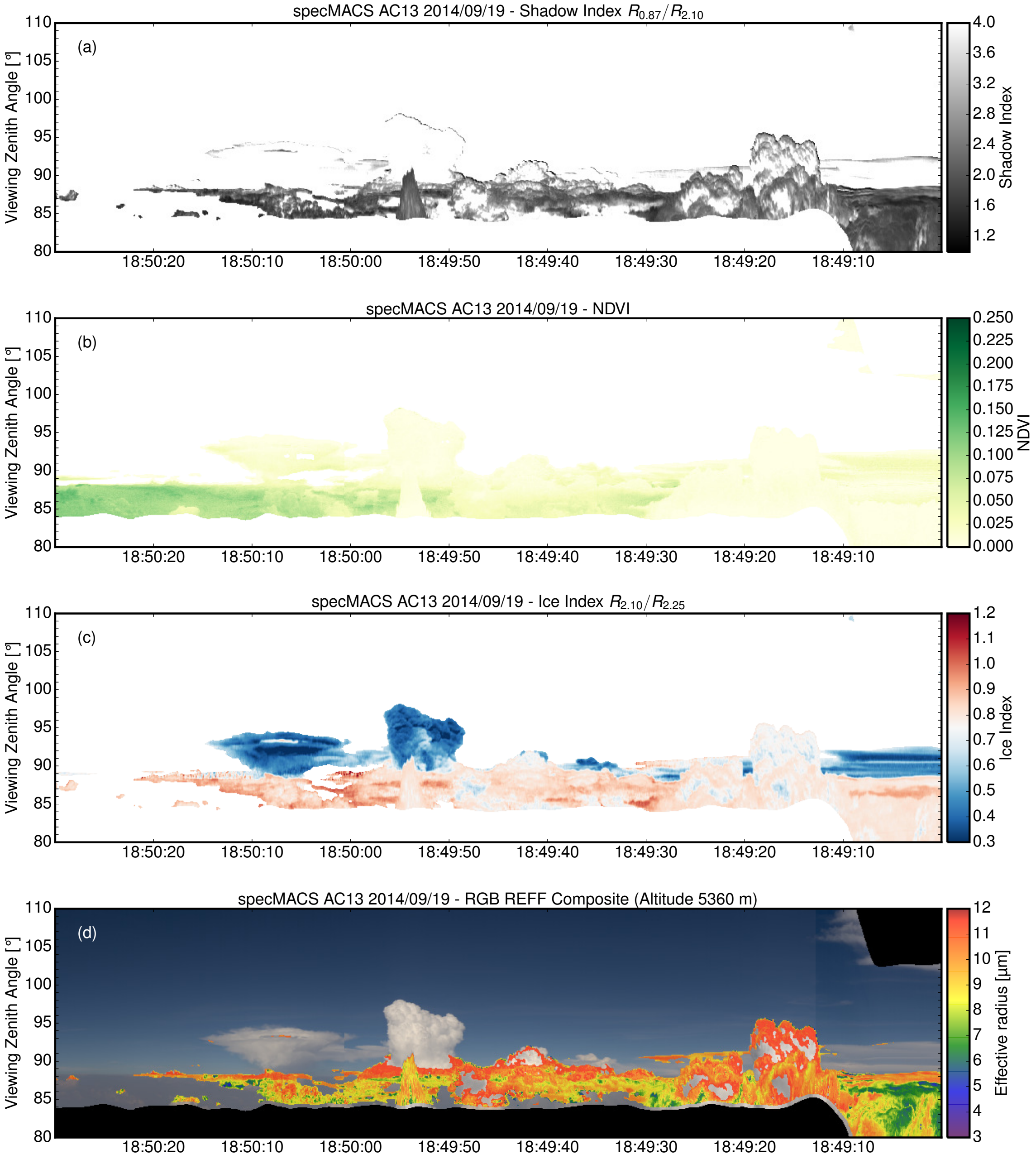

Figure 6.9: Retrieval results between 18 h 49 min 0 s and 18 h 50 min 30 s UTC as derived for flight AC13 during the ACRIDICON-CHUVA 2014 campaign, Brazil. **(a)** Reflectance ratio $R_{0.87}/R_{2.10}$ between 870 µm and 2.10 µm is used as shadow mask ($R_{0.87}/R_{2.10} > 3.5$) **(b)** Contamination of radiances with vegetation albedo specified by the NDVI between 672 nm and 747 nm. **(c)** Reflectance ratio $R_{2.10}/R_{2.25}$ between 2.10 µm and 2.25 µm used as cloud phase indication (ice: $R_{2.10}/R_{2.25} < 0.75$). **(d)** Mean effective radius r_{eff} in µm as retrieved with the statistical approach described in this thesis.

NDVI values in Figure 6.9b. Due to the higher flight altitude, this case includes more cloud tops and therefore less cloud bases with potential ground albedo influence. The ice index in the next panel (Figure 6.9c) shows now clear signs of ice beginning from the flight level at a viewing zenith angle of $\vartheta = 90°$ upwards. With an ice index approaching the 0.75 threshold, the convective cell around $18\,\mathrm{h}\ 49\,\mathrm{min}\ 15\,\mathrm{s}$ shows signs of an onset of icing. The phase of the cloud deck at the beginning of the measurement should still be liquid according to its ice index. The result of the effective radius retrieval is shown in the last panel (Figure 6.9d). Compared to the first case study, this retrieval results show a slightly different picture with even larger values for r_{eff} and regions with excluded ice phase or undetected mixed-phase regions. Here, the retrieval results are not masked out until a phase index of < 0.70 (instead of using the 0.75 threshold) in order to show the retrieval behavior in the transition region between liquid and mixed-phase cloud. Nevertheless, a profile with increasing values for r_{eff} with altitude is still detectable within the liquid phase region. For the cloud deck at the beginning of the measurement, the retrieval returns effective radii between $6\,\mu\mathrm{m}$ and $8\,\mu\mathrm{m}$. At the flight altitude of $h \approx 5400\,\mathrm{m}$, larger effective radii between $9\,\mu\mathrm{m}$ and $11\,\mu\mathrm{m}$ are retrieved for the horizontal viewing direction ($\vartheta = 90°$). These retrieval results have to be considered carefully, though: due to the potential of mixed-phase cloud regions, the retrieved effective radius values could be too large for the cloud droplets that are still liquid. At higher altitudes $h > 5400\,\mathrm{m}$, very large effective radii $r_{\mathrm{eff}} > 11\,\mu\mathrm{m}$ are returned by the retrieval, with many pixels outside the lookup table. These results should clearly be rejected since most pixels above the flight level show ice index values of 0.75 or below.

Just like for the first case study, the *CAS-DPOL* measurements were used to compare the in situ effective radii with the results from the statistical retrieval in Figure 6.10. The cloud profile measurement started around $17\,\mathrm{h}\ 0\,\mathrm{min}$, with the first flight leg at cloud base. In total, cloud penetrations were performed at 11 flight levels, starting from cloud base at $2100\,\mathrm{m}$ going up to $9300\,\mathrm{m}$ in steps of $75\,\mathrm{m}$ to $665\,\mathrm{m}$. Again, $1\,\mathrm{Hz}$ *CAS-DPOL* r_{eff} measurements were filtered for LWC $> 0.1\,\mu\mathrm{m}$ to exclude only partly cloudy sections. Like in the first case, very high aerosol particle concentrations of over $3000\,\mathrm{cm}^{-1}$ could be measured below cloud base. At cloud base, the mean effective radii were therefore quite small with $4.2\,\mu\mathrm{m}$. Droplet sizes then increased in size, reaching $5.8\,\mu\mathrm{m}$ at $3500\,\mathrm{m}$, $6.3\,\mu\mathrm{m}$ at $3200\,\mathrm{m}$ and $9.4\,\mu\mathrm{m}$ at $6400\,\mathrm{m}$. Beginngin at this level, with temperatures ($T = 269\,\mathrm{K}$) slighly below the freezing point, ice particles and liquid droplets were simultaneous measured in mixed-phase cloud regions with an effective liquid water droplet radius of $10\,\mu\mathrm{m}$.

At the time the *specMACS* measurement was taken at an altitude of ($h = 3200\,\mathrm{m}$), the aircraft was descending from this mixed-phase cloud region with r_{eff} between $9\,\mu\mathrm{m}$ and $10\,\mu\mathrm{m}$ above this altitude. The mean effective radius of $9.6\,\mu\mathrm{m}$ retrieved for the horizontal viewing direction ($\vartheta = 90°$) would be in very good agreement with the in situ measurements above. Like in the first airborne example, the in situ effective radii of $r_{\mathrm{eff}} = 7.7\,\mu\mathrm{m}$ measured at the same altitude $h = 3200\,\mathrm{m}$ (around $18\,\mathrm{h}\ 40\,\mathrm{min}$ UTC) are again smaller by around $\Delta r_{\mathrm{eff}} = 2\,\mu\mathrm{m}$ compared to the retrieved effective radii at the horizon. Summarized, all three examples showed the same trend to larger effective radii (with $\Delta r_{\mathrm{eff}} = 2\,\mu\mathrm{m}$) compared to the in situ measurements.

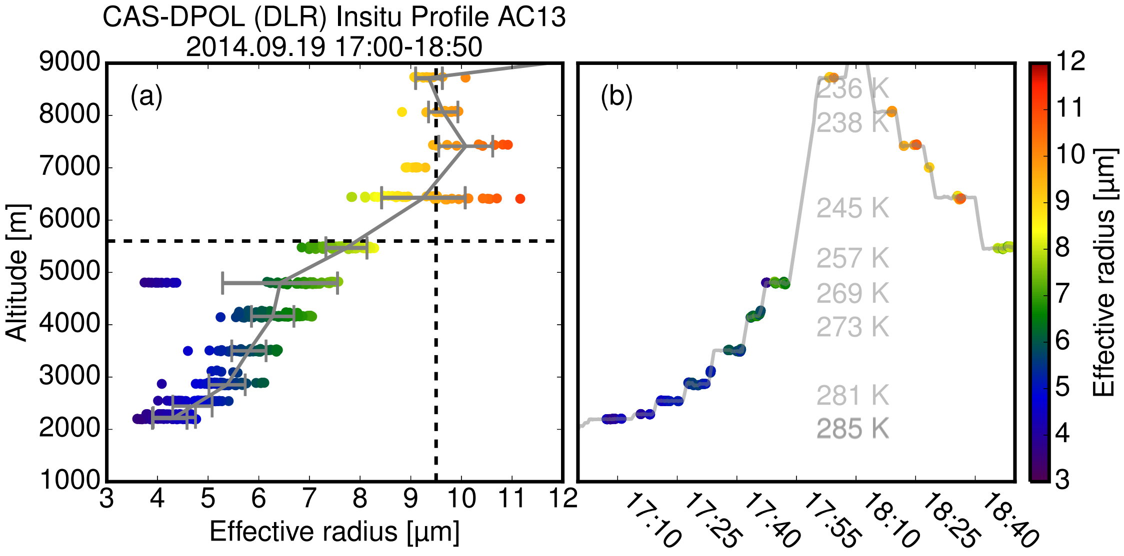

Figure 6.10: **(a)** Profile of effective cloud droplet radii as measured by the *CAS-DPOL* in situ probe for the cloud ensemble shown in Figure 6.8a. Dashed lines indicate the flight altitude and the mean effective radius (in situ) during the remote sensing retrieval of r_{eff} shown in Figure 6.9d. **(b)** Flight profile with effective radii during the cloud probing which was performed between $17\,\mathrm{h}\ 0\,\mathrm{min}$ and $18\,\mathrm{h}\ 50\,\mathrm{min}$ UTC (data courtesy of Tina Jurkat, DLR).

CHAPTER 7

Discussion of uncertainties

The previous chapter has shown that the statistical effective radius retrieval can be applied to airborne as well as to ground-based measurements of cloud sides. The statistical retrieval detected effective radii increasing with height in agreement with measured in situ profiles. However, the comparison of retrieval results at the horizon ($\vartheta = 90°$) with in situ measurements at the same altitude suggest an overestimation of effective radii of around $\Delta r_{\text{eff}} = 2\,\mu\text{m}$ by the retrieval. This bias turned out to be consistent in all three cases. The overestimation by $\Delta r_{\text{eff}} = 2\,\mu\text{m}$ cannot be explained solely by the already discussed retrieval uncertainties since the numerical analysis of the statistical retrieval uncertainty in Section 4.3.2 showed uncertainties in the range of $1\,\mu\text{m} \text{to} 1.5\,\mu\text{m}$ but no significant bias.

7.1 Differences with in situ measurements

There exist several possibilities to explain this difference between retrieved and in situ measured droplet sizes. First and foremost, the in situ measurements were done mostly in the inner core of clouds. In contrast, the cloud side retrieval is sensitive to cloud droplet sizes within the outer cloud shell. Although many in situ studies have shown that r_{eff} is constant at a certain height (*Blyth and Latham*, 1991, *Brenguier et al.*, 2000, *Freud et al.*, 2008), the negatively buoyant subsiding shell found in convective clouds by *Wang et al.* (2009) and *Katzwinkel et al.* (2014) can have an impact on cloud microphysics. Larger cloud droplets from above could be transported down, leading to larger droplet sizes within this subsiding shell when compared to the inner core of the cloud. A further explanation could be the influence of lateral entrainment on microphysics which was already introduced in Section 3.2.2. There exist several studies which suggest that entrainment can lead to a *super-adiabatic droplet growth* such that larger cloud droplets are found at cloud edges and not within cloud cores (*Baker et al.*, 1980, *Jensen et al.*, 1985). The cause for this *droplet spectrum broadening* is either seen in higher supersaturation due to a diminished number of cloud droplets in diluted cloud regions (*Lasher-trapp et al.*, 2005, *Yang et al.*, 2016) or is attributed to turbulence which can substantially accelerate the appearance of large droplets (*Falkovich et al.*, 2002, *Pinsky and Khain*, 1997). However, the actual microphysical processes during the mixing of clear air parcels with cloudy parcels are still a matter of scientific debate.

A further issue to consider is the fact that the in situ measured clouds were not exactly the same clouds measured with *specMACS*. Another problem could be connected with the proposed retrieval technique itself. On the one hand, higher aerosol concentrations could extinguish more solar radiation between sun and cloud or cloud and observer and could thus lead to larger droplet sizes. On the other hand, the absolute radiometric uncertainty of *specMACS* could introduce a bias towards lower radiances. This could also lead to larger droplet sizes. While the influence of varying aerosol concentrations is left to be discussed in Chapter 8, the following section will put the retrieval uncertainty associated with the absolute radiometric uncertainty of *specMACS* into context with the statistical retrieval uncertainty. On the basis of this comparison, the absolute radiometric uncertainty and the suitability of the *specMACS* instrument to retrieve effective radius profiles from cloud sides will be discussed.

7.2 Comparison of uncertainties

In the following, the *statistical retrieval uncertainty* is the 1-sigma standard deviation of the posterior distribution for r_{eff} as already defined in Equation 4.31. Reciting the radiometric accuracy requirements specified in Section 5.1.2, the radiometric calibration uncertainty should be well below this statistical retrieval uncertainty. This should also apply to the absolute radiometric uncertainty of a specific cloud scene which is determined following the overall radiometric uncertainty budget in Section 5.3.1. In order to compare the absolute radiometric uncertainty in $mW\,m^{-2}\,sr^{-1}\,nm^{-1}$with the statistical retrieval uncertainty of r_{eff} in μm, the absolute radiometric uncertainty is converted into a retrieval uncertainty in r_{eff}. Figure 7.1 illustrates the conversion of absolute radiometric uncertainties in $L_{0.87}$ and $L_{2.10}$ into a corresponding retrieval uncertainty in r_{eff}. To this end, additional retrievals of r_{eff} (red crosses in Figure 7.1) are made by alternately adding and subtracting the corresponding absolute radiometric uncertainties of $L_{0.87}$ and $L_{2.10}$. Indicated by the green arrow in Figure 7.1, the maximum difference between obtained r_{eff} values is subsequently determined. This difference is halved to make it comparable with the standard deviations describing the statistical retrieval uncertainty. Hereafter, the retrieval uncertainty due to the absolute radiometric uncertainty will be referred to as the *radiometric retrieval uncertainty*.

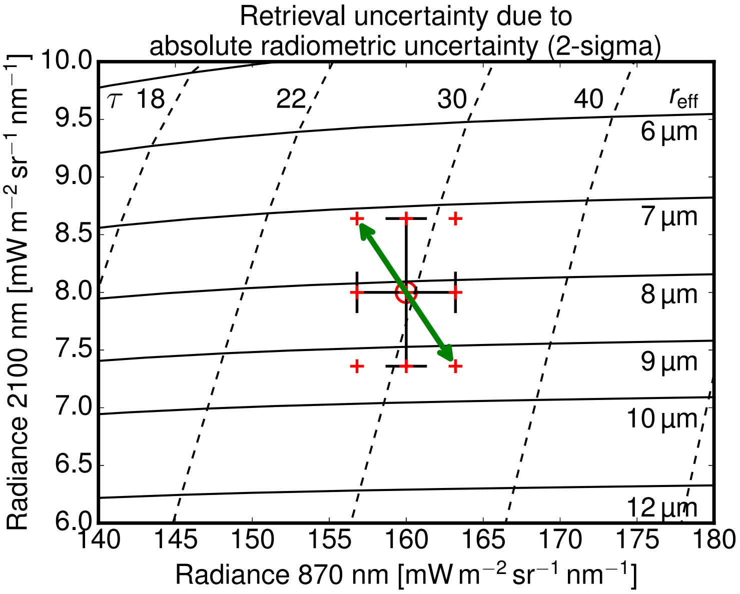

Figure 7.1: Illustration how maximum radiometric uncertainties in $L_{0.87}$ and $L_{2.10}$ (error bars) are converted into a maximum retrieval uncertainty in r_{eff} which is indicated by the green arrow. Drawn lines are isolines of r_{eff}, dashed lines are isolines of τ.

7.2.1 Ground-based measurement of shallow cumulus clouds

For the ground-based measurement of shallow cumulus clouds in Section 6.1.1, the comparison between statistical retrieval uncertainty and radiometric retrieval uncertainty is shown in Figure 7.2 The first two panels (Figure 7.2a, Figure 7.2b) display the absolute radiometric uncertainty in percent for spectral radiances at $\lambda = 870\,\mathrm{nm}$ and $\lambda = 2100\,\mathrm{nm}$. As described in the overall radiometric uncertainty budget in Section 5.3.1, maximum errors (Δ) are being used here to approximate the 2-sigma bounds for the absolute radiometric uncertainty. While the absolute radiometric uncertainty for well-lit cloud sides ($L_{0.87} > 100\,\mathrm{mW\,m^{-2}\,sr^{-1}\,nm^{-1}}$) averages out at 3.3 % at $\lambda = 870\,\mathrm{nm}$ for the VNIR spectrometer, it adds up to 9.2 % at $\lambda = 2100\,\mathrm{nm}$ for the SWIR spectrometer. For these well-lit cloud sides, the absolute radiometric accuracy for both wavelengths is limited by the radiometric calibration uncertainty. At very low signal levels, e.g. for clear sky measurements, uncertainty due to dark signal drift dominates and increases the absolute radiometric uncertainty well above 10 % for the VNIR and well above 20 % for the SWIR. The next panel (Figure 7.2c) shows the statistical retrieval uncertainty in r_{eff} corresponding to the 1-sigma standard deviation of the posterior distribution for r_{eff}. In comparison, the last panel (Figure 7.2d) shows the radiometric retrieval uncertainty in r_{eff}. Apparently, the mean of this radiometric retrieval uncertainty with 0.35 µm is well below the mean statistical retrieval uncertainty of 1.82 µm. Even though maximum radiometric uncertainties are being used to estimate the influence on the retrieval, the statistical retrieval uncertainty is considerably larger compared to the radiometric retrieval uncertainty.

7.2.2 Airborne measurement of warm cumulus clouds (AC17)

For the first discussed example measured on flight AC17, Figure 7.3 summarizes the comparison between statistical retrieval uncertainty and radiometric retrieval uncertainty. Figure 7.3a shows the absolute radiometric uncertainty in percent for $\lambda = 870\,\mathrm{nm}$, while the following Figure 7.3b shows it for $\lambda = 2100\,\mathrm{nm}$. Like in the first case, the absolute radiometric accuracy for the well-lit cloud sides ($L_{0.87} > 100\,\mathrm{mW\,m^{-2}\,sr^{-1}\,nm^{-1}}$) is mainly limited by the radiometric calibration uncertainty. Therefore, the absolute radiometric uncertainty amounts to similar 3.1 % at $\lambda = 870\,\mathrm{nm}$ and to 8.9 % at $\lambda = 2100\,\mathrm{nm}$ for these cloud sides. Using the 1-sigma standard deviation of the posterior distribution for r_{eff}, the statistical retrieval uncertainty in r_{eff} is shown in Figure 7.3c. This is contrasted with the radiometric retrieval uncertainty in r_{eff} in Figure 7.3d. Similar to the ground-based case, the mean radiometric retrieval uncertainty with 0.41 µm is well below the mean statistical retrieval uncertainty of 1.35 µm.

7.2.3 Airborne measurement of deep convection (AC13)

For the second airborne case (flight AC13), Figure 7.4 shows the comparison between statistical and radiometric retrieval uncertainty. Again, the first two panels (Figure 7.4a and Figure 7.4b) show the absolute radiometric uncertainty in percent for spectral radiances at $\lambda = 870\,\mathrm{nm}$ and $\lambda = 2100\,\mathrm{nm}$. Very similar to the first airborne case, the absolute radiometric uncertainty for well-lit cloud sides is around 3.4 % at $\lambda = 870\,\mathrm{nm}$ for the VNIR spectrometer and around 9.1 % at $\lambda = 2100\,\mathrm{nm}$ for the SWIR spectrometer. Where signal levels are very low, e.g. clear sky measurements but also cloud shadows, the dark signal drift remains the dominating factor for the absolute radiometric uncertainty with levels above 10 % for the VNIR and well above 20 % for the SWIR. The following two panels (Figure 7.4c, Figure 7.4d) again compare the statistical retrieval uncertainty with the radiometric retrieval uncertainty. In line with the first airborne example, the absolute radiometric uncertainty causes a mean radiometric retrieval uncertainty of 0.47 µm, while the statistical retrieval uncertainty is around 1.50 µm.

In summary, it can be concluded that the radiometric retrieval uncertainty remains well below the statistical retrieval uncertainty in all three discussed cases. Consequently, the radiometric retrieval uncertainty can not explain the observed retrieval overestimation observed in all three cases. Overall, the estimated radiometric retrieval uncertainty is three times smaller than the 1-sigma standard deviation of the posterior distribution for r_{eff}. This 1-sigma standard deviation is intrinsically limited by three-dimensional radiative transfer effects in cloud sides. In contrast, the actual 1-sigma radiometric retrieval uncertainty will be even smaller since maximum error estimates have been used to cover dark signal drift, nonlinearity uncertainty, polarization sensitivity and during the effective radius conversion in Section 7.2. Moreover, the radiometric retrieval uncertainty can be further lowered as soon as the absolute radiometric standard accuracy is increased by the *PTB* or a reliable dark signal drift model becomes available.

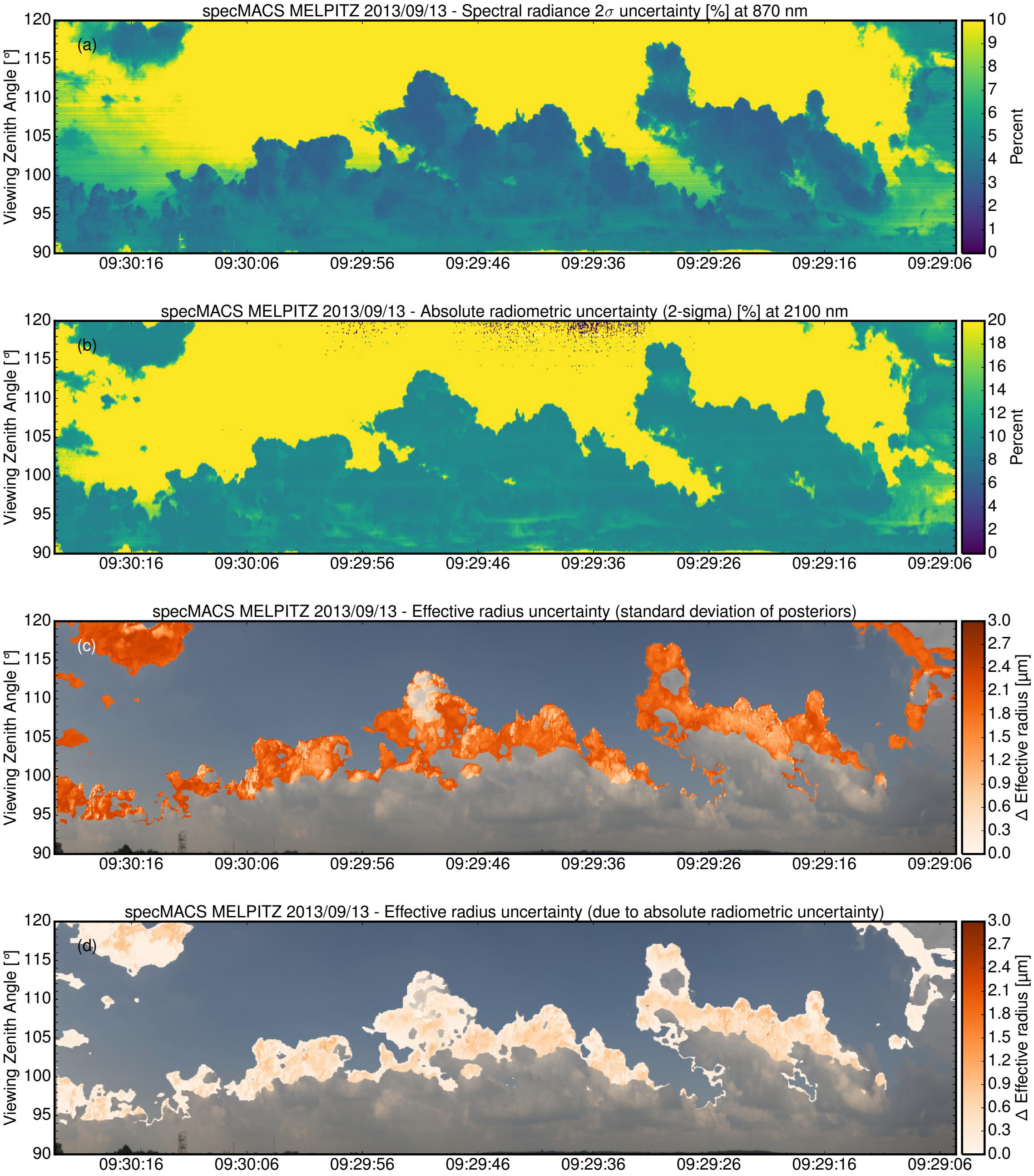

Figure 7.2: Comparison between retrieval and absolute radiometric uncertainties for the ground-based scene shown in Figure 6.1. **(a)** Absolute radiometric uncertainty (2-sigma) in percent for the spectral radiance at $\lambda = 870$ nm determined as described in Section 5.3.1. **(b)** Absolute radiometric uncertainty (2-sigma) for $\lambda = 2100\,\mathrm{nm}$ which is significantly higher due to the higher uncertainty of the radiometric standard and lower sensor sensitivity. Where signal levels are very low (clear sky), uncertainty due to dark signal drift dominates. **(c)** Statistical retrieval uncertainty in r_{eff} corresponding to the 1-sigma standard deviation of the posterior distribution for r_{eff} as described by Equation 4.31. **(d)** Radiometric retrieval uncertainty in r_{eff} due to the absolute radiometric uncertainty at wavelengths $\lambda = 870\,\mathrm{nm}$ and $\lambda = 2100\,\mathrm{nm}$.

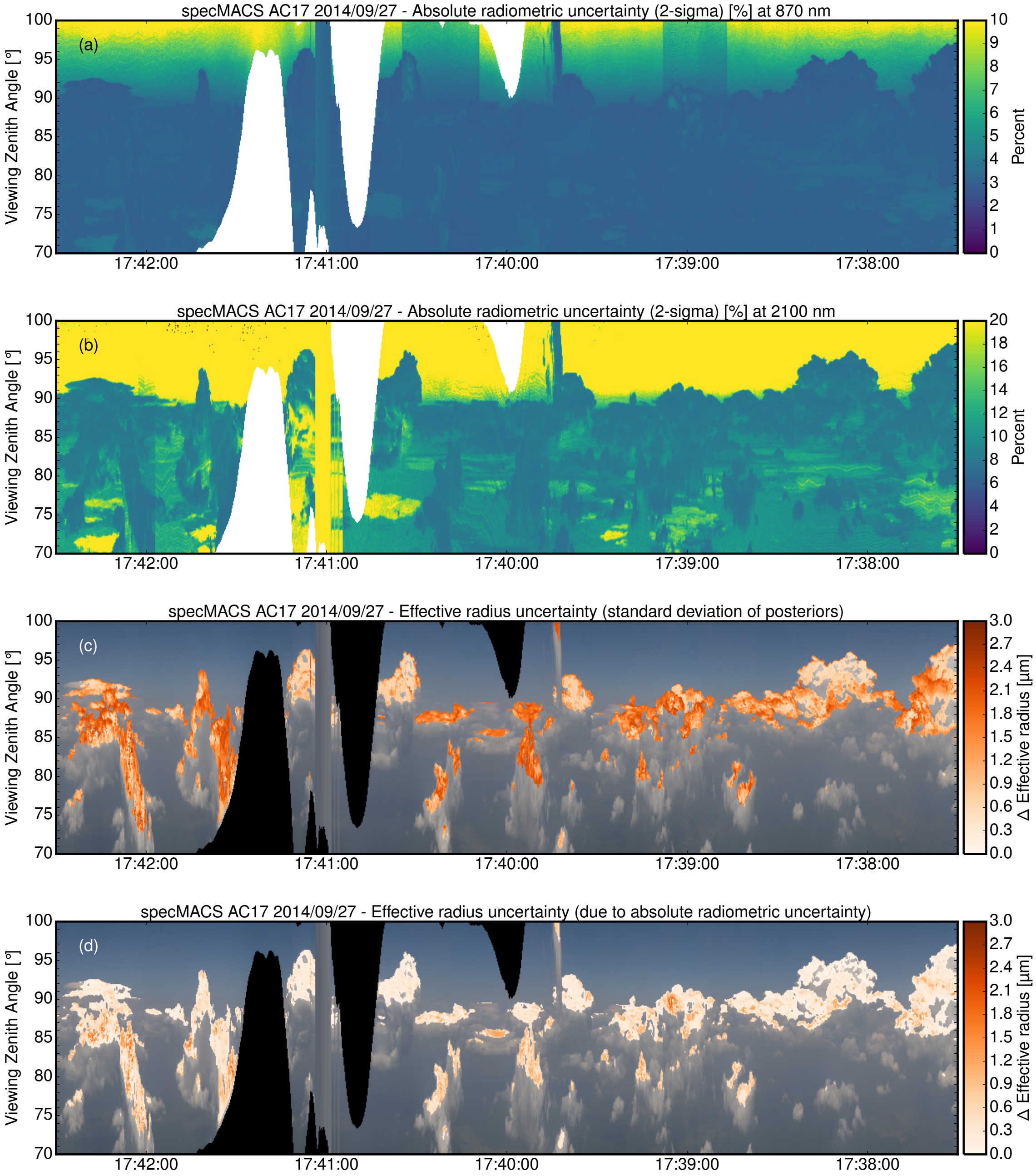

Figure 7.3: Comparison between retrieval and absolute radiometric uncertainties for the scene from flight AC17 shown in Figure 6.5. **(a)** Absolute radiometric uncertainty (2-sigma) in percent for the spectral radiance at $\lambda = 870\,\mathrm{nm}$ determined as described in Section 5.3.1. **(b)** Absolute radiometric uncertainty (2-sigma) for $\lambda = 2100\,\mathrm{nm}$ which is significantly higher due to the higher uncertainty of the radiometric standard and lower sensor sensitivity. Where signal levels are very low (clear sky), uncertainty due to dark signal drift dominates. **(c)** Statistical retrieval uncertainty in r_{eff} corresponding to the 1-sigma standard deviation of the posterior distribution for r_{eff} as described by Equation 4.31. **(c)** Radiometric retrieval uncertainty in r_{eff} due to the absolute radiometric uncertainty at wavelengths $\lambda = 870\,\mathrm{nm}$ and $\lambda = 2100\,\mathrm{nm}$.

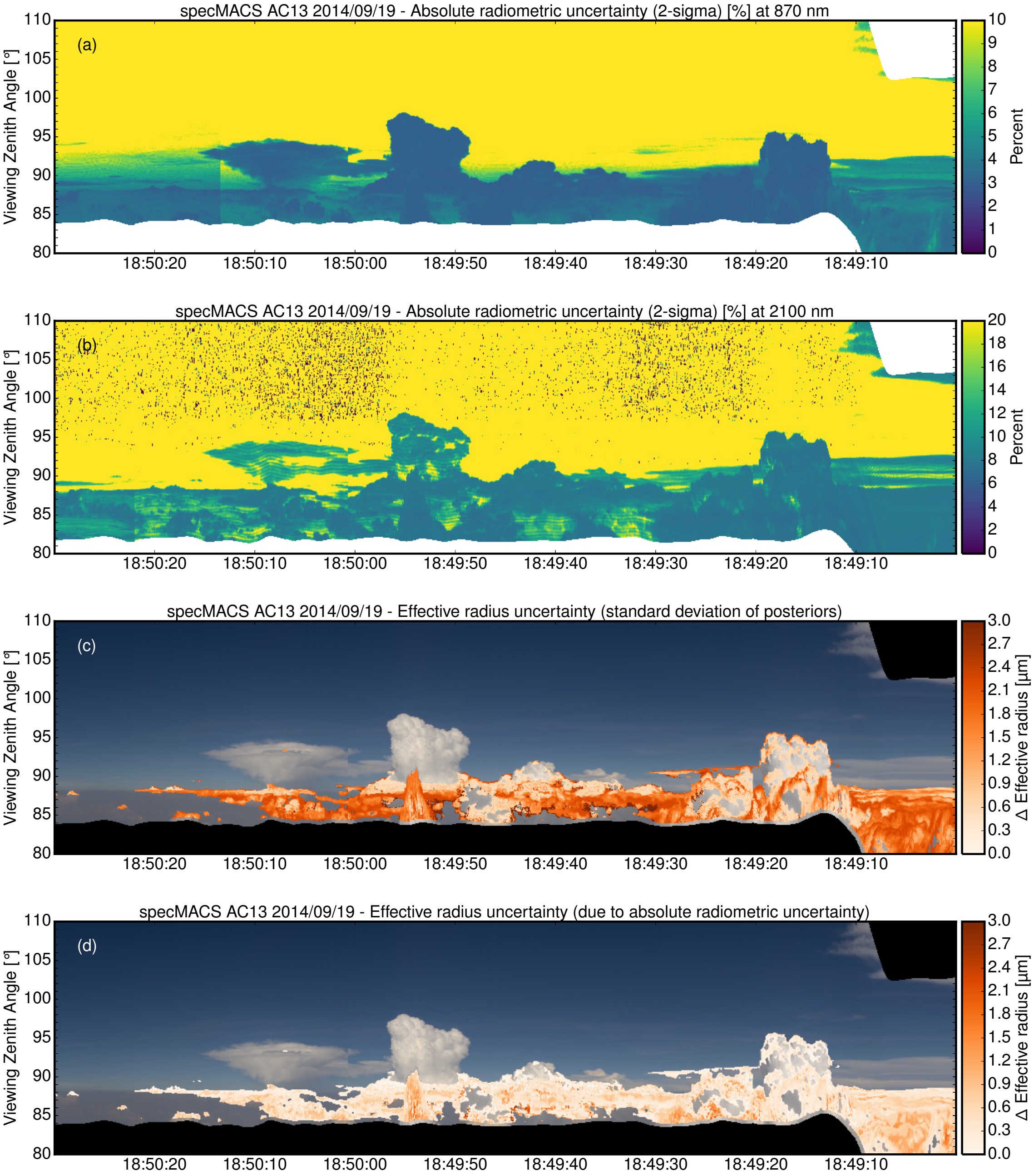

Figure 7.4: Comparison between retrieval and absolute radiometric uncertainties for the scene from flight AC13 shown in Figure 6.8. **(a)** Absolute radiometric uncertainty (2-sigma) in percent for the spectral radiance at $\lambda = 870\,\mathrm{nm}$ determined as described in Section 5.3.1. **(b)** Absolute radiometric uncertainty (2-sigma) for $\lambda = 2100\,\mathrm{nm}$ which is significantly higher due to the higher uncertainty of the radiometric standard and lower sensor sensitivity. Where signal levels are very low (clear sky), uncertainty due to dark signal drift dominates. **(c)** Statistical retrieval uncertainty in r_{eff} corresponding to the 1-sigma standard deviation of the posterior distribution for r_{eff} as described by Equation 4.31. **(c)** Radiometric retrieval uncertainty in r_{eff} due to the absolute radiometric uncertainty at wavelengths $\lambda = 870\,\mathrm{nm}$ and $\lambda = 2100\,\mathrm{nm}$.

7.3 Further uncertainties and outstanding issues

After all, the influence on direct and reflected solar radiation by a variable aerosol concentration was not considered during this work. An estimation of this influence and an assessment of its importance for the proposed technique will be given in the following outlook section. Throughout this work, the direct irradiance onto clouds as source of the measured radiance reflected from cloud sides was assumed to be known. Furthermore, the amount of atmospheric aerosol between observer and cloud side was held fixed by using the continental average mixture from the Optical Properties of Aerosols and Clouds (OPAC) package (*Hess et al.*, 1998). Consequently, stronger or weaker extinction by higher or lower atmospheric aerosol concentration was not covered in this thesis. Since this topic has many aspects, like viewing angle dependence, time of day, distance to cloud or aerosol type and concentration, this outlook will only give an estimate of the aerosol influence. The comparison with discussed uncertainties will serve as a guide for further studies.

Serving as the base of the statistical retrieval, the ensemble of Monte Carlo radiative transfer simulations of cloud sides was done using the *continental average* aerosol profile contained in OPAC. According to *Hess et al.* (1998) it can be used to describe anthropogenically influenced continental areas and contains soot and an increased amount of the insoluble and water-soluble components. The aerosol optical depth of this profile at $550\,\mathrm{nm}$ is $\tau_{550} = 0.151$. In order to assess the influence of aerosol concentration on retrieval results, the already used cloud side scene was simulated with different aerosol profiles. Thereby, a more clean aerosol profile (*continental clean*, OPAC) with an AOD of $\tau_{550} = 0.064$ and a more polluted (*continental polluted*, OPAC) with an AOD of $\tau_{550} = 0.327$ were used. While the clean profile represents remote continental areas with very low anthropogenic influences, and consequently less than $0.1\,\mu\mathrm{g\,m^{-3}}$ soot, the polluted profile represents areas highly polluted by man-made activities with $2\,\mu\mathrm{g\,m^{-3}}$ soot (*Hess et al.*, 1998). Figure 7.5 shows RGB cloud side images for the ground-based (top) and the airborne perspective (bottom) with the clean profile (Figures 7.5a and 7.5c) on the left, while the same scene with the polluted profile is shown on the right (Figures 7.5b and 7.5d). For the polluted profile, the aerosol influence, corresponding to a solar zenith angle of $\vartheta_0 = 45°$, can be seen as *brown haze* on the horizon. When these two profiles are used as an lower and upper bound to estimate the variability of aerosol concentration, a spectral radiance bias can be calculated. Figure 7.6 shows this bias between the clean and the polluted profile for the ground-based perspective (top) and airborne perspective (bottom), distinguished between $L_{0.87}$ (Figures 7.6a and 7.6c) on the left and $L_{2.10}$ (Figures 7.6b and 7.6d) on the right. For both perspectives and both wavelengths, a higher aerosol concentration leads to a decreased radiance by extinction of light between sun–cloud and cloud–observer, while the radiance strongly increases

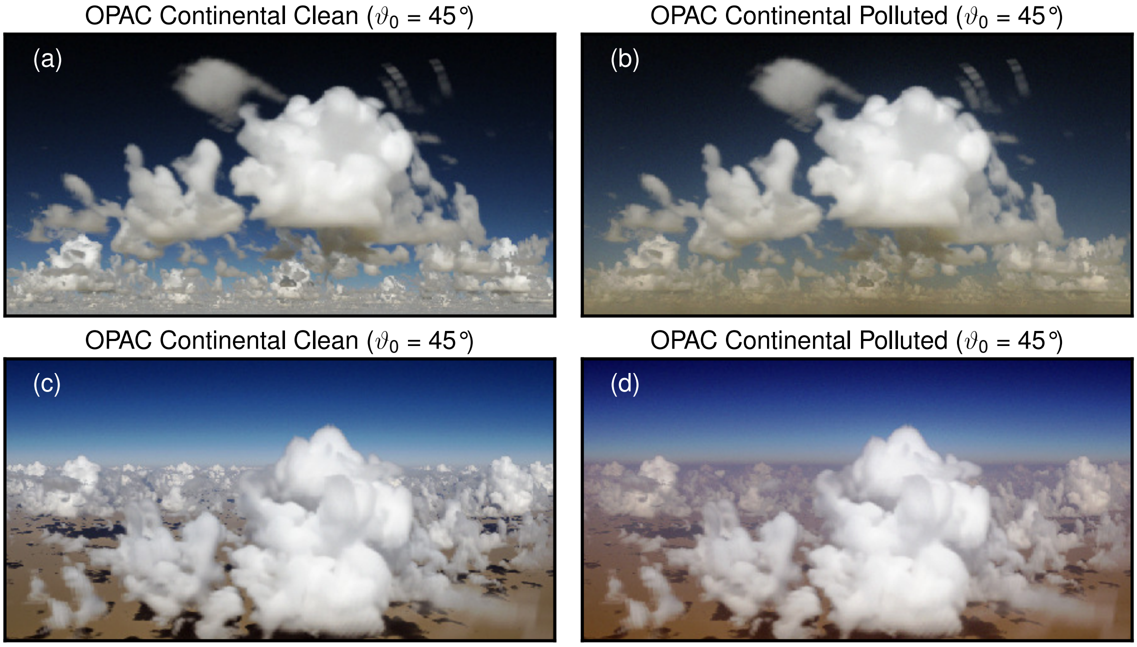

Figure 7.5: Influence of different aerosol concentrations under a solar zenith angle of $\vartheta_0 = 45°$ **(a,c)** for a OPAC continental clean aerosol profile and **(b,d)** for a OPAC continental polluted aerosol profile.

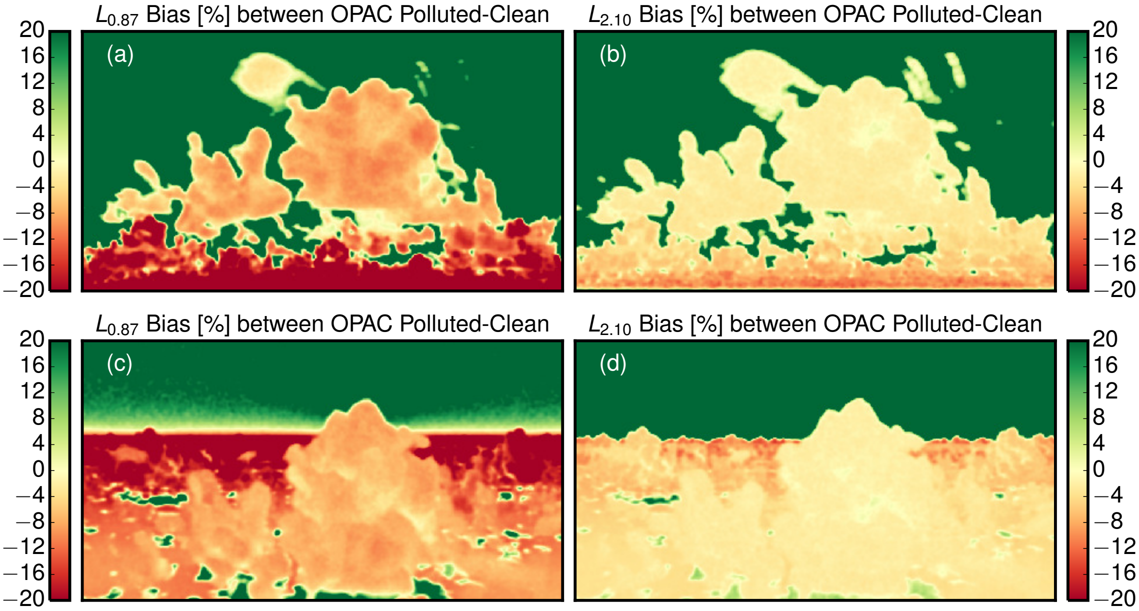

Figure 7.6: Spectral radiance bias between OPAC continental clean and polluted aerosol profile for the exemplary cloud scene used in this thesis. **(a, c)** Bias is shown for $L_{0.87}$ and **(b, d)** for $L_{2.10}$.

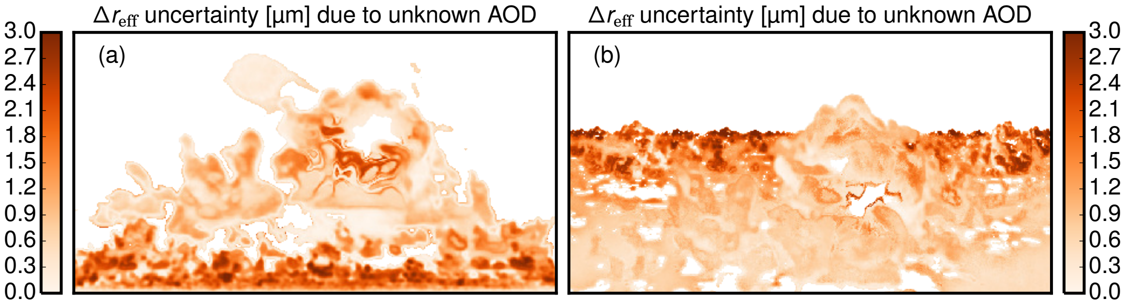

Figure 7.7: Retrieval uncertainty in r_{eff} due to a unknown aerosol optical depth (between OPAC continental clean and polluted) for **(a)** the ground-based perspective and **(b)** for the airborne perspective.

by more than 50% for clear-sky regions by additional scattering of light. With longer paths through the aerosol layer, the radiance bias gets stronger towards the horizon. Interestingly, there is a notable difference between the aerosol influence between the two wavelengths. While the radiance at $\lambda = 870\,\mathrm{nm}$ decreases between -10% for nearby ($\Delta x \lesssim 5\,\mathrm{km}$) and over -20% for distant ($\Delta x \gtrsim 5\,\mathrm{km}$) clouds, the radiance at $\lambda = 2100\,\mathrm{nm}$ decreases only by -4% for nearby and up to -10% for distant clouds.

Compared to the absolute radiometric uncertainties at the two wavelengths of *specMACS*, the aerosol influences for nearby clouds seems to be smaller at $2100\,\mathrm{nm}$ and larger at $870\,\mathrm{nm}$ This observation can be explained by the relatively small aerosol particles found in continental aerosol profiles. Most aerosol particles are located in the *accumulation mode* with radii between $0.1\,\mu\mathrm{m} < r < 2.5\,\mu\mathrm{m}$. While the extinction efficiency Q_{ext} of the accumulation mode is quite large for shorter wavelengths (e.g. $870\,\mathrm{nm}$), Q_{ext} gets much smaller for longer wavelengths (e.g. $2100\,\mathrm{nm}$). For this reason, scattering of infrared light by continental aerosol is mostly in the Rayleigh regime, with much lower AODs compared to $870\,\mathrm{nm}$ or $550\,\mathrm{nm}$.

Analogous to the method described in Section 7.2, Figure 7.7 shows the retrieval uncertainty in r_{eff} due to a unknown AOD (between OPAC continental clean and polluted). This retrieval uncertainty is mostly below $\Delta r_{eff} < 1\,\mu\mathrm{m}$ for nearby clouds, but reaches values of over $\Delta r_{eff} > 3\,\mu\mathrm{m}$ for clouds at the horizon. For most cloud regions, higher aerosol concentrations lead to an overestimation of r_{eff} by a reduction in $L_{2.10}$. Looking at the isolines for r_{eff} in the Nakajima-King plot (Figure 2.21) in the beginning of this thesis, higher aerosol concentrations can also lead to an underestimation of r_{eff} by a reduction in $L_{0.87}$. This effect is responsible for the larger retrieval uncertainties seen for the ground-based perspective (Figure 7.7a) in the vicinity of shadowed parts in the center of the cloud side. Overall, the influence of aerosol on the remote sensing of effective radii from cloud sides remains relatively small for nearby clouds, but becomes a dominating factor for distant clouds and long atmospheric paths. However, subsequent studies are needed to investigate the role of viewing angle, time of day, distance to cloud or aerosol type and to develop techniques to mitigate the aerosol influence. The same is true for overlaying, sub-visible cloud fields (e.g. cirrus clouds), which have an influence on the direct solar radiation. Further effort should be made to eliminate the assumption about the direct solar radiation being constant. Rather, direct measurements with *specMACS* or measurements of the clear-sky radiance should be exploited to get information about direction solar radiation and aerosol concentration.

A further important point is the development of a *depth map* for the retrieval. The height and location assignment of retrieval results is not just of uttermost importance for the comparison with in situ measurements and models, but also essential to estimate the cloud distance for a potential aerosol correction. Here, first promising results could be achieved by exploiting the oxygen A-band absorption at $\lambda = 760\,\mathrm{nm}$. The possibility of determining cloud-top height by inferring photon path lengths from backscattered solar radiances in- and outside the oxygen A-band absorption is a longstanding technique used in satellite remote sensing (*Fischer and Grassl*, 1991, *Rozanov et al.*, 2004, *van Diedenhoven et al.*, 2007).

7.4 Conclusions regarding specMACS

One the instrument side, there are also several points which have not been considered during the described effort to characterize the instrument thoroughly. Without claiming completeness, the following effects might be worth investigating further:

1. Dark signal variability has only partially been explored in a controlled fashion. Since dark signals are measured frequently in the described setup, variations are directly considered and do not need to be characterized. If future applications change the measurement mode, for which timely dark measurements are not possible, a more in-depth characterization would be needed.

2. The dark signal behavior for very large temperature swings has not been thoroughly investigated. Frequent dark frame measurements and the avoidance of direct sunlight onto the instrument are therefore essential during outside ground-based measurements.

3. The radiometric response R, including FPN, might change over time and environment conditions (e.g. temperature). Reliable statements about the long term calibration stability can only be made in subsequent calibration efforts in the future.

4. Due to the difficulty of establishing a bright light source with spectrally stable and precisely linearly adjustable intensity, the radiometric nonlinearity

has not been investigated directly in terms of incoming radiance alone. A deeper investigation of this behavior might show additional nonlinearity effects. There is some indication that these additional effects might not be dominant, as suggested in Sec. 5.3.1.

5. The effectiveness of the final stray light protection has only been simulated and subjectively assessed. A dedicated characterization would yield final evidence for the effectiveness.

Despite these open points, the overall radiometric uncertainty estimation can be relied on, if the the following points are considered during the measurement with *specMACS* and during the subsequent calibration of scientific data:

1. For both instruments no serious internal stray light and ghost images have been found. When direct sunlight impinges on the front optics, stray light baffles become indispensable.

2. Due to the variable dark current level of the SWIR sensor prompt and frequent dark signal measurements for every used integration time and sensor temperature are essential to achieve the specified radiometric accuracy. Interpolation of dark signal frames from before and after each measurement are needed to compensate for the SWIR dark signal drift ($\leqslant 30\,\mathrm{DN}$ per minute). In contrast, the VNIR dark signal shows no strong dependence on integration time or sensor temperature since it is mainly caused by readout noise.

3. The radiometric response R given from the manufacturer does not differ by more than 10 % from R found in this work. Although R seems to be quite stable, the calibration should be repeated over time since the radiometric uncertainty is about 3% in the best wavelength region.

4. For the SWIR, we have found a small mismatch between the integration time set t_{set} and the actual integration time t_{int}. For this reason we introduced an additional term t_{ofs} to compensate for this mismatch.

5. The radiometric response of the VNIR shows a nonlinear behavior at medium to large signal levels, which leads to an underestimation of the absolute radiometric signal if not corrected.

6. During the spatial characterization, the VNIR sharpness turned out to be suboptimal. Besides a slight achromatism, the focus seems to shift in the across-track direction with wavelength.

7. The spectral bandwidth is within specifications for both spectrometers. The spectral sampling is sufficient for both instruments, while the oversampling of the VNIR spectrometer allows the reduction of the spectral sampling by half without losing information significantly.

8. During the spectral and spatial characterization, no significant spectral smile or keystone was found for both cameras.
9. Both sensors exhibit a certain polarization sensitivity, which for the most part remains well below 5 %. In the worst case of completely polarized light with unknown polarization orientation, this results in an additional radiometric uncertainty of 5.3 %.

The final evaluation shows that the instrument performance complies with the accuracy requirements stated in Section 5.1.2. Absolute radiometric accuracy well below the mentioned 3-D radiative effects can be achieved when the described signal calibration procedure is applied. The radiometric error budget proves that the radiometric uncertainty for well illuminated cloud scenes can be kept well below 20 % over the full wavelength range of the instrument. This is also confirmed by the good agreement between both spectrometers in the overlap region around 1000 nm. As demanded in Section 5.1.2, the spectral bandwidth is the limiting factor for the spectral accuracy of the instrument. More precisely, the spectral bandwidth of the VNIR with 3.1 nm is well above the found spectral smile of 0.3 nm and one order of magnitude larger than the spectral calibration accuracy of ±0.1 nm. As well, the SWIR spectral bandwidth of 10.3 nm is larger by one magnitude than its spectral smile of 1.1 nm and larger by two magnitudes compared to the spectral calibration accuracy of ±0.2 nm. Spectral calibration accuracy fully meets the requirements of current microphysical cloud retrievals and enables reliable identification of gaseous absorption lines. The spectral bandwidth below 1000 nm should be sufficient for the analysis of absorption line depths of features like the oxygen A-band.

CHAPTER 8

Summary

This section provides a short summary of the main topics and the major findings of this thesis. In its *Fifth Assessment Report* (IPCC, 2013), the *Intergovernmental Panel on Climate Change* stressed again that the close interactions between clouds and aerosols are still not fully understood. In order to observe the vertical development of cloud droplets from aerosol activation to rain-out, *Marshak et al.* (2006b), *Martins et al.* (2011), *Zinner et al.* (2008) and *Ewald et al.* (2013a) proposed a remote sensing technique to retrieve vertical profiles of cloud droplet effective radius using solar reflectance from cloud sides. Testing the feasibility of their proposal, in theory as well as in practice, is a central motivation of this thesis.

In a first step, this work introduced a statistical framework for the proposed remote sensing of cloud sides following *Marshak et al.* (2006b). A statistical relationship between reflected sunlight in a near-visible and near-infrared wavelength and droplet size is found following the classical approach by (*Nakajima and King*, 1990) which is based on a bijective relationship. By simulating the three-dimensional radiative transfer in highly resolved LES model clouds using the Monte Carlo code for the physically correct tracing of photons in cloudy atmospheres (MYSTIC), probability distributions for this relationship were sampled. These *posterior* distributions describe the probability to find a specific droplet size after a specific solar reflectance pair has been measured. In contrast to many other effective radius retrievals, this work thereby provides essential information about the retrieval uncertainties which are intrinsically linked with the reflectance ambiguities caused by three-dimensional radiative effects. In the course of this work, the framework was not only tested numerically, but also applied to real-world measurements of convective cloud sides. For that purpose, this work introduced and characterized the imaging spectrometer of the Munich Aerosol Cloud Scanner (*specMACS*). Furthermore, the proposed technique was validated with independent in situ measurements of cloud droplet size from airborne platforms. The observed differences between the retrieved and the in situ measured effective radii were in good agreement with the predicted statistical retrieval uncertainty.

For a final assessment of the obtained results, the questions posed at the beginning are revisited. Reiterating the list mentioned in the introduction, following scientific objectives were identified:

Sensitivity of reflected radiances from cloud sides to effective radii

The objective to determine the sensitivity of reflected radiances to cloud droplet radii was covered in Section 4.1. The numerical analysis of the statistical retrieval showed a retrieval uncertainty (mean standard deviation of posterior distributions) of around $1\,\mu m$ to $1.5\,\mu m$. For both perspectives, the statistical retrieval reliably detected the present effective radius profile, while sanity checks showed no prior bias of the retrieval towards cloud droplet size increasing or decreasing with height. This is an essential prerequisite to proof or disprove the hypothesis of increasing cloud droplet sizes with height. Furthermore, the retrieval performance remained the same when faced with unknown cloud side scenes not included in the *posterior* distributions. It can therefore be concluded that the retrieval is not over-fitted and that it represents the statistical relationship between reflected radiance and cloud droplet size for this cloud side perspective. Limited to optically thick water clouds, this work investigated the main reason for reflectance ambiguities from cloud sides. Summarized, the unknown geometry of cloud sides under-determine the remote sensing of cloud droplet sizes following the technique of *Nakajima and King* (1990). Compared to visible light, near-infrared light has a smaller penetration depth into the cloud due to a stronger absorption by water droplets. It was shown how this penetration depth is central to the angular dependence of the reflected radiation. Smaller penetration depths lead to a more uniform reflection, while larger penetration depths lead to a stronger reflection perpendicular to the cloud surface. Within the same 3D cloud side scene, viewing perspectives onto cloud surfaces can be steeper or more oblique as the illumination angle. As a consequence, the correlation between reflected solar radiance pairs and droplet sizes gets ambiguous. The spectral width of cloud droplet size distributions seems to have a negligible effect on reflected radiances (Section 4.1.1), confirming the suitability of using the scalar moments r_{eff} and LWC with a fixed spectral width to describe the reflection of different cloud droplet ensembles. Only near the backscatter geometry, in the region of the glory, radiances biases caused by different spectral widths are comparable with radiance bias caused by the absolute radiometric uncertainty of *specMACS*. Furthermore, this work developed a technique (Section 4.1.2) to resolve radiance ambiguities (as much as possible) when no information about the cloud surface orientation is available. More precisely, additional information from surrounding pixels was used to classify the environment of the considered pixel.

Investigation of external influences

Three main external influences to the cloud side remote sensing of cloud droplet radii were identified: (1) Cloud shadows, (2) Ground albedo reflection and (3) Cloud phase. For all three cases, mitigation techniques were developed and tested. Cloud shadows and cloud phase were filtered by using global thresholds of radiance ratios using the enhanced absorption of photons in shadowed and glaciated cloud regions. Ground albedo reflection was identified and filtered out by exploiting the *near infrared edge* of vegetation in the spectral region between 680–730 nm where cloud reflectance has a spectrally flat signature.

Introduction and characterization of specMACS

In order to bring the theoretical concept into real-world application, Chapter 5 introduced and characterized the newly developed specMACS imager as a significant part of this thesis. The hardware design and the modular and resilient software design enables the *specMACS* system to be used as a versatile data acquisition system for hyperspectral measurements in the wavelength range of $417\,\mathrm{nm}$ to $2496\,\mathrm{nm}$. The design can easily be adapted to ground and airborne measurements and can be extended to or combined with even more sensors naturally (like a long wave infrared camera). The software concept proved to be reliable and facilitated measurements throughout the whole ACRIDICON 2014 campaign autonomously and without any measurement interruptions. The laboratory characterization of the VNIR and SWIR sensors of *specMACS* revealed important details of the behavior of the sensors needed for a scientific application of *specMACS*. Of particular value is the characterization of the previously unknown nonlinear behavior of the VNIR. It enables a consistent calibration of data measured with both sensors simultaneously and thereby allows for a sound comparison between signals of both sensors. The available error budget calculation now allows to estimate the significance of different radiometric uncertainties. For the VNIR, major contributions to the overall radiometric uncertainty of around 5 % are caused by the calibration uncertainty of R (error of $\approx 3\,\%$) and the polarization sensitivity for highly polarized light (error $\leqslant$ 5% for fully polarized light). Without the nonlinearity correction, the radiometric signal would furthermore be strongly biased (-9 % at high signal levels). For the SWIR, major error contributions to the overall radiometric uncertainty of around 10 % are caused by the uncertainty of the absolute radiometric standard itself (error of 5 to 10 %, $\lambda > 1700\,\mathrm{nm}$) and the dark signal drift for low exposed regions (error of 20 % and more, depending on the frequency of dark frame measurements).

Feasibility to apply the method to realistic measurements

Following the introduction of *specMACS*, Chapter 6 demonstrated the possibility to retrieve effective radius profiles from cloud sides in real-world application.

Specifically, this work demonstrated in three test cases that the proposed retrieval technique can be applied to airborne as well as to ground-based measurements of cloud sides. In agreement with measured in situ profiles, the statistical retrieval detected effective radii increasing with height in all three cases. However, the comparison of retrieval results with in situ measurements at the same altitude suggested an overestimation of effective radii of around $\Delta r_{\text{eff}} = 2\,\mu\text{m}$ by the retrieval. This bias turned out to be consistent in all three cases. In Section 7.1, several possibilities to explain this difference were discussed. Beside intrinsic differences between in situ measurements of r_{eff} in cloud cores and r_{eff} at cloud edges, problems with the retrieval technique itself were discussed. Here, the retrieval uncertainty associated with the absolute radiometric uncertainty of *specMACS* could be ruled out as influential factor in Section 7.2.

Nevertheless, measurements acquired during the mentioned ground-based and airborne campaign offer many possibilities for data analysis. The simultaneously acquired in situ data from other participating institutions yields a unique opportunity to validate retrieved remote sensing results with directly measured cloud properties. Furthermore, the spectral resolution of *specMACS* is a promising opportunity to derive a *depth map* for the horizontal and vertical localisation of the retrieval results using oxygen A-band absorption features.

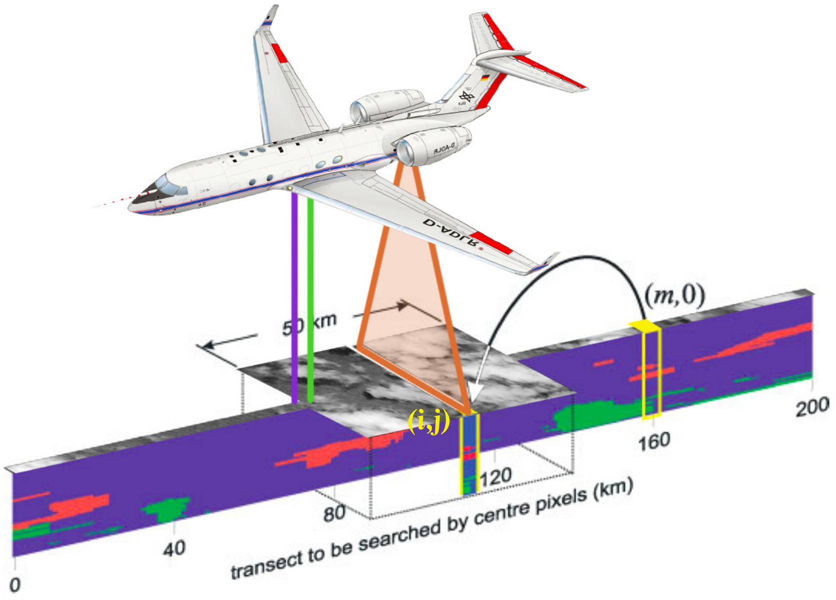

Figure 8.1: Following the approach of *Barker et al.* (2011), the proposed objective is a reconstruction of a cloud scene using vertical 2D curtains from radar and lidar instruments on board the HALO aircraft in combination with horizontal 2D curtains from *specMACS*. The imaging spectrometer would complement the HALO instrumentation into the 1st airborne radar/lidar/imager missing in preparation to the upcoming EarthCARE mission (*Illingworth et al.*, 2014).

Another promising approach to reconstruct the unknown cloud geometry directly is the combination with active methods, like the combination with a scanning cloud radar. In *Ewald et al.* (2015), this reconstruction technique is demonstrated by using measurements of convective clouds with the *MIllimeter RAdar of the Aerosol Cloud Scanner (miraMACS)* owned by the Meteorological Institute Munich. A further prospect on future developments is the downward-looking deployment of *specMACS* on board the *HALO* research aircraft. In combination with active methods (e.g. the cloud radar *HAMP*, *Mech et al.* (2014), and the High Spectral Resolution Lidar System *WALES*, *Wirth et al.* (2009)), the *specMACS* instrument could complement the *HALO* profiler payload with horizontal curtains of spectral radiances. Following the approach of *Barker et al.* (2011) shown in Figure 8.1, this setup could be used to test techniques for a 3D reconstruction of cloud microphysics proposed for the planned *EarthCARE* satellite mission.

In conclusion, the present work applied a working effective radius retrieval to measurements of clouds sides and thus paved the way for further research on this topic. For the first time, this work demonstrated the feasibility to retrieve cloud particle size profiles from cloud sides and thus marks a further important step towards an operational application of this technique.

APPENDIX A

Annex

A.1 Monte Carlo Sampling

Table A.1: Cloud side observation perspectives (included in lookup table) that were used to investigate the retrieval bias.

Time	φ	ϑ_0	$x[m]$	$y[m]$
12 : 00	45°	75°	2675	2725
12 : 10	135°	65°	2875	5150
12 : 40	315°	45°	1975	6150
12 : 40	315°	75°	1975	6150
13 : 40	135°	65°	5225	2925
13 : 40	225°	25°	300	3300
13 : 50	225°	65°	525	2200
13 : 50	45°	65°	2900	3350
13 : 50	315°	75°	5150	3300

Table A.2: Cloud side observation perspectives (not included in lookup table) that were used to test for potential overfitting.

Time	φ	ϑ_0	$x[m]$	$y[m]$
12 : 40	0°	65°	3925	250
12 : 40	270°	65°	950	3725
13 : 30	270°	45°	2725	1475
13 : 40	180°	45°	5725	5050
13 : 40	270°	65°	6250	5025

A.2 Instrument automation

Auto exposure

The main task of the auto exposure control system, setting the integration time t_{int} to an optimized value, was designed with three goals of descending importance in mind: Since clouds as the main object of interest are typically the brightest parts of a scene, overexposure is to be avoided in any case. To limit the number of distinct dark current measurements and to facilitate later data analysis, only a few discrete integration times will be used. These are indicated as $t_{\text{int}}(i)$ in the following. However, to recover from very bright scenes and to use the available dynamic range of the sensor in an optimal way, integration time should be increased after a certain time span of underexposed conditions.

In Fig. A.1 the overall logic of the integration time regulation of the auto exposure software is illustrated. The logic is based on a histogram of the signal which is evaluated in real-time over all spatial and spectral pixels. From the histogram, the 99th percentile (q_{99}) is calculated and stored for subsequent analysis. The q_{99} was chosen since it turned out to be a more stable indicator for current signal levels than the maximum value, which is sensitive to signal noise and bad pixels.

A limited set of integration times $t_{\text{int}}(i)$ were used during the aircraft measurement campaign ACRIDICON 2014: 0.5, 0.85, 1, 1.2, 1.5, 2, 3, 5, 8, 12, 18 and 25 ms. These values were chosen as a compromise between a sufficient range of values, reasonably small steps (less then a factor of 2) between integration times and the goal to have only a limited amount of distinct integration times.

The following algorithm is in principle independent of the frame rate, but was tested and optimized for 30 fps. To avoid overexposure, the 99th percentile q_{99} of the signal histogram is limited to 3/4 of the full dynamic range of the sensor in order to provide headroom for transient radiance peaks. If this limit is exceeded for more than four frames within the last 150 frames (5 sec @ 30 fps), the integration time $t_{\text{int}}(i)$ is reduced to the next allowed value $t_{\text{int}}(i-1)$. After such an overexposure protection is triggered, no increments to longer integration times are allowed during the following 1800 frames (1 min @ 30 fps).

To recover from a reduced integration time, the auto exposure control periodically tries to increase the integration time t_{int}. To this end, the histograms of the last 150 frames are periodically (e.g. every 30 sec) extrapolated to the next longer integration time $t_{\text{int}}(i+1)$. If the extrapolated histograms do not trigger the overexposure protection described above, $t_{\text{int}}(i)$ is increased to $t_{\text{int}}(i+1)$. Thereby any increase of integration time is tested before it is actually performed and suppressed if the signal limit set by the quantile limit would be exceeded.

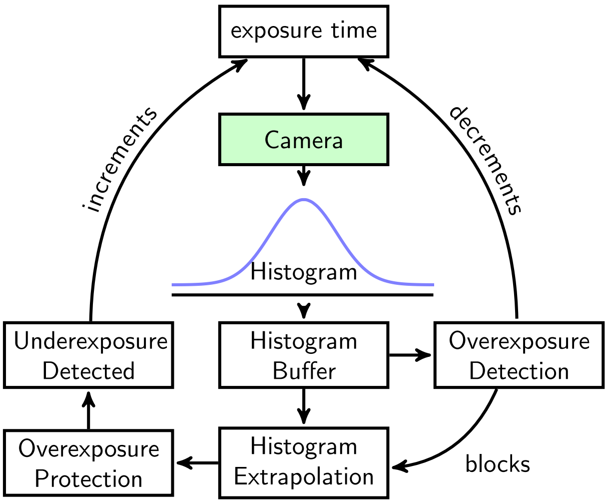

Figure A.1: Overview of the automated exposure control system.

Automatic dark frame

Another task of the control software is the automation of dark signal measurements. During dark signal measurements, it is obviously not possible to perform real measurements, so the amount of time spent with dark signal measurements is to be minimized. However, the dark signal varies with time, so the automation is set up to measure approximately 30 dark frames at least every two minutes. Since the dark signal additionally changes with integration time $t_{\text{int}}(i)$, the system checks if a recent dark signal measurement with the current sensor settings was obtained and if not, triggers a dark signal measurement before changing $t_{\text{int}}(i)$.

Bibliography

Ackerman, A. S., O. B. Toon, D. E. Stevens, A. J. Heymsfield, V. Ramanathan, and E. J. Welton (2000), Reduction of Tropical Cloudiness by Soot, *Science*, *288*(5468), 1042–1047, doi:10.1126/science.288.5468.1042. (Cited on page 3)

Aikio, M. (2001), *Hyperspectral prism-grating-prism imaging spectrograph*, Technical Research Centre of Finland Heinola, Finland. (Cited on pages 124 and 126)

Albrecht, B. A. (1989), Aerosols, cloud microphysics, and fractional cloudiness, *Science*, *245*(4923), 1227–1230. (Cited on pages 2 and 3)

Anderson, G., S. Clough, F. Kneizys, J. Chetwynd, and E. Shettle (1986), Afgl atmospheric constituent profiles (0-120 km), *Tech. Rep. AFGL-TR-86-0110*. (Cited on pages 41, 50, and 98)

Arabas, S., H. Pawlowska, and W. W. Grabowski (2009), Effective radius and droplet spectral width from in-situ aircraft observations in trade-wind cumuli during rico, *Geophys. Res. Lett.*, *36*(11), L11,803, doi:10.1029/2009GL038257. (Cited on pages 3, 12, and 57)

Arking, A., and J. Childs (1985), Retrieval of cloud cover parameters from multispectral satellite images., *Journal of Applied Meteorology*, *24*, 322–334. (Cited on page 5)

Babey, S., and C. Anger (1989), A compact airborne spectrographic imager (casi), in *Quantitative remote sensing: An economic tool for the Ninetie*, vol. 2, pp. 1028–1031. (Cited on page 122)

Baker, M. B., R. G. Corbin, and J. Latham (1980), The influence of entrainment on the evolution of cloud droplet spectra: I. A model of inhomogeneous mixing, *Quarterly Journal of the Royal Meteorological Society*, *106*(449), 581–598, doi:10.1002/qj.49710644914. (Cited on pages 15 and 177)

Baldridge, A. M., S. J. Hook, C. I. Grove, and G. Rivera (2009), The ASTER spectral library version 2.0, *Remote Sensing of Environment*, *113*(4), 711–715, doi:10.1016/j.rse.2008.11.007. (Cited on page 90)

Barker, H., and A. Marshak (2001), Inferring optical depth of broken clouds above green vegetation using surface solar radiometric measurements, *Journal of the Atmospheric Sciences*, *58*, 2989–3006. (Cited on page 90)

Barker, H. W., M. P. Jerg, T. Wehr, S. Kato, D. P. Donovan, and R. J. Hogan (2011), A 3d cloud-construction algorithm for the EarthCARE satellite mission, *Quarterly Journal of the Royal Meteorological Society*, *137*(657), 1042–1058, doi:10.1002/qj.824. (Cited on pages 194 and 195)

Baum, B., D. Kratz, P. Yang, S. Ou, Y. Hu, P. Soulen, and S.-C. Tsay (2000), Remote sensing of cloud properties using modis airborne simulator imagery during success. 1. data and models, *Journal of Geophysical Research*, *105*(D9), 11,767–11,780. (Cited on page 40)

Baum, B., Y. Hu, and S. Platnick (2007), The sensitivity of ice cloud optical and microphysical passive satellite retrievals to cloud geometrical thickness, *Geoscience and ...*. (Cited on page 92)

Baumgardner, D., et al. (2011), Airborne instruments to measure atmospheric aerosol particles, clouds and radiation: A cook's tour of mature and emerging technology, *Atmospheric Research*, *102*(1–2), 10–29, doi:10.1016/j.atmosres.2011.06.021. (Cited on page 165)

Baumgartner, A. (2013), Characterization of Integrating Sphere Homogeneity with an Uncalibrated Imaging Spectrometer, in *Proc. WHISPERS 2013*, pp. 1–4, Gainsville, Florida, USA. (Cited on pages 137 and 140)

Baumgartner, A., P. Gege, C. H. Köhler, K. Lenhard, and T. Schwarzmaier (2012), Characterisation methods for the hyperspectral sensor HySpex at DLR's calibration home base, http://elib.dlr.de/78685/. (Cited on pages 148 and 152)

Beard, K. V., and H. T. Ochs (1993), Warm-Rain Initiation: An Overview of Microphysical Mechanisms, *Journal of Applied Meteorology*, *32*(4), 608–625, doi:10.1175/1520-0450(1993)032⟨0608:WRIAOO⟩2.0.CO;2. (Cited on page 64)

Berry, E. X., and R. L. Reinhardt (1974), An Analysis of Cloud Drop Growth by Collection: Part I. Double Distributions, *Journal of the Atmospheric Sciences*, *31*(7), 1814–1824, doi:10.1175/1520-0469(1974)031⟨1814:AAOCDG⟩2.0.CO;2. (Cited on page 12)

Bierwirth, E., A. Ehrlich, M. Wendisch, J.-F. Gayet, C. Gourbeyre, R. Dupuy, A. Herber, R. Neuber, and A. Lampert (2013), Optical thickness and effective radius of Arctic boundary-layer clouds retrieved from airborne nadir and imaging spectrometry, *Atmos. Meas. Tech.*, *6*(5), 1189–1200, doi:10.5194/amt-6-1189-2013. (Cited on page 122)

Blyth, A., and J. Latham (1991), A climatological parameterization for cumulus clouds., *Journal of Atmospheric Sciences*, *48*, 2367–2372. (Cited on pages 13, 15, and 177)

Boers, R., and R. M. Mitchell (1994), Absorption feedback in stratocumulus clouds Influence on cloud top albedo, *Tellus A*, *46*(3), 229–241, doi:10.1034/j.1600-0870.1994.00001.x. (Cited on page 3)

Bohndiek, S. E., A. Blue, A. Clark, M. Prydderch, R. Turchetta, G. Royle, and R. Speller (2008), Comparison of Methods for Estimating the Conversion Gain of CMOS Active Pixel Sensors, *IEEE Sensors Journal*, *8*(10), 1734–1744, doi:10.1109/JSEN.2008.2004296. (Cited on page 142)

Bohren, C., E. Clothiaux, N. Johnson, et al. (2007), Fundamentals of atmospheric radiation, *American Journal of Physics*, *75*, 671. (Cited on pages 36 and 37)

Boucher, O., et al. (2013), *Clouds and Aerosols*, book section 7, pp. 571–658, Cambridge University Press, Cambridge, United Kingdom and New York, NY, USA, doi:10.1017/CBO9781107415324.016. (Cited on pages 1, 2, 3, and 4)

Brenguier, J., H. Pawlowska, L. Schüller, R. Preusker, J. Fischer, and Y. Fouquart (2000), Radiative properties of boundary layer clouds: Droplet effective radius versus number concentration, *Journal of the Atmospheric Sciences*, *57*(6), 803–821. (Cited on pages 3, 12, 13, 14, 15, and 177)

Brenguier, J.-L., F. Burnet, and O. Geoffroy (2011), Cloud optical thickness and liquid water path – does the k coefficient vary with droplet concentration?, *Atmos. Chem. Phys.*, *11*(18), 9771–9786, doi:10.5194/acp-11-9771-2011. (Cited on page 3)

Bréon, F., and M. Doutriaux-Boucher (2005), A comparison of cloud droplet radii measured from space, *Geoscience and Remote Sensing, IEEE Transactions on*, *43*(8), 1796–1805. (Cited on page 123)

Bugliaro, L., T. Zinner, C. Keil, B. Mayer, R. Hollmann, M. Reuter, and W. Thomas (2011), Validation of cloud property retrievals with simulated satellite radiances: a case study for SEVIRI, *Atmos. Chem. Phys.*, *11*(12), 5603–5624, doi:10.5194/acp-11-5603-2011. (Cited on page 5)

Buras, R., and B. Mayer (2011), Efficient unbiased variance reduction techniques for monte carlo simulations of radiative transfer in cloudy atmospheres: the solution, *J. Quant. Spectrosc. Radiat. Transfer*, *112*, 434–447. (Cited on pages 52 and 99)

Cahalan, R. F., W. Ridgway, W. Wiscombe, and T. Bell (1994), The albedo of fractal stratocumulus clouds, *Journal of the Atmospheric Sciences*, *51*, 2434–2455. (Cited on pages 63 and 72)

Chandrasekhar, S. (1950), *Radiative transfer*. (Cited on page 30)

Chang, F.-L., and Z. Li (2005), A New Method for Detection of Cirrus Overlapping Water Clouds and Determination of Their Optical Properties, *Journal of the Atmospheric Sciences*, *62*(11), 3993–4009, doi:10.1175/JAS3578.1. (Cited on page 40)

Chiu, J. C., et al. (2012), Cloud droplet size and liquid water path retrievals from zenith radiance measurements: examples from the atmospheric radiation measurement program and the aerosol robotic network, *Atmos. Chem. Phys.*, *12*(21), 10,313–10,329, doi:10.5194/acp-12-10313-2012. (Cited on page 5)

Christensen, M. W., and G. L. Stephens (2011), Microphysical and macrophysical responses of marine stratocumulus polluted by underlying ships: Evidence of cloud deepening, *Journal of Geophysical Research: Atmospheres*, *116*(D3), D03,201, doi:10.1029/2010JD014638. (Cited on page 4)

Coakley, J. A., R. L. Bernstein, and P. A. Durkee (1987), Effect of Ship-Stack Effluents on Cloud Reflectivity, *Science*, *237*(4818), 1020–1022, doi:10.1126/science.237.4818.1020. (Cited on page 3)

Coddington, O., P. Pilewskie, and T. Vukicevic (2012), The Shannon information content of hyperspectral shortwave cloud albedo measurements: Quantification and practical applications, *Journal of Geophysical Research: Atmospheres*, *117*(D4), D04,205, doi:10.1029/2011JD016771. (Cited on page 5)

Coddington, O. M., et al. (2010), Examining the impact of overlying aerosols on the retrieval of cloud optical properties from passive remote sensing, *Journal of Geophysical Research*, *115*(D10), D10,211, doi:10.1029/2009JD012829. (Cited on page 5)

Cornet, C., J.-C. Buriez, J. Riédi, H. Isaka, and B. Guillemet (2005), Case study of inhomogeneous cloud parameter retrieval from MODIS data, *Geophysical Research Letters*, *32*(13), L13,807, doi:10.1029/2005GL022791. (Cited on page 123)

Cotton, W. R., et al. (2003), RAMS 2001: Current status and future directions, *Meteorology and Atmospheric Physics*, *82*(1-4), 5–29, doi:10.1007/s00703-001-0584-9. (Cited on page 53)

Crank, J. (1979), *The Mathematics of Diffusion*, Clarendon Press. (Cited on page 61)

Davis, A. B., and A. Marshak (2001), Multiple Scattering in Clouds: Insights from Three-Dimensional Diffusion/P_1 Theory, *Nuclear Science and Engineering*, *137*(3), 251–280. (Cited on page 61)

Davis, J., T. McKee, and S. Cox (1985), Application of the monte carlo method to problems in visibility using a local estimate: an investigation, *Applied Optics*, *24*(19), 3193–3205. (Cited on page 51)

Deirmendjian, D. (1969), *Electromagnetic Scattering on Spherical Polydispersions*, print: none. (Cited on page 33)

Dobson, G. M. B. (1931), A photoelectric spectrophotometer for measuring the amount of atmospheric ozone, *Proceedings of the Physical Society*, *43*(3), 324, doi:10.1088/0959-5309/43/3/308. (Cited on page 4)

Downing, M., D. Baade, P. Sinclaire, S. Deiries, and F. Christen (2006), CCD riddle: a) signal vs time: linear; b) signal vs variance: non-linear, p. 627609, doi:10.1117/12.671457. (Cited on page 142)

Dubovik, O., M. Herman, A. Holdak, T. Lapyonok, D. Tanré, J. L. Deuzé, F. Ducos, A. Sinyuk, and A. Lopatin (2011), Statistically optimized inversion algorithm for enhanced retrieval of aerosol properties from spectral multi-angle polarimetric satellite observations, *Atmos. Meas. Tech.*, *4*(5), 975–1018, doi:10.5194/amt-4-975-2011. (Cited on page 84)

Dury, M. R., T. Theocharous, N. Harrison, N. Fox, and M. Hilton (2007), Common black coatings – reflectance and ageing characteristics in the $0.32 - 14.3 \mu m$ wavelength range, *Optics Communications*, *270*(2), 262–272, doi:10.1016/j.optcom.2006.08.038. (Cited on page 127)

Ehrlich, A., E. Bierwirth, M. Wendisch, J.-F. Gayet, G. Mioche, A. Lampert, and J. Heintzenberg (2008), Cloud phase identification of Arctic boundary-layer clouds from airborne spectral reflection measurements: test of three approaches, *Atmos. Chem. Phys.*, *8*(24), 7493–7505, doi:10.5194/acp-8-7493-2008. (Cited on pages 5 and 157)

Ehrlich, A., M. Wendisch, E. Bierwirth, J.-F. Gayet, G. Mioche, A. Lampert, and B. Mayer (2009), Evidence of ice crystals at cloud top of arctic boundary-layer mixed-phase clouds derived from airborne remote sensing, *Atmos. Chem. Phys.*, *9*, 9401–9416. (Cited on page 5)

Eichler, H., A. Ehrlich, M. Wendisch, G. Mioche, J.-F. Gayet, M. Wirth, C. Emde, and A. Minikin (2009), Influence of ice crystal shape on retrieval of cirrus optical thickness and effective radius: A case study, *Journal of Geophysical Research: Atmospheres*, *114*(D19), D19,203, doi:10.1029/2009JD012215. (Cited on page 5)

Ewald, F. (2012), Implications of cloud geometry for the remote sensing of particle size profiles, Master's thesis, Ludwig–Maximilians–University. (Cited on pages 59, 60, 61, 74, 75, 97, and 99)

Ewald, F., T. Zinner, and B. Mayer (2013a), Remote sensing of particle size profiles from cloud sides: Observables and retrievals in a 3d environment, in *AIP Conference Proceedings*, vol. 1531, pp. 83–86, AIP Publishing, doi:10.1063/1.4804713. (Cited on pages 6, 7, and 191)

Ewald, F., L. Bugliaro, H. Mannstein, and B. Mayer (2013b), An improved cirrus detection algorithm MeCiDA2 for SEVIRI and its evaluation with MODIS, *Atmos. Meas. Tech.*, *6*(2), 309–322, doi:10.5194/amt-6-309-2013. (Cited on page 40)

Ewald, F., C. Winkler, and T. Zinner (2015), Reconstruction of cloud geometry using a scanning cloud radar, *Atmos. Meas. Tech.*, *8*(6), 2491–2508, doi:10.5194/amt-8-2491-2015. (Cited on pages 121 and 195)

Falkovich, G., A. Fouxon, and M. G. Stepanov (2002), Acceleration of rain initiation by cloud turbulence, *Nature*, *419*(6903), 151–154, doi:10.1038/nature00983. (Cited on page 178)

Feingold, G., S. M. Kreidenweis, B. Stevens, and W. R. Cotton (1996), Numerical simulations of stratocumulus processing of cloud condensation nuclei through collision-coalescence, *Journal of Geophysical Research: Atmospheres*, *101*(D16), 21,391–21,402, doi:10.1029/96JD01552. (Cited on page 53)

Feingold, G., R. Boers, B. Stevens, and W. R. Cotton (1997), A modeling study of the effect of drizzle on cloud optical depth and susceptibility, *Journal of Geophysical Research: Atmospheres*, *102*(D12), 13,527–13,534, doi:10.1029/97JD00963. (Cited on page 3)

Feingold, G., H. Jiang, and J. Y. Harrington (2005), On smoke suppression of clouds in Amazonia, *Geophysical Research Letters*, *32*(2), L02,804, doi:10.1029/2004GL021369. (Cited on page 3)

Fischer, J., and H. Grassl (1991), Detection of Cloud-Top Height from Backscattered Radiances within the Oxygen A Band. Part 1: Theoretical Study, *Journal of Applied Meteorology*, *30*(9), 1245–1259, doi:10.1175/1520-0450(1991)030⟨1245:DOCTHF⟩2.0.CO;2. (Cited on pages 124 and 188)

Fishman, G. (2003), *Monte Carlo: Concepts, Algorithms, and Applications*, 1st ed. 1996. corr. 4th printing 2003 ed., Springer, New York. (Cited on page 104)

Fossum, E. (1997), CMOS image sensors: electronic camera-on-a-chip, *IEEE Transactions on Electron Devices*, *44*(10), 1689–1698, doi:10.1109/16.628824. (Cited on page 126)

Freud, E., D. Rosenfeld, M. Andreae, A. Costa, P. Artaxo, et al. (2008), Robust relations between ccn and the vertical evolution of cloud drop size distribution in deep convective clouds, *Atmospheric Chemistry and Physics*, *8*(6), 1661–1675. (Cited on pages 13, 15, and 177)

Fu, Q., M. Cribb, H. Barker, S. Krueger, and A. Grossman (2000), Cloud geometry effects on atmospheric solar absorption, *Journal of the Atmospheric Sciences*, *57*(8), 1156–1168. (Cited on page 63)

Gao, B.-C., A. F. H. Goetz, and W. J. Wiscombe (1993), Cirrus cloud detection from Airborne Imaging Spectrometer data using the 1.38 µm water vapor band, *Geophysical Research Letters*, *20*(4), 301–304, doi:10.1029/93GL00106. (Cited on page 122)

Gasteiger, J., C. Emde, B. Mayer, R. Buras, S. A. Buehler, and O. Lemke (2014), Representative wavelengths absorption parameterization applied to satellite channels and spectral bands, *Journal of Quantitative Spectroscopy and Radiative Transfer*, *148*, 99–115, doi:10.1016/j.jqsrt.2014.06.024. (Cited on pages 50 and 101)

Gege, P., J. Fries, P. Haschberger, P. Schötz, B. Suhr, W. Vreeling, H. Schwarzer, P. Strobl, and G. Ulbrich (2009), A new laboratory for the characterisation of hyperspectral airborne sensors, http://elib.dlr.de/58527/. (Cited on pages 130, 148, 151, and 152)

Gerber, H. (1996), Microphysics of Marine Stratocumulus Clouds with Two Drizzle Modes, *Journal of the Atmospheric Sciences*, *53*(12), 1649–1662, doi:10.1175/1520-0469(1996)053⟨1649:MOMSCW⟩2.0.CO;2. (Cited on page 3)

Gerber, H. (2006), Entrainment, mixing, and microphysics in rico cumulus, *Proc. 12th Conf. On Cloud Physics*. (Cited on page 13)

Gerber, H. E., G. M. Frick, J. B. Jensen, and J. G. Hudson (2008), Entrainment, Mixing, and Microphysics in Trade-Wind Cumulus, *Journal of the Meteorological Society of Japan. Ser. II*, *86A*, 87–106, doi:10.2151/jmsj.86A.87. (Cited on pages 15 and 57)

Giuseppe, F. D., and A. Tompkins (2003), Effect of spatial organization on solar radiative transfer in three-dimensional idealized stratocumulus cloud fields, *Journal of the Atmospheric Sciences*, *60*(15), 1774–1794. (Cited on page 63)

Green, R. O., et al. (1998), Imaging Spectroscopy and the Airborne Visible/Infrared Imaging Spectrometer (AVIRIS), *Remote Sensing of Environment*, *65*(3), 227–248, doi:10.1016/S0034-4257(98)00064-9. (Cited on page 122)

Han, Q., W. Rossow, and A. Lacis (1994), Near-global survey of effective droplet radii in liquid water clouds using isccp data, *Journal of Climate*, *7*, 465–497. (Cited on page 5)

Hansen, J. (1971a), Circular polarization of sunlight reflected by clouds, *Journal of the Atmospheric Sciences*, *28*, 1515–1516. (Cited on page 35)

Hansen, J. (1971b), Multiple scattering of polarized light in planetary atmospheres. part i. the doubling method, *Journal of the Atmospheric Sciences*, *28*, 120–125. (Cited on page 145)

Hansen, J., and J. Pollack (1970), Near-infrared light scattering by terrestrial clouds, *Journal of the Atmospheric Sciences*, *27*, 265–281. (Cited on pages 5, 32, and 41)

Hansen, J., and L. Travis (1974a), Light scattering in planetary atmospheres, *Space Sci. Rev.*, *16*, 527–610. (Cited on pages 34 and 35)

Hansen, J. E., and L. D. Travis (1974b), Light scattering in planetary atmospheres, *Space Sci. Rev.*, *16*, 527–610. (Cited on page 63)

Hatzianastassiou, N., W. Wobrock, and A. Flossmann (1997), The role of droplet spectra for cloud radiative properties, *Q. J. R. Meteorol. Soc.*, *123*, 2215–2230. (Cited on page 64)

Hausmann, P. (2012), Ground-based remote sensing of optically thin ice clouds, Master's thesis, Ludwig–Maximilians–University. (Cited on page 90)

Heidinger, A., and G. Stephens (2000), Molecular line absorption in a scattering atmosphere. part ii: Application to remote sensing in the o2a band, *Journal of the Atmospheric Sciences*, *57*, 1616–1634. (Cited on page 124)

Heidinger, A., and G. Stephens (2002), Molecular line absorption in a scattering atmosphere. part iii: Pathlength characteristics and effects of spatially heterogeneous clouds, *Journal of the Atmospheric Sciences*, *59*, 1641–1654. (Cited on page 98)

Henyey, L., and J. Greenstein (1941), Diffuse radiation in the galaxy, *Astrophys. Journal*, *93*, 70–83. (Cited on pages 30 and 81)

Hess, M., P. Koepke, and I. Schult (1998), Optical properties of aerosols and clouds: The software package OPAC, *Bulletin of the American Meteorological Society*, *79*(5), 831–844, doi:10.1175/1520-0477(1998)079⟨0831:OPOAAC⟩2.0.CO;2. (Cited on pages 101 and 185)

Heus, T., C. F. J. Pols, H. J. J. Jonker, H. E. A. V. D. Akker, and D. H. Lenschow (2009), Observational validation of the compensating mass flux through the shell around cumulus clouds, *Q.J.R. Meteorol. Soc.*, *135*(638), 101–112, doi:10.1002/qj.358. (Cited on page 15)

Hill, A. A., G. Feingold, and H. Jiang (2009), The Influence of Entrainment and Mixing Assumption on Aerosol–Cloud Interactions in Marine Stratocumulus, *Journal of the Atmospheric Sciences*, *66*(5), 1450–1464, doi:10.1175/2008JAS2909.1. (Cited on page 57)

Holben, B., et al. (1998), Aeronet - a federated instrument network and data archive for aerosol characterization, *Remote Sens. Environ.*, *66*, 1–16. (Cited on page 5)

Hyvarinen, T. S., E. Herrala, and A. Dall'Ava (1998), Direct sight imaging spectrograph: a unique add-on component brings spectral imaging to industrial applications, in *Digital Solid State Cameras: Designs and Applications*, vol. 3302, pp. 165–175, doi:10.1117/12.304581. (Cited on page 146)

Illingworth, A. J., et al. (2014), The EarthCARE Satellite: The Next Step Forward in Global Measurements of Clouds, Aerosols, Precipitation, and Radiation, *Bulletin of the American Meteorological Society*, *96*(8), 1311–1332, doi:10.1175/BAMS-D-12-00227.1. (Cited on page 194)

IPCC (2013), *Index*, book section Index, pp. 1523–1535, Cambridge University Press, Cambridge, United Kingdom and New York, NY, USA, doi:10.1017/CBO9781107415324. (Cited on page 191)

Itten, K. I., et al. (2008), APEX - the Hyperspectral ESA Airborne Prism Experiment, *Sensors*, *8*(10), 6235–6259, doi:10.3390/s8106235. (Cited on page 122)

Jäkel, E., J. Walter, and M. Wendisch (2013), Thermodynamic phase retrieval of convective clouds: impact of sensor viewing geometry and vertical distribution of cloud properties, *Atmos. Meas. Tech.*, *6*(3), 539–547, doi:10.5194/amt-6-539-2013. (Cited on pages 5 and 40)

Janesick, J. R. (2007), *Photon Transfer*, SPIE Publications, Bellingham, Wash. (Cited on pages 134 and 142)

Jensen, J. B., P. H. Austin, M. B. Baker, and A. M. Blyth (1985), Turbulent Mixing, Spectral Evolution and Dynamics in a Warm Cumulus Cloud, *Journal of the Atmospheric Sciences*, *42*(2), 173–192, doi:10.1175/1520-0469(1985)042⟨0173:TMSEAD⟩2.0.CO;2. (Cited on pages 15 and 177)

Jiang, G. M., and Z. L. Li (2009), Cross-calibration of msg1-seviri infrared channels with terra-modis channels, *Int. J. Remote Sensing*, *30*(3), 753–769, doi:http://dx.doi.org/10.1080/01431160802392638. (Cited on pages 53, 54, and 57)

Jiang, H., G. Feingold, H. H. Jonsson, M.-L. Lu, P. Y. Chuang, R. C. Flagan, and J. H. Seinfeld (2008), Statistical comparison of properties of simulated and observed cumulus clouds in the vicinity of Houston during the Gulf of Mexico Atmospheric Composition and Climate Study (GoMACCS), *Journal of Geophysical Research: Atmospheres*, *113*(D13), D13,205, doi:10.1029/2007JD009304. (Cited on page 53)

Jørgensen, R. N. (2002), *The VTTVIS line imaging spectrometer: principles, error sources, and calibration*, Risø National Laboratory. (Cited on page 124)

Katzwinkel, J., H. Siebert, T. Heus, and R. A. Shaw (2014), Measurements of Turbulent Mixing and Subsiding Shells in Trade Wind Cumuli, *Journal* *of the Atmospheric Sciences*, *71*(8), 2810–2822, doi:10.1175/JAS-D-13-0222.1. (Cited on pages 15 and 177)

Khain, A., D. Rosenfeld, and A. Pokrovsky (2005), Aerosol impact on the dynamics and microphysics of deep convective clouds, *Q.J.R. Meteorol. Soc.*, *131*(611), 2639–2663. (Cited on page 3)

Kikuchi, N., T. Nakajima, H. Kumagai, H. Kuroiwa, A. Kamei, R. Nakamura, and T. Y. Nakajima (2006), Cloud optical thickness and effective particle radius derived from transmitted solar radiation measurements: Comparison with cloud radar observations, *Journal of Geophysical Research: Atmospheres*, *111*(D7), D07,205, doi:10.1029/2005JD006363. (Cited on page 5)

King, M. (1981), A method for determining the single scattering albedo of clouds through observation of the internal scattered radiation field, *Journal of the Atmospheric Sciences*, *38*, 2031–2044. (Cited on page 5)

King, M. (1987), Determination of the scaled optical thickness of clouds from reflected solar radiation measurements, *Journal of the Atmospheric Sciences*, *44*(13), 1734–1751. (Cited on page 5)

King, M., L. Radke, and P. Hobbs (1990), Determination of the spectral absorption of solar radiation by marine stratocumulus clouds from airborne measurements within clouds, *Journal of the Atmospheric Sciences*, *47*, 894–907. (Cited on page 5)

King, M., Y. Kaufman, W. Menzel, and D. Tanre (1992), Remote sensing of cloud, aerosol, and water vapor properties from the moderate resolution imaging spectrometer (MODIS), *IEEE Transactions on Geoscience and Remote Sensing*, *30*(1), 2–27, doi:10.1109/36.124212. (Cited on pages 41 and 42)

King, M., S. Platnick, P. Yang, G. Arnold, M. Gray, J. Riedi, A. Ackermann, and K. Liou (2004), Remote sensing of liquid water and ice cloud optical thickness and effective radius in the arctic: Application of airborne multispectral mas data, *Journal of Atmospheric and Oceanic Technology*, *21*(6), 857–875. (Cited on pages 5 and 41)

Kirchhoff, G. (1866), *Untersuchungen über das Sonnenspectum und die Spectren der chemischen Elemente von G. Kirchhoff*, vol. 153, Ferd. Dümmler's Verlagsbuchhandlung. (Cited on page 22)

Kokhanovski, A. (2004), Optical properties of terrestrial clouds, *Earth-Science Reviews*, *64*, 189–241. (Cited on page 32)

Koop, T. (2004), Homogeneous Ice Nucleation in Water and Aqueous Solutions, *Zeitschrift für Physikalische Chemie/International journal of research in physical chemistry and chemical physics*, *218*(11/2004), 1231–1258, doi:10.1524/zpch.218.11.1231.50812. (Cited on page 11)

Krautstrunk, M., and A. Giez (2012), The Transition From FALCON to HALO Era Airborne Atmospheric Research, in *Atmospheric Physics*, edited by U. Schumann, Research Topics in Aerospace, pp. 609–624, Springer Berlin Heidelberg. (Cited on pages 154 and 155)

Kunkel, K., and J. Weinma (1976), Monte carlo analysis of multiply scattered lidar returns, *Journal of the Atmospheric Sciences*, *33*, 1772–1781. (Cited on page 51)

Kurucz, R. L. (1994), Synthetic Infrared Spectra, in *Infrared Solar Physics*, *IAU Symposium*, vol. 154, edited by D. M. Rabin, J. T. Jefferies, & C. Lindsey, p. 523. (Cited on pages 38, 50, and 101)

Langmore, I., A. Davis, and G. Bal (2013), Multipixel Retrieval of Structural and Optical Parameters in a 2-D Scene With a Path-Recycling Monte Carlo Forward Model and a New Bayesian Inference Engine, *IEEE Transactions on Geoscience and Remote Sensing*, *51*(5), 2903–2919, doi:10.1109/TGRS.2012.2217380. (Cited on page 84)

Lasher-trapp, S. G., W. A. Cooper, and A. M. Blyth (2005), Broadening of droplet size distributions from entrainment and mixing in a cumulus cloud, *Quarterly Journal of the Royal Meteorological Society*, *131*(605), 195–220, doi:10.1256/qj.03.199. (Cited on page 177)

LeBlanc, S. E., P. Pilewskie, K. S. Schmidt, and O. Coddington (2015), A spectral method for discriminating thermodynamic phase and retrieving cloud optical thickness and effective radius using transmitted solar radiance spectra, *Atmos. Meas. Tech.*, *8*(3), 1361–1383, doi:10.5194/amt-8-1361-2015. (Cited on page 5)

Lee, J., P. Yang, A. Dessler, B. Baum, and S. Platnick (2006), The influence of thermodynamic phase on the retrieval of mixed-phase cloud microphysical and optical properties in the visible and near-infrared region, *Geoscience and Remote Sensing Letters, IEEE*, *3*(3), 287–291. (Cited on page 92)

Lenhard, K., A. Baumgartner, and T. Schwarzmaier (2015), Independent laboratory characterization of NEO HySpex imaging spectrometers VNIR-1600 and SWIR-320m-e, *IEEE Transactions on Geoscience and Remote Sensing*, *53*(4), 1828–1841, doi:10.1109/TGRS.2014.2349737. (Cited on pages 124, 129, 143, 146, and 147)

Liu, Y. D. (2002), A generalized systems theory for the effect of varying fluctuations on cloud droplet size distributions, *Journal of the Atmospheric Sciences*, *59*, 2279–2290. (Cited on page 3)

Loeb, N. G., B. A. Wielicki, D. R. Doelling, G. L. Smith, D. F. Keyes, S. Kato, N. Manalo-Smith, and T. Wong (2009), Toward Optimal Closure of the Earth's

Top-of-Atmosphere Radiation Budget, *Journal of Climate*, *22*(3), 748–766, doi: 10.1175/2008JCLI2637.1. (Cited on page 2)

Lu, M.-L., G. Feingold, H. H. Jonsson, P. Y. Chuang, H. Gates, R. C. Flagan, and J. H. Seinfeld (2008), Aerosol-cloud relationships in continental shallow cumulus, *Journal of Geophysical Research: Atmospheres*, *113*(D15), D15,201, doi: 10.1029/2007JD009354. (Cited on page 3)

Lu, Z., Q. Zhang, and D. G. Streets (2011), Sulfur dioxide and primary carbonaceous aerosol emissions in China and India, 1996–2010, *Atmos. Chem. Phys.*, *11*(18), 9839–9864, doi:10.5194/acp-11-9839-2011. (Cited on page 4)

Marchuk, G., G. Mikhailov, M. Nazaraliev, R. Darbinjan, B. Kargin, and B. Elepov (1980), *The Monte Carlo Methods in Atmospheric Optics*, iSBN-13: 978-0387094021. (Cited on page 51)

Marques Vatus, C., and P. Magnan (2004), Analysis and potentialities of backside-illuminated thinned CMOS imagers, in *Proc. SPIE 5251, Detectors and Associated Signal Processing*, vol. 5251, pp. 178–186, doi:10.1117/12.513893. (Cited on page 138)

Marshak, A., A. B. Davis, W. J. Wiscombe, and R. F. Cahalan (1995), Radiative smoothing in fractal clouds, *J. Geophys. Res*, *100*(26), 247–26. (Cited on pages 42 and 98)

Marshak, A., A. Davis, W. Wiscombe, W. Ridgway, and R. F. Cahalan (1998), Biases in shortwave column absorption in the presence of fractal clouds, *Journal of Climate*, *11*, 431–446. (Cited on page 63)

Marshak, A., Y. Knyazikhin, A. B. Davis, W. J. Wiscombe, and P. Pilewskie (2000), Cloud-vegetation interaction: Use of normalized difference cloud index for estimation of cloud optical thickness, *Geophys. Res. Lett.*, *27*(12), 1695–1698. (Cited on page 90)

Marshak, A., S. Platnick, T. Varnai, G. Wen, and R. F. Cahalan (2006a), Impact of three-dimensional radiative effects on satellite retrievals of cloud droplet sizes, *Journal of Geophysical Research*, *111*(D9), D09,207, doi:10.1029/2005JD006686. (Cited on pages 6, 43, and 123)

Marshak, A., J. V. Martins, V. Zubko, and Y. Kaufman (2006b), What does reflection from cloud sides tell us about vertical distribution of cloud droplet sizes?, *Atmospheric Chemistry & Physics*, *6*(4), 7207–7233. (Cited on pages 6, 7, 41, 43, 52, and 191)

Martin, G. M., D. W. Johnson, and A. Spice (1994), The Measurement and Parameterization of Effective Radius of Droplets in Warm Stratocumulus Clouds, *Journal of the Atmospheric Sciences*, *51*(13), 1823–1842, doi:10.1175/1520-0469(1994)051⟨1823:TMAPOE⟩2.0.CO;2. (Cited on pages 13, 14, and 56)

Martin, W., B. Cairns, and G. Bal (2014), Adjoint methods for adjusting three-dimensional atmosphere and surface properties to fit multi-angle/multi-pixel polarimetric measurements, *Journal of Quantitative Spectroscopy and Radiative Transfer*, *144*, 68–85, doi:10.1016/j.jqsrt.2014.03.030. (Cited on page 84)

Martins, J., et al. (2011), Remote sensing the vertical profile of cloud droplet effective radius, thermodynamic phase, and temperature, *Atmos. Chem. Phys*, *11*, 9485–9501. (Cited on pages 6, 7, 40, 41, 45, 123, 157, and 191)

Maxwell, J. (1865), A dynamical theory of the electromagnetic field, *Philosophical Transactions of the Royal Society of London*, *155*, 459–512. (Cited on page 17)

Mayer, B. (1998), Mystic, monte carlo code for the physically correct tracing of photons in cloudy atmospheres. (Cited on pages 50 and 51)

Mayer, B. (2009), Radiative transfer in the cloudy atmosphere, *European Physical Journal Conferences*, *1*, 75–99. (Cited on pages 50 and 51)

Mayer, B., and A. Kylling (2005), Technical note: The libradtran software package for radiative transfer calculations - description and examples of use, *Atmospheric Chemistry and Physics*, *5*(7), 1855–1877, doi:10.5194/acp-5-1855-2005. (Cited on page 50)

Mayer, B., M. Schröder, R. Preusker, and L. Schüller (2004), Remote sensing of water cloud droplet size distributions using the backscatter glory: a case study, *Atmos. Chem. . . .*, *4*(5), 1255–1263. (Cited on pages 68 and 122)

McBride, P. J., K. S. Schmidt, P. Pilewskie, A. S. Kittelman, and D. E. Wolfe (2011), A spectral method for retrieving cloud optical thickness and effective radius from surface-based transmittance measurements, *Atmos. Chem. Phys.*, *11*(14), 7235–7252, doi:10.5194/acp-11-7235-2011. (Cited on page 5)

McFarlane, S., K. Evans, and A. Ackerman (2002), A bayesian algorithm for the retrieval of liquid water cloud properties from microwave radiometer and millimeter radar data, *J. Geophys. Res*, *107*(D16), 10.1029. (Cited on page 47)

Mech, M., E. Orlandi, S. Crewell, F. Ament, L. Hirsch, M. Hagen, G. Peters, and B. Stevens (2014), HAMP – the microwave package on the High Altitude and LOng range research aircraft (HALO), *Atmos. Meas. Tech.*, *7*(12), 4539–4553, doi:10.5194/amt-7-4539-2014. (Cited on page 195)

Meier, R., J. Lee, and D. Anderson (1978), Atmospheric scattering of middle uv radiation from an internal source, *Applied Optics*, *17*(20), 3216–3225. (Cited on page 51)

Mie, G. (1908), Beiträge zur optik trüber medien, speziell kolloidaler metallösungen, *Annalen der Physik, Vierte Folge*, *25*(3), 377–445. (Cited on page 29)

Mosegaard, K., and A. Tarantola (1995), Monte Carlo sampling of solutions to inverse problems, *Journal of Geophysical Research: Solid Earth*, *100*(B7), 12,431–12,447, doi:10.1029/94JB03097. (Cited on pages 46, 48, and 94)

Myhre, G., et al. (2013), *Anthropogenic and Natural Radiative Forcing*, book section 8, pp. 659–740, Cambridge University Press, Cambridge, United Kingdom and New York, NY, USA, doi:10.1017/CBO9781107415324.018. (Cited on page 2)

Nakajima, T. Y., and M. D. King (1990), Determination of the optical thickness and effective particle radius of clouds from reflected solar radiation measurements. part i: Theory, *J. Atmos. Sci*, *47*(15), 1878–1893. (Cited on pages 5, 32, 41, 63, 64, 70, 71, 104, 123, 191, and 192)

Nakajima, T. Y., and M. Tanaka (1988), Algorithms for radiative intensity calculations in moderately thick atmospheres using a truncation approximation, *J. Qunat. Spectrosc. Radiat. Transfer*, *40*(1), 51–69. (Cited on page 50)

Pilewskie, P., and S. Twomey (1987), Discrimination of ice from water in clouds by optical remote sensing, *Atmospheric Research*, *21*(2), 113–122, doi:10.1016/0169-8095(87)90002-0. (Cited on page 40)

Pilewskie, P., J. Pommier, R. Bergstrom, W. Gore, M. Rabbette, B. Schmid, P. V. Hobbs, and S. C. Tsay (2003), Solar spectral radiative forcing during the Southern African regional science initiative, *J. Geophys. Res.*, *108*, doi:10.1029/2002JD002,411. (Cited on page 5)

Pincus, R., and M. B. Baker (1994), Effect of precipitation on the albedo susceptibility of clouds in the marine boundary layer, *Nature*, *372*(6503), 250–252, doi:10.1038/372250a0. (Cited on page 4)

Pinsky, M. B., and A. P. Khain (1997), Turbulence effects on droplet growth and size distribution in clouds—A review, *Journal of Aerosol Science*, *28*(7), 1177–1214, doi:10.1016/S0021-8502(97)00005-0. (Cited on page 178)

Planck, M. (1900), Zur theorie des gesetzes der energieverteilung im normalspektrum, in *Verhandlungen der Deutschen physikalischen Gesellschaft*. (Cited on page 23)

Plass, G. N., and G. W. Kattawar (1968), Influence of single scattering albedo on reflected and transmitted light from clouds, *Applied Optics*, *7*(2), 361–367, doi:10.1364/AO.7.000361. (Cited on page 5)

Platnick, S. (2000), Vertical photon transport in cloud remote sensing problems, *Journal of Geophysical Research*, *105*(D18), 22,919–22,935. (Cited on pages 58, 59, and 61)

Platnick, S., J. Li, M. D. King, H. Gerber, and P. Hobbs (2001), A solar reflectance method for retrieving the optical thickness and droplet size of liquid water clouds over snow and ice surfaces, *Journal of Geophysical Research*, *106*, 15. (Cited on pages 5 and 41)

Platnick, S., M. King, A. Ackermann, W. Menzel, B. Baum, J. Riedi, and R. Frey (2003), The modis cloud products: Algorithms and examples from terra, *IEEE Transactions on Geoscience and Remote Sensing*, *41*, 459–473. (Cited on page 41)

Popp, C., D. Brunner, A. Damm, M. Van Roozendael, C. Fayt, and B. Buchmann (2012), High-resolution NO2 remote sensing from the Airborne Prism EXperiment (APEX) imaging spectrometer, *Atmos. Meas. Tech.*, *5*(9), 2211–2225, doi:10.5194/amt-5-2211-2012. (Cited on page 122)

Raoult, F. (1887), Loi générale des tensions de vapeur des dissolvants, *Comptes rendus des séances de lacadémie des sciences, Paris*, *104*, 1430–1433. (Cited on page 11)

Rauber, R. M., et al. (2007), Rain in Shallow Cumulus Over the Ocean: The RICO Campaign, *Bulletin of the American Meteorological Society*, *88*(12), 1912–1928, doi:10.1175/BAMS-88-12-1912. (Cited on page 53)

Rayleigh, L. (1899), On the transmission of light through an atmosphere containing small particles in suspension, and on the origin of the blue sky, *Phil. Mag.*, *47*, 375–384, doi:10.1080/14786449908621276. (Cited on page 28)

Roebeling, R. A., A. J. Feijt, and P. Stammes (2006), Cloud property retrievals for climate monitoring: Implications of differences between spinning enhanced visible and infrared imager (seviri) on meteosat-8 and advanced very high resolution radiometer (avhrr) on noaa-17, *Journal of Geophysical Research*, *111*(D20), D20,210, doi:10.1029/2005JD006990. (Cited on page 5)

Rosenfeld, D., and I. Lensky (1998), Satellite-based insights into precipitation formation processes in continental and maritime convective clouds, *Bull Amer Met Soc*, *79*(11). (Cited on page 40)

Rosenfeld, D., U. Lohmann, G. B. Raga, C. D. O'Dowd, M. Kulmala, S. Fuzzi, A. Reissell, and M. O. Andreae (2008), Flood or drought: How do aerosols affect precipitation?, *Science*, *321*(5894), 1309–1313. (Cited on pages 2, 3, 4, and 40)

Rosenfeld, D., E. Williams, M. O. Andreae, E. Freud, U. Pöschl, and N. O. Rennó (2012), The scientific basis for a satellite mission to retrieve CCN concentrations and their impacts on convective clouds, *Atmos. Meas. Tech.*, *5*(8), 2039–2055, doi:10.5194/amt-5-2039-2012. (Cited on pages 3 and 7)

Rothman, L. S., et al. (2005), The hitran 2004 molecular spectroscopic database, *Journal of Quantitative Spectroscopy and Radiative Transfer*, *96*(2 SPEC. ISS.), 139–204. (Cited on page 50)

Rouse, J. W., Jr., R. H. Haas, J. A. Schell, and D. W. Deering (1974), Monitoring Vegetation Systems in the Great Plains with Erts, *NASA Special Publication*, *351*, 309. (Cited on page 90)

Rozanov, V., A. Kokhanovsky, and J. Burrows (2004), The determination of cloud altitudes using gome reflectance spectra: multilayered cloud systems, *IEEE Transcations on Geoscience and Remote Sensing*, *42*(5), 1009–1017. (Cited on page 188)

Saunders, R., and K. Kriebel (1988), An improved method for detecting clear sky and cloudy radiances from avhrr data, *Int. J. Remote Sensing*, *9*(1), 123–150. (Cited on page 40)

Schaepman, M. E., et al. (2015), Advanced radiometry measurements and Earth science applications with the Airborne Prism Experiment (APEX), *Remote Sensing of Environment*, *158*, 207–219, doi:10.1016/j.rse.2014.11.014. (Cited on page 122)

Schäfer, M., E. Bierwirth, A. Ehrlich, F. Heyner, and M. Wendisch (2013), Retrieval of cirrus optical thickness and assessment of ice crystal shape from ground-based imaging spectrometry, *Atmos. Meas. Tech.*, *6*(8), 1855–1868, doi:10.5194/amt-6-1855-2013. (Cited on page 122)

Schäfer, M., E. Bierwirth, A. Ehrlich, E. Jäkel, and M. Wendisch (2015), Airborne observations and simulations of three-dimensional radiative interactions between Arctic boundary layer clouds and ice floes, *Atmos. Chem. Phys.*, *15*(14), 8147–8163, doi:10.5194/acp-15-8147-2015. (Cited on page 122)

Scheirer, R. (2003), Cloud inhomogeneity and broadband solar fluxes, *Journal of Geophysical Research*, *108*(D19), 4599, doi:10.1029/2002JD003321. (Cited on page 43)

Schmidt, K., P. Pilewskie, S. Platnick, G. Wind, P. Yang, and M. Wendisch (2007), Comparing irradiance fields derived from moderate resolution imaging spectroradiometer airborne simulator cirrus cloud retrievals with solar spectral flux radiometer measurements, *J. Geophys. Res*, *112*, D24,206. (Cited on page 5)

Schwarzmaier, T., A. Baumgartner, P. Gege, C. Köhler, and K. Lenhard (2012), The Radiance Standard RASTA of DLR's calibration facility for airborne imaging spectrometers, http://elib.dlr.de/78117/. (Cited on page 137)

Scott, D. W., R. A. Tapia, and J. R. Thompson (1977), Kernel density estimation revisited, *Nonlinear Analysis: Theory, Methods & Applications*, *1*(4), 339–372, doi:10.1016/S0362-546X(97)90003-1. (Cited on page 48)

Segelstein, D. J. (1981), The complex refractive index of water, Master's thesis, University of Missouri–Kansas City. (Cited on pages 25 and 26)

Seinfeld, J. H., and S. N. Pandis (2012), *Atmospheric Chemistry and Physics: From Air Pollution to Climate Change*, John Wiley & Sons. (Cited on page 10)

Shaw, R. A., W. C. Reade, L. R. Collins, and J. Verlinde (1998), Preferential Concentration of Cloud Droplets by Turbulence: Effects on the Early Evolution of Cumulus Cloud Droplet Spectra, *Journal of the Atmospheric Sciences*, *55*(11), 1965–1976, doi:10.1175/1520-0469(1998)055⟨1965:PCOCDB⟩2.0.CO;2. (Cited on page 64)

Siebert, H., K. Lehmann, M. Wendisch, H. Franke, R. Maser, D. Schell, E. Wei Saw, and R. A. Shaw (2006), Probing Finescale Dynamics and Microphysics of Clouds with Helicopter-Borne Measurements, *Bulletin of the American Meteorological Society*, *87*(12), 1727–1738, doi:10.1175/BAMS-87-12-1727. (Cited on page 164)

Slingo, A., S. Nicholls, and J. Schmetz (1982), Aircraft observations of marine stratocumulus during JASIN, *Quarterly Journal of the Royal Meteorological Society*, *108*(458), 833–856, doi:10.1002/qj.49710845807. (Cited on page 12)

Stamnes, K., S. Tsay, W. Wiscombe, and K. Jayaweera (1988), A numerically stable algorithm for discrete-ordinate-method radiative transfer in multiple scattering and emitting layered media, *Applied Optics*, *27*(12), 2502–2509. (Cited on pages 38 and 50)

Stamnes, K., S.-C. Tsay, W. Wiscombe, and I. Laszlo (2000), Disort, a general-purpose fortran program for discrete-ordinate-method radiative transfer in scattering and emitting layered media: Documentation of methodology, *Tech. rep.* (Cited on page 50)

Stefanov, K. (2014), A Statistical Model for Signal-Dependent Charge Sharing in Image Sensors, *IEEE Transactions on Electron Devices*, *61*(1), 110–115, doi:10.1109/TED.2013.2291448. (Cited on page 142)

Stephens, G. L., and C. M. R. Platt (1987), Aircraft Observations of the Radiative and Microphysical Properties of Stratocumulus and Cumulus Cloud Fields, *Journal of Climate and Applied Meteorology*, *26*(9), 1243–1269, doi:10.1175/1520-0450(1987)026⟨1243:AOOTRA⟩2.0.CO;2. (Cited on page 12)

Stier, P., J. H. Seinfeld, S. Kinne, and O. Boucher (2007), Aerosol absorption and radiative forcing, *Atmospheric Chemistry and Physics*, *7*(19), 5237–5261, doi:10.5194/acp-7-5237-2007. (Cited on page 3)

Strahler, A., J. Muller, and M. S. T. Members (1999), Modis brdf/albedo product: Algorithm theoretical basis document version 5.0. (Cited on page 90)

Stubenrauch, C. J., et al. (2013), Assessment of Global Cloud Datasets from Satellites: Project and Database Initiated by the GEWEX Radiation Panel, *Bulletin of the American Meteorological Society*, *94*(7), 1031–1049, doi:10.1175/BAMS-D-12-00117.1. (Cited on page 1)

Thompson, D. R., et al. (2015), Real-time remote detection and measurement for airborne imaging spectroscopy: a case study with methane, *Atmos. Meas. Tech.*, *8*(10), 4383–4397, doi:10.5194/amt-8-4383-2015. (Cited on page 122)

Thomson, W. (1871), Lx. on the equilibrium of vapour at a curved surface of liquid, *Philosophical Magazine Series 4*, *42*(282), 448–452. (Cited on page 10)

Todd, J. T., E. J. L. Egan, and F. Phillips (2014), Is the Perception of 3d Shape from Shading Based on Assumed Reflectance and Illumination?, *i-Perception*, *5*(6), 497–514, doi:10.1068/i0645. (Cited on page 43)

Tucker, C. J. (1979), Red and photographic infrared linear combinations for monitoring vegetation, *Remote Sensing of Environment*, *8*(2), 127–150, doi:10.1016/0034-4257(79)90013-0. (Cited on page 90)

Twomey, S. (1977), The influence of pollution on the shortwave albedo of clouds, *Journal of the Atmospheric Sciences*, *34*, 1149–1152. (Cited on pages 2 and 3)

Twomey, S., and T. Cocks (1982), Spectral reflectance of clouds in the near–infrared: comparison of measurements and calculations, *J. Met. Soc. of Japan*, *60*, 583–592. (Cited on page 41)

Twomey, S., and T. Cocks (1989), Remote sensing of cloud parameters from spectral reflectance in the near-infrared, *Beiträge zur Physik der Atmosphäre*, *62*(3), 172–179. (Cited on pages 5 and 32)

Tzivion, S., G. Feingold, and Z. Levin (1987), An efficient numerical solution to the stochastic collection equation, *Journal of the Atmospheric Sciences*, *44*(21), 3139–3149, doi:10.1175/1520-0469(1987)044⟨3139:AENSTT⟩2.0.CO;2. (Cited on pages 53 and 54)

van de Hulst, H. (1980), *Radiation and Cloud Processes in the Atmosphere. Theory, Observation and Modeling, Multiple Light Scattering, Volume 1*, Academic Press, New York. (Cited on page 97) van Diedenhoven, B., O. P. Hasekamp, and J. Landgraf (2007), Retrieval of cloud parameters from satellite-based reflectance measurements in the ultraviolet and the oxygen A-band, *Journal of Geophysical Research: Atmospheres*, *112*(D15), D15,208, doi:10.1029/2006JD008155. (Cited on page 188)

Vant-Hull, B., A. Marshak, L. Remer, and Z. Li (2007), The effects of scattering angle and cumulus cloud geometry on satellite retrievals of cloud droplet effective radius, *Geoscience and Remote Sensing, IEEE Transactions on*, *45*(4), 1039–1045. (Cited on pages 41, 43, 63, and 72)

vanZanten, M. C., et al. (2011), Controls on precipitation and cloudiness in simulations of trade-wind cumulus as observed during RICO, *Journal of Advances in Modeling Earth Systems*, *3*(2), M06,001, doi:10.1029/2011MS000056. (Cited on page 53)

Varnai, T., and A. Marshak (2002a), Observations of the three-dimensional radiative effects that influence modis cloud optical thickness retrievals, *Journal of the Atmospheric Sciences*, *59*, 1607–1618. (Cited on pages 43 and 72)

Varnai, T., and A. Marshak (2002b), Observations of three-dimensional radiative effects that influence satellite retrievals of cloud properties, *Quarterly Journal of the Hungarian Meteorological Society*, *106*, 265–278. (Cited on page 123)

Varnai, T., and A. Marshak (2003), A method for analyzing how various parts of clouds influence each other's brightness, *Journal of Geophysical Research*, *108*(D22), 4706, doi:10.1029/2003JD003561. (Cited on pages 42 and 84)

Varnai, T., and A. Marshak (2007), View angle dependence of cloud optical thicknesses retrieved by moderate resolution imaging spectroradiometer (modis), *Journal of Geophysical Research*, *112*(D6), D06,203, doi:10.1029/2005JD006912. (Cited on page 6)

Varnai, T., and A. Marshak (2009), Modis observations of enhanced clear sky reflectance near clouds, *Geophys. Res. Lett.*, *36*(6), L06,807, doi:10.1029/2008GL037089. (Cited on page 6)

von Helmholtz, H. (1865), *Helmholtz's Treatise on Physiological Optics, Vol. 1*, Dover Publications, New York in 1962. (Cited on page 51)

Wang, J., and L. Rong (2009), A model for cascading failures in scale-free networks with a breakdown probability, *Physica A: Statistical Mechanics and its Applications*, *388*(7), 1289–1298. (Cited on page 13)

Wang, Y., B. Geerts, and J. French (2009), Dynamics of the cumulus cloud margin: An observational study, *Journal of the Atmospheric Sciences*, *66*(12), 3660–3677, doi:10.1175/2009JAS3129.1. (Cited on pages 15 and 177)

Warner, J. (1955), The Water Content of Cumuliform Cloud, *Tellus*, *7*(4), 449–457, doi:10.1111/j.2153-3490.1955.tb01183.x. (Cited on pages 3, 13, and 57)

Warner, J. (1969), The Microstructure of Cumulus Cloud. Part I. General Features of the Droplet Spectrum, *Journal of the Atmospheric Sciences*, *26*(5), 1049–1059, doi:10.1175/1520-0469(1969)026⟨1049:TMOCCP⟩2.0.CO;2. (Cited on page 12)

Warren, G. (1984), Optical constants of ice from the ultraviolet to the microwave, *Applied Optics*, *23*(8), 1206–1225. (Cited on pages 25 and 26)

Wen, G., A. Marshak, R. F. Cahalan, L. A. Remer, and R. G. Kleidman (2007), 3-d aerosol-cloud radiative interaction observed in collocated modis and aster images of cumulus cloud fields, *Journal of Geophysical Research*, *112*(D13), D13,204, doi:10.1029/2006JD008267. (Cited on page 6)

Wendisch, M., and B. Mayer (2003), Vertical distribution of spectral solar irradiance in the cloudless sky - a case study, *Geophys. Res. Lett.*, *30*, doi:10.1029/2002GL016,529. (Cited on page 5)

Wendisch, M., D. Müller, D. Schell, and J. Heintzenberg (2001), An airborne spectral albedometer with active horizontal stabilization, *Journal of Atmospheric and Oceanic Technology*, *18*, 1856–1866. (Cited on pages 5 and 155)

Wendisch, M., et al. (2008), Radiative and dynamic effects of absorbing aerosol particles over the pearl river delta, china. (Cited on page 3)

Wendisch, M., et al. (submitted), The ACRIDICON-CHUVA campaign to study tropical deep convective clouds and precipitation using the new german research aircraft HALO, *Bulletin of the American Meteorological Society*. (Cited on pages 154 and 165)

Wendling, P., et al. (2002), Aerosol–radiation interaction in the cloudless atmosphere during LACE 98 2. Aerosol-induced solar irradiance changes determined from airborne pyranometer measurements and calculations, *Journal of Geophysical Research: Atmospheres*, *107*(D21), 8131, doi:10.1029/2000JD000288. (Cited on page 122)

Werner, F., H. Siebert, P. Pilewskie, T. Schmeissner, R. A. Shaw, and M. Wendisch (2013), New airborne retrieval approach for trade wind cumulus properties under overlying cirrus, *Journal of Geophysical Research: Atmospheres*, *118*(9), 3634–3649, doi:10.1002/jgrd.50334. (Cited on page 40)

Wien, W. (1896), Ueber die energievertheilung im emissionsspectrum eines schwarzen körpers, *Annalen der Physik*, *294*(8), 662–669. (Cited on page 24)

Wirth, M., A. Fix, P. Mahnke, H. Schwarzer, F. Schrandt, and G. Ehret (2009), The airborne multi-wavelength water vapor differential absorption lidar WALES: system design and performance, *Applied Physics B*, *96*(1), 201–213, doi:10.1007/s00340-009-3365-7. (Cited on page 195)

Wiscombe, W. (1977), The delta-m method: Rapid yet accurate radiative flux calculations for strongly asymmetric phase functions, *Journal of the Atmospheric Sciences*, *34*, 1408–1421. (Cited on page 50)

Wiscombe, W., and S. Warren (1980), A model for the spectral albedo of snow. i: Pure snow, *Journal of the Atmospheric Sciences*, *37*, 2712–2733. (Cited on page 50)

Witt, A. (1977), Multiple scattering in reflection nebulae. i - a monte carlo approach., *Astrophysical Journal Supplement Series*, *35*, 1–6, doi:10.1086/190463. (Cited on page 51)

Xue, H., G. Feingold, and B. Stevens (2008), Aerosol Effects on Clouds, Precipitation, and the Organization of Shallow Cumulus Convection, *Journal of the Atmospheric Sciences*, *65*(2), 392–406, doi:10.1175/2007JAS2428.1. (Cited on page 4)

Yang, F., R. Shaw, and H. Xue (2016), Conditions for super-adiabatic droplet growth after entrainment mixing, *Atmospheric Chemistry and Physics Discussions*, pp. 1–24, doi:10.5194/acp-2016-94. (Cited on page 177)

Yang, P., H. Wei, B. Baum, H. Huang, A. Heymsfield, Y. Hu, B. Gao, and D. Turner (2003), The spectral signature of mixed-phase clouds composed of non-spherical ice crystals and spherical liquid droplets in the terrestrial window region, *Journal of Quantitative Spectroscopy and Radiative Transfer*, *79*, 1171–1188. (Cited on pages 40, 59, and 60)

Yuan, T., J. V. Martins, Z. Li, and L. A. Remer (2010), Estimating glaciation temperature of deep convective clouds with remote sensing data, *Geophysical Research Letters*, *37*(8), L08,808, doi:10.1029/2010GL042753. (Cited on page 41)

Yuter, S. E., and R. A. Houze (1995), Three-Dimensional Kinematic and Microphysical Evolution of Florida Cumulonimbus. Part II: Frequency Distributions of Vertical Velocity, Reflectivity, and Differential Reflectivity, *Monthly Weather Review*, *123*(7), 1941–1963, doi:10.1175/1520-0493(1995)123⟨1941:TDKAME⟩2.0.CO;2. (Cited on page 54)

Zdunkowski, W., T. Trautmann, and A. Bott (2007), *Radiation in the atmosphere: a course in theoretical meteorology*, Cambridge Univ Pr. (Cited on page 31)

Zhang, R., P.-S. Tsai, J. Cryer, and M. Shah (1999), Shape-from-shading: a survey, *IEEE Transactions on Pattern Analysis and Machine Intelligence*, *21*(8), 690–706, doi:10.1109/34.784284. (Cited on page 43)

Zinner, T., and B. Mayer (2006), Remote sensing of stratocumulus clouds: Uncertainties and biases due to inhomogeneity, *Journal of Geophysical Research*, *111*(D14), D14,209, doi:10.1029/2005JD006955. (Cited on pages 6, 63, 72, 122, and 123)

Zinner, T., A. Marshak, S. Lang, J. V. Martins, and B. Mayer (2008), Remote sensing of cloud sides of deep convection: towards a three-dimensional retrieval of cloud particle size profiles, *Atmos. Chem. Phys.*, *8*, 4741–4757. (Cited on pages 6, 7, 41, 43, 45, 47, 52, 59, 92, 123, and 191)

Symbols

Symbol	Unit	Description	Page
τ_c	-	Cloud optical thickness	64
g	-	Asymmetry parameter	35
ω_0	-	Single scattering albedo	35
$\langle\tau\rangle_{mc}$	-	Mean apparent optical thickness (MC)	98
σ_{geo}	m^2	Geometric cross-section	27
σ_{ext}	m^2	Extinction cross-section	32
σ_{sca}	m^2	Scattering cross-section	27
σ_{abs}	m^2	Absorption cross-section	24
k_{ext}	m^{-1}	Extinction coefficient	29
k_{sca}	m^{-1}	Scattering coefficient	27
k_{abs}	m^{-1}	Absorption coefficient	24
Q_{ext}	-	Extinction efficiency	35
Q_{sca}	-	Scattering efficiency	27
Q_{abs}	-	Absorption efficiency	36
r_{vol}	μm	Volumetric radius	13
r_{sca}	μm	Mean radius for scattering	33
r_{eff}	μm	Effective radius	12
v_{eff}	μm^2	Effective variance	34
N_d	cm^{-1}	Total cloud droplet concentration	14
$n(r)$	-	Cloud droplet size distribution	63
$\langle r_{eff}\rangle_{app}$	μm	Apparent effective radius (analytic)	58
$r_{eff\,mc,i}$	μm	Apparent effective radius (MC)	59
$\langle r_{eff}\rangle_{mc}$	μm	Mean apparent effective radius (MC)	60
$\lambda_{mc,i}$	-	Optical path length (MC)	59
$\langle\lambda\rangle_{mc}$	-	Mean optical path length (MC)	60
$\hat{\mathbf{n}}_{mc,i}$	-	Cloud surface normal (MC)	61
$\langle\hat{\mathbf{n}}_{mc}\rangle$	-	Mean cloud surface normal (MC)	62
$\Gamma_{d,ad}$	$K\,km^{-1}$	Dry adiabatic lapse rate	9
$\Gamma_{m,ad}$	$K\,km^{-1}$	Moist adiabatic lapse rate	9
RH	%	Relative humidity	9
T	K	Temperature of air	9

Symbol	Unit	Description	Page
p	Pa	Pressure of air	9
e	Pa	Vapor pressure of water	9
e_s	Pa	Saturated vapor pressure of water	9
q_l	$\mathrm{g\,kg^{-1}}$	Mixing ratio of liquid water	10
q_v	$\mathrm{g\,kg^{-1}}$	Mixing ratio of water vapor	10
q_t	$\mathrm{g\,kg^{-1}}$	Mixing ratio of total water	10
q_v^s	$\mathrm{g\,kg^{-1}}$	Saturation mixing ratio of water vapor	10
$\hat{\mathbf{s}}$	-	Solar direction vector	71
$\hat{\mathbf{v}}$	-	Viewing direction vector	71
$\hat{\mathbf{n}}$	-	Cloud surface normal vector	61
L_{1D}	$\mathrm{mW\,m^{-2}\,sr^{-1}\,nm^{-1}}$	Spectral radiance (DISORT)	97
L_{3D}	$\mathrm{mW\,m^{-2}\,sr^{-1}\,nm^{-1}}$	Spectral radiance (MYSTIC)	98
$L_{0.87}$	$\mathrm{mW\,m^{-2}\,sr^{-1}\,nm^{-1}}$	Spectral radiance at 870 nm	47
$L_{2.10}$	$\mathrm{mW\,m^{-2}\,sr^{-1}\,nm^{-1}}$	Spectral radiance at 2100 nm	47

Acknowledgments

First and foremost, I would like to thank my two supervisors Dr. Tobias Zinner and Prof. Dr. Bernhard Mayer for giving me the opportunity to work in such a stimulating research environment. Many thanks to Tobias Zinner for his permanent support, stimulating discussions and the helpful guidance throughout the course of this research. I am particularly grateful to Prof. Dr. Bernhard Mayer for his open ear and advice to any question that came up throughout the years.

Special thanks go to Tobias Kölling, who contributed directly to this work during the further development and characterization of *specMACS* in the scope of his master thesis I supervised. The memories during our time on campaigns in Melpitz and in Brazil will last a lifetime! This also applies to Christian Winkler who helped me a lot during our measurement campaign in Jülich and with whom I developed a technique to reconstruct cloud geometry using the miraMACS cloud radar during his master thesis. I am also grateful to Petra Hausmann, Linda Forster and Hans Grob for their support during campaigns, enlightening talks and for being great roommates!

A big thanks goes to Markus Garhammer and Hilbert Wendt for solving administrative matters and Meinhard Seefeldner and Anton Lex for their great support in constructing and building the stray light protection and many other mechanical parts for the specMACS system. Karim Lenhard and Peter Gege (IMF) are acknowledged for their support during the laboratory characterization. Without the help and contribution of Andreas Baumgartner (IMF), the detailed characterization of *specMACS* would not have been possible. I would also like to thank enviscope GmbH (Dr. D. Schell), Uni Leipzig (Prof. M. Wendisch), Max Planck Institute for Chemistry (Prof. U. Pöschl) and DLR Institute of Atmospheric Physics (Prof. M. Rapp) for their support in adapting and operating specMACS on HALO. Thanks also go to Holger Siebert (TROPOS) and Tina Jurkat (DLR) for providing the in situ measurements. I am also grateful to Silke Groß who has generously given me time to finish this thesis in her group. Parts of this work were founded by the German Research Foundation (DFG) under grant number MA 2548/9-1.

I would like to acknowledge all colleagues from the Meteorological Institute Munich and the German Aerospace Center (DLR) for fruitful discussions and creating a pleasant working atmosphere. I could never have reached my goal without the support and comfort of the people around me, especially my family and friends. I especially want to thank my parents for the fundamental support and my girlfriend Lisa for her understanding and love during this time.